PHD

Molecular Simulations of MOF Nanoparticles for Drug Delivery (Alternative Format Thesis)

Thompson, Megan

Award date:
2021

Awarding institution:
University of Bath

Molecular Simulations of MOF Nanoparticles for Drug Delivery (Alternat Format Thesis)

Thompson, Megan

Award date:
2021

Awarding institution:
University of Bath

MOLECULAR SIMULATIONS OF MOF NANOPARTICLES FOR DRUG DELIVERY

Megan Thompson

A thesis submitted for the degree of Doctor of Philosophy

University of Bath

Department of Chemical Engineering

September 2020

COPYRIGHT STATEMENT

DECLARATION OF AUTHORSHIP

This thesis is composed of my original work and contains no material previously published or written by another person except where due reference has been made in the text. The contributions by others to the Journal articles used in this thesis is clearly stated in my thesis. The work published in the thesis was carried out since the commencement of my Research degree at the University of Bath and do not include any other work submitted to qualify for another degree or diploma at any other institution.

Signature of Author: 

ACKNOWLEDGMENTS

Firstly, I would like to thank my supervisor Professor Tina Düren for her kind help and support, not only throughout this project (without it I would not have been able to complete this thesis) but also throughout my undergraduate degree, and for convincing me that I was good enough to do a PhD in the first place. You're an amazing supervisor, thank you.

Secondly, I would like to thank the IT department at the University of Bath, as well as the current and former members of MOLSIM for the technical (and not so technical) support and discussions. In particular, a massive thank you to Dr Claire Hobday for her support and patience during the steep learning curve at the start of my PhD, and to Dr Stephen Wells for his collaboration and listening to my rantings when learning how to bash script.

Thirdly, thank you to my friends both at and outside the university. To those outside the university, thank you for your patience with me over the past couple of years, and for making me laugh and escape it all. To the friends I've made during my PhD, thank you for the countless lunches, cups of coffee, and the random outings. I had a great time with you (albeit sometimes painful thinking of all the running!).

Next to my family both present and otherwise. The last few years have been difficult for everyone, but despite everything you've always encouraged me to do the best that I can. Sometimes I forget how lucky I am to have all the support that you provide. Thank you for everything and helping me to get to where I am today, I couldn't have done it without you.

Finally, to my fiancée / pandemic lockdown husband, Alastair. I could write a list of the reasons why I am grateful to you, but that would be a thesis in itself!

ABSTRACT

Metal-organic framework (MOF) nanoparticles are highly promising drug delivery carriers for chemotherapy due to their tailorable properties, biocompatibility and responsiveness to external stimuli. However, MOFs are typically characterised as infinite repeating crystals, and there is limited thermodynamic insight as to how the properties and performance of a MOF change as a function of its particle size. It is also not clear what properties are ideal for drug delivery, or what simulation methods should be used to best mimic drug uptake and delivery experiments.

In this thesis, molecular simulations were used to elucidate the particle-size influence on guest-molecule adsorption and induced framework flexibility in a flexible MOF, DUT-8(Ni), with various external surface functionalities. Standard and novel simulation techniques were also used to model the uptake and release of cisplatin (a chemotherapy drug) inside biocompatible MOFs UiO-66 and UiO-66(NH_2) and compared to experimental results to test the advantages and limitations of each method. The simulation methods were finally used to test property – performance relationships in a series of biocompatible and pH sensitive MOFs as cisplatin delivery carriers, to pinpoint a selection criterion for MOFs used in further cancer-treatment research.

Overall, the external surface is not important for simulations in which the results mainly depend on the non-bonded interactions because the influence of the external surface on interaction energies is short-ranged. However, the external surface significantly contributes to the internal energy of the framework, hence it is important when characterising a MOF's structural responses to external stimuli. Experimental drug uptake and delivery is carried out in aqueous solution. Simulations with and without water show that the non-solvated models can be misleading, and it is therefore crucial to understand the limitations of solvent free models whenever they are applied in drug delivery research. Finally, simulations of cisplatin uptake and release in potential MOF carriers show that wide pores interconnected by large windows will enhance drug molecule uptake from solution, which relies on the accessible pore volume and the driving force / energy barriers associated with uptake. Retention can be enhanced by creating large diffusion energy barriers. This can be achieved by functionalising the framework's channels to get strong, dispersed adsorption sites, or by reducing the pore-window size, however the latter will also compromise drug-molecule uptake.

TABLE OF CONTENTS

LIST OF ABBREVIATIONS

Main Acronyms

MOF	Metal-organic Framework
CPT	Cisplatin (*cis*-diaminedichloroplatinum (II))
SOL	Water
MC	Monte Carlo
MD	Molecular dynamics
GCMC	Grand-canonical Monte Carlo
DFT	Density functional theory
SMD	Steered molecular dynamics
GASP	Geometric analysis and simulation of polyhedra
OFAST	Osmotic framework adsorbed solution theory
BAR	Bennetts acceptance ratio
BFDH	Bravais-Friedel-Donnay-Harker
PBC	Periodic boundary conditions

MOF Related Acronyms

UiO	University of Oslo
DUT	Dresden University of Technology
ZIF	Zeolitic-imidazole framework
IRMOF	Iso-reticular metal-organic framework
BDC	Benzene dicarboxylate
BPDC	Biphenyl dicarboxylate
TPDC	Triphenyl dicarboxylate
NDC	Naphthalene dicarboxylate
IM	Imidazole

Other

CSD	Cambridge Structural Database
BET	Brunauer–Emmett–Teller
KS	Kohn Sham
PW	Planewaves
PBE	Perdew–Burke-Ernzerhof
STO	Slater type orbitals
GTO	Gaussian type orbitals
GPW	Gaussian planewaves
LDA	Local density approximation
GGA	Generalised gradient approximation

CHAPTER 1. INTRODUCTION

1.1. Metal-organic frameworks

Metal-organic frameworks (MOFs) consist of metal nodes attached by coordination bonds to multidentate organic ligands, forming typically microporous (pore diameter < 2 nm [1]) or mesoporous (pore diameter 2 – 50 nm [1]) crystalline materials. The metal nodes consist of either a single metal cation (for example, a subclass of MOF, "zeolitic imidazole frameworks" consist of single metal ions such as Zn(II) or Co(II) connected by imidazolate-type organic ligands [2]) or a cationic inorganic cluster (for example, a prototypical MOF called UiO-66 consists of $Zr_6O_4(OH)_4$ nodes coordinated by bidentate aromatic ligands [3]). These precursors self-assemble into crystals when exposed to the correct solvothermal conditions (i.e. the application of solvent and high temperatures to enhance interactions between the precursors spurring crystallisation).

One of the first documentations of MOFs was in 1965 when Tomic formed "coordination polymers" (another term used to describe MOFs) via solvothermal synthesis. They found that the thermal stability of the as-made structures depended on the metal used, for instance metal ions less-able to change their ionic valency form more stable structures [4]. In their work, the as-made materials were not strictly porous because they contained solvent, however it induced the idea that MOFs could exhibit permanent porosity because of space between the metal nodes created by the organic ligands. There was limited research in the decades following this preliminary work, largely due to difficulties associated with the synthesis of MOFs. More specifically, the aim of synthesis is to create a material with predetermined properties (such as pore size, in the case of porous materials). This is particularly troublesome with MOFs because their insolubility means synthesis must be carried out in a single step. Therefore, the reactants must be subunits of the target material (the "molecular building block" approach in which literal fragments of the product are used as reactants), and the methodology must be capable of using those subunits to create a crystalline product [5]. Other issues with MOF synthesis that initially hindered their production included the lack of control associated with the orientation of building units, and accessing the pores was difficult due to strong guest-host interaction energies which caused frameworks to collapse upon solvent removal [6, 7].

It was over 30 years since the work of Tomic that MOF research rapidly accelerated following pioneering work from Yaghi and co-workers: In 1999, they used the molecular building block approach to synthesise one of the first MOFs to display permanent porosity, MOF-5. Their work showed (by determining N_2 adsorption isotherms) that MOF-5 was highly porous after desolvation (something that had been previously difficult to achieve due to framework collapse during solvent removal), with a pore volume of ~ 0.6 cm^3/cm^3 (compared to < 0.47 cm^3/cm^3 for zeolites), and that MOF-5 undergoes reversible adsorption/desorption, hence exhibits permanent porosity [8]. X-Ray diffraction showed that the structure of MOF-5 could be predicted from the building units (BDC and $Zn(NO_3)_2.4H_2O$) and that it is stable up to 300 °C. X-ray diffraction of N_2 and Ar adsorbed in MOF-5 showed that it had a larger surface area than expected (3,800 m^2/g) due to surprising adsorption sites surrounding the aromatic functional group of the BDC ligands [8, 9]. Amongst other uses, high surface area adsorbents are used to reduce the energy intensity of gas adsorption processes, hence the high surface area of MOF-5 compared to conventional adsorbents (such as zeolites ~ < 720 m^2/g [10], and activated carbons ~ 500 – 1,500 m^2/g, though the maximum reported < 3,000 m^2/g [11, 12]) sparked a lot of interest in the development of MOFs.

Shortly after the initial synthesis and characterisation of MOF-5, Eddaoudi et al systematically synthesised a collection of MOFs with the same underlying topology as MOF-5 but with different pore sizes and chemical functionalities. Each of these isoreticular MOFs (i.e. a collection of MOFs with the same underlying topology, in this case known as the IRMOF series) was synthesised using the same reaction conditions but different organic ligands. Therefore, based on the secondary building units added to the reaction mixture, they had prior knowledge of the structures before they were synthesised [13]. As well as desirable material properties such as the porosity and surface area, this pioneering research highlighted several important advantages of MOFs compared to other microporous materials. Firstly, the pore size and shape can be dictated by precursors, meaning MOFs can be tailored for specific applications. Secondly, reticular synthesis (i.e. the systematic design of MOFs based on precursors and the ability to predict structures pre-synthesis) allows structural properties to be tuned methodologically. Finally, MOFs with the same topology can have different functionalities (or a variety of functionalities in the same framework) by adding functional groups to the ligands [14].

Since these pioneering works, MOFs have been extensively shown to exhibit large pore cavity sizes and porosities typically exceeding 50 % [14], enabling a high loading of guest molecules [15] or the incorporation of large guest molecules [16] into the framework. Furthermore, their typically well-defined pore windows have demonstrated the potential of MOFs in applications reliant upon molecular sieving (e.g. separation [17] and target-specific catalysis [18]), and their large internal surface areas (typical BET surface areas for MOFs are > 1,000 m^2/g [14]) have shown huge potential for enhanced adsorption (e.g. in gas storage and catalysis applications [19]). Because of the clear advantages of MOFs compared to more conventional porous materials, there has been an exponential increase in the number of MOFs synthesised, characterised, and published in the Cambridge Structural Database (CSD) [20]. In 2019, there was ~ 96,000 MOFs recorded in the CSD and based on a hypothetical database built up from all possible combinations of molecular building units, there could be ~138,000 in future [21, 22]. As seen by the large number of published structures, MOF synthesis and characterisation techniques are now well developed, however there remain challenges, for example associated with precise control of functional group positions, pore size, shape and stability [23].

The exponential growth of MOF entries in the CSD has been largely due to vast amounts of research on enhancing their properties for specific applications. For example, to enhance the internal surface area, ligands with high denticity and distributed functional groups tend to be used [24]. To date, DUT-60 has the largest recorded accessible surface area (7,800 m^2/g) and pore volume (90.3 %) [25], and hypothetically MOFs with surface areas > 14,000 m^2/g could be synthesised, but there remain challenges in achieving this goal such as the collapse of frameworks upon desolvation and interpenetration of frameworks during crystal formation (i.e. frameworks grow into each other's pore space, a problem which can be solved in some cases by varying the concentrations of reactants) [19]. In situations where larger guest molecules are used, researchers have also focussed on increasing the pore size to accommodate such guests. Intuitively, the main approach to increase the pore size would be to use longer ligands, however this results in synthesis challenges such as the interpenetration of frameworks [14]. Rod-shaped molecular building units (i.e. chains of metal – carboxylate) were found to prevent interpenetration due to their intrinsic packing in crystals (for example, the mesoporous framework MOF-74 is only accessible via 1-D [26]).

As in the pioneering work of Edduadi et al [13], a lot of the structural development of MOFs was carried out using the concept of reticular synthesis in which the properties of a

prototypical structure such as HKUST-1 [27] and UiO-66 [3, 28] are modified. One of the key reasons for the use of reticular synthesis is to create a family of MOFs with a shared desired property. For example, similar to many MOFs MOF-5 has limited industrial use because weak Zn(II) – O bonds are susceptible to water, meaning it will degrade in moist conditions [29]. In comparison, UiO-66 consists of the same 1,4-BDC ligands, but instead has $Zr_6O_4(OH)_4$ nodes which coordinate to twelve ligands (as opposed to six ligands that coordinate the Zn_4O nodes in MOF-5). Zirconium forms strong bonds with the carboxylate groups of 1,4-BDC ligands, and its high valency (forming the large metal clusters) results in a high charge density of the nodes, enhancing coordination bonds in UiO-66, granting it stability in water, organic solvents, and across a broad range of temperatures making it a strong potential candidate for a variety of industrial processes. To retain the good stability whilst increasing the pore volume and window aperture, Cavka et al used the same metal nodes but increased the ligand size to synthesise the isoreticular structures UiO-67 (biphenyl-dicarboxylate ligands) and UiO-68 (terphenyl dicarboxylate ligands) [3]. These concepts are illustrated in Figure 1.1.

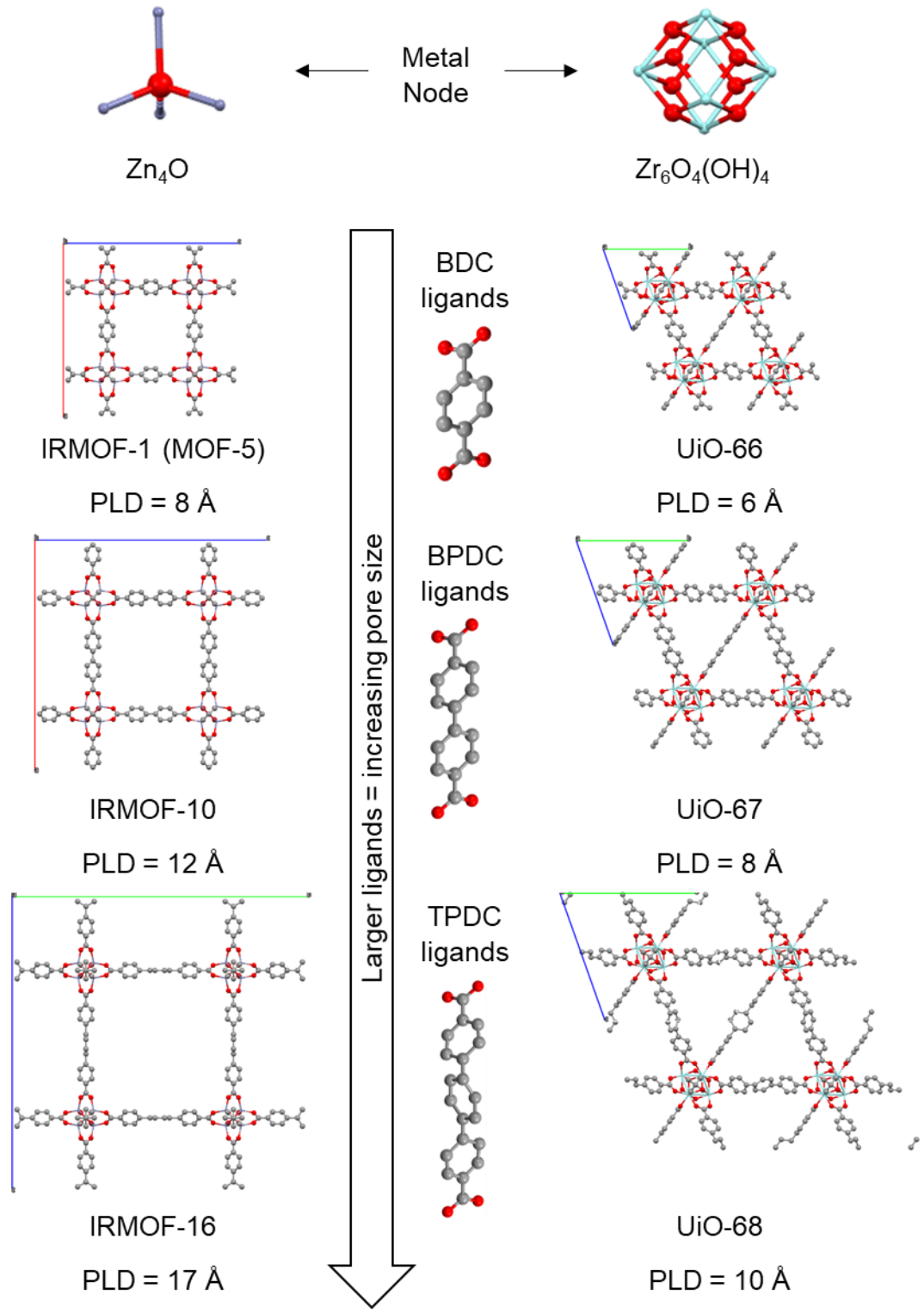

Figure 1.1. Fine-tuning the properties of metal-organic frameworks by variation of the metal nodes and organic ligands [3, 13, 30]. Colour scheme: purple = Zn, blue = Zr, grey = C, red = O. Hydrogens have been omitted for clarity. (PLD = pore-limiting diameter, the smallest opening that a guest molecule would need to pass in order to diffuse through the crystal)

Overall, numerous important achievements have been made which highlight the potential of MOFs in real-life applications [31]. For instance, as mentioned many MOFs are susceptible to hydrolysis, therefore losing their porosity in the presence of water vapour. However, based on prototypical structures (such as ZIF-8 [2] and UiO-66 [3]) a variety of MOFs which are less susceptible to chemical degradation due to strong covalent bonding and hydrophobicity have been developed, as highlighted in the review by Ding et al [32]. As well as the record internal surface areas and porosities, other major achievements include (but are not limited to) the synthesis of MOFs that can host catalytic reactions inside the pores (e.g. in MOF-11, "open metal sites" / unsaturated nodes are created by removing water from the Cu-paddlewheel post synthesis forming Lewis acid sites [33]), the addition of amine functionality inside the frameworks (e.g. using ligands with electronegative groups that can coordinate to amine functionalised molecules [34]), the precise control of particle size (e.g. by manipulating the rate of nucleation in the reaction mixture [35]), and the development of MOFs that respond to external stimuli such as pressure and temperature [36].

MOFs have been successfully used in some industrial applications, such as trapping toxic gas and fruit ripening reduction [37]. Other upcoming industrial applications for MOFs include their use in separation processes (e.g. CO_2 or SO_2 capture from flue gas, because the uniformly sized micropores of MOFs segregate molecules based on their size and shape, and they can be synthesised with open metal sites, which are strong adsorption sites for electron rich species such as sulphurous compounds, water and so on [38, 39]), gas storage (e.g. large quantities of H_2, a green renewable fuel, can be stored at low pressure because of the large internal surface areas and porosity of MOFs [40]), and heterogeneous catalysis (e.g. methanol synthesis from syngas, because the uniform, open pore network of MOFs will hinder the diffusivity of large guest molecules whilst allowing smaller guest molecules to pass unhindered, and their large internal surface areas allow for a high density of active sites [31, 41, 42]).

Though MOFs are promising for such industrial applications, it is unlikely that they will replace the established adsorbents such as zeolites or activated carbons currently used. Firstly, many MOFs show poor stability in the presence of polar compounds (which interfere with the coordination bonds between the metal nodes and organic ligands [29, 43]), and they are associated with high production costs (nearly an order of magnitude higher than the production cost of most zeolites, due to the cost and lack of availability of the organic ligands) [44]. Secondly, industrial-scale applications require good space-time-yields of

synthesis for economic efficiency, which is difficult because MOFs are typically formed in dilute solutions with long reaction times (that said, promising contributions have recently been made towards the large-scale synthesis of MOFs such as those described in the review by Dunne et al [45]) [46]. Instead, it is far more likely that MOFs will be commercially used in smaller, more niche applications (i.e. in sectors with typically higher production costs and consumer prices, such as the pharmaceutical industry).

Recently there has been a major focus on the use of MOFs in biomedical applications (as highlighted in the review by Yang et al [47]), largely due to the aforementioned economic reasons, and the fact that some MOFs are endogenous (with zinc or calcium metal nodes). One of the major applications is as bioimaging agents. For example, Sene et al loaded an MRI contrasting agent (maghemite) onto the external surface of MIL-100(Fe) and an anticancer drug (doxorubicin) into the pores. The contrasting agent enhanced relaxivity (relaxation rates of proton spins in nearby water molecules, used to improve the contrast of MRI scan images), while the loaded doxorubicin achieved targeted drug delivery [48]. Another biomedical application for MOFs is biosensing. For example, Hu et al loaded gold nanoparticles into MIL-101 and incorporated glucose oxidase and lactate oxidase onto the external surface for the detection of glucose and lactate. Upon detection, an inactive reporter molecule (leucomalachite green) oxidised into an active probe molecule (malachite green) enhancing the Raman signals (which provide information of the chemical structures) [49]. Bio-catalysis is another area where MOFs are highly promising, for example Navarro-Sánchez loaded the enzyme protease into the mesopores of MIL-101(Al)-NH_2 and exposed it to harsh environments that would otherwise denature the enzyme (extreme pH, temperatures up to 95 °C, and competitor enzymes), finding that the MOF stabilised protease enabling higher activities under the tested conditions [50]. Finally, MOFs are extremely promising drug delivery carriers.

1.2. Drug delivery

Currently, one of the main drug delivery challenges is associated with chemotherapy. As an overview, one in two people are diagnosed with cancer in their lifetime, and the main method for treating cancer is chemotherapy. During chemotherapy, drugs ("chemotherapeutics" which are usually cytotoxic) are intravenously administered into the patients. One of the most common World Health Organisation [51] approved chemotherapeutics is cisplatin (*cis*-diamminedichloroplatinum (II), $Pt(NH_3)_2Cl_2$), which is effective against various types of

cancer, for example soft tissue cancer and sarcomas. Cisplatin is a cytotoxic drug that attacks dividing cells by cross-linking with purine bases in DNA. Cell regulation mechanisms attempt to fix the damaged DNA, and when this fails the cells undergo controlled self-destruction (apoptosis) [52]. Unfortunately however, cancer is difficult to treat for a multitude of reasons, including (but not limited to) its reoccurrence (a general belief is that tumours grow from a single stem cell which are slow growing and hence resistant to chemotherapeutics), the similarity of cancer DNA to normal DNA, that no two cancers are the same, and that there are no specific biomarkers thus making tumours difficult to target [53]. Because of the lack of distinguishing features, chemotherapeutics such as cisplatin are non-specific and will target any dividing cells (cancerous or not), leading to the harmful side effects of chemotherapy such as (but not limited to) nausea, immunosuppression, haemorrhages and kidney problems. Non-specific drug administration also reduces the dosage reaching the tumour, enabling it to develop drug resistance [52].

Targeted drug delivery would be a viable method to overcome most of the aforementioned issues. One tactic is to tailor the drugs to target cancer cells. For example, healthy cells metabolise using oxidative phosphorylation in normal aerobic conditions, whereas cancer cells mainly use glycolysis. Attempts have been made to inhibit glycolysis, however this has so far been unsuccessful as cancer cells can shift their primary metabolism mechanism. More recent research has been aimed at using cationic drugs to target the cancer cell mitochondria, which have a more negative potential compared to normal mitochondria [54]. Instead, World Health Organisation approved cytotoxic drugs (which are known to be effective against cancer [51]) can be loaded into a non-toxic carrier. An ideal carrier would harbour the cargo through healthy parts of the body and only release it in the vicinity of a tumour, enhancing the payload whilst reducing harmful side effects.

The hunt for an ideal nanocarrier is often met with a compromise. Organic carriers (e.g. liposomes [55], dendrimers [56], micelles [57], and peptides [58]) are biocompatible (non-toxic), however they tend suffer from premature release and low drug loading capacity [47]. Instead, inorganic carriers (such as silica nanoparticles [59] and oxides [60]) were established to improve the quantity of drugs reaching the tumour, yet they themselves have harmful side effects (for instance they can be poisonous and/or induce an immune response) [61]. MOFs on the other hand are one of the most promising nanocarriers, because their large porosities and surface areas enable high drug loading capacities, weak coordination bonds and careful selection of building units (e.g. the use of Zn ions as opposed to toxic

alternatives) render some MOFs biocompatible, and the vast number of building units make it possible to fine tune the framework properties (for example to improve colloidal stability, prevent premature release, or to induce target recognition) [47].

Several experimental studies have highlighted the strong potential of MOF nanocarriers in chemotherapy [47]. For example, Zhoe et al loaded a MOF (PCN-333) with a non-toxic drug (paracetamol) and tyrosinase enzyme. This system acted as a nanoreactor, and when PCN-333 was taken up by cancer cells the tyrosinase converted the paracetamol to produce toxic products [62]. Another advantage of MOF nanocarriers is that they can respond to certain external stimuli (such as pH). Structural variation in response to pH change is particularly interesting for cancer research as the extracellular pH surrounding a tumour tends to be acidic (increased rates of glycolysis by cancer cells increases their extracellular acidity: pH<6.8 compared to pH=7.2 in healthy areas of the body [63]). For example. Zhang et al loaded doxorubicin into a mesoporous MOF (MIL-101) with functionalised external surface. Benzoic-imine bonds on the surface induced a pH responsiveness which released the drug cargo [64].

There still however remain several challenges associated with the use of MOFs as nanocarriers. Firstly, to enhance uptake into cancer cells (i.e. active targeting) or accumulation in the vicinity of a tumour (i.e. passive targeting which uses the enhanced permeability and retention effect) while reducing bioaccumulation in healthy parts of the patient and the possibility of an immune response, the external surfaces need to be functionalised and there needs to be a precise tailoring of the particle morphology (typically nanoparticles ~ 20 – 200 nm diameter are needed) [47, 65]. Secondly, there are severely limited in-vivo studies to validate the biocompatibility of MOFs which otherwise shown impressive drug delivery capabilities, and toxicology reports in literature are often contradictory [66]. For example the contrasting toxicology studies on ZIF-8 nanoparticles by Vasconcelos et al (who reported that ZIF-8 is non-cytotoxic [67]) and Tamames-Tabar et al (who reported that ZIF-8 is toxic as zinc competes with Fe and Ca ion in ion channels [68]). Typically, a safe choice would be MOFs consisting of endogenous or bioactive building blocks (e.g. Fe, Zr, or Zn nodes) [47]. Finally, though these and other experimental studies have been very promising and provided extremely insightful results, research has predominantly focussed on well-known MOFs (e.g. MIL-100, MIL-101, ZIF-8, UiO-66) with no clear indication as to why these MOFs were chosen and whether they are the best suited candidate for the job. In other words, for a drug carrier system, it is not yet clear what

structural properties researchers should be aiming for in a MOF to achieve the best uptake and delivery. This is where molecular simulations come in handy.

1.3. Molecular simulations of drug delivery

Molecular simulations in no way can replace experimental studies, instead they complement each other. In experiments, real-life macroscopic data is gathered (averaged across many particles and often the time duration of the experiment). Molecular simulations mimic experimental results by calculating microscopic properties of an atomistic system (which due to computational limitations, are typically less than several thousand atoms). For comparison to experimental results, the microscopic properties are averaged across sufficiently large ensemble collections or long simulation times, using simulation techniques called Monte Carlo (MC) and Molecular Dynamics (MD) respectively. Ultimately, by collecting the same data using atomistic scale models, it is possible to uncover in-depth thermodynamic details behind experimental results that would not otherwise be possible. To ensure a theoretical model is reliable, simulation results must be validated against experimental data. Discrepancies between experimental and theoretical results are usually caused by incorrect definitions of interatomic interactions or imperfections in the real-life (versus the idealised simulated) material. If the model-derived properties are compared to the experimental values and they agree, this suggests the interatomic interactions are correctly defined. A good model can then be used to test new theories, that is if an analytical theory matches the simulated results that apply the same theory, it can be validated [69]. As well as theory validation and the provision of in-depth thermodynamic insights, a working model can also be used to highlight the most influential parameters on certain properties. Furthermore, it can be tested on hypothetical materials or extreme conditions that would not be possible experimentally. Finally, simulations can often be transferred between similar systems to produce vast quantities of data quickly, which for instance is particularly useful when screening MOFs for drug delivery [70, 71].

Drug uptake and release depend on host-guest interaction energies and the MOF pore network. However, as detailed in the review by Kotzabasaki et al, there is limited thermodynamic insight into drug uptake and release mechanisms. The available studies in literature tend to use standard MC and MD simulations to capture the aforementioned effects [71]. For example, several groups (Liu et al [72], Wang et al [73], Li et al [74]) used grand-canonical MC (GCMC) simulations to get insightful information behind the uptake and

release of an anticancer drug 5-FU (Fluorouracil). They found that uptake and release are predominantly governed by the pore volume and isosteric heats of adsorption (a direct measure for the strength of the interaction between the solid and the fluid) respectively. To enhance loading whilst reducing release rates, several groups have focussed on adding defects to MOFs (missing ligands or nodes from the crystalline structure) or functionalising them (by incorporating for instance hydrophilic/hydrophobic groups such as NH_2, OH, CH_3 to the organic ligands). For example, Filippousi et al compared MOFs (UiO-66 and UiO-67) with missing ligand defects for their interaction energies and uptake of cisplatin and paclitaxel using first principles (*ab-initio*) MD simulations (AIMD). They found that defects create favourable adsorption sites, and that the accessibility of these adsorption sites increases with the pore size [75]. GCMC and *ab-initio* simulations have also been used to highlight that improved interaction energies (hence release kinetics) are achievable by functionalising MOFs, for example adding polar groups to the organic ligands which establish hydrophilic drug-framework hydrogen bonding or hydrophobic groups to increase water stability. The addition of functional groups also reduces the pore volume reducing uptake [71, 76-78].

1.4. Research motivation

Most computational studies focus on characterising MOFs based on the properties of the bulk material (i.e. the repeating crystalline unit). As mentioned, to avoid an immune response and enhance uptake into cancer cells, MOF nanoparticles (20 – 200 nm diameter) are required [47, 65]. At this length scale, the external surface area per unit volume increases (comparing 100 μm and 100 nm diameter spherical crystals, the external surface areas per unit volume are 6×10^4 m^2/m^3 and 6×10^7 m^2/m^3 respectively). Therefore, the external surface will be more influential on performance related properties such as the guest molecule uptake and guest-host interaction energies [79]. In Chapter 3, nanoparticles and microparticles of a complex MOF called DUT-8(Ni) [80] have been simulated to study the effects of the external surface on the framework properties. Due to the complexity of the framework (discussed further in the chapter) and the availability of experimental data to corroborate the simulations, a relatively simple N_2 guest molecule has been employed to focus predominantly on how the external surface influences properties such as the MOF internal energy and its structural changes as a result of guest molecule adsorption. In doing so, it has been determined whether it is enough to model the bulk material or if it is important to consider surface effects.

In Chapters 4 – 6, the uptake and release of one of the world leading cytotoxic chemotherapeutics (cisplatin) [51], is quantified in a variety of different MOFs:

Chapter 4 focusses on the validity of different simulation techniques when quantifying cisplatin uptake and release. To do this, biocompatible MOF UiO-66 and an amine functionalised version UiO-66(NH_2) have been used due to the available experimental data for comparison [81]. As mentioned, the majority of computational studies to date have utilised standard techniques such as MC, MD and *ab-initio* simulations [71]. As well as these, less common techniques such as steered-MD, umbrella sampling [82, 83], alchemical simulations [84], and GASP [85] have been used to look at the insight and limitations associated with different computational methods. Furthermore, the inclusion of water in MOF – drug delivery simulations is novel, and whilst the majority of simulation papers do not include water [71] it is integral in uptake and release experiments [47]. The impact of water on cisplatin uptake and release is also uncovered in Chapter 4, to test whether or not it is needed in drug – MOF simulations involving such polar guest molecules.

Using the methods investigated in Chapter 4, Chapter 5 compares the feasibility of two different techniques commonly used to enhance the uptake and retention of drug molecules in MOFs – adding defects [75, 86] or increasing the ligand size whilst adding functional groups [71, 76-78]. For this purpose, the water stable, biocompatible series of MOFs with increasing pore size: UiO-66, UiO-67, and UiO-68 were used [3] with and without hydrophilic amine functional groups [87, 88]. Due to the high connectivity of UiO-66 nodes and the use of monodentate carboxylic acids (modulators) during synthesis [87], UiO-66 is prone to missing ligand defects [88]. *Ab-initio* simulations have been used to predict the likelihood of synthesising a given defect concentration when using modulators of varying acidity, and MD simulations were used to determine the cisplatin retention properties of defective UiO-66 against UiO-67 and UiO-68 with and without hydrophilic functional groups.

Finally, Chapter 6 uses the previously drawn conclusions regarding modelling nanoparticles (Chapter 3), modelling techniques and their limitations for drug delivery (Chapter 4), and the most reliable method for improving release kinetics while maintaining a good hypothetical uptake (Chapter 5), to screen a selection of pH sensitive ZIFs as cisplatin drug delivery carriers [89]. The benefit of the selected ZIFs include their biocompatibility as well

as their stability in normal parts of the body (pH = 7.2) and lack of stability in the acidic extracellular space surrounding a tumour (pH < 6.8) [63].

1.5. Chapter 1 References

1. Sing, K.S.W., *Reporting physisorption data for gas/solid systems with special reference to the determination of surface area and porosity (Recommendations 1984).* Pure & Applied Chemistry, 1985. **57**(4): p. 603.
2. Park, K.S., et al., *Exceptional chemical and thermal stability of zeolitic imidazolate frameworks.* Proceedings of the National Academy of Sciences, 2006. **103**(27): p. 10186-10191.
3. Cavka, J.H., et al., *A New Zirconium Inorganic Building Brick Forming Metal Organic Frameworks with Exceptional Stability.* Journal of the American Chemical Society, 2008. **130**(42): p. 13850-13851.
4. Tomic, E.A., *Thermal stability of coordination polymers.* Journal of Applied Polymer Science, 1965. **9**(11): p. 3745-3752.
5. Yaghi, O.M., M. O'Keeffe, and M. Kanatzidis, *Design of Solids from Molecular Building Blocks: Golden Opportunities for Solid State Chemistry.* Journal of Solid State Chemistry, 2000. **152**(1): p. 1-2.
6. Yaghi, O.M., et al., *Synthetic Strategies, Structure Patterns, and Emerging Properties in the Chemistry of Modular Porous Solids.* Accounts of Chemical Research, 1998. **31**(8): p. 474-484.
7. J. Kepert, C. and M. J. Rosseinsky, *Zeolite-like crystal structure of an empty microporous molecular framework.* Chemical Communications, 1999(4): p. 375-376.
8. Li, H., et al., *Design and synthesis of an exceptionally stable and highly porous metal-organic framework.* Nature, 1999. **402**(6759): p. 276-279.
9. Kaye, S.S., et al., *Impact of Preparation and Handling on the Hydrogen Storage Properties of Zn4O(1,4-benzenedicarboxylate)3 (MOF-5).* Journal of the American Chemical Society, 2007. **129**(46): p. 14176-14177.
10. Hauchhum, L. and P. Mahanta, *Carbon dioxide adsorption on zeolites and activated carbon by pressure swing adsorption in a fixed bed.* International Journal of Energy and Environmental Engineering, 2014. **5**(4): p. 349-356.

11. Otowa, T., R. Tanibata, and M. Itoh, *Production and adsorption characteristics of MAXSORB: High-surface-area active carbon.* Gas Separation & Purification, 1993. **7**(4): p. 241-245.
12. Saleem, J., et al., *Production and applications of activated carbons as adsorbents from olive stones.* Biomass Conversion and Biorefinery, 2019. **9**(4): p. 775-802.
13. Eddaoudi, M., et al., *Systematic design of pore size and functionality in isoreticular MOFs and their application in methane storage.* Science, 2002. **295**(5554): p. 469-72.
14. Furukawa, H., et al., *The Chemistry and Applications of Metal-Organic Frameworks.* Science, 2013. **341**(6149): p. 1230444.
15. Furukawa, H., et al., *Ultrahigh Porosity in Metal-Organic Frameworks.* Science (New York, N.Y.), 2010. **329**: p. 424-8.
16. Férey, G., *Hybrid porous solids: past, present, future.* Chemical Society Reviews, 2008. **37**(1): p. 191-214.
17. Li, W., et al., *Transformation of metal-organic frameworks for molecular sieving membranes.* Nature Communications, 2016. **7**(1): p. 11315.
18. Chang, N., et al., *Metal–Organic-Framework-Based Tandem Molecular Sieves as a Dual Platform for Selective Microextraction and High-Resolution Gas Chromatographic Separation of n-Alkanes in Complex Matrixes.* Analytical Chemistry, 2011. **83**(18): p. 7094-7101.
19. Farha, O.K., et al., *Metal–Organic Framework Materials with Ultrahigh Surface Areas: Is the Sky the Limit?* Journal of the American Chemical Society, 2012. **134**(36): p. 15016-15021.
20. Moghadam, P.Z., et al., *Development of a Cambridge Structural Database Subset: A Collection of Metal–Organic Frameworks for Past, Present, and Future.* Chemistry of Materials, 2017. **29**(7): p. 2618-2625.
21. Li, A., et al., *Enabling efficient exploration of metal–organic frameworks in the Cambridge Structural Database.* CrystEngComm, 2020. **22**(43): p. 7152-7161.
22. Wilmer, C.E., et al., *Large-scale screening of hypothetical metal–organic frameworks.* Nature Chemistry, 2012. **4**(2): p. 83-89.
23. Bosch, M., et al., *Stepwise Synthesis of Metal–Organic Frameworks.* Accounts of Chemical Research, 2017. **50**(4): p. 857-865.
24. Schnobrich, J.K., et al., *A Framework for Predicting Surface Areas in Microporous Coordination Polymers.* Langmuir, 2010. **26**(8): p. 5808-5814.

25. Hönicke, I.M., et al., *Balancing Mechanical Stability and Ultrahigh Porosity in Crystalline Framework Materials.* Angewandte Chemie International Edition, 2018. **57**(42): p. 13780-13783.
26. Rosi, N.L., et al., *Rod Packings and Metal−Organic Frameworks Constructed from Rod-Shaped Secondary Building Units.* Journal of the American Chemical Society, 2005. **127**(5): p. 1504-1518.
27. Furukawa, H., et al., *Isoreticular Expansion of Metal–Organic Frameworks with Triangular and Square Building Units and the Lowest Calculated Density for Porous Crystals.* Inorganic Chemistry, 2011. **50**(18): p. 9147-9152.
28. Garibay, S.J. and S.M. Cohen, *Isoreticular synthesis and modification of frameworks with the UiO-66 topology.* Chemical Communications, 2010. **46**(41): p. 7700-7702.
29. Greathouse, J.A. and M.D. Allendorf, *The Interaction of Water with MOF-5 Simulated by Molecular Dynamics.* Journal of the American Chemical Society, 2006. **128**(33): p. 10678-10679.
30. Panter, S. and P. Zarabadi-Poor, *Computational Exploration of IRMOFs for Xenon Separation from Air.* ACS omega, 2018. **3**(12): p. 18535-18541.
31. Czaja, A.U., N. Trukhan, and U. Müller, *Industrial applications of metal–organic frameworks.* Chemical Society Reviews, 2009. **38**(5): p. 1284-1293.
32. Ding, M., X. Cai, and H.-L. Jiang, *Improving MOF stability: approaches and applications.* Chemical Science, 2019. **10**(44): p. 10209-10230.
33. Chen, B., et al., *Cu2(ATC)·6H2O: Design of Open Metal Sites in Porous Metal−Organic Crystals (ATC: 1,3,5,7-Adamantane Tetracarboxylate).* Journal of the American Chemical Society, 2000. **122**(46): p. 11559-11560.
34. Keenan, L.L., et al., *Secondary amine-functionalised metal–organic frameworks: direct syntheses versus tandem post-synthetic modifications.* CrystEngComm, 2016. **18**(30): p. 5710-5717.
35. Usman, K.A.S., et al., *Downsizing metal–organic frameworks by bottom-up and top-down methods.* NPG Asia Materials, 2020. **12**(1): p. 58.
36. Liu, Z., L. Zhang, and D. Sun, *Stimuli-responsive structural changes in metal–organic frameworks.* Chemical Communications, 2020. **56**(66): p. 9416-9432.
37. *Frameworks for commercial success.* Nature Chemistry, 2016. **8**(11): p. 987-987.
38. Zhang, Z., et al., *MOFs for CO2 capture and separation from flue gas mixtures: the effect of multifunctional sites on their adsorption capacity and selectivity.* Chemical Communications, 2013. **49**(7): p. 653-661.

39. Zhang, Y., et al., *Efficient SO2 Removal Using a Microporous Metal–Organic Framework with Molecular Sieving Effect.* Industrial & Engineering Chemistry Research, 2020. **59**(2): p. 874-882.
40. Ahmed, A., et al., *Exceptional hydrogen storage achieved by screening nearly half a million metal-organic frameworks.* Nature Communications, 2019. **10**(1): p. 1568.
41. An, B., et al., *Confinement of Ultrasmall Cu/ZnOx Nanoparticles in Metal–Organic Frameworks for Selective Methanol Synthesis from Catalytic Hydrogenation of CO2.* Journal of the American Chemical Society, 2017. **139**(10): p. 3834-3840.
42. Li, Z., et al., *Platinum–nickel frame within metal-organic framework fabricated in situ for hydrogen enrichment and molecular sieving.* Nature Communications, 2015. **6**(1): p. 8248.
43. Chen, Y., et al., *Antenna-Protected Metal–Organic Squares for Water/Ammonia Uptake with Excellent Stability and Regenerability.* ACS Sustainable Chemistry & Engineering, 2017. **5**(6): p. 5082-5089.
44. Vikrant, K., et al., *Metal–organic frameworks (MOFs): potential and challenges for capture and abatement of ammonia.* Journal of Materials Chemistry A, 2017. **5**(44): p. 22877-22896.
45. Dunne, P.W., E. Lester, and R.I. Walton, *Towards scalable and controlled synthesis of metal–organic framework materials using continuous flow reactors.* Reaction Chemistry & Engineering, 2016. **1**(4): p. 352-360.
46. Yilmaz, B., N. Trukhan, and U. MÜLler, *Industrial Outlook on Zeolites and Metal Organic Frameworks.* Chinese Journal of Catalysis, 2012. **33**(1): p. 3-10.
47. Yang, J. and Y.-W. Yang, *Metal–Organic Frameworks for Biomedical Applications.* Small, 2020. **16**(10): p. 1906846.
48. Sene, S., et al., *Maghemite-nanoMIL-100(Fe) Bimodal Nanovector as a Platform for Image-Guided Therapy.* Chemistry, 2017. **3**(2): p. 303-322.
49. Hu, Y., et al., *Surface-Enhanced Raman Scattering Active Gold Nanoparticles with Enzyme-Mimicking Activities for Measuring Glucose and Lactate in Living Tissues.* ACS Nano, 2017. **11**(6): p. 5558-5566.
50. Navarro-Sánchez, J., et al., *Translocation of enzymes into a mesoporous MOF for enhanced catalytic activity under extreme conditions.* Chemical Science, 2019. **10**(14): p. 4082-4088.
51. *The selection and use of essential medicines.* World Health Organisation Technical Report Series, 2008(950): p. backcover, vii-174.

52. Dasari, S. and P.B. Tchounwou, *Cisplatin in cancer therapy: molecular mechanisms of action.* European journal of pharmacology, 2014. **740**: p. 364-378.
53. Chakraborty, S. and T. Rahman, *The difficulties in cancer treatment.* Ecancermedicalscience, 2012. **6**: p. ed16-ed16.
54. Kalyanaraman, B., *Teaching the basics of cancer metabolism: Developing antitumor strategies by exploiting the differences between normal and cancer cell metabolism.* Redox Biology, 2017. **12**: p. 833-842.
55. Catanzaro, D., et al., *Cisplatin liposome and 6-amino nicotinamide combination to overcome drug resistance in ovarian cancer cells.* Oncotarget, 2018. **9**(24): p. 16847-16860.
56. Myc, A., et al., *Targeting the efficacy of a dendrimer-based nanotherapeutic in heterogeneous xenograft tumors in vivo.* Anti-cancer drugs, 2010. **21**(2): p. 186-192.
57. Zhuang, W., et al., *A fully absorbable biomimetic polymeric micelle loaded with cisplatin as drug carrier for cancer therapy.* Regenerative Biomaterials, 2017. **5**(1): p. 1-8.
58. Lai, Y., et al., *An effective peptide cargo carrier for the delivery of cisplatin in ovarian cancer cells.* Dyes and Pigments, 2017. **143**: p. 342-347.
59. Park, S.S., et al., *Functionalised mesoporous silica nanoparticles with excellent cytotoxicity against various cancer cells for pH-responsive and controlled drug delivery.* Materials & Design, 2019. **184**: p. 108187.
60. Rosli, N.F., et al., *Graphene Oxide Nanoplatelets Potentiate Anticancer Effect of Cisplatin in Human Lung Cancer Cells.* Langmuir, 2019. **35**(8): p. 3176-3182.
61. Sheikh Tanzina, H. and C. Ezharul Hoque, *Recent Progress in Delivery of Therapeutic and Imaging Agents Utilizing Organic-Inorganic Hybrid Nanoparticles.* Current Drug Delivery, 2018. **15**(4): p. 485-496.
62. Lian, X., et al., *Enzyme-MOF Nanoreactor Activates Nontoxic Paracetamol for Cancer Therapy.* Angewandte Chemie International Edition, 2018. **57**(20): p. 5725-5730.
63. Sun, H., et al., *Warburg Effects in Cancer and Normal Proliferating Cells: Two Tales of the Same Name.* Genomics, Proteomics & Bioinformatics, 2019. **17**(3): p. 273-286.
64. Wang, X.G., et al., *A multifunctional metal-organic framework based tumor targeting drug delivery system for cancer therapy.* Nanoscale, 2015. **7**(38): p. 16061-70.

65. Abánades Lázaro, I., et al., *Surface-Functionalization of Zr-Fumarate MOF for Selective Cytotoxicity and Immune System Compatibility in Nanoscale Drug Delivery.* ACS Applied Materials & Interfaces, 2018. **10**(37): p. 31146-31157.
66. Sajid, M., *Toxicity of nanoscale metal organic frameworks: a perspective.* Environmental Science and Pollution Research, 2016. **23**(15): p. 14805-14807.
67. Vasconcelos, I.B., et al., *Cytotoxicity and slow release of the anti-cancer drug doxorubicin from ZIF-8.* RSC Advances, 2012. **2**(25): p. 9437-9442.
68. Tamames-Tabar, C., et al., *Cytotoxicity of nanoscaled metal–organic frameworks.* Journal of Materials Chemistry B, 2014. **2**(3): p. 262-271.
69. Frenkel, D. and B. Smit, *Understanding molecular simulation : from algorithms to applications. 2nd ed*. Vol. 50. 1996.
70. Bernini, M.C., et al., *Screening of bio-compatible metal–organic frameworks as potential drug carriers using Monte Carlo simulations.* Journal of Materials Chemistry B, 2014. **2**(7): p. 766-774.
71. Kotzabasaki, M. and G.E. Froudakis, *Review of computer simulations on anti-cancer drug delivery in MOFs.* Inorganic Chemistry Frontiers, 2018. **5**(6): p. 1255-1272.
72. Liu, J.-Q., et al., *A combined experimental and computational study of novel nanocage-based metal–organic frameworks for drug delivery.* Dalton Transactions, 2015. **44**(44): p. 19370-19382.
73. Wang, J., et al., *Combined experimental and theoretical insight into the drug delivery of nanoporous metal–organic frameworks.* Royal Society of Chemistry Advances, 2015. **5**(104): p. 85606-85612.
74. Li, F., et al., *Encapsulation of pharmaceutical ingredient linker in metal–organic framework: combined experimental and theoretical insight into the drug delivery.* Royal Society Chemistry Advances, 2016. **6**(53): p. 47959-47965.
75. Filippousi, M., et al., *Biocompatible Zr-based nanoscale MOFs coated with modified poly(ε-caprolactone) as anticancer drug carriers.* International Journal of Pharmaceutics, 2016. **509**(1): p. 208-218.
76. Chalati, T., et al., *Porous metal organic framework nanoparticles to address the challenges related to busulfan encapsulation.* Nanomedicine, 2011. **6**(10): p. 1683-1695.
77. Ma, D.-Y., et al., *Hydrostable and Nitryl/Methyl-Functionalized Metal–Organic Framework for Drug Delivery and Highly Selective CO2 Adsorption.* Inorganic Chemistry, 2015. **54**(14): p. 6719-6726.

78. Kotzabasaki, M., et al., *OH-functionalization strategy in Metal-Organic Frameworks for drug delivery.* Chemical Physics Letters, 2017. **685**: p. 114-118.
79. Zhang, C., et al., *Crystal-Size-Dependent Structural Transitions in Nanoporous Crystals: Adsorption-Induced Transitions in ZIF-8.* The Journal of Physical Chemistry C, 2014. **118**(35): p. 20727-20733.
80. Klein, N., et al., *Monitoring adsorption-induced switching by (129)Xe NMR spectroscopy in a new metal-organic framework Ni(2)(2,6-ndc)(2)(dabco).* Physical Chemistry Chemical Physics, 2010. **12**(37): p. 11778-84.
81. Mocniak, K.A., et al., *Incorporation of cisplatin into the metal–organic frameworks UiO66-NH2 and UiO66 – encapsulation vs. conjugation.* Royal Society Chemistry Advances, 2015. **5**(102): p. 83648-83656.
82. Torrie, G.M. and J.P. Valleau, *Nonphysical sampling distributions in Monte Carlo free-energy estimation: Umbrella sampling.* Journal of Computational Physics, 1977. **23**(2): p. 187-199.
83. Kumar, S., et al., *THE weighted histogram analysis method for free-energy calculations on biomolecules. I. The method.* Journal of Computational Chemistry, 1992. **13**(8): p. 1011-1021.
84. Bennett, C.H., *Efficient estimation of free energy differences from Monte Carlo data.* Journal of Computational Physics, 1976. **22**(2): p. 245-268.
85. Wells, S.A. and A. Sartbaeva, *GASP: software for geometric simulations of flexibility in polyhedral and molecular framework structures.* Molecular Simulation, 2015. **41**(16-17): p. 1409-1421.
86. Lin, S.-X., et al., *Effective loading of cisplatin into a nanoscale UiO-66 metal–organic framework with preformed defects.* Dalton Transactions, 2019. **48**(16): p. 5308-5314.
87. Schaate, A., et al., *Modulated Synthesis of Zr-Based Metal–Organic Frameworks: From Nano to Single Crystals.* Chemistry – A European Journal, 2011. **17**(24): p. 6643-6651.
88. Katz, M.J., et al., *A facile synthesis of UiO-66, UiO-67 and their derivatives.* Chemical Communications, 2013. **49**(82): p. 9449-9451.
89. Howarth, A.J., et al., *Chemical, thermal and mechanical stabilities of metal–organic frameworks.* Nature Reviews Materials, 2016. **1**(3): p. 15018.

CHAPTER 2: THEORY

Molecular simulations mimic real-life systems using atomistic models. Different levels of theory can be used to construct the model depending on the nature of the system and the properties of interest. “Classical simulations” are particularly useful when the properties of interest mainly rely on intermolecular interactions (e.g. adsorption and diffusion). In these simulations, atoms are treated as point nuclei that obey the laws of classical mechanics. Interatomic interactions in classical simulations are calculated from parameter sets called forcefields, and this calculation is relatively quick meaning that classical simulations can be used to model large systems within computational limitations. Forcefields tend to be derived from experiments or *ab-initio* simulations, therefore the reliable use of a forcefield depends on how it was parameterised and its transferability between systems. *Ab-initio* simulations also treat atoms as point nuclei, but the forces between atoms are determined from the electronic structure which is resolved for every static configuration of nuclei. Therefore, *ab-initio* simulations determine energies and forces with far greater accuracy than classical simulations. However, the high computational cost (that scales exponentially with the number of atoms) limits the system size that can be feasibly modelled using *ab-initio* simulations.

2.1. Crystallographic models

Both classical and *ab-initio* molecular simulations require an input model that is representative of the of the real-life system. For MOFs, the input models are normally crystallographic structures which have been refined using experimental techniques such as X-ray diffraction [1] and collated in databases such as the Cambridge Structural Database (CSD) [2]. Within reasonable computational limitations, classical simulations can handle several thousand atoms, and *ab-initio* simulations can handle several hundred atoms [3]. However, even small MOF nanoparticles (normally < 100 nm [4]) contain millions of atoms. For example, take UiO-66 which consists of 456 atoms in a 2.1 nm^3 unit cell. Now imagine a small spherical UiO-66 nanoparticle of 50 nm diameter. It has a volume of 65500 nm^3 and contains 14 million atoms. To work around this problem, periodic boundary conditions (PBCs) are employed in this work, which make use of the fact that MOF crystals are built up of repeating unit cells.

PBCs duplicate the original unit cell into an infinite lattice of identical cells. Atoms within the primitive unit cell then interact with other atoms in the unit cell as well as atoms in neighbouring unit cells. If the simulation moves an atom through the PBC (i.e. out of the original primitive unit cell into a neighbouring cell), an identical atom reappears at the opposite edge of the primitive unit cell. To prevent atoms inside the primitive cell interacting with their own periodic image, the "minimum image convention" is used. This means that the size of the primitive unit cell must be at least double the cut-off radius (i.e. the distance at which pairwise interactions are truncated, see Section 2.3.1). If the minimum image convention is not obeyed, unrealistic artefacts result from interactions between a particle and its periodic image [5]. Figure 2.1 illustrates these concepts more clearly.

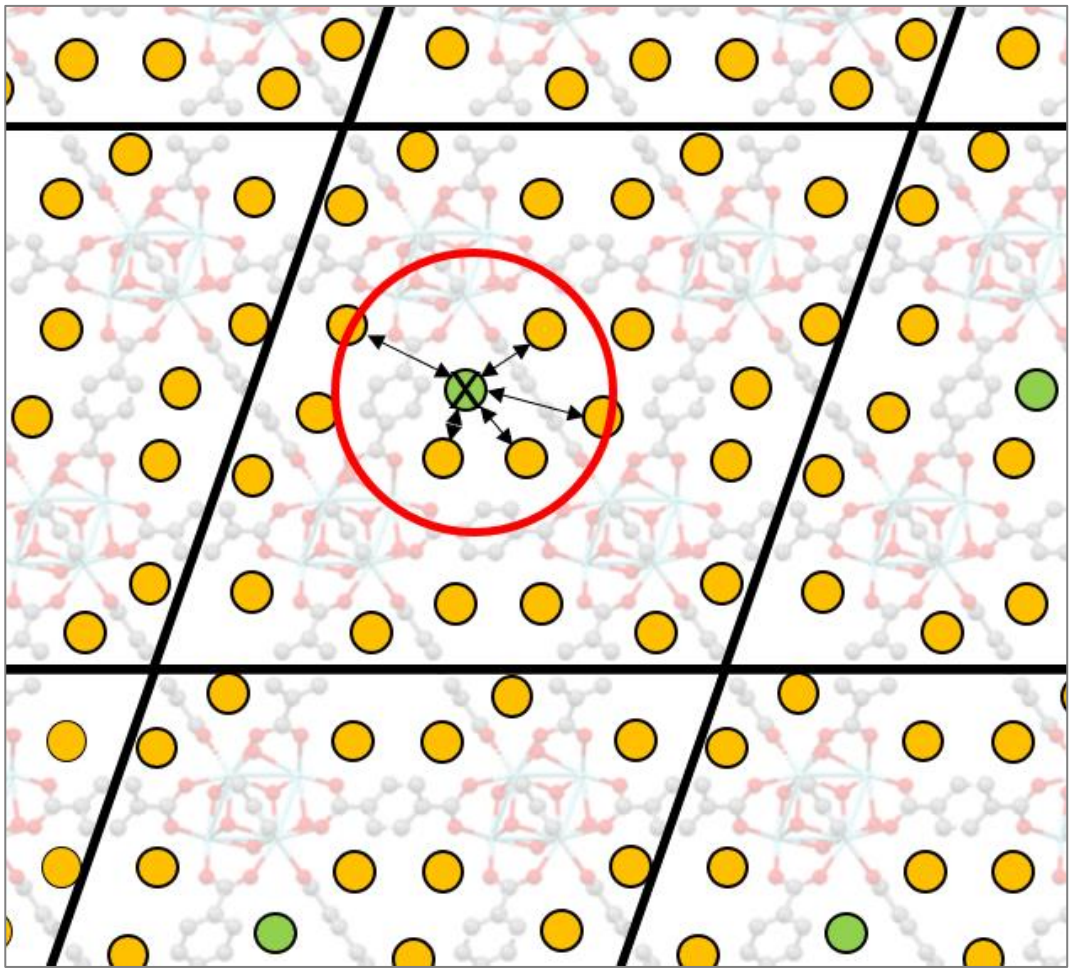

Figure 2.1. Periodic boundary conditions (represented by thick black lines) surrounding the unit cell of UiO-66 as an example. For the system to obey the minimum image convention, pairwise interactions must be truncated using a cutoff radius (thick red line) less than or equal to half the unit cell length.

The input model will significantly influence how well the simulations represent real-life experiments. For example, if large microparticles were modelled using finite boundary

conditions (i.e. impenetrable walls that completely segregate the system), a substantial fraction of atoms would be on an effective external surface. This is an unrealistic representation of real-life microparticles which must be modelled using PBCs in three dimensions [5]. Conversely, MOF nanoparticles have large external surface area to volume ratios, and therefore the external surface will influence the framework properties [6]. Either finite boundary conditions or PBCs can be used to model the external surface if there is a sufficient vacuum gap implemented between the MOF surface and the unit cell boundary. To model segregated nanoparticles, "sufficient vacuum gap" entails that the external surfaces of MOF nanoparticles in adjacent unit cells do not interact (when PBCs are used) and that fluid next to the boundary exhibits bulk-like behaviour (i.e. it is far enough away from the MOF surface not to interact with it). Furthermore, due to the small diameter of simulated nanoparticles compared to real-life nanoparticles, care must be taken to ensure that there is a region in the crystal which does not experience interaction energies from any external surface (thus representing the "bulk" region of the nanoparticle as oppose to the "surface" region).

Finally, as shown in Figure 2.2, MOF nanoparticles can be modelled as completely segregated frameworks surrounded by vacuum in three dimensions ("core-shell" model, as in the work of Zhang et al [6]), or as a two-dimensional infinite slab (as in the work by Semino et al [7]). In this work, the latter method has been used because it is computationally cheaper (fewer atoms are needed to model nanoparticles of a given diameter and there is a smaller vacuum gap hence fewer fluid molecules at pressures close to the saturation pressure). Furthermore, the slab models provide more insight into how individual surfaces (that vary depending on the direction of crystal cleavage and the surface functionality) influence the framework properties (such as its internal energy and host-guest interaction energies).

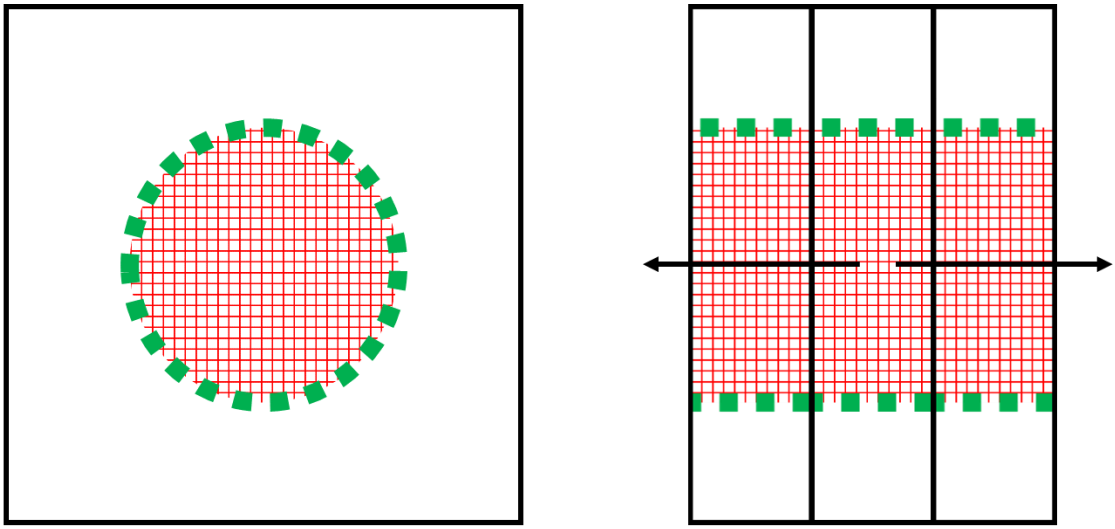

Figure 2.2. Nanoparticle models, showing the "core-shell" and infinite slab models.

2.2. *Ab-initio* simulations

Subsection 2.2 was adapted from the confirmation report affiliated with the same Doctor of Philosophy qualification as this thesis [8].

Ab-initio (first-principle) simulations use quantum methods to determine the electronic structure of a static configuration of atoms. The electronic structure details the energy and forces acting on individual atoms. For systems involving MOFs, this information can be used (for example) to derive host-guest interaction energies [9], or partial atomic charges of the framework (which can then be used in classical simulations [10]). Furthermore, *ab-initio* simulations can be used to determine the internal energies of structures, which can then be used to calculate binding energies (e.g. of ligands to nodes [11]) and relax the atomic coordinates to obtain the structure at its local energy minima (hence the most favourable conformation at a given guest loading) [12, 13]. For these applications (which are also used in this thesis), there is a need to find the lowest energy ground state of electrons. In simulations where the atoms can move (e.g. system relaxation towards its local minima on the adiabatic energy surface), the ground state needs to be found as a function of the nuclei coordinates [14].

Ab-initio simulations determine the electronic ground state by solving Schrödinger's equation:

$$\hat{H}\varphi = E\varphi \qquad \text{Equation 2.1}$$

Where $\hat{H}$ is the Hamiltonian operator (in this case for a system of N electrons and M nuclei), φ is the electronic wave function (i.e. a unique set of solutions / eigenstates for the Hamiltonian operator), and E is the ground state energy (i.e. a set of the eigenvalues, E_N, that correspond to each eigenstate, φ_N) [14] . It is not possible to analytically solve Schrödinger's equation because it is a multibody problem (M nuclei and N electrons interacting) that results in a complex Hamiltonian which consists of the electron kinetic energy, $\hat{K}_E$, neutron kinetic energy, $\hat{K}_N$, and the potential energy between electrons, $\hat{U}_{EE}$, neutrons, $\hat{U}_{NN}$, and electrons and neutrons, $\hat{U}_{NE}$:

$$\hat{H} = \hat{K}_E + \hat{K}_N + \hat{U}_{EE} + \hat{U}_{NN} + \hat{U}_{NE} \qquad \text{Equation 2.2}$$

Simplifications exist and have been validated to solve Schrödinger's equation. For example, the Born-Oppenheimer approximation assumes that the nuclei are fixed and hence $\hat{K}_N$ can be neglected. This approximation is justified since the nuclei are > 1,800 times heavier than atoms. Since the nuclei are assumed static, the potential energy between nuclei is a fixed value, hence $\hat{U}_{NN}$ is a solvable constant. These assumptions simplify the wavefunction to a 3N variable ($\hat{K}_E$, $\hat{U}_{EE}$, $\hat{U}_{NE}$), which is still considerable given the number of electrons in typical MOF systems. Two common methods for solving Schrödinger's equation after these assumptions are the Hartree-Fock method (HF) and Density Functional Theory (DFT) [14].

HF approximates the electronic wave function as a determinant of individual electron wavefunctions ($\varphi = \sum_{i=1}^{N} \varphi_i(r)$) [14]. However, this method requires a complete set of single-electron wave functions, and it does not account of the electron correlation (i.e. interactions between electrons that couple their movement). Not taking into account the electron correlation leads to discrepancy with experiments, and although post-HF corrections can be implemented they are limited to systems with a few atoms [15].

DFT is similar to HF in the sense that the many-bodied system is reduced to a series of single-electron equations, but it does not suffer from the limitations of the HF method and

is hence more applicable to larger scale systems such as those used in this thesis [15]. It relies on the one-to-one mapping between the electronic ground state and electron density. Specifically, the electron density ($\eta(r)$) that minimises the energy functional ($E = fn(\eta(r))$ provides the solution to Schrödinger's equation (thus reducing the 3N-dimensional problem to a 3-dimensional problem that depends on the spatial coordinates of electrons, r). Unfortunately, this energy functional is not known. Instead, the ground state energy can be found using Kohn-Sham (KS) equations [14].

For an N-electron system, DFT splits Schrödinger's equation into N single electron KS equations (Equation 2.3), which compared to HF are relatively easy to solve:

$$\left[-\frac{\hbar^2}{2m}\nabla^2 + V(r) + V_H(r) + V_{XC}(r)\right]\varphi_i(r) = \varepsilon_i\varphi_i(r) \qquad \text{Equation 2.3}$$

Here, $\varphi_i(r)$ is the single electron wavefunction and ε_i is the orbital energy. The first term in the KS equation ($-\frac{\hbar^2}{2m}\nabla^2$) is the kinetic energy of the singular electron which is known ($\hbar$ is Planck's constant, m is the electron mass). The second term ($V(r)$) is the electron – nuclei interaction energy which is also known. The Coulombic repulsion between the electron of interest and the total electron density ($V_H(r)$) depends on the electron density (to which the electron of interest contributes). The corrective removal of this contribution is accounted for by the exchange correlation energy term ($V_{XC}(r)$). $V_{XC}(r)$ is the functional derivative of the exchange – correlation energy ($V_{XC}(r) = \frac{\delta E_{XC}(r)}{\delta \eta(r)}$) and it is unknown in Equation 2.3.

The exchange – correlation energy accounts for quantum electron-electron interactions and differences in the kinetic energy. There is no explicit function to determine V_{XC}, instead it is approximated using either the localised density approximation (LDA) or the generalised gradient approximation (GGA) [14]. The LDA method approximates the position-dependent exchange correlation energy as that of an electron gas ($V_{XC}^{electrongas}$) which has the same electron density as the spatial interval of interest ($\eta(r)$) [14]:

$$V_{XC}^{LDA}(r) = V_{XC}^{electrongas}[\eta(r)] \qquad \text{Equation 2.4}$$

Realistically the electron density is non-uniform across any region of space, and therefore cannot accurately be described by the LDA model. A popular improvement is the GGA method which calculates the exchange – correlation energy using both the localised electron

density and its gradient. Various functionals (such as PBE [16]) have been developed to incorporate the local electron density gradient into $V_{XC}^{GGA}(r)$ [14]. So far, only the local Pauli repulsion forces between electrons and the electron cloud (represented by LDA or GGA) have been included in the exchange correlation term. Non-local van der Waals forces can be included as a summative addition to $V_{XC}(r)$ to improve the accuracy of the exchange correlation energy. In this work, (at a compromise between cost and accuracy), the PBE functional [16] was used to approximate the Pauli repulsion contribution to the exchange correlation energy, and DFT-D3 dispersion corrections [17, 18] were implemented.

$$V_{XC}(r) = V_{LDA}(r) + V_{GGA}(r) + V_{VDW}(r) \qquad \text{Equation 2.5}$$

By defining each term in Equation 2.3, it becomes clear that there is a circular loop present (i.e. the Hartree potential depends on the electron density which needs to be solved using the Hartree potential). The Kohn-Sham equations therefore must be solved iteratively in a self-consistent field: Firstly, a trial $\eta(r)$ is defined. The Kohn Sham equations are solved using $\eta(r)$ to calculate the single electron wavefunctions ($\varphi_i(r)$). The electron density is then recalculated ($\eta_{KS}(r) = 2\sum_i \varphi_i^*(r)\varphi_i(r)$). If $\eta_{KS}(r) \neq \eta(r)$, the trial density is updated, and the steps reiterated. If $\eta_{KS}(r) = \eta(r)$, the density is at its ground state and can be used to calculate the total energy. In other words, at the electronic ground state, the combined single electron density given by the N-Kohn Sham equations is equal to the electron density of a many-bodied system [14, 15].

When solving the KS equations, the wavefunction is expanded using atomic basis sets (functions that define the spatial distribution of electrons surrounding a nucleus). The basis sets can be a linear combination of atomic orbitals or planewaves (PW). Slater type orbitals (STOs) accurately represent the short and long ranged electron distribution surrounding atomic nuclei, however they must be solved numerically. Gaussian type orbitals (GTOs) can be solved analytically, however they are less accurate as they cannot represent the cusp of the molecular orbital (near to the nucleus) as well as STOs. However, a linear combination of GTOs provides similar accuracy to STOs. As opposed to the nuclei centred basis sets, PWs use efficient fast Fourier transformations to efficiently expand the wavefunction, which is particularly useful in periodic systems. However, the small region of real-space occupied by core electron would require a large energy cut-off to capture all the necessary detail in reciprocal space which would be very computationally demanding. Therefore, PWs need to

be used with pseudopotentials (smoothing functions) to implicitly model core electrons [19], whereas valence electrons (important for chemical bonding) are treated explicitly.

The *ab-initio* simulations in this work use an efficient Gaussian-Planewave (GPW) method (as implemented in CP2K) to get the benefits of both GTO and PW basis sets. In the GPW method, the valence electrons are represented using Gaussian basis sets for the wavefunction (and KS matrix), and planewaves for the electron density [20-25]. For all simulations, the planewave cut-off was carefully chosen by determining the smallest cut-off which does not influence the system energy. The pseudopotentials used were those developed by Goedecker, Teter and Hutter [21, 26, 27], and Gaussians were modelled using MOLOPT (molecular optimised) basis sets [28]. These parameter sets have been tried and tested in multiple MOF simulation papers (for example [29-31]).

2.3. Classical simulations

2.3.1. Interaction energies

Calculation of interatomic interaction energies is essential for constructing molecular simulations, regardless of whether an ensemble or time-based approach is used to determine the thermodynamic observable of interest. Rather than solving Schrödinger's equation for every atomic configuration, classical simulations calculate the energy and forces acting on atoms using parameter sets called "forcefields". Forcefields are derived from experiments or *ab-initio* simulations and they therefore allow a comparatively quick and efficient calculation of the energy and forces acting on atoms, at the cost of accuracy. In classical simulations, the overall potential energy (U_{Total}) is the sum of non-bonded and bonded interaction energies.

$$U_{Total} = \underbrace{U_{Non-Coulombic} + U_{Coulombic}}_{\text{Non-bonded energies}} + \underbrace{U_{Torsion} + U_{Bend} + U_{Stretch}}_{\text{Bonded energies}} \quad \text{Equation 2.6}$$

In this work, ensemble-based GCMC simulations (see Section 2.3.3) are used to calculate the adsorption isotherms for N_2 in DUT-8(Ni) (Chapter 3). In Chapters 4 and 6, they are also used to calculate the maximum loading of cisplatin and MOF – cisplatin interaction energy in various frameworks. In this thesis, to reduce computational cost the bonded contribution

to the energies were ignored in the GCMC simulations (i.e. the MOF and guest molecules are modelled as being rigid). This is justifiable for N_2 as it consists of strong, rigid, triple covalent bonds. The only MOF which shows substantial structural changes is DUT-8(Ni) [32] and these structural changes are accounted for using the osmotic framework adsorbed solution theory, in which separate GCMC simulations are carried out in a set of rigid structures (see Section 2.4.2) [13]. Finally, though cisplatin is flexible [33], GCMC simulations are used only to provide an initial, screening value for the maximum uptake and interaction energies, as discussed in the relevant chapters. On the other hand, all time-based MD simulations account for the flexibility of water, cisplatin, and the frameworks since the properties being measured strongly depend on it (for example the guest molecule diffusivity, adsorption sites and interaction energies in densely packed systems).

Non-bonded energy terms

In all classical simulations, non-Coulombic interactions between two atoms (i and j) separated at a distance, $r_{i,j}$, were calculated using the 12-6 Lennard Jones potential, which describes the pairwise interaction energy ($U_{Non-Coulombic}$) as the difference between the short-ranged repulsive (Pauli repulsion, $\left(\sigma_{i,j}/r_{i,j}\right)^{12}$) and long-ranged attractive (dispersion, $\left(\sigma_{i,j}/r_{i,j}\right)^{6}$) interactions [44]:

$$U_{Non-Coulombic} = 4\varepsilon_{i,j}\left(\left(\frac{\sigma_{i,j}}{r_{i,j}}\right)^{12} - \left(\frac{\sigma_{i,j}}{r_{i,j}}\right)^{6}\right) \qquad \text{Equation 2.7}$$

The parameters $\varepsilon_{i,j}$ and $\sigma_{i,j}$ refer to the depth of potential well (i.e. the most favourable interaction energy between atoms i and j) and the collision diameter between the two atoms of interest (i.e. the nuclei separation when two atoms are touching). They are calculated for each combination of atoms using the Lorentz-Berthelot mixing rules ($\sigma_{i,j} = (\sigma_i + \sigma_j)/2$ and $\varepsilon_{i,j} = \sqrt{\varepsilon_i \varepsilon_j}$ [34]). Coulomb's law was used to calculate the electrostatic contribution to the potential energy ($U_{Coulombic}$):

$$U_{Coulombic} = \frac{q_i q_j}{4\pi\varepsilon_0 r_{i,j}} \qquad \text{Equation 2.8}$$

Here, ε_0 is the dielectric constant and q represents the partial atomic charges.

As a rule of thumb, as $r_{i,j} \rightarrow 2.5\sigma_{i,j}$ the non-Coulombic potential becomes negligible ($U_{Non-Coulombic} \rightarrow 0$) [5]. For efficient computation, a cut-off radius (r_{cutoff}) is therefore implemented to truncate the non-Coulombic potential between pairs of atoms where $r_{i,j} > r_{cutoff}$. Of course, the factor 2.5 is a generalised rule of thumb, and therefore the suitable cutoff radius is selected as the atomic separation whereby $U_{Non-Coulombic} \approx 0$. Recommended values of r_{cutoff} are normally published with the forcefield.

A simple cut-off radius cannot be accurately used when truncating Coulombic interactions because they converge over longer distances (i.e. multiple periodic images of the unit cell). Instead, Ewald summation uses a Fourier transformation to split the Coulombic potential energy into its slowly converging and rapidly converging contributions. Truncation errors are therefore avoided since the slow converging Coulombic potential converges rapidly in Fourier space [35]. Adaptations to the Ewald method are available such as the particle-mesh Ewald (PME) summation. In PME, instead of multiple calculations to determine the contribution of potential from the reciprocal space, the charges are assigned to a grid using interpolation, which allows for a much more efficient single calculation of the reciprocal term [36]. Finally, the Wolf summation method directly calculates pairwise Coulombic interactions. To do this, the pairwise Coulombic potentials are shifted so that the energy is negligible at a given cut-off radius [37].

In this work, the GCMC simulations were carried out using the Multipurpose Simulation Code (MuSiC, known for its computational efficiency [38, 39]). Since the MOF is static, MuSiC uses Ewald summation to accurately capture an electrostatic potential grid, prior to the GCMC simulation. During the GCMC simulation, to improve computational efficiency the Coulombic interactions between guest molecules and the fixed framework are calculated by interpolating the values saved in this grid. Coulombic interactions between guest molecules on the other hand are calculated using the Wolf Summation method. (This combination of pre-emptive grid building and on-the-fly calculations is very common [39]). The MD simulations were carried out using the GROningen Machine for Chemical Simulations (GROMACS, known for being one of the fastest and most comprehensive MD simulation packages [40, 41]) which offers use of the efficient PME method.

Bonded energy terms

Bonded contributions to the potential energy arise from bond stretching (2-body interaction), bond bending (3-body interaction), and bond torsion (4-body interaction). Figure 2.3 describes these terms and provides examples of the functions used to calculate the potential energy attributed to each (note that the exact function used to calculate each term depends on the forcefield).

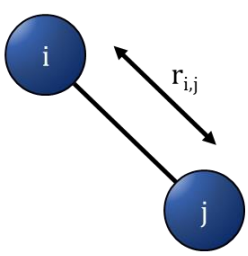

$$U_{Stretch} = \frac{1}{2} k_{i,j}^{stretch} \left(r_{i,j} - b_{i,j}\right)^2$$

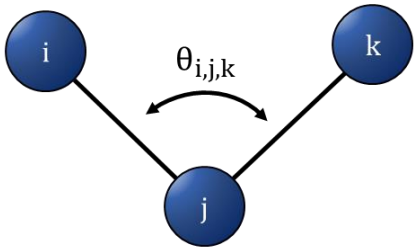

$$U_{Bend} = \frac{1}{2} k_{i,j,k}^{\theta} \left(cos(\theta_{i,j,k}) - cos(\theta_{i,j,k}^{0})\right)^2$$

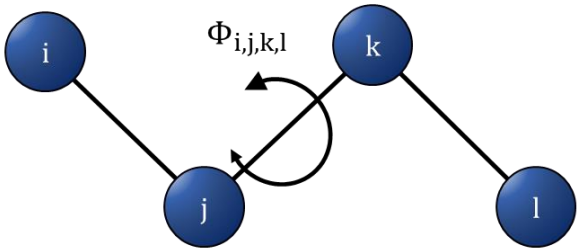

$$U_{Torsion} = k_{i,j,k,l}^{\Phi}\left(1 + \cos\left(n\Phi_{i,j,k,l} - \Phi_S\right)\right)$$

Figure 2.3. Principles of bond stretching, bending and torsion with example functions used to calculate each contribution to the potential energy. Atom specific force constants ($k_{i,j}^{stretch}$, $k_{i,j,k}^{\theta}$, $k_{i,j,k,l}^{\Phi}$) and constants related to the equilibrium bond length, angle and torsion angle ($b_{i,j}$, $\theta_{i,j,k}^{0}$, Φ_S) are obtained from forcefields.

Forcefield parameters

It is useful to assume that parameters used to calculate the potential energy (ε, σ, force constants, bond equilibrium values) are transferrable between atoms in similar chemical environments. For this reason, standardised forcefields have been developed to universally describe parameters for the derivation of potential energy (e.g. the Dreiding forcefield [42] or Universal Force Field [43] used to model the MOFs in this work). Though generic, these

standardised forcefields are transferrable and have been shown to reproduce experimental data. As well as the non-Coulombic and bonded parameters, partial atomic charges (q) are also available in most forcefields. However, they are less transferrable, hence the partial atomic charges for MOFs used in this thesis were obtained from DFT simulations (see Section 2.2).

All N_2 parameters (ε, σ, q) were taken from the Transferable Potentials for Phase Equilibria (TraPPE) forcefield (in which parameters are based on vapour-liquid phase equilibrium data [44, 45]). As shown in Chapter 3, this combination of forcefields accurately reproduced experimental adsorption inside DUT-8(Ni). For cisplatin, the *ab-initio* derived forcefield by Yesylevskyy et al [33] was used. In their work, they use a standardised, well accepted method to derive the forcefield (i.e. DFT optimisation, followed by energy calculations of cisplatin configurations with constrained bond lengths and angles around the equilibrium structure). This method produced similar parameter sets as other groups who used *ab-initio* simulations and vibrational spectroscopy experiments [46, 47]. Yesylevskyy et al also performed MD simulations in TIP3P water (also used in this work) to compare the standard forcefield parameters to parameters derived using novel methods in solution, concluding that while the results differ they show the same qualitative trends [33]. In this work, the forcefield created using the (more widely accepted) standardised methods was used because many of the simulations are carried out in a solvent-free system. As shown in the relevant chapters, results (such as the interaction energy and potential energy barriers) were compared to *ab-initio* simulations and experimental data where available.

Now that the interaction energies have been explained the following subsections detail how they are used to obtain thermodynamic properties from classical simulations.

2.3.2. Statistical thermodynamics

Simulations provide microscopic properties (e.g. atomic velocities, atomic positions, pairwise interaction energies) that are not directly relatable to the macroscopic properties measured experimentally (e.g. adsorption enthalpy, uptake). Statistical thermodynamics provides a mathematical method of relating microscopic to macroscopic properties. Take for example adsorption experiments; at equilibrium guest molecules rapidly fluctuate between different configurations inside the MOF as well as between the MOF and reservoir. This generates many microstates (that have different energies and number of adsorbed guest

molecules), all of which correspond to different values of the thermodynamic property of interest. The recorded measurement (e.g. the adsorption energy or uptake) is then an average value across these microstates, which should have a net constant value provided enough sampling time. In simulations, the same average thermodynamic properties would be calculated using a time-independent ensemble average (ensemble meaning a collection of microstates generated using common constraints set to represent the macroscopic system). Assuming the system is ergodic (i.e. over a sufficiently large dataset all possible configurations have been visited) and representative of the macroscopic system, the experimental time-average and simulated time-independent ensemble average should be equal provided a sufficient sampling size and time are used (Equation 2.9) [5, 48]:

[5] $$M_{observed} = \langle M \rangle = \sum_i M_i P_i$$ Equation 2.9

Equation 2.9 essentially means that the thermodynamic property of interest (M) observed in time-dependent experiments averaged over a large number of particles ($M_{observed}$) should be equal to the simulated time-averaged measurement ($\langle M \rangle$) and the simulated ensemble average (M_i is the value in microstate i, and P_i is the probability of being in microstate i) [5].

To ensure that the macroscopic system is being represented by the microstates generated during molecular simulations, a set of constraints are applied to the system. Three popular sets of constraints (which are also used in this thesis) include:

1- Canonical ensemble (N, V, T): Represents a closed isothermal system as the number of particles N, volume V and temperature T are kept constant.
2- Isothermal-isobaric ensemble (N, P, T): Represents an isolated system as the number of molecules N, pressure P and temperature T are constant.
3- Grand-canonical ensemble (μ, V, T): Represents an open isothermal system as the chemical potential μ, volume V and temperature T are constant

2.3.3. Grand-canonical Monte Carlo simulations

Subsection 2.3.3 was adapted from the confirmation report affiliated with the same Doctor of Philosophy qualification as this thesis [8].

Adsorption experiments consist of a reservoir (e.g. of bulk gas at fixed temperature and pressure) exposed to the MOF. Guest molecules can enter and leave the MOF from the reservoir (i.e. the number of particles, N, can fluctuate). At equilibrium, guest molecules in the reservoir and the MOF share the same temperature and chemical potential. Therefore, the most appropriate set of ensemble constraints to model adsorption experiments is the grand-canonical ensemble (in which N can vary, but μ, V, and T are fixed), which is the focus of this section [5].

Deriving an ensemble average

In GCMC simulations, thermodynamic properties are calculated using an ensemble average of the microstates when the system is at equilibrium. The probability of a system with N particles occupying microstate i (P_i with an associated energy U_i) is:

$$P_i(N;\mu,V,T) = \frac{e^{-\frac{U_i(N,V)}{k_BT}} e^{\frac{N\mu}{k_BT}}}{\Xi(\mu,V,T)} \qquad \text{Equation 2.10}$$

Where k_B and T are the Boltzmann constant and the absolute temperature [48]. The grand partition function ($\Xi(\mu,V,T)$) is the sum of Boltzmann factors ($e^{-\frac{U_i(N,V)}{k_BT}} e^{\frac{N\mu}{k_BT}}$) across the entire ensemble:

$$\Xi(\mu,V,T) = \sum_{i,N} e^{-\frac{U_i(N,V)}{k_BT}} e^{\frac{N\mu}{k_BT}} \qquad \text{Equation 2.11}$$

The grand-canonical partition function can be used to describe thermodynamic state variables as an ensemble average [48]:

$$\langle M \rangle_{\mu,V,T} = \frac{1}{\Xi(\mu,V,T)} \sum_i M_i e^{-\frac{U_i(N,V)}{k_BT}} e^{\frac{N\mu}{k_BT}} \qquad \text{Equation 2.12}$$

Equation 2.12 is currently written in a quantum sense. More specifically, the Boltzmann factor (as written in Equation 2.12) would need to be solved for each microstate using Schrödinger's Equation for a many-bodied system. The thermodynamic average would then need to be calculated from many microstates. Instead, by rewriting Equation 2.12 in the classical limit it becomes an easier to solve function of the particle coordinates r and momenta p. For this purpose, the energy is expressed as a Hamiltonian ($\mathcal{H}(r,p)$) of the

potential (U(r)) and kinetic ($\mathcal{K}$(p)) energies [5]. The sum across all microstates can be rewritten as:

$$\langle M \rangle = \int M(r,p)Q(r,p)\,drdp \qquad \text{Equation 2.13}$$

The classical probability distribution (Q(r, p)) can now be expressed as a function of $\mathcal{K}$(p) and U(r):

$$Q(r) = \frac{1}{\Xi} e^{-\frac{\mathcal{H}(r,p)}{k_B T}} e^{\frac{N\mu}{k_B T}} = \frac{1}{\Xi} e^{-\frac{\mathcal{K}(p)}{k_B T}} e^{-\frac{U(r)}{k_B T}} e^{\frac{N\mu}{k_B T}} \qquad \text{Equation 2.14}$$

The kinetic energy can be analytically solved as $\mathcal{K}(\mathrm{p}) = \mathrm{V}/\Lambda^3$ (where V is the system volume), and the de Broglie wavelength is $\Lambda = \hbar\sqrt{\beta/2\pi\mathrm{m}}$ (where $\hbar$ is Planck's constant and m is the particle mass). In a system containing N indistinguishable particles, the kinetic energy becomes $\mathcal{K}(\mathrm{p}) = \mathrm{V^N}/\mathrm{N!}\,\Lambda^{3\mathrm{N}}$ [48]). Hence, Equations 2.13 and 2.14 become:

$$Q(r) = \frac{V^N}{N!\Lambda^{3N}} \frac{1}{\Xi} e^{-\left(\frac{1}{k_B T}\right)\left(U(r^N)-\mu N\right)} \qquad \text{Equation 2.15}$$

$$\langle M \rangle = \frac{1}{\Xi} \sum_N \frac{V^N}{N!\Lambda^{3N}} \int M(r^N) e^{-\left(\frac{1}{k_B T}\right)\left(U(r^N)-\mu N\right)} \qquad \text{Equation 2.16}$$

As a function of the spatial coordinates of particles, the potential energy renders the integrand in Equation 2.16 unsolvable via analytical techniques. Due to the multidimensionality of N particles with 3-D coordinates, standard numerical methods also cannot be used. This is where Monte Carlo comes in handy.

Monte Carlo is a stochastic method in which random configurations of particles in the system are generated to solve the integrand. In the simplest of Monte Carlo schemes, this would involve generating entirely random configurations (regardless of how high the energy is) and evaluating the integral for each case. As the sample size tends to infinity, the integrand should converge to the correct answer. However, since high energy regions are included in the statistical set, random sampling is inefficient, especially in dense systems such as the pore space in MOFs.

To improve the simulation efficiency, configurations should only be sampled in areas where the Boltzmann factor is non-negligible (importance sampling). To achieve importance sampling, prior knowledge of the probability distribution (i.e. the likelihood of configurations according to the Boltzmann factor) would be required. Unfortunately, the probability distribution is not known explicitly. Instead, importance sampling can be achieved using the Metropolis algorithm [5].

Metropolis algorithm

Monte Carlo methods evaluate thermodynamic properties as in Equation 2.17. To do this efficiently, the probability density ($\mathrm{Q(r)}$) is required (but it is not known explicitly). If it were known, by randomly generating a large number ($\mathrm{N_{MC}}$) of configurations according to $\mathrm{Q(r)}$, the ensemble average of the thermodynamic property could be calculated [49]:

$$\langle M \rangle = \frac{1}{N_{MC}} \sum_{i=1}^{N_{MC}} M(r_i^N) \qquad \text{Equation 2.17}$$

Although $\mathrm{Q(r)}$ is not known explicitly, it is possible to sample the system according to the Boltzmann factor using the Metropolis method. Basically, the configurations are generated from a "random walk" in the energy space. More specifically, a small random displacement (see *Trial Moves*) is imparted on the system, transforming it from the old to the new configuration ($\mathrm{o} \rightarrow \mathrm{n}$). Each step in the walk is accepted or rejected based on the change in energy caused by this displacement. The acceptance criteria in this Markov chain (i.e. sequence of microstates where the probability of each configuration depends only on the current configuration) gradually lowers the potential energy (whether it is lowered at a particular step in the chain depends on a probability defined in the acceptance criteria, as described below). Once equilibrated, the system is independent of the initial configuration, and further Metropolis iterations keep the system in equilibrium [49].

To reach its equilibrium distribution, the system sampling must be ergodic (i.e. all possible configurations are sampled as $\mathrm{N_{MC}} \rightarrow \infty$) and the condition of detailed balance must be satisfied (i.e. the net flux between two states at equilibrium must be zero). From a mathematical perspective, $\mathrm{Q(r)}$ defines the likelihood of being in a particular configuration. The overall probability of moving the system from $\mathrm{o} \rightarrow \mathrm{n}$ is given by a translation matrix ($\pi_{\mathrm{o}\rightarrow\mathrm{n}} = \alpha_{\mathrm{o}\rightarrow\mathrm{n}} p_{\mathrm{o}\rightarrow\mathrm{n}}$) which accounts for the probability of attempting the move ($\alpha_{\mathrm{o}\rightarrow\mathrm{n}}$) and the probability of accepting the move ($p_{\mathrm{o}\rightarrow\mathrm{n}}$). Detailed balance implies: $\mathrm{Q(n)}\pi_{\mathrm{n}\rightarrow\mathrm{o}} =$

$Q(o)\pi_{o\to n}$, and in the Metropolis algorithm, the displacement is imparted on a random particle (hence $\alpha_{o\to n} = \alpha_{n\to o}$ and $Q(o)p_{o\to n} = Q(n)p_{n\to o}$). Provided enough iterations of the algorithm (and based on the acceptance criteria detailed below), the system will converge to its equilibrium distribution: $Q(eq) = \lim_{N_{MC}\to\infty} Q(o)p_{(N_{MC}-1)\to N_{MC}}$ [5, 49]:

1) Calculate the potential energy of the current configuration ($U(o)$)
2) Impart a small random displacement on a random particle
3) Calculate the potential energy of the new configuration ($U(n)$)
4) Determine the acceptance probability:

   $p_{o\to n} = \frac{Q(n)}{Q(o)} = e^{-\beta(U(n)-U(o))} < 1$ (If: $U(o) < U(n)$)

   $p_{o\to n} = 1$ (If: $U(o) > U(n)$)
5) Generate a random number (r_{and}) equally distributed between 0 – 1. If $r_{and} < p_{o\to n}$ accept the trial move. If $r_{and} > p_{o\to n}$ reject the trial move
6) Repeat steps 1 – 5 to get a sufficiently large ensemble.

Trial moves

In the Metropolis method, random displacements are imparted on particles to establish a Markov chain. For the grand canonical Monte Carlo simulations used in this work, the trial moves are to insert, delete, rotate or translate a randomly selected guest molecule. For rotation or translation moves, a particle is selected at random and given new, random coordinates. The acceptance ratio for such displacements is: $p_{o\to n} = e^{-\beta(U(n)-U(o))}$ as described above.

Insertion and deletion trial moves add a particle with random coordinates or remove a randomly selected particle. If in state o the number of particles is N, insertion and deletion moves are accepted with the probabilities [5]:

$$p(N \to N+1) = \min\left[1, \frac{V}{\Lambda^3(N+1)} e^{\beta(\mu - U(N+1)+U(N))}\right] \quad \text{(insertion)}$$

$$p(N \to N-1) = \min\left[1, \frac{\Lambda^3 N}{V} e^{-\beta(\mu + U(N-1)+U(N))}\right] \quad \text{(deletion)}$$

For gasses, the chemical potential can be calculated from the pressure: $\mu = k_B T \ln\left(\frac{\Lambda^3 N}{V}\right) = k_B T \ln(\Lambda^3 \beta P)$ [5]. At high pressures in the tight confinement of micropores, gas will exhibit

non-ideal behaviour. For this reason, the Peng Robinson equation of state was used to calculate the fugacity in Chapter 3 [50].

2.3.4. Molecular dynamics simulations

Unlike Monte Carlo simulations which calculate an ensemble average, molecular dynamics simulations mimic experiments by calculating the time evolution of a trajectory. Properties are expressed as a function of the momentum and positions of particles. In theory, once equilibrated thermodynamic properties obtained from MD and MC simulations should be equal provided a large enough simulation time and ensemble size are used to overcome statistical error (Equation 2.9). The most applicable type of simulation depends on the system and properties of interest. For example, MC simulations have no concept of time, hence for transport properties only MD is applicable. In MD simulations, if there are large energy barriers associated with the system of interest (e.g. cisplatin moving through narrow pore windows in a MOF), then the system can become trapped in a favourable energy configurations and the simulations will not be able to sample the entire phase space [51]. Finally, when modelling dense systems (such as cisplatin + water in micropores as described in Chapters 4-6), MC simulations can result in many rejected moves which is not an efficient use of computational resource.

MD simulations are initiated by defining the positions of atoms and their velocities. To resolve the time-based trajectory, pairwise potential energies are calculated at each time step using Equation 2.6. The force acting on each particle (f_i) is then the derivative of the potential energy (U_i) with respect to the position of the particle (r_i) [52]:

$$f_i = \frac{\partial U_i}{\partial r_i} = m_i \frac{\partial^2 r_i}{\partial t^2} \qquad \text{Equation 2.18}$$

Based on Newton's equation of motion (which states that the force is a product of mass, m_i and acceleration $(\partial^2 r_i)/(\partial t^2)$), the particle acceleration can be calculated, hence the particle velocity, hence the particle coordinates. However, the equation of motion cannot be solved analytically because the force is a continuous function of the position, therefore the motion of many particles is coupled. Instead, it is solved using finite difference numerical integration, and so to avoid instability of the numerical method a small timestep is required [52]. For example, numerical integration is commonly implemented using Verlet [53], velocity Verlet [54] or leap-frog [55] algorithms. The small timestep (typically ~ 1-2

femtosecond) is a bottleneck for the simulation time (picosecond – nanosecond scale), which must be sufficiently large that the net value of the property being measured does not change with time and hence it is independent the initial configuration. For this reason, MD simulations are normally equilibrated prior to a production simulation over which the property of interest is recorded.

As in MC, MD simulations make use of an ensemble to represent the macroscopic system, normally the canonical ensemble (NVT) or the isothermal-isobaric ensemble (NPT). The temperature of a system depends on the kinetic energy of particles ($\frac{3}{2}k_BT = \frac{1}{2}mv^2$) and therefore their velocity. Different thermostats can be applied to control the temperature. For example, the efficient Berendsen thermostat algorithm rescales the particle velocities, yet the suppression of the kinetic energy means that the isothermal ensembles are not correctly implemented, so in this work the Berendsen thermostat was only used during equilibration [56]. A modified version of this thermostat ("velocity-rescaling") adds an additional stochastic term to enable the correct kinetic energy distribution while retaining a good control of the temperature [57]. Alternatively, as in the case of Andersen [58] and Nosé-Hoover [59, 60] thermostats, the system is coupled to an imaginary heat bath and a random particle is allocated a new velocity or energy from a Maxwell-Boltzmann distribution respectively (this corresponds to the transfer of momentum or energy caused by a collision between the random particle and a particle in the constant temperature heat bath). The allowance of temperature (hence kinetic energy) oscillations means that the latter algorithms can correctly monitor the temperature in the canonical ensemble. Therefore, in this work the Nosé-Hoover thermostat was used during production simulations. The pressure of a system can be regulated using a barostat. The Berendsen barostat couples the system to a pressure bath and rescales the box volume and particle coordinates to maintain a constant pressure. However, it dampens fluctuations in the pressure preventing fluctuations in the kinetic and potential energies that are representative of the NPT ensemble [56]. Alternatively, the Parrinello-Rahman barostat (used in production simulations in this thesis) couples the system to a variable volume "piston". The position of the piston defines the energy terms added to the Hamiltonian and independently changes the box vectors so that the volume can fluctuate [61, 62].

Diffusion energy barrier

The self-diffusivity of a molecule (D) can be calculated from equilibrated MD simulations using Einstein's equation:

$$D = \lim_{t\to\infty}\left(\frac{<|r(t)-r(0)|^2>}{2dt}\right) \qquad \text{Equation 2.19}$$

Where t is the simulation time, r is the position of the molecule of interest, d is the number of dimensions of the system (in these simulations, $d = 3$). The numerator is called the mean-square displacement which can be plotted as a function of time to calculate the self-diffusivity.

As mentioned, MD simulations may not adequately sample the phase space if large energy barriers associated with the system prevent a molecule from moving out of a potential well. To overcome this, additional energy can be added to the system by increasing the temperature, thus increasing the probability of the molecule escaping the energy well. Diffusivity of a molecule is related to the temperature by an Arrhenius equation:

$$D = D_0 e^{-\frac{E_a}{RT}} \qquad \text{Equation 2.20}$$

Where D_0 is a constant relating to the frequency of attempts to move and the step size, E_a is the diffusion activation energy, R is the universal gas constant and T is the absolute temperature. A semi-log plot of the diffusion coefficient and inverse temperature can therefore be used to calculate the diffusion energy barrier [63].

Steered-MD and umbrella sampling

At low temperatures, high energy barriers can result in an inaccessibility of some regions of the system within reasonable MD times. While increasing the temperature enables the calculation of a diffusion energy barrier, it is not clear what part of the system corresponds to this energy barrier. Instead, steered-MD (SMD) and umbrella sampling simulations offer a means of computing the various energy barriers at different positions in the system.

In SMD, an external force or velocity is imposed on a group of atoms (SMD atoms, e.g. the group that is being pulled through the system, in Chapters 4-6 cisplatin) to direct them along a predetermined reaction coordinate. This is implemented for instance by applying a constant

velocity to an auxiliary (dummy) atom which moves it along the coordinate path of interest. Typically, a harmonic spring binds the SMD atoms to the auxiliary atom, forcing the SMD atoms along the coordinate path while imposing no constraints in other directions (assuming a single reaction coordinate).

$$U_{SMD} = \frac{k_{spring}}{2}(r - r_0)^2 \qquad \text{Equation 2.21}$$

Where U_{SMD} is the harmonic potential around the auxiliary atom, k_{spring} is the spring stiffness, r is the position of the SMD atoms (i.e. centre of mass), and r_0 is the position of the auxiliary atom which moves at a constant velocity along the reaction coordinate [64]. In this thesis, k_{spring} and the velocity of the auxiliary atom were tested to ensure that the simulation path is reproducible, i.e. the variation in force along the reaction coordinate is not a function of k_{spring} (which is sufficiently large) and the velocity (which is sufficiently slow).

Results from SMD simulations (without further analysis or simulations) are useful when looking at dynamic mechanisms or estimates for the individual contributions to the change in potential energy as the SMD atoms move along the reaction coordinate [65]. However, work applied to the system renders it no longer in equilibrium, and very slow velocities (hence inaccessibly large simulation times) would be required in SMD simulations to bring the system to equilibrium. Instead, techniques such as Jarzynski's equality exist to relate the work done during non-equilibrium SMD to the free energy difference between a start and an end configuration [66]. Alternatively, to get accurate changes in free energy as a function of the reaction coordinate, snapshots can be extracted from the SMD simulations and used as initial configuration windows for umbrella sampling.

Umbrella sampling can be used to investigate guest molecule diffusion in microporous materials [67]. Compared to metadynamics, a similar method that is also widely used, umbrella sampling (which is used in this thesis) has the advantage that the free energy profile is less dependent on input parameters (e.g. in the case of metadynamics the height and width of Gaussians need to be defined) and there are less likely to be errors in in the profile as a result of poor sampling convergence [68].

The free energy of a system (Helmholtz, $A(N, V, T)$ or Gibb's $G(N, P, T)$ depending on the ensemble, for now denoted F) is related to the partition function: $F = -k_B T \ln(\Xi)$. The

change in free energy as a system with N particles transitions from state i to state j is then: $\Delta F = F_j - F_i = -k_B T \ln\left(\frac{\Xi_j}{\Xi_i}\right)$. In umbrella sampling, the Boltzmann factor is replaced using a weighting function ($w(r)$) which describes the probability of visiting a point in the configuration space. Therefore, the change of free energy can be rewritten as a ratio of averages of the probability distributions proportional to $w(r)$ (see Frenkel and Smit, Chapter 7 for details of this derivation [5]).

$$e^{-\frac{\Delta F}{k_B T}} = \frac{\langle e^{-\frac{U_j}{k_B T}} / w \rangle_w}{\langle e^{-\frac{U_i}{k_B T}} / w \rangle_w} \qquad \text{Equation 2.22}$$

In practice, to carry out umbrella sampling configuration windows along the reaction coordinate are extracted from the SMD simulations (each window represented as i). An artificial, (usually) harmonic potential is imposed on each window ($U_{bias}(r)_i = \frac{1}{2} k_{spring}(r - r_i)^2$) keeping the SMD atoms within its constraints (though it is allowed to move without constraint within the window). This bias potential allows high energy regions of the system to be adequately sampled. The total window potential ($U_{US,i}$) is then a sum of the bias ($U_{bias}(r)_i = -k_B T \ln(w(r)_i)$) and unbiased potential energies ($U_{unbias,i}$):

$$U_{US,i} = U_{unbias,i} + U_{bias}(r)_i \qquad \text{Equation 2.23}$$

Individual MD simulations constrained to each sampling window are carried out to calculate the system forces as a function of the reaction coordinate. By running the MD simulations for long enough, the probability distribution function in each window is converged. As calculated from the series of MD simulations, the probability distribution contains bias terms for each window which influences the free energy. The free energy in each window and the overall unbiased probability function depend on each other. Therefore, an iterative process is needed to calculate the unbiased free energy differences along the reaction coordinate (the potential mean force, PMF). The most widely used method for doing this is the weighted histogram analysis method (WHAM) [69]. WHAM normalizes the probabilities in each window using the weighting function derived from the bias potential, then sums the normalised probabilities across all windows to obtain a total unbiased distribution function [70]. For the analysis to work, there needs to be significant overlap of the weight function between the sampling windows, otherwise (as shown in Frenkel and Smit [5]) there is a divide by zero error (and hence the PMF diminishes to zero).

Alchemical MD

GCMC simulations are not appropriate for determining drug loading in micropores filled with water. The high density will result in atom overlap and hence many rejected moves. Instead, the free energy difference between cisplatin in solution and cisplatin in a solvated framework was calculated using the Bennett Acceptance Ratio (BAR) [71]. BAR estimates the free energy between two states i and j based on an identity similar to Equation 2.22:

$$e^{\frac{\Delta F}{k_B T}} = \frac{\langle we^{-\frac{U_j}{k_B T}} \rangle_j}{\langle we^{-\frac{U_j}{k_B T}} \rangle_i} \qquad \text{Equation 2.24}$$

(As before, w is a weighting function and the derivation can be found in Frenkel and Smit, Chapter 7 [5]). The weighting function is calculated based on minimising the variance of averages on the right-hand side of Equation 2.24 using Lagrange multipliers [5]. Further details of how this technique was applied to model cisplatin uptake from solution are explained in Chapter 4.

2.4. Material characterisation

2.4.1. Pore network

When comparing MOFs for use in an application such as drug delivery, it is useful to compare their performance against structural properties such as the accessible surface area, pore volume, pore cavity size and pore window diameter (illustrated in Figure 2.4). In this work, these structural properties were calculated using Poreblazer [72].

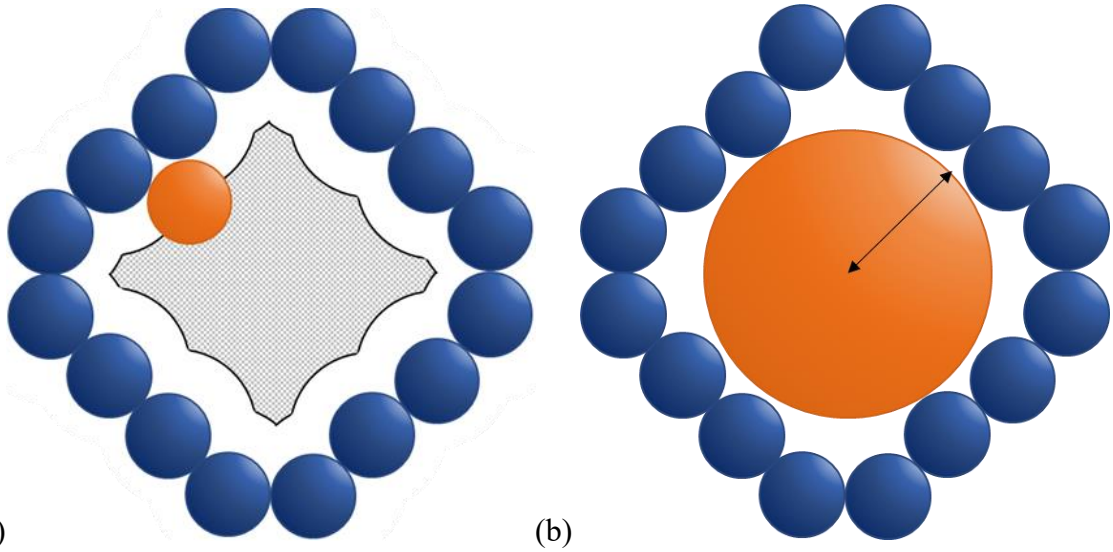

(a) (b)

Figure 2.4. Illustration of (a) the accessible surface area (solid black line) and accessible pore volume (grey) for a probe (orange) inside the pore of a MOF (blue) [72], and (b) the pore-size.

The accessible surface area is the area that a probe (diameter σ_P) occupies as it rolls around the framework atoms (diameters represented as σ_A). Computationally this is achieved using a Monte Carlo algorithm that randomly picks positions on a sphere surrounding each framework atom in turn, with a diameter of $\sigma_T = \sigma_A + \sigma_P$. The probe at each point on the sphere is then tested for overlap with other framework atoms, and from this the fraction of points without overlap (ω) can be calculated. The accessible area surrounding a framework atom i is then $a_i = \omega\pi\sigma_{T,i}^2$ and the total accessible surface area is $A = \sum_i^{N_{MOF}} a_i$. Normally the probe diameter is equal to the collision diameter of N_2 (σ_P = 3.261 Å) as this is useful when comparing resulting surface areas to experimental BET (Brunauer–Emmett–Teller [73]) values [72]. The collision diameter of framework atoms were taken from the Universal Forcefield [43].

The pore-size distribution (PSD) defines the pore cavity sizes present in a MOF. Poreblazer calculates the PSD using MC simulations in which a random test point is defined in the system and a probe is added at this point and tested for overlap with the framework atoms. If no overlaps are found, a larger probe is added at the same trial position (and so on) until the largest probe that can occupy that point in the system is identified [72].

Finally, the accessible pore volume defines the availability of space that is translocated throughout the periodic system. Poreblazer calculates this by splitting the simulation box into cubes, placing a probe in each cube and testing for overlap between the probe and the

framework atoms. If there is no overlap, the cube is added to a list of cubes that can be occupied. Two cubes are connected if they are adjacent in PBCs. Poreblazer tests the accessibility by finding the largest cluster of cubes in the system and testing the connectivity as a continuous path of occupiable cubes across PBCs. This is carried out for probes of increasing size to find the largest probe that can be translocated through the system, and such an algorithm also allows the pore window diameter to be calculated [72].

2.4.2. Framework flexibility and OFAST

Some MOFs exhibit framework flexibility, a significant and reversible structural change in response to external stimuli such as the exposure to guest molecules. In this work, framework flexibility specifically refers to the opening and closing of pores to enhance or reduce the pore volume (a.k.a. gate-opening and gate-closing). The phenomenon occurs because the structure (and in this case the guest molecules) is transitioning between two states of equilibrium that correspond to two variations of the external conditions. This framework flexibility is of particular interest in biomedical applications where a specific biological conditions could trigger a response of the MOF nanocarrier [74].

Framework flexibility can be modelled using MD simulations, for example Salles et al used MD to model the framework response of MIL-53(Cr) to CO_2 adsorption. Their results were able to capture the breathing effect previously seen in in-situ X-Ray powder diffraction experiments [75]. Hybrid MD/MC is another approach to investigate flexibility as a function of guest molecule loading, for example Ghoufi et al used hybrid MD/MC to model CO_2 adsorption in MIL-53(Cr) obtaining adsorption isotherms that closely match experimental data [76]. However, due to the complexity of framework flexibility (i.e. such as its reliance on detailed properties such as the metal node spin state) the use of transferrable forcefields is not appropriate and forcefields must be carefully fitted to experiments or *ab-initio* simulations. On the other-hand, *ab-initio* MD can be used [77] but the re-evaluation of Schrödinger's equation at every timestep would be extremely computationally demanding.

In comparison, the Osmotic Framework Adsorbed Solution Theory (OFAST) is simple to use and computationally cheap. It was successfully used (and developed) by Coudert et al to predict the "gate-opening" pressure (i.e. the pressure of guest molecule at which framework flexibility occurs) for Cu(4,4′-bipy)$(dhbc)_2$ and MIL-53(Al) [13]. The theory uses Equation

2.25 to calculate the osmotic potential ($\Omega_k^{os}(T, P)$) of the open and closed pore phases (phases are denoted as k).

$$\Omega_k^{os}(T,P) = F_k^{host}(T) + PV_k - \int_0^P \left(\sum_i N_i(T,P) V_{m,i}(T,P)\right) dP \qquad \text{Equation 2.25}$$

Three factors contribute to the osmotic potential (hence gate-opening/closing): the free energy of the empty framework ($F_k^{host}(T)$), the gas-gas interaction energy (represented as a multiple of the pressure P and volume V_k), and the MOF-gas interaction energy (represented as the integral of the adsorption isotherm, where N_i is the moles of gas adsorbed and $V_{m,i}$ is the molar volume). For each pressure, the structure with the lowest osmotic potential will be the structure that is most likely to occur. At gate-opening/closing, the open and closed pore structures will be at equilibrium and hence $\Omega_{open}^{os} = \Omega_{closed}^{os}$.

2.4.3. Morphology prediction

The morphology of MOFs (i.e. the crystallographic faces that appear in the final particles) govern its performance properties such as the mass transfer of guest molecules into the pore cavities, especially in the case of MOFs with 1-D channels (more examples can be found in [78]). Another important property influenced by particle morphology is the framework flexibility (see Section 2.4.2). To understand why the morphology influences properties such as guest molecule uptake and framework flexibility, there is a need to know the crystal morphology so that the correct surfaces can be captured in the simulations. Unfortunately, it is not easy to accurately predict the morphology since it is heavily dependent upon the reaction conditions (i.e. solvents, impurities, additives). It is however also dependent upon factors that are already known (i.e. atomic positions, unit cell dimensions, bond strengths), and therefore it is possible to get a reasonable prediction of the crystal morphology [79].

The equilibrium morphology of a MOF is that which minimises the external surface energy per unit volume. This equilibrium shape can be determined using a Wulff plot which is a series of vectors perpendicular to each Miller plane drawn from a midpoint. Surface free energies of the associated Miller plane dictate the length of each vector. Once constructed perpendicular lines are drawn from each vector (i.e. parallel to each Miller plane) to establish the equilibrium shape [80]. Surface energies ($E_{surface}$) can be calculated by performing DFT optimisations on slab models (see Figure 2.2):

$$E_{surface} = \lim_{N \to \infty} \frac{1}{2}\left(E_{slab}^{N} - NE_{bulk}\right) \qquad \text{Equation 2.26}$$

Where, N is the number of atoms, E_{slab}^{N} is the total energy of the slab, and E_{bulk} is the energy of a bulk unit cell [81]. This calculation is very computationally demanding, however. Firstly, considerations previously mentioned (i.e. having long enough slabs that $E_{surface} \propto$ slab length and ensuring $E_{surface} \neq$ f(vacuum length)) needs to be considered by performing multiple DFT optimisations on a variety of large structures. Secondly "large structures" means in excess of several hundred atoms, which in DFT terms is extremely expensive.

Smaller crystals are more likely to exhibit their equilibrium shape (typically near-spherical), because the shape of larger crystals are dominated by the rate at which new material attaches to the surface during crystallisation [80]. The method used in this work (Bravais-Friedel-Donnay-Harker) uses this theory. This method assumes that the interplanar spacing (i.e. space between adjacent parallel hkl planes) is directly proportional to the bond length and indirectly proportional to the number of bonds. Faces that grow more slowly are more likely to appear in the final crystal structure (as the faster growing faces form the vertices). These slower growing faces will have larger interplanar spacing and lower attachment energies (hence more favourable surface energies) [79].

There are more detailed methods to predict the crystal morphology, (for example the periodic-bond chain method), yet they tend to rely on the use of either DFT simulations (and so are expensive) or forcefields (making the predictions dependent on the forcefield parameters) [80]. Because of its simplicity, BFDH is extremely quick (the only input is the bulk crystallographic structure, i.e. the unit cell and its symmetry operators) and it can correctly predict the morphology provided that the building units are uniformly distributed throughout the crystal [79]. Therefore, a reasonable morphology should be predicted since MOFs form crystalline lattices. Furthermore, (as mentioned) properly shaped nanoparticles cannot be modelled due to computational constraints, hence the use of expensive morphology predictions would be wasteful. On the other hand, BFDH can be used to screen faces likely to appear in the crystal. These faces can then be used in slab models to determine the properties of interest, such as their influence on adsorption and the framework energetics.

2.5. Chapter 2 References

1. Gandara, F. and T. Bennett, *Crystallography of metal–organic frameworks.* International Union of Crystallography Journal, 2014. **1**: p. 563-570.
2. Groom, C.R., *The Cambridge Structural Database*, A. Crystallographica, Editor. 2016.
3. Steinhauser, M., *Computational Multiscale Modeling of Fluids and Solids*. 2008, Berlin: Springer.
4. Wang, S., et al., *Metal–Organic Framework Nanoparticles.* Advanced Materials, 2018. **30**(37): p. 1800202.
5. Frenkel, D. and B. Smit, *Understanding molecular simulation : from algorithms to applications. 2nd ed*. Vol. 50. 1996.
6. Zhang, C., et al., *Crystal-Size-Dependent Structural Transitions in Nanoporous Crystals: Adsorption-Induced Transitions in ZIF-8.* The Journal of Physical Chemistry C, 2014. **118**(35): p. 20727-20733.
7. Semino, R., et al., *Understanding the origins of metal–organic framework/polymer compatibility.* Chemical Science, 2018. **9**(2): p. 315-324.
8. Thompson, M., *Confirmation Report: Modelling MOF Nanoparticles*. 2017, University of Bath.
9. Halder, S., et al., *Density Functional Theory Analysis of Host–Guest Interactions in Cu(II)-Based Metal–Organic Frameworks for Pesticide Detection.* ACS Applied Nano Materials, 2019. **2**(9): p. 5469-5474.
10. Hamad, S., et al., *Atomic charges for modeling metal–organic frameworks: Why and how.* Journal of Solid State Chemistry, 2015. **223**: p. 144-151.
11. Bristow, J.K., et al., *Free Energy of Ligand Removal in the Metal–Organic Framework UiO-66.* The Journal of Physical Chemistry C, 2016. **120**(17): p. 9276-9281.
12. Nazarian, D., et al., *Large-Scale Refinement of Metal−Organic Framework Structures Using Density Functional Theory.* Chemistry of Materials, 2017. **29**(6): p. 2521-2528.
13. Coudert, F.-X., *The osmotic framework adsorbed solution theory: predicting mixture coadsorption in flexible nanoporous materials.* Physical Chemistry Chemical Physics, 2010. **12**(36): p. 10904-10913.
14. Sholl, S.S., J., *Density Functional Theory: A Practical Introduction*. 2009: Wiley.

15. Amusia, M.Y., A.Z. Msezane, and V.R. Shaginyan, *Density Functional Theory versus the Hartree–Fock Method: Comparative Assessment.* Physica Scripta, 2003. **68**(6): p. C133-C140.
16. Perdew, J.P., K. Burke, and M. Ernzerhof, *Generalized Gradient Approximation Made Simple.* Physical Review Letters, 1996. **77**(18): p. 3865-3868.
17. Grimme, S., S. Ehrlich, and L. Goerigk, *Effect of the damping function in dispersion corrected density functional theory.* Journal of Computational Chemistry, 2011. **32**(7): p. 1456-65.
18. Grimme, S., et al., *A consistent and accurate ab initio parametrization of density functional dispersion correction (DFT-D) for the 94 elements H-Pu.* The Journal of Chemical Physics, 2010. **132**(15): p. 154104.
19. Jensen, F., *Atomic orbital basis sets.* WIREs Computational Molecular Science, 2013. **3**(3): p. 273-295.
20. Hutter, J., et al., *cp2k: atomistic simulations of condensed matter systems.* Wiley interdisciplinary reviews. Computational molecular science, 2014. **4**: p. 25.
21. VandeVondele, J., et al., *Quickstep: Fast and accurate density functional calculations using a mixed Gaussian and plane waves approach.* Computer Physics Communications, 2005. **167**(2): p. 103-128.
22. Borštnik, U., et al., *Sparse matrix multiplication: The distributed block-compressed sparse row library.* Parallel Computing, 2014. **40**(5): p. 47-58.
23. Frigo, M. and S.G. Johnson, *The Design and Implementation of FFTW3.* Proceedings of the Institute of Electrical and Electronics Engineers, 2005. **93**(2): p. 216-231.
24. VandeVondele, J. and J. Hutter, *An efficient orbital transformation method for electronic structure calculations.* The Journal of Chemical Physics, 2003. **118**(10): p. 4365-4369.
25. Lippert, B.G., J.H. Parrinello, and Michele, *A hybrid Gaussian and plane wave density functional scheme.* Molecular Physics, 1997. **92**(3): p. 477-488.
26. Hartwigsen, C., S. Goedecker, and J. Hutter, *Relativistic separable dual-space Gaussian pseudopotentials from H to Rn.* Physical Review B, 1998. **58**(7): p. 3641-3662.
27. Goedecker, S., M. Teter, and J. Hutter, *Separable dual-space Gaussian pseudopotentials.* Physical Review B, 1996. **54**(3): p. 1703-1710.
28. VandeVondele, J. and J. Hutter, *Gaussian basis sets for accurate calculations on molecular systems in gas and condensed phases.* The Journal of Chemical Physics, 2007. **127**(11): p. 114105.

29. Ehrling, S., et al., *Crystal size versus paddle wheel deformability: selective gated adsorption transitions of the switchable metal–organic frameworks DUT-8(Co) and DUT-8(Ni).* Journal of Materials Chemistry A, 2019. **7**(37): p. 21459-21475.
30. Ongari, D., et al., *Building a Consistent and Reproducible Database for Adsorption Evaluation in Covalent-Organic Frameworks.* ACS central science, 2019. **5**(10): p. 1663-1675.
31. Hajek, J., et al., *On the intrinsic dynamic nature of the rigid UiO-66 metal-organic framework.* Chemical science, 2018. **9**(10): p. 2723-2732.
32. Klein, N., et al., *Monitoring adsorption-induced switching by (129)Xe NMR spectroscopy in a new metal-organic framework Ni(2)(2,6-ndc)(2)(dabco).* Physical Chemistry Chemical Physics, 2010. **12**(37): p. 11778-84.
33. Yesylevskyy, S., et al., *Empirical force field for cisplatin based on quantumdynamics data: case study of new parameterization scheme for coordinationcompounds.* Journal of Molecular Modeling, 2015. **21**(10): p. 268.
34. Lorentz, H.A., *Ueber die Anwendung des Satzes vom Virial in der kinetischen Theorie der Gase.* Annalen der Physik, 1881. **248**(1): p. 127-136.
35. Wells, B.A. and A.L. Chaffee, *Ewald Summation for Molecular Simulations.* Journal of Chemical Theory and Computation, 2015. **11**(8): p. 3684-3695.
36. Darden, T., D. York, and L. Pedersen, *Particle mesh Ewald: An N·log(N) method for Ewald sums in large systems.* The Journal of Chemical Physics, 1993. **98**(12): p. 10089-10092.
37. Wolf, D., et al., *Exact method for the simulation of Coulombic systems by spherically truncated, pairwise r−1 summation.* The Journal of Chemical Physics, 1999. **110**(17): p. 8254-8282.
38. Gupta, A., et al., *Object-oriented Programming Paradigms for Molecular Modeling.* Molecular Simulation, 2003. **29**(1): p. 29-46.
39. Gowers, R., et al., *Automated analysis and benchmarking of GCMC simulation programs in application to gas adsorption.* Molecular Simulation, 2017. **00**: p. 1-22.
40. Bekker, H., et al., *Gromacs - a Parallel Computer for Molecular-Dynamics Simulations.* Physics Computing '92, 1993: p. 252-256.
41. Adcock, S.A. and J.A. McCammon, *Molecular dynamics: survey of methods for simulating the activity of proteins.* Chemical Reviews, 2006. **106**(5): p. 1589-1615.
42. Mayo, S.L., B.D. Olafson, and W.A. Goddard, *DREIDING: a generic force field for molecular simulations.* The Journal of Physical Chemistry, 1990. **94**(26): p. 8897-8909.

43. Rappe, A.K., et al., *UFF, a full periodic table force field for molecular mechanics and molecular dynamics simulations.* Journal of the American Chemical Society, 1992. **114**(25): p. 10024-10035.
44. Potoff, J.J. and J.I. Siepmann, *Vapor–liquid equilibria of mixtures containing alkanes, carbon dioxide, and nitrogen.* American Institute of Chemical Engineers Journal, 2001. **47**(7): p. 1676-1682.
45. Eggimann, B.L., et al., *An online parameter and property database for the TraPPE force field.* Molecular Simulation, 2014. **40**(1-3): p. 101-105.
46. Seminario, J.M., *Calculation of intramolecular force fields from second-derivative tensors.* International Journal of Quantum Chemistry, 1996. **60**(7): p. 1271-1277.
47. Dodoff, N., *"A DFT/ECP-Small Basis Set Modelling of Cisplatin: Molecular Structure and Vibrational Spectrum".* Computational Molecular Bioscience, 2012. **2**: p. 35-40.
48. Hill, T., *Introduction to Statistical Thermodynamics*. 1986: Dover Publications.
49. Earl, D. and M. Deem, *Monte Carlo Simulations.* Methods in molecular biology (Clifton, N.J.), 2008. **443**: p. 25-36.
50. Peng, D.-Y. and D.B. Robinson, *A New Two-Constant Equation of State.* Industrial & Engineering Chemistry Fundamentals, 1976. **15**(1): p. 59-64.
51. Jorgensen, W.L. and J. Tirado-Rives, *Monte Carlo vs Molecular Dynamics for Conformational Sampling.* The Journal of Physical Chemistry, 1996. **100**(34): p. 14508-14513.
52. Hospital, A., et al., *Molecular dynamics simulations: advances and applications.* Advances and applications in bioinformatics and chemistry, 2015. **8**: p. 37-47.
53. Verlet, L., *Computer "Experiments" on Classical Fluids. II. Equilibrium Correlation Functions.* Physical Review, 1968. **165**(1): p. 201-214.
54. Swope, W.C., et al., *A computer simulation method for the calculation of equilibrium constants for the formation of physical clusters of molecules: Application to small water clusters.* The Journal of Chemical Physics, 1982. **76**(1): p. 637-649.
55. Hockney, R.W., S.P. Goel, and J.W. Eastwood, *Quiet high-resolution computer models of a plasma.* Journal of Computational Physics, 1974. **14**(2): p. 148-158.
56. Berendsen, H.J.C., et al., *Molecular dynamics with coupling to an external bath.* The Journal of Chemical Physics, 1984. **81**(8): p. 3684-3690.
57. Bussi, G., D. Donadio, and M. Parrinello, *Canonical sampling through velocity rescaling.* The Journal of Chemical Physics, 2007. **126**(1): p. 014101.

58. Andersen, H.C., *Molecular dynamics simulations at constant pressure and/or temperature.* The Journal of Chemical Physics, 1980. **72**(4): p. 2384-2393.
59. Nosé, S., *A unified formulation of the constant temperature molecular dynamics methods.* The Journal of Chemical Physics, 1984. **81**(1): p. 511-519.
60. Hoover, W.G., *Canonical dynamics: Equilibrium phase-space distributions.* Physical Review A, 1985. **31**(3): p. 1695-1697.
61. Parrinello, M. and A. Rahman, *Polymorphic transitions in single crystals: A new molecular dynamics method.* Journal of Applied Physics, 1981. **52**(12): p. 7182-7190.
62. Nosé, S. and M.L. Klein, *Constant pressure molecular dynamics for molecular systems.* Molecular Physics, 1983. **50**(5): p. 1055-1076.
63. Askeland, D.R., *Atom Movement in Materials*. The Science and Engineering of Materials. 1996, Boster: Springer.
64. Ozer, G., S. Quirk, and R. Hernandez, *Adaptive steered molecular dynamics: Validation of the selection criterion and benchmarking energetics in vacuum.* The Journal of Chemical Physics, 2012. **136**(21): p. 215104.
65. Shen, L., et al., *Steered Molecular Dynamics Simulation on the Binding of NNRTI to HIV-1 RT.* Biophysical Journal, 2003. **84**(6): p. 3547-3563.
66. Jarzynski, C., *Nonequilibrium Equality for Free Energy Differences.* Physical Review Letters, 1997. **78**(14): p. 2690-2693.
67. Camp, J.S. and D.S. Sholl, *Transition State Theory Methods To Measure Diffusion in Flexible Nanoporous Materials: Application to a Porous Organic Cage Crystal.* The Journal of Physical Chemistry C, 2016. **120**(2): p. 1110-1120.
68. Barducci, A., M. Bonomi, and M. Parrinello, *Metadynamics.* WIREs Computational Molecular Science, 2011. **1**(5): p. 826-843.
69. Kumar, S., et al., *THE weighted histogram analysis method for free-energy calculations on biomolecules. I. The method.* Journal of Computational Chemistry, 1992. **13**(8): p. 1011-1021.
70. Abrams, C. and G. Bussi, *Enhanced Sampling in Molecular Dynamics Using Metadynamics, Replica-Exchange, and Temperature-Acceleration.* Entropy, 2014. **16**.
71. Bennett, C.H., *Efficient estimation of free energy differences from Monte Carlo data.* Journal of Computational Physics, 1976. **22**(2): p. 245-268.

72. Sarkisov, L. and A. Harrison, *Computational structure characterisation tools in application to ordered and disordered porous materials.* Molecular Simulation, 2011. **37**(15): p. 1248-1257.
73. Brunauer, S., P.H. Emmett, and E. Teller, *Adsorption of Gases in Multimolecular Layers.* Journal of the American Chemical Society, 1938. **60**(2): p. 309-319.
74. Horcajada, P., et al., *Flexible Porous Metal-Organic Frameworks for a Controlled Drug Delivery.* Journal of the American Chemical Society, 2008. **130**(21): p. 6774-6780.
75. Salles, F., et al., *Molecular Dynamics Simulations of Breathing MOFs: Structural Transformations of MIL-53(Cr) upon Thermal Activation and CO2 Adsorption.* Angewandte Chemie International Edition, 2008. **47**(44): p. 8487-8491.
76. Ghoufi, A. and G. Maurin, *Hybrid Monte Carlo Simulations Combined with a Phase Mixture Model to Predict the Structural Transitions of a Porous Metal−Organic Framework Material upon Adsorption of Guest Molecules.* The Journal of Physical Chemistry C, 2010. **114**(14): p. 6496-6502.
77. Chen, L., et al., *Elucidating the breathing of the metal-organic framework MIL-53(Sc) with ab initio molecular dynamics simulations and in situ X-ray powder diffraction experiments.* Journal of the American Chemical Society, 2013. **135**(42): p. 15763-73.
78. Hwang, J., et al., *Controlling the morphology of metal–organic frameworks and porous carbon materials: metal oxides as primary architecture-directing agents.* Chemical Society Reviews, 2020. **49**(11): p. 3348-3422.
79. Hartman, P. and W.G. Perdok, *An interpretation of the law of donnay and harker.* American Mineralogist, 1956. **41**(5-6): p. 449-459.
80. Dandekar, P., Z.B. Kuvadia, and M.F. Doherty, *Engineering Crystal Morphology.* Annual Review of Materials Research, 2013. **43**(1): p. 359-386.
81. Fiorentini, V. and M. Methfessel, *Extracting convergent surface energies from slab calculations.* Journal of Physics: Condensed Matter, 1996. **8**(36): p. 6525-6529.

CHAPTER 3. SIZE-DEPENDENT ADSORPTION AND FRAMEWORK FLEXIBILITY IN DUT-8(Ni)

3.1. Motivation: importance of the external surface in nanoparticle models

Compared to typical microparticles, MOF nanoparticles have large external surface areas per unit volume. Therefore, the external surface will be more influential on the performance properties of MOFs, such as their ability to uptake guest molecules and their guest-induced framework flexibility. This size-dependent adsorption and flexibility has been experimentally observed in a variety of different MOFs [1-3]. However, there have been very few computational studies to date [4] which explore the underlying thermodynamics behind why (or if) the external surface influences these performance properties.

This chapter focusses on understanding the thermodynamics behind size-dependent adsorption and framework flexibility in DUT-8(Ni). Experiments have shown that "normal" synthesis conditions form DUT-8(Ni) microparticles that have very narrow pores when purged of guest molecules (gate-closing). Upon exposure to guest-molecules such as N_2, the narrow pores open to accommodate guest molecules (gate-opening). This transition between the open (*op*) and closed (*cp*) pore form is reversible [5-7]. However, a slightly modified synthesis that enhances the rate of nucleation yields DUT-8(Ni) nanoparticles that cannot undergo gate-closing [5]. Simulations were used to understand the difference between flexible microparticles and rigid nanoparticles, and to determine whether it truly is the external surface that is responsible or if other factors are the cause of this discrepancy.

3.2. Summary: GCMC and DFT simulations to predict N_2 uptake and N_2 – induced gate-closing

DUT-8(Ni) microparticles and nanoparticles were represented as the bulk unit cell (duplicated in PBCs) and 2-D infinite slab models as described in Figure 2.2. The latter was based on the most likely faces to appear in the final crystal structure, as calculated using the BFDH method (see Section 2.4.3 [8]) and validated from face-indexing of single crystals using a diffractometer. DFT cell optimisations (i.e. the relaxation of the atomic coordinates and unit cell parameters) were then used to equilibrate and subsequently calculate the internal energies of the empty bulk unit cells and slab models. Each equilibrated structure was then used to perform GCMC simulations to calculate the N_2 adsorption isotherms and

determine how they differ with particle size. Experimental volumetric gas adsorption experiments allowed the computationally derived isotherms to be validated, hence the adsorption sites and interaction energies could also be validated. By combining the internal energies of the empty framework and GCMC derived adsorption isotherms into OFAST (see Section 2.4.2 [9]), the gate-closing pressure could be predicted and validated against experimental adsorption isotherms in the microparticles.

3.3. Results: the external surface has limited influence on the performance properties, therefore MOF nanoparticles can be modelled using the bulk unit cell

The GCMC simulations showed that the external surface of DUT-8(Ni) nanoparticles changes the shape of the N_2 adsorption isotherm. Reduced DUT-8(Ni) – N_2 interaction energies on the surface decrease the uptake at low pressures, smoothing the knee of the adsorption isotherm. Presence of the vacuum gap creates an inflection in the isotherms at high pressures, caused by extracrystalline adsorption as also seen experimentally. Although the external surface reduces the interaction energies and the amount adsorbed (at low pressures), its influence is short-ranged and does not significantly influence adsorption in the intact, non-cleaved pores regardless of how close they are to the external surface.

OFAST reveals that a slightly modified conformational isomer of DUT-8(Ni) cannot undergo gate-closing regardless of the N_2 pressure (this was also seen by Petkov et al who used *ab-initio* MD simulations [10]). It can also accurately predict the gate-closing pressure of the isomer obtained in experimental microparticles. The simulations show that the external surface can shift the gate-closing pressure, and this is something that can be manipulated by varying the capping groups used to coordinate the external surface. They further show that the external surface is not the cause of rigid nanoparticles because the variation in gate-closing pressure is within the experimentally used pressure limits.

Ultimately (for the purpose of screening simulations in Chapters 4, 5, and 6), when modelling nanoparticles, it is valid to simply model the bulk unit cell without accounting for the external surface since its influence on interaction energies and guest molecule adsorption are short-ranged. However, it should be noted that this conclusion is based on very simplistic, flat, perfectly cleaved external surfaces with small capping groups. In reality, surface effects (i.e. imperfections) could penetrate deeper into the crystal and in biomedical applications the external surfaces would typically be capped with large groups (such as bio-receptors).

Another limitation is that this conclusion is based on simulations which do not account for the variation in diffusivity from the external surface to the bulk crystal. However, based on the short-ranged variation of MOF-guest interaction energies from the external surface into the bulk crystal, it is not likely that idealised surfaces such as those used in this work will significantly change diffusion regimes.

3.4. Errata

No errata at the date of submission

3.5. Chapter 3 Preamble References

1. Kundu, T., et al., *Solvent-Induced Control over Breathing Behavior in Flexible Metal–Organic Frameworks for Natural-Gas Delivery.* Angewandte Chemie International Edition, 2019. **58**(24): p. 8073-8077.
2. Krause, S., et al., *The impact of crystal size and temperature on the adsorption-induced flexibility of the Zr-based metal-organic framework DUT-98.* Beilstein journal of nanotechnology, 2019. **10**: p. 1737-1744.
3. Krause, S., et al., *The effect of crystallite size on pressure amplification in switchable porous solids.* Nature Communications, 2018. **9**(1): p. 1573.
4. Zhang, C., et al., *Crystal-Size-Dependent Structural Transitions in Nanoporous Crystals: Adsorption-Induced Transitions in ZIF-8.* The Journal of Physical Chemistry C, 2014. **118**(35): p. 20727-20733.
5. Miura, H., et al., *Tuning the gate-opening pressure and particle size distribution of the switchable metal–organic framework DUT-8(Ni) by controlled nucleation in a micromixer.* Dalton Transactions, 2017. **46**(40): p. 14002-14011.
6. Kavoosi, N., et al., *Tailoring adsorption induced phase transitions in the pillared-layer type metal-organic framework DUT-8(Ni).* Dalton Transactions, 2017. **46**(14): p. 4685-4695.
7. Ehrling, S., *Crystal size versus paddle wheel deformability: selective gated adsorption transitions of the switchable metal–organic frameworks DUT-8(Co) and DUT-8(Ni).* Journal of materials chemistry A, 2019. **v. 7**(no. 37): p. pp. 21459-21475-2019 v.7 no.37.
8. Hartman, P. and W.G. Perdok, *An interpretation of the law of donnay and harker.* American Mineralogist, 1956. **41**(5-6): p. 449-459.

9. Coudert, F.-X., *The osmotic framework adsorbed solution theory: predicting mixture coadsorption in flexible nanoporous materials.* Physical Chemistry Chemical Physics, 2010. **12**(36): p. 10904-10913.
10. Petkov, P.S., et al., *Conformational isomerism controls collective flexibility in metal–organic framework DUT-8(Ni).* Physical Chemistry Chemical Physics, 2019. **21**(2): p. 674-680.

This declaration concerns the article entitled:			
Size-dependent adsorption and framework flexibility in DUT-8(Ni)			
Publication status (tick one) **Draft manuscript** [ ] **Submitted** [ ] **In review** [/] **Accepted** [ ] **Published** [ ]			
Publication details (reference)	Thompson, M. Hobday, C. Senkovska, I. Bon, V. Ehrling, Maliuta, M. S. Kaskel, S. Düren, T. 2020. Size-dependent adsorption and framework flexibility in DUT-8(Ni).		
Copyright status (tick the appropriate statement) I hold the copyright for this material [ ] Copyright is retained by the publisher, but I have been given permission to replicate the material here [/]			
Candidate's contribution to the paper (provide details, and also indicate as a percentage)	The candidate contributed to / considerably contributed to / predominantly executed the… Formulation of ideas: The candidate predominantly formulated the detailed ideas (60 %). General ideas for the paper were developed by C. Hobday, T. Düren, I. Senkovska, and S. Kaskel. (40 %). Design of methodology: The candidate predominantly designed the method for the simulations (90 %). Collaborators affiliated with TU Dresden designed the method for experiments (10 %). Experimental work: The candidate predominantly conducted the simulations (80 %). Collaborators affiliated with TU Dresden conducted the experiments (20 %). Presentation of data in journal format: The candidate predominantly presented the work in a journal format (100 %)		
Statement from Candidate	This paper reports on original research I conducted during the period of my Higher Degree by Research candidature.		
Signed		**Date**	01/09/2020

Influence of particle size and external surface on adsorption and framework flexibility in DUT-8(Ni)

Megan J. Thompson[¶], *Claire L. Hobday*[¶,†], *Irena Senkovska*[#], *Volodymyr Bon*[#], *Sebastian Ehrling*[#], *Mariia Maliuta*[#], *Stefan Kaskel*[#], *Tina Düren*[*,¶]

[¶] Centre for Advanced Separations Engineering, Department of Chemical Engineering, University of Bath, BA2 7AY, UK

[†] Current address: EaStChem School of Chemistry and Centre for Science at Extreme Conditions, University of Edinburgh, David Brewster Road, Joseph Black Building, Edinburgh, EH9 3FJ, UK

[#] Chair of Inorganic Chemistry, Department of Chemistry and Food Chemistry, TU Dresden, Bergstraße 66, 01069 Dresden, Germany

AUTHOR ADDRESS Prof. T. Düren, Centre for Advanced Separations Engineering, Department of Chemical Engineering, University of Bath, BA2 7AY, UK
E-mail: t.duren@bath.ac.uk

ABSTRACT

Flexible MOF nanoparticles, i.e. MOF nanoparticles that change their structure upon external stimuli such as guest uptake, are promising for numerous applications including advanced gas adsorption, drug delivery and sensory devices. However, the properties of MOFs are typically characterised based on the bulk material with no consideration of how the particle size and external surface influences their performance. This combined computational and experimental contribution investigates the influence of the particle size and surface functionalisation on the flexibility of DUT-8(Ni) (Ni_2 (2,6-ndc)$_2$ dabco, ndc = naphthalene dicarboxylate, dabco = 1,4-diazabicyclo[2.2.2]octane, DUT=Dresden University of Technology). In DUT-8, nanoparticles remain rigid in their open pore form while microparticles, synthesised under slightly different conditions, undergo gate opening

upon nitrogen adsorption. Simulations reveal that while the adsorption environment at the surface capped with modulators smaller than the 2,6-ndc ligand is very different compared to the bulk of the crystal with considerably weaker guest-framework interaction, the nanoparticles should close. We conclude that the size of the nanoparticles is not the major contributor for keeping DUT-8 nanoparticles open but that it is more likely that defects or nucleation barriers dominate. Moreover, our work reveals for the first time that functionalising the external surface of nanoparticles with different modulators or capping groups offers the opportunity to manipulate the gate opening / closing pressure. This principle is generally applicable and could be exploited to tune the gate openig / closing pressure for the application of interest.

INTRODUCTION

Metal-organic frameworks (MOFs) consist of metal nodes connected by organic ligands forming porous crystalline materials. They have record internal surface areas (up to ~7800 m^2/g) [1], high porosities [2], and their properties can be systematically tailored by using different building units [3]. These properties have resulted in extensive research towards the application of MOFs in gas separation [4], storage [5], and catalysis [6].

Some MOFs also exhibit framework flexibility due to their weak intramolecular bonding (for instance, π-π bonds, and hydrogen bonds). Framework flexibility is an exciting property whereby the crystal switches between stable structures upon exposure to external stimuli such as guest molecules, electromagnetic radiation, or changes in temperature or pressure [7]. Some MOFs are more flexible than others, and so the phase transition can cause marginal or major changes in the structure. ZIF-8 (zeolitic imidazole framework), for example, is a relatively rigid structure that shows a reversible rotation of its 2-methyl-imidazole linkers during the phase transition. This modest structural change results in a relatively small step in the adsorption isotherm [8]. On the other hand, MOFs such as MIL-53 and DUT-8 show transitions between open and closed pore structures associated with larger volume changes, which results in a large change in the porosity and consequently pronounced steps and hysteresis in the adsorption isotherms [9, 10].

Framework flexibility can have severe consequences for the use of MOFs in practical applications. For instance, finely tuned pore sizes and window diameters are used to exclude larger molecules in molecular sieving applications, which is forfeited if the pores can change shape [7]. On the other hand, framework flexibility also opens up new applications for MOFs, such as their use in sensory devices [11, 12], advanced gas separations [13] or as carriers for drug delivery [7, 14]. In sensing devices, the well-defined topologies and highly porous nature of MOFs means they offer enhanced sensitivity and selectivity towards the analyte [15]. Contact with the analyte typically induces a phase transition that can be detected by changes in the MOF's optical properties [16] or conformational changes of a reporter molecule [17]. As carriers for drug delivery, flexible MOFs will adapt to optimize their geometric and energetic properties, so the guest-host interaction energies can be tailored to retain the drug and decrease its rate of release [18]. Finally, due to differences in gate-opening pressures, flexible MOFs offer the ability to separate gases with similar physiochemical properties at near ambient conditions [19].

In many of these applications, it is preferable to use MOF nanoparticles. Whilst nanoparticles exhibit the physiochemical properties of typical microparticles, their properties are also largely governed by the external surface, which can be functionalized to improve the particle stability and incorporation into the system of interest. For example, in gas separation applications, the incorporation of smaller MOF nanoparticles into mixed-matrix membranes increases the MOF-polymer contact area. This reduces voids between the two materials, hence the structure retains its selectivity [20].

It is clear from the previous examples that flexible MOF nanoparticles have a huge potential in many applications. However, MOFs are normally characterized based on the typical micrometre-sized particles, the properties of which are governed by the "bulk" crystal (i.e. the repeating unit cell) and surprisingly few studies have addressed the influence of particle size and the external surface on the properties of flexible MOFs. For several gating and breathing MOFs, particle-size dependent flexibility was observed, including MIL-53(Al) [21], DUT-49 [22], DUT-98 [23] and interpenetrated pillared layer MOFs such as $Cu_2(bdc)_2(bpy)$ (bdc = 1,4-benzenedicarboxylate, bpy = 4,4′-bipyridine) [24]. In a detailed experimental and simulation study Zhang *et al.* shed light on why the gate-opening pressure of ZIF-8 increases with decreasing

particle size [25]. From theory, it is well known that the pressure of the phase transition depends on: (a) the free energy of the empty framework, (b) the external work imposed on the system, and (c) the guest-host interaction energy [26]. In the case of ZIF-8, it was proposed that weaker adsorption energies at the external surface are the underlying cause for the crystal-size dependence on gate-opening [25].

Another MOF for which particle size dependence on phase transition has been observed is the pillared layer MOF DUT-8(Ni) which consists of Ni_2 paddle wheel units that are each coordinated by four 2,6-ndc (2,6-naphthalenedicarboxylate) anions, forming 2-D square nets. The 3-D structure arises from the axial coordination of Ni metal sites to dabco molecules (1,4-diazabicyclo[2.2.2]octane), connecting the neighbouring nets [10]. DUT-8 is unusual as it can be obtained as a flexible material when synthesised as micrometre-sized crystals or as a rigid material when synthesized as at submicron size (< 500 nm) [27-29].

Using a mixture of DMF, MeOH, and a defined dabco concentration during the synthesis results in micrometre-sized crystals in the open pore form (*op*). Immediately upon the removal of solvent, DUT-8(Ni) microparticles undergo a phase transition from the open pore (*op*) to the closed pore (*cp*) form. During the physisorption of N_2 at 77 K, CO_2 at 195 K, *n*-butane at 273 K, ethane at 185 K or ethylene at 169 K, desolvated DUT-8(Ni) microparticles switch back to the *op* form, if a certain adsorptive pressure is reached which depends on the guest molecule [30]. This transition between a closed and open pore structure leads to a large change in pore volume and hence a large, abrupt step in the adsorption isotherm [10]. Moreover, it was shown that repeated adsorption/desorption in this system leads to the changes in flexibility and adsorption behaviour, manifested in the slope of the adsorption isotherms [31].

However, if DUT-8(Ni) is synthesized using a somewhat modified preparation method in pure DMF with an excess of dabco, this results in the fast deprotonation of H_2(2,6-ndc) ligands and rapid nucleation. This gives rise to DUT-8(Ni) nanoparticles (50 nm – 500 nm in size) that remain rigid in their open pore (presumably metastable) phase after solvent removal and gas physisorption [27, 28]. Synthesis of DUT-8(Ni) in a microreactor (which allows precise tailoring of the particle size) confirmed that

small particles remain rigid [27]. A comparable behaviour is observed for DUT-8(Co) demonstrating the stiffening effect for smaller particles [29].

It was recently found that the open pore form of the larger microcrystals of DUT-8(Ni) exists in two conformational isomers, A and B [32]. However, these isomers only represent two limiting, ordered instances of a much larger configurational landscape [33]. As shown in Figure 1, conformer A describes the isomer in which all four 2,6-ndc ligands around a Ni_2 unit point in the same direction. In conformer B, two pairs of adjacent 2,6-ndc ligands point in opposite directions around the metal node. X-ray diffraction experiments show that the "as-made" (i.e. solvent containing) larger *op* microparticles are either conformer B, or a disordered structure containing both conformers A and B. For example, a disordered phase, containing both conformers A*op* and B*op*, is initially observed after synthesis in DMF and methanol [29]. Desolvation of the microparticles transforms the "as-made" structure into conformer B*cp*. During gas adsorption, the pores in the microparticles open forming a gas@B*op* conformer, where the structures differ slightly depending on the accommodated guest molecules [30, 32]. In contrast, the exact conformation of the smaller, rigid (*op*) nanoparticles is still challenging to resolve due to peak broadening and hence limited information from X-ray diffraction analysis. However, electron diffraction demonstrates disordered superstructures to persist on the nanodomain level [29].

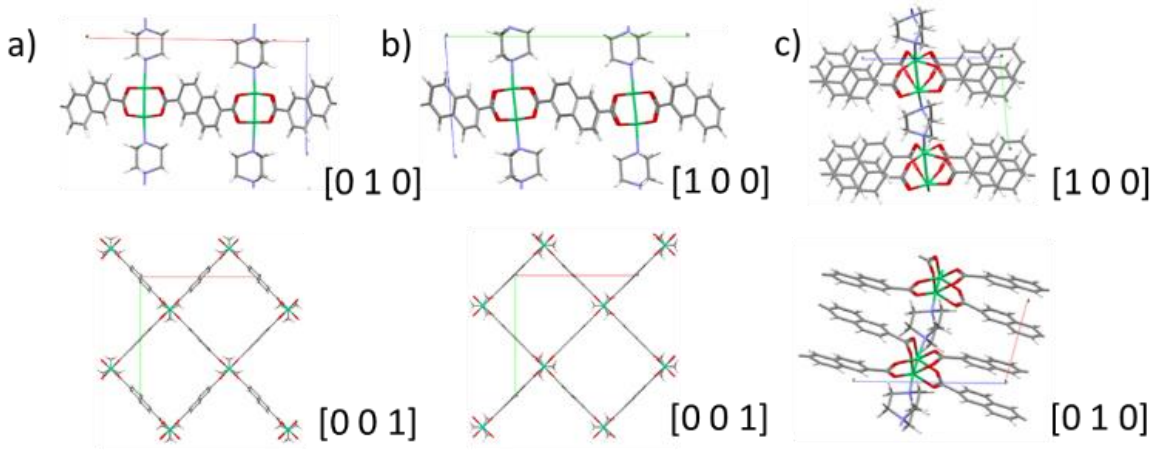

Figure 1. Structures of (from left to right) Conformers A*op*, B*op*, and B*cp* [30] [34]. Colour scheme: red = oxygen, grey = carbon, white = hydrogen, blue = nitrogen, green = nickel.

Recent computational work has shown that the phase transition A*op* → A*cp* is energetically unfavourable and that the phase transition from open to closed pore form has to go through

B*op* → B*cp* [32]. While these results show unequivocally that the closed pore form must be B*cp* we cannot deduce that the rigid nanoparticles consist of A*op* and therefore that the rigidity is caused by the conformer as there is preliminary experimental evidence that A*op* can convert into B*op* [29]. The different conformers of DUT-8(Ni) are therefore unlikely to be the origin of the different flexibility behaviour resulting from the different synthesis pathways.

The different synthesis pathways, however, result in very different crystallization conditions. Supersaturation in the synthesis of the rigid nanoparticles leads to rapid nucleation and small crystals while the higher solubility during the synthesis of the flexible microparticles leads to slower crystallization and larger crystals [28]. Using continuous wave electron paramagnetic resonance (EPR) spectroscopy studies, Mendt *et al.* showed that the rigid nanoparticles contain considerably more defects in the form of missing 2,6-ndc^{2-} and dabco linkers and defective paddle wheel units with only one Ni^{2+} ion [35].

Despite being generally accepted that defects play an important role in determining the flexibility behaviour it remains unclear what role the external surface plays. In this paper, we therefore investigate how the external surface influences the flexibility behaviour of the flexible microparticles and the rigid nanoparticles, and what influence surface groups capping the surface of the nanoparticles have. We use a combination of experiments, density functional theory (DFT) and grand-canonical Monte Carlo (GCMC) simulations to study the size-dependent uptake and phase transition witnessed during N_2 adsorption in DUT-8(Ni).

METHODS

COMPUTATIONAL METHODS

Structural Models: For DUT-(Ni) two different conformers, A and B, can be considered as the limiting cases depending on the orientation of the 2,6-ndc^{2-} linkers [32]. For both conformer A and B, the open and closed pore DUT-8(Ni) microparticles were modelled as the bulk unit cell duplicated in periodic boundary conditions to mimic the bulk behaviour. To understand how adsorption varies across the nanoparticles, the optimized conformer B (*op* and *cp*) bulk unit cells were

extended and cleaved to form (001) and (110) surfaces. These faces have high BFDH (Bravais Friedel Donnay Harker) morphological indices (full BFDH morphologies are given in the SI, Section S1) [36, 37] and are also observed experimentally. To ensure a fair comparison between the different phases, each slab type was cut to have the same number of atoms in the open and closed pore structure. This resulted in 2-D infinite slabs of length 40 – 70 Å (surface to surface). A vacuum gap of 20 Å was implemented either side of the external surface to prevent overlapping surface energies and to mimic adsorption in a nanoparticle surrounded by the "bulk" gas phase. During the surface creation coordination bonds were cleaved as opposed to covalent bonds which would be less energetically favourable. Uncoordinated nickel atoms on the surface were then saturated according to the surface termination – (001) surfaces were saturated with protonated dabco or DMF molecules, whereas (110) surfaces were saturated with monoprotonated 2,6-ndc or formic acid groups (see the SI, Section S2 for more information). The terminations were used to determine their influence on adsorption, and whether differences in strain and dispersion on the surface contribute to phase transition pressure of DUT-8 particles.

Ab-initio cell and geometry optimizations: Prior to their use in GCMC simulations, all of the models were optimized in terms of their atomic positions and unit cell lengths using the Quickstep module in CP2K [38-43]. Quickstep uses a Gaussian and planewave (GPW) approach, in which Gaussian basis functions are centred on the atoms and the electron density is propagated with planewaves, resulting in efficient computation of the energy. Prior to optimization, appropriate values of the planewave cut-off and relative cut-off were determined based on the convergence of single-point static energy calculations. The cut-off and relative cut-off values used are 700 Ry and 50 Ry for the slabs, and 600 Ry and 50 Ry for the bulk. Non-classical exchange correlation terms were approximated using the PBE functional [44] with DFT-D3 dispersion corrections [45, 46]. To reduce computational cost, the core electrons were modelled using pseudopotentials derived by Goedecker, Teter, and Hutter (GTH) [47]. Quickstep solves the Kohn Sham matrix by representing the wavefunction as Gaussian type basis sets. Triple-zeta Gaussian type basis sets (TZV2P-MOLOPT) were used to describe all atoms with the exception of nickel which was described using double-zeta functions (DZVP-MOLOPT) [48]. As with the planewaves, core electrons were described by GTH pseudopotentials [49, 50]. All structures were fully relaxed (both in terms of the atomic coordinates and unit cell parameters) using a

BFGS optimizer. Tolerances for convergence were set to 0.003 and 0.0015 Bohr for the maximum and root-mean-square of atomic displacements, and 0.0004 and 0.0003 Bohr/Ha for the maximum and root-mean-square of the atomic forces. During the minimizations, each bulk structure optimized to the same phase and conformer as the input (i.e. no gate-closing was observed). Hence, each phase and conformer are local minima on the DUT-8(Ni) energy landscape.

Grand-canonical Monte Carlo simulations: N_2 adsorption at 77 K was modelled using GCMC simulations as implemented in the multipurpose simulation code MuSiC [51] using rigid frameworks. N_2 - DUT-8(Ni) non-Coulombic interactions were calculated using the Lennard-Jones (LJ) 12-6 potential, and N_2 – DUT-8(Ni) Coulombic interactions were calculated using Ewald summation [52]. N_2 – N_2 Coulombic and LJ interactions were calculated on-the-fly using the Wolf summation method [53] and the LJ 12-6 potential respectively. A cut-off radius of 18 Å was used for all interactions. DUT-8(Ni) partial atomic charges were taken as the Mulliken charges from DFT minimized structures. LJ parameters for the framework were taken from the Dreiding force field [54], with the exception of nickel, for which the parameters were taken from the Universal Force Field [55]. LJ parameters and partial atomic charges for the N_2 molecules were taken from the TraPPE force field which describes N_2 molecules as three spheres, with two nitrogen atoms (partial charges of -0.482 e) separated at a distance of 0.55 Å from a dummy atom at the centre of mass which neutralizes the overall charge and has Lennard-Jones parameters of nil [56]. Microstates were generated using four GCMC moves: insertion, deletion, translation and rotation. 10 million iterations were used for each pressure point, and the first 40 % of microstates were neglected to ensure the ensemble average is taken at equilibrium. Finally, to calculate the fugacity, the Peng Robinson equation of state was used [57]. In the slab models, there is early onset condensation in the confined space of the vacuum gap and therefore the size of the vacuum gap influences the adsorption isotherm when extracrystalline adsorption begins. A simple normalization (as described in the SI, Section S3) was used to correct for the influence of the vacuum gap, meaning the high pressure region of the isotherm can be captured.

Phase-transition pressure prediction*:* The osmotic framework adsorbed solution theory (OFAST) [26] was used to determine the phase-transition pressure of DUT-8(Ni) microparticles and nanoparticles (see the SI, Section S4 for details). The free

energies of the empty frameworks were assumed to equal the internal energies calculated using *ab-initio* optimizations on the bulk and slab models. Isotherms used to analyse the N_2 contributions to the osmotic potential were obtained using GCMC simulations.

EXPERIMENTAL METHODS

icrocrystals and nanoparticles were synthesised according to the published procedure [28]. The samples were characterised by powder X-ray diffraction to ensure the crystallinity and the phase purity of the synthetized materials. After synthesis, the solvent in the pores was exchanged to dichloromethane in case of microcrystals and to ethanol in case of nanoparticles for three days. After solvent exchange, the microcrystals were evacuated first at 25 °C for 16 h and additionally at 120 °C for 4 h. The nanoparticles were desolvated at 150 °C in vacuum for 16 h.

The cyclic nitrogen physisorption experiments on DUT-8(Ni) microcrystals at 77 K were performed on BELSORP-Max instrument (Microtrac BEL, Japan). Between the measurements the sample was evacuated for 2 h at 25 °C. Adsorption isotherms for DUT-8(Ni) nanoparticles were measured on Autosorb IQ gas sorption analyser (Quantachrome). Scanning electron microscopy (SEM) was performed with a HITACHI SU 8020 instrument.

RESULTS AND DISCUSSION

In order to contrast the N_2 adsorption behaviour for the micro- and nanoparticles, we first look at N_2 adsorption in the microparticles represented by infinite periodic structures in the GCMC simulations. Figure 2 shows negligible difference between the simulated A*op* and B*op* isotherms, in which the pores saturate at a loading of ~ 600 cm^3(STP)/g at $p/p_0 \approx 0.0025$.

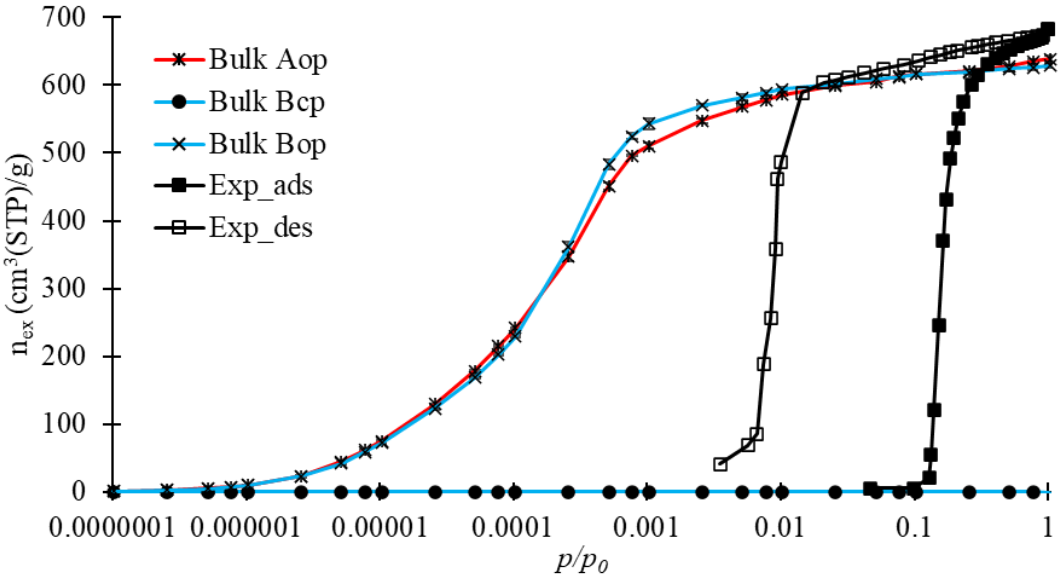

Figure 2. Simulated adsorption isotherms of N_2 in bulk conformers A and B, and the initial experimental N_2 adsorption isotherm at 77 K on a fresh sample (large particles) without cycling.

This maximum loading is similar to that observed experimentally in a fresh sample of DUT-8 (note that as previously reported [31], DUT-8 delaminates upon cycling which results in smaller domains, reduced maximum uptake, and an increase in the gate opening and closing pressures - see Section S5 in the SI). No adsorption is expected in B*cp* as the maximum pore diameter (2.3 Å) is smaller than the collision diameter of N_2 (3.7 Å).

To illustrate the adsorption mechanism, Figure 3 presents the Boltzmann distribution as a probability map for N_2 adsorption in the bulk conformer B*op* at 77 K (note that the maps for A*op* are nearly identical to those for B*op*, see Figure S7 in the SI). The most favourable adsorption site (site 1) is situated in the pore corners next to the Ni_2 unit, at which N_2 molecules experience overlapping interactions from adjacent 2,6-ndc^{2-} ligands, resulting in a relative adsorption probability of 1. There are weaker adsorption sites next to the dabco ligands (site 2) and next to the 2,6-ndc^{2-} ligands (site 3). At sites 2 and 3, N_2 molecules experience interactions from a high number of surrounding nitrogen and/or carbon atoms, resulting in relative adsorption probabilities of ~ 0.1. Finally, there is a non-distinct, low probability region for adsorption elsewhere in the pores, as indicated by the dark blue regions on the maps. These adsorption sites are the same as those observed by Hoffmann et al. who simulated xenon adsorption in DUT-8(Ni) [58].

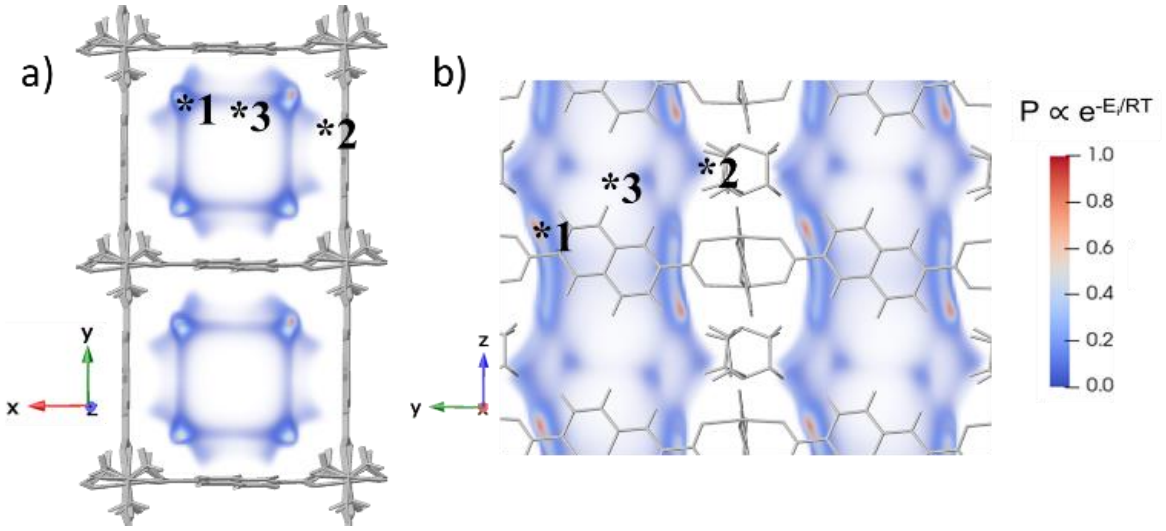

Figure 3. Boltzmann probability distribution for N_2 at 77 K inside the bulk conformer Bop. The maximum probability (P=1) corresponds to an adsorption energy of -6.7 kJ mol^{-1}. Showing (a) view down z-axis, and (b) view down x-axis.

To represent the nanoparticles and capture the effect of the external surface, infinite slab models were used in the simulations where nickel exposed at the external surface of the slabs were coordinated with functional groups based on the synthesis mixture: $H(2,6\text{-ndc})^-$, dabco, DMF or formate. Due to the expense of the simulations and the negligible difference between adsorption in A*op* and B*op*, only conformer B was studied. Indexing of the single crystal faces on a diffractometer (Figure 4) shows the (110) and (001) faces dominate the shape of DUT-8(Ni), thus the slab surfaces were created along these indices.

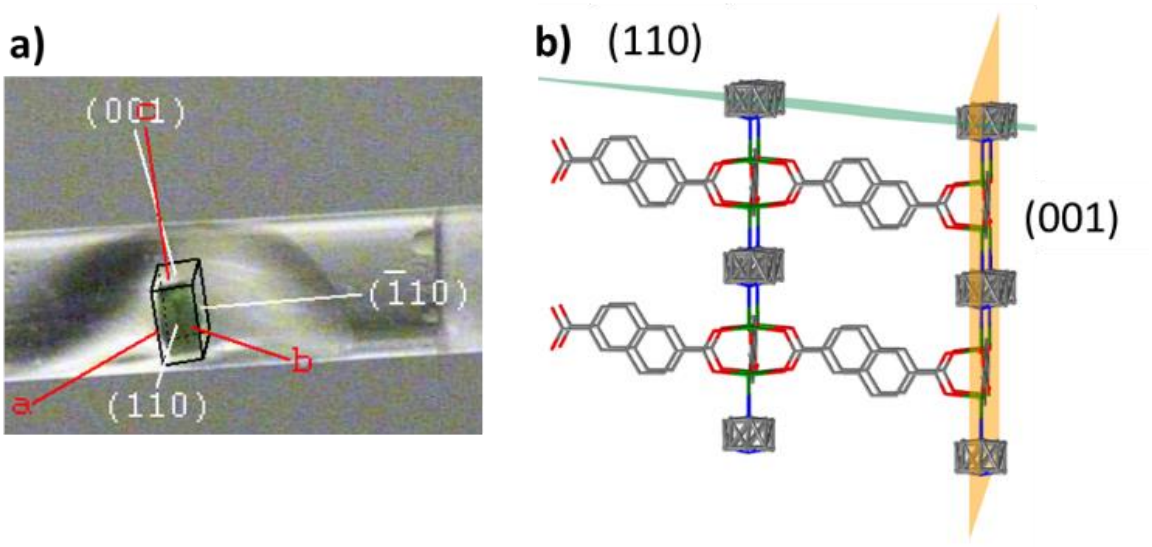

Figure 4. a) Assignment of the crystal faces for DUT-8(Ni) conformer B*op*, b) Planes in the DUT-8(Ni) conformer B*op* crystal structure, corresponding to the surface termination of crystal faces.

Figure 5 shows that there is very little difference in the simulated isotherms in the slab models capped with different surface groups. Compared to the bulk, the uptake and slope of the slab isotherms are lower at pressures $p/p_0 < 0.25$, because a lower density of framework atoms on the external surface reduces N_2-DUT-8 interaction energies. As the pressure exceeds $p/p_0 = 0.25$, the bulk isotherm levels off whilst the slab isotherms continue to rise due to extracrystalline adsorption. This is also seen in the experimental isotherm for small, rigid DUT-8 particles (also shown for comparison). Extracrystalline adsorption is also responsible for the uptake observed in slabs of B*cp* where the bulk pores, i.e. those not in direct contact with the surface and experiencing the same chemical environment as the period bulk unit cell, are too small to accommodate any N_2 molecules.

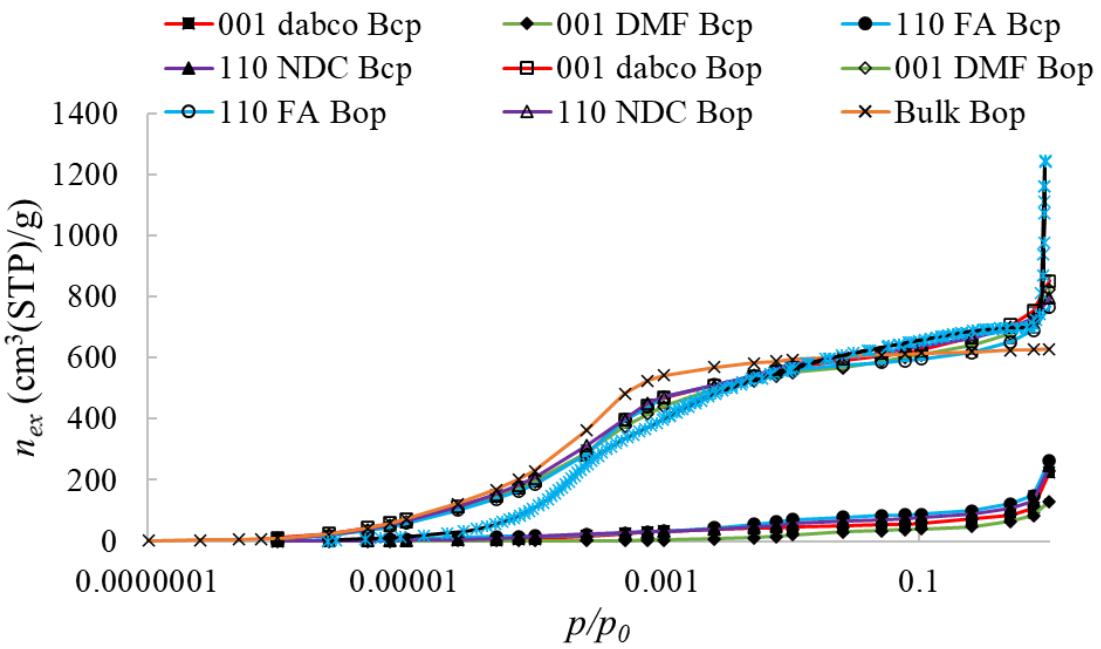

Figure 5. N_2 adsorption isotherms at 77 K inside the simulated Bop slabs and bulk, and the experimental isotherm in rigid DUT-8 nanoparticles. Slabs are capped with: dabco, dimethylformamide (DMF), formate (FA), or H(2,6-ndc$^-$) (NDC).

Probability maps for N_2 adsorption in the B*op* slabs (Figure 6) show that N_2 molecules occupy the same adsorption sites in the bulk pores of the slab, regardless of their position relative to the external surface. Hence, ignoring kinetic hindrance, the same amount will adsorb in all of the bulk pores regardless of their position in the particle. In contrast, adsorption sites on the external surface depend on the capping group. For B*op* slabs capped with H(2,6-ndc$^-$) or a dabco ligand, the same adsorption sites are present on the external surface as in the bulk, albeit, the interaction energies at the surface are weaker as half the groups that would contribute to the interaction energy are missing. Replacing the capping ligands with smaller capping groups (formate or DMF) further reduces the strength of interactions at the surface. These reduced interaction energies at the surface contribute to a shift in the gate-opening/closing pressures to higher values.

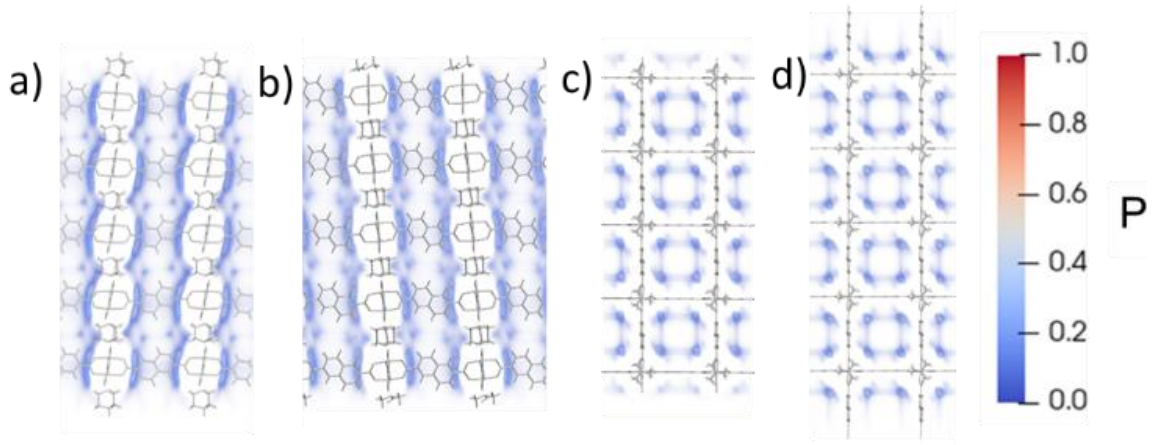

Figure 6. Probability maps for N_2 adsorption at 77 K in the conformer Bop slab models: a) 001 dabco, b) 001 DMF, c) 110 formate, and d) 110 ndc.

In line with the results for the microcrystals, N_2 is too large to fit inside the bulk pores of B*cp* slabs (Figure 7 and Figure 8). On the external surface however, there is a strong and very localised adsorption site next to the narrow corner of the pore (site 1). In contrast, the probability of N_2 adsorption in the wide pore corners (site 2) is lower because the 2,6-ndc^{2-} ligands are further spread. At site 1, N_2 interactions will overcome the dispersion interactions, likely acting as a driving force for gate-opening.

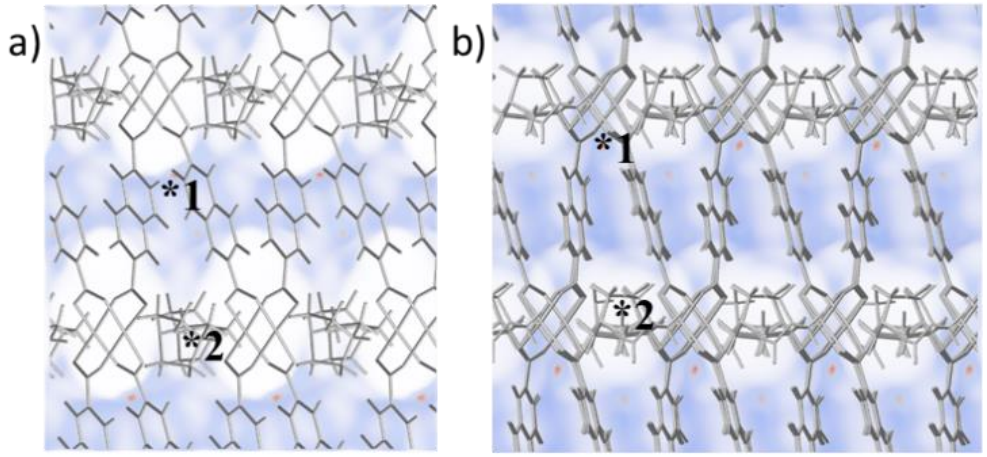

Figure 7. Probability maps for N_2 adsorption at 77 K in the B*cp* slabs. Viewing the surface pores of a) 001 dabco, and b) 001 DMF capped B*cp* slabs facing into the structure. *1 and *2 mark the adsorption sites in the "narrow" and "wide" pore corners. Note that the diameter of the bulk pores of B*cp* are too narrow to accommodate N_2 molecules.

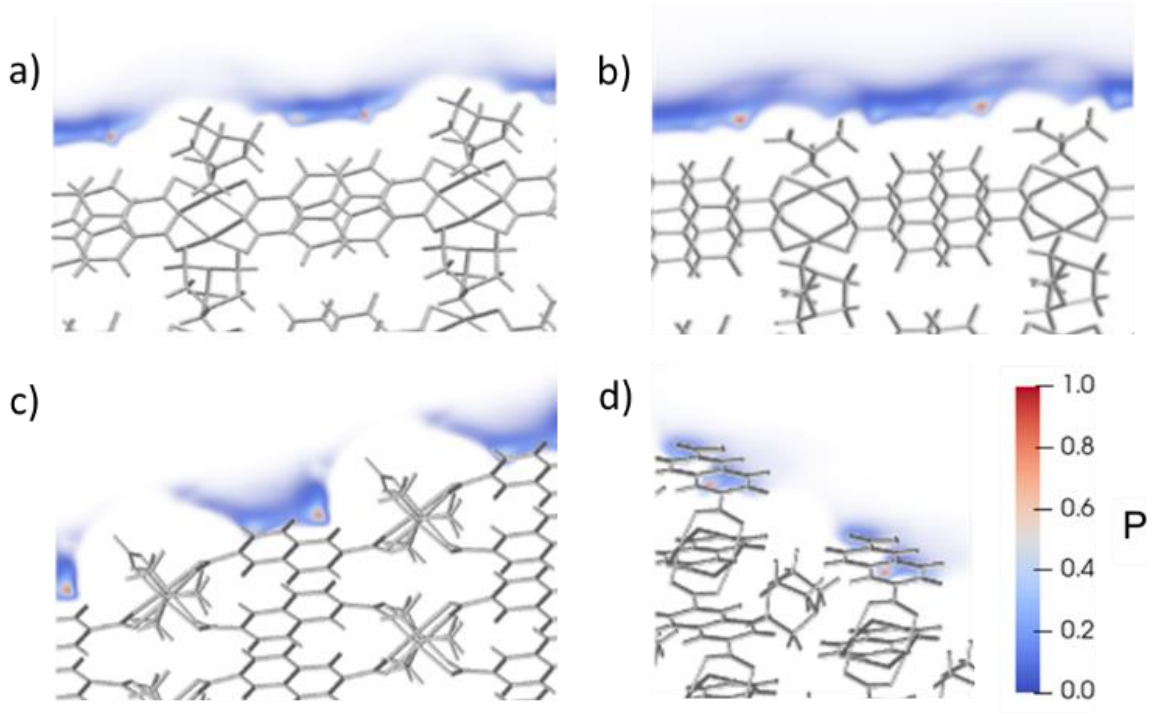

Figure 8. Magnified probability maps for N_2 adsorption at 77 K on one of the external surfaces of the conformer B*cp* slabs, showing a) 001 dabco, b) 001 DMF, c) 110 FA (formate), and d) 110 ndc. (The slabs and probability distributions were generated in the same way as the B*op* slabs shown in Figure 6).

It is clear that weak N_2-DUT-8 interaction energies on the external surface increase the gate-opening/closing pressure in the flexible microparticles. However, this does not explain why the rigid DUT-8 nanoparticles, obtained by changing the synthesis conditions, favour the *op* form. To get more insight, the osmotic framework adsorbed solution theory (OFAST) was applied to predict the gate-closing pressure. OFAST states that when two structures (e.g. the *op* and *cp* structures) are in equilibrium, those structures have equal osmotic potentials [26]. The calculations are based on the system energy when N_2 molecules are present inside the pores, therefore they determine the gate-closing pressure. Gate-opening requires N_2 molecules to open the pores from the external surface inwards, therefore is dominated by kinetics. For the periodic, bulk structure representing the microparticles, OFAST predicts a gate-closing pressure of p/p_0=0.005 (0.5 kPa), which is within the experimentally observed range for gate-closing in DUT-8(Ni) microparticles ~ 0.5-1 kPa (see the SI, Section S8 for details).

Figure 9 shows the B*cp* → B*op* energy difference normalized with respect to the number of bulk unit cells (i.e. "complete" DUT-8 unit cells) in each slab which illustrates how capping groups influence the flexibility behaviour.

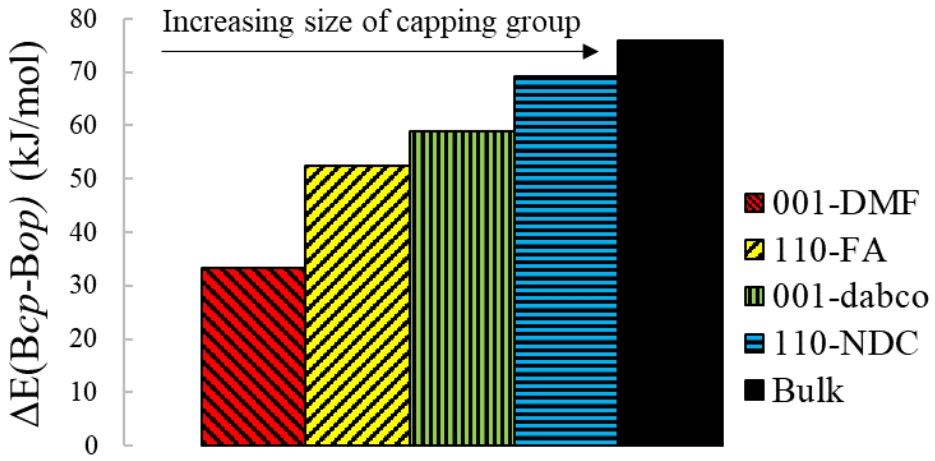

Figure 9. Normalized B*cp* → B*op* energy differences inside the guest-free bulk and slab models

As with the bulk, the internal energies show that each B*cp* slab is more favourable than the corresponding solvent free B*op* slab because of dispersion interactions between the ligands. If ligands are removed (i.e. by introducing an external surface), B*cp* becomes relatively less favourable (i.e. the B*cp* → B*op* energy difference decreases). Similarly, if the size of ligands is reduced, reduced dispersion interactions decrease the B*cp* → B*op* energy difference.

In a thermally induced phase transition the change in volume Gibbs free energy (ΔG_V) is typically proportional to the latent heat of transformation (L)

$$\Delta G_V \cong \frac{-L\Delta T}{T_e}$$

where for undercooling $\Delta T = T_e - T$ with T_e being the equilibrium phase transition temperature [59]. Hence, considering only the empty host, the reduced dispersion interactions decrease the energy difference and latent heat of the B*op* → B*cp* phase transition. As ΔG_V is the driving force for this phase transition, it is reasonable to obtain B*op* nanoparticles as a metastable form upon desolvation.

Considering additionally host-guest interactions, this in turn means that overall, as the particle size decreases, weaker N_2-DUT-8 interaction energies on the external surface will increase the gate-opening/closing pressure as more N_2 molecules are needed to overcome the B*cp* → B*op* barrier. On the other-hand, weaker dispersion interactions on the surface reduce the energy difference between B*op* and B*cp*, reducing the gate-opening/closing pressure. To determine which of the two effects dominate the shift in gate-opening/closing pressure, OFAST was applied to the slab models. Figure 10 shows that the gate-closing pressure, i.e. the pressure where the relative osmotic potential ($\Omega_{Bop\text{-}Bcp}$) is equal to zero, varies depending on the surface group but is in the same order of magnitude as calculated for the periodic bulk material (p/p_0=0.005 (0.5 kPa)). These results indicate that the influence of the surface is not a major contributing factor to why the nanoparticles are rigid and do not show gate closing for DUT-8(Ni).

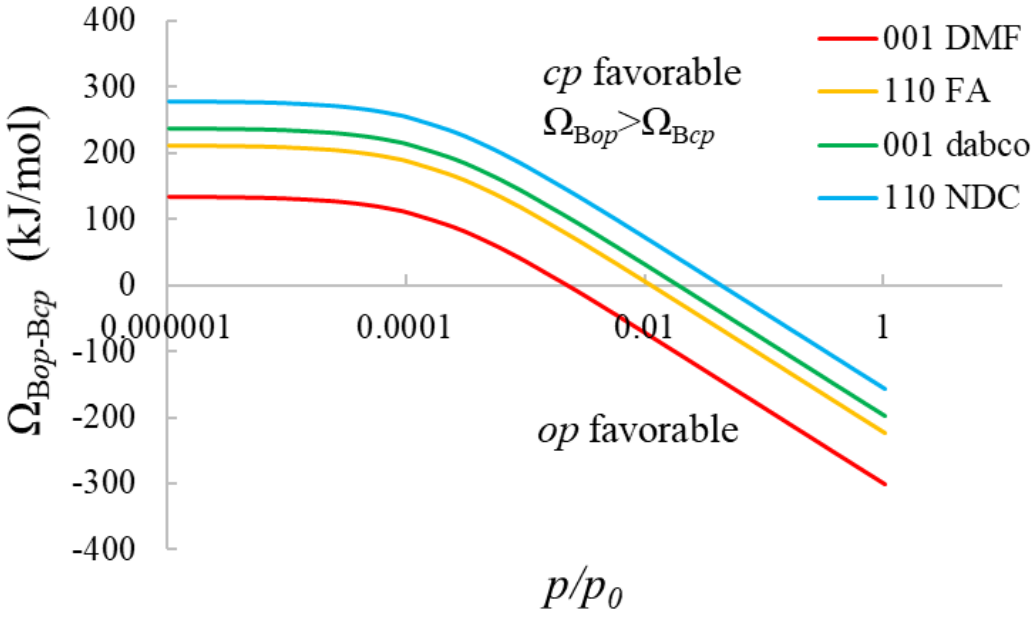

Figure 10. Relative osmotic potentials, $\Omega_{Bop\text{-}Bcp}$ in the slab models with different capping groups as function of pressure. The gate closing pressure can be found at $\Omega_{Bop\text{-}Bcp} = 0$.

However, closer inspection of Figure 9 and Figure 10 reveals the complex interplay of two opposing effects: reduced N_2 – DUT-8 interaction energies at the surface leading to an increase in the gate-transition pressure and reduced dispersion interactions between the capping groups, leading to a decrease in the gate-transition pressure which can be exploited to modify the gate closing pressure. Compared to the bulk (p/p_0=0.005; p = 0.5 kPa), the transition pressure is slightly reduced for the 001-

DMF slab (p/p_0 = 0.003; p = 0.3 kPa). This slab has the smallest capping group, and hence the lowest B*cp* → B*op* energy barrier (Figure 9). Since the other slabs have larger capping groups which result in larger dispersion interactions, the reduced N_2-framework interaction energies on the surface outweigh the decreased B*cp* → B*op* energy difference compared to the bulk. Hence relative to the bulk the gate-closing pressure increases up to p/p_0 = 0.05 (p = 5 kPa) for ndc (see Table S1 in the SI for the energy differences and the actual values of the gate closing pressures). Overall, these results show that the targeted capping of flexible nanoparticles could in general provide a powerful handle to modify the gate closing pressure in a systematic way tailoring it for the application of interest.

CONCLUSIONS

We used a combination of experimental and simulation techniques to study N_2 adsorption in DUT-8(Ni). In particular we looked at the influence of the external surface on the gate opening / closing behaviour of DUT-8(Ni) comparing nanoparticles, which experimentally remain rigid in their *op* form, to microparticles, synthesized using slightly different conditions, which undergo N_2 induced gate-opening/closing. Cyclic adsorption of these flexible DUT-8 microparticles leads to their disintegration and mosaic structure formation leading to an increase in the gate-opening pressures. Simulations in slabs of DUT-8, to account for surface effects, reveal that on the surface, where paddle wheel units are capped with modulators substantially smaller than the 2,6-ndc ligands, the adsorption environment for guest molecules is very different with considerably weaker guest-framework interaction. This effect is, however, short-ranged and as soon as the nitrogen molecules encounter paddle wheel units with four coordinated linkers even in the pores exposed at the surface the adsorption environment is nearly identical to the bulk material.

Calculations using the osmotic framework adsorbed solution theory (OFAST) [26] using slabs capped with different surface groups representing DUT-8(Ni) nanoparticles revealed that the nanoparticles should close. Therefore, we conclude that the size of the nanoparticles and the capping of the surface with surface group is not a major contributor to keeping DUT-8(Ni) nanoparticles open as observed experimentally and that it is more likely that defects and/or nucleation barriers dominate [35]. However, the reduced energy difference between the open and the

closed form ($E_{B\mathit{op}\text{-}B\mathit{cp}}$) in nanoparticles reduces the driving force for the *op* → *cp* transition increasing the probability to obtain metastable *op* polymorphs as a result of a kinetically hindered nucleation. Moreover, our results reveal, for the first time, that surface groups capping nanoparticles offer the opportunity to manipulate the gate opening / closing pressure. For the four surface groups that we investigated, the complex interplay between guest-framework and framework interactions lead to a lower (0.3 kPa for DMF) or increased (5 kPa for ndc) gate closing pressure compared to the bulk (0.5 kPa). This principle is generally applicable and could be exploited to tune the gate opening / closing pressure for the application of interest.

CONFLICTS OF INTEREST

There are no conflicts to declare.

ACKNOWLEDGEMENTS

This work was supported by funding from the European Research Council (ERC) under the European Union's Horizon 2020 research and innovation programme (grant agreement No 648283 "GROWMOF") and the DFG through the FOR2433 program. It made use of the Balena High Performance Computing (HPC) Service at the University of Bath. The authors acknowledge T. Gorelik for collecting TEM images.

REFERENCES

1. Hönicke, I.M., et al., *Balancing Mechanical Stability and Ultrahigh Porosity in Crystalline Framework Materials.* Angewandte Chemie International Edition, 2018. **57**(42): p. 13780-13783.
2. Furukawa, H., et al., *Ultrahigh Porosity in Metal-Organic Frameworks.* Science, 2010. **329**(5990): p. 424-428.
3. Rowsell, J.L.C. and O.M. Yaghi, *Metal–organic frameworks: a new class of porous materials.* Microporous and Mesoporous Materials, 2004. **73**(1): p. 3-14.
4. Lin, R.-B., et al., *Exploration of porous metal–organic frameworks for gas separation and purification.* Coordination Chemistry Reviews, 2019. **378**: p. 87-103.

5. Li, B., et al., *Porous Metal–Organic Frameworks for Gas Storage and Separation: What, How, and Why?* The Journal of Physical Chemistry Letters, 2014. **5**(20): p. 3468-3479.
6. Ma, L. and W. Lin, *Designing Metal-Organic Frameworks for Catalytic Applications*, in *Functional Metal-Organic Frameworks: Gas Storage, Separation and Catalysis*, M. Schröder, Editor. 2010, Springer Berlin Heidelberg: Berlin, Heidelberg. p. 175-205.
7. Schneemann, A., et al., *Flexible metal-organic frameworks.* Chemical Society Reviews, 2014. **43**(16): p. 6062-6096.
8. Fairen-Jimenez, D., et al., *Opening the gate: framework flexibility in ZIF-8 explored by experiments and simulations.* Journal of the American Chemical Society, 2011. **133**(23): p. 8900-2.
9. Bourrelly, S., et al., *Different Adsorption Behaviors of Methane and Carbon Dioxide in the Isotypic Nanoporous Metal Terephthalates MIL-53 and MIL-47.* Journal of the American Chemical Society, 2005. **127**(39): p. 13519-13521.
10. Klein, N., et al., *Monitoring adsorption-induced switching by 129Xe NMR spectroscopy in a new metal–organic framework Ni2(2,6-ndc)2(dabco).* Physical Chemistry Chemical Physics, 2010. **12**(37): p. 11778-11784.
11. Freund, P., I. Senkovska, and S. Kaskel, *Switchable Conductive MOF–Nanocarbon Composite Coatings as Threshold Sensing Architectures.* ACS Applied Materials & Interfaces, 2017. **9**(50): p. 43782-43789.
12. Freund, P., et al., *MIL-53(Al)/Carbon Films for CO2-Sensing at High Pressure.* ACS Sustainable Chemistry & Engineering, 2019. **7**(4): p. 4012-4018.
13. Yang, L., et al., *A highly sensitive flexible metal–organic framework sets a new benchmark for separating propyne from propylene.* Journal of Materials Chemistry A, 2018. **6**(47): p. 24452-24458.
14. Cai, W., et al., *Metal–Organic Framework-Based Stimuli-Responsive Systems for Drug Delivery.* Advanced Science, 2019. **6**(1): p. 1801526.
15. Liu, D., et al., *Metal–Organic Frameworks as Sensory Materials and Imaging Agents.* Inorganic Chemistry, 2014. **53**(4): p. 1916-1924.
16. Mehlana, G. and S.A. Bourne, *Unravelling chromism in metal–organic frameworks.* CrystEngComm, 2017. **19**(30): p. 4238-4259.
17. Yanai, N., et al., *Gas detection by structural variations of fluorescent guest molecules in a flexible porous coordination polymer.* Nature Materials, 2011. **10**(10): p. 787-93.

18. Horcajada, P., et al., *Flexible Porous Metal-Organic Frameworks for a Controlled Drug Delivery.* Journal of the American Chemical Society, 2008. **130**(21): p. 6774-6780.
19. Li, L., et al., *Flexible Metal–Organic Frameworks with Discriminatory Gate-Opening Effect for the Separation of Acetylene from Ethylene/Acetylene Mixtures.* European Journal of Inorganic Chemistry, 2016. **2016**(27): p. 4457-4462.
20. Ghalei, B., et al., *Enhanced selectivity in mixed matrix membranes for CO2 capture through efficient dispersion of amine-functionalized MOF nanoparticles.* Nature Energy, 2017. **2**: p. 17086.
21. Kundu, T., et al., *Solvent-Induced Control over Breathing Behavior in Flexible Metal–Organic Frameworks for Natural-Gas Delivery.* Angewandte Chemie International Edition, 2019. **58**(24): p. 8073-8077.
22. Krause, S., et al., *The effect of crystallite size on pressure amplification in switchable porous solids.* Nature Communications, 2018. **9**(1): p. 1573.
23. Krause, S., et al., *The impact of crystal size and temperature on the adsorption-induced flexibility of the Zr-based metal-organic framework DUT-98.* Beilstein journal of nanotechnology, 2019. **10**: p. 1737-1744.
24. Sakata, Y., et al., *Shape-Memory Nanopores Induced in Coordination Frameworks by Crystal Downsizing.* Science, 2013. **339**(6116): p. 193-196.
25. Zhang, C., et al., *Crystal-Size-Dependent Structural Transitions in Nanoporous Crystals: Adsorption-Induced Transitions in ZIF-8.* Journal of Physical Chemistry C, 2014. **118**(35): p. 20727-20733.
26. Coudert, F.-X., *The osmotic framework adsorbed solution theory: predicting mixture coadsorption in flexible nanoporous materials.* Physical Chemistry Chemical Physics, 2010. **12**(36): p. 10904-10913.
27. Miura, H., et al., *Tuning the gate-opening pressure and particle size distribution of the switchable metal–organic framework DUT-8(Ni) by controlled nucleation in a micromixer.* Dalton Transactions, 2017. **46**(40): p. 14002-14011.
28. Kavoosi, N., et al., *Tailoring adsorption induced phase transitions in the pillared-layer type metal-organic framework DUT-8(Ni).* Dalton Transactions, 2017. **46**(14): p. 4685-4695.
29. Ehrling, S., *Crystal size versus paddle wheel deformability: selective gated adsorption transitions of the switchable metal–organic frameworks DUT-8(Co) and DUT-8(Ni).* Journal of materials chemistry A, 2019. **7**(37): p. pp. 21459-21475.

30. Bon, V., et al., *Exceptional adsorption-induced cluster and network deformation in the flexible metal–organic framework DUT-8(Ni) observed by in situ X-ray diffraction and EXAFS.* Physical Chemistry Chemical Physics, 2015. **17**(26): p. 17471-17479.
31. Bon, V., et al., *Tolerance of Flexible MOFs toward Repeated Adsorption Stress.* ACS Applied Materials & Interfaces, 2015. **7**(40): p. 22292-22300.
32. Petkov, P.S., et al., *Conformational isomerism controls collective flexibility in metal–organic framework DUT-8(Ni).* Physical Chemistry Chemical Physics, 2019. **21**(2): p. 674-680.
33. Ehrling, S., et al., *Adaptive Response of a Metal–organic Framework Through Reversible Disorder–disorder Transitions*. 2020.
34. Groom, C.R., et al., *The Cambridge Structural Database.* Acta Crystallographica Section B, 2016. **72**(2): p. 171-179.
35. Mendt, M., et al., *EPR Insights into Switchable and Rigid Derivatives of the Metal–Organic Framework DUT-8(Ni) by NO Adsorption.* The Journal of Physical Chemistry C, 2016. **120**(26): p. 14246-14259.
36. Macrae, C.E., P; McCabe, P; Pidcock, E; Shields, G; Taylor, R; Towler, M; van de Streek, J, *Mercury.* Journal of Chemical Information and Modeling, 2006. **44**: p. 2133-2144.
37. Donnay, J.H., D, *A new law of crystal morphology extending the law of Bravais.* American Mineralogist, 1937. **22**(463): p. 446-467.
38. Hutter, J., et al., *cp2k: atomistic simulations of condensed matter systems.* Wiley interdisciplinary reviews. Computational molecular science, 2014. **4**: p. 25.
39. VandeVondele, J., et al., *Quickstep: Fast and accurate density functional calculations using a mixed Gaussian and plane waves approach.* Computer Physics Communications, 2005. **167**(2): p. 103-128.
40. Borštnik, U., et al., *Sparse matrix multiplication: The distributed block-compressed sparse row library.* Parallel Computing, 2014. **40**(5): p. 47-58.
41. Frigo, M. and S.G. Johnson, *The Design and Implementation of FFTW3.* Proceedings of the IEEE, 2005. **93**(2): p. 216-231.
42. VandeVondele, J. and J. Hutter, *An efficient orbital transformation method for electronic structure calculations.* The Journal of Chemical Physics, 2003. **118**(10): p. 4365-4369.
43. Lippert, B.G., J.H. Parrinello, and Michele, *A hybrid Gaussian and plane wave density functional scheme.* Molecular Physics, 1997. **92**(3): p. 477-488.

44. Perdew, J.P., K. Burke, and M. Ernzerhof, *Generalized Gradient Approximation Made Simple.* Physical Review Letters, 1996. **77**(18): p. 3865-3868.
45. Grimme, S., S. Ehrlich, and L. Goerigk, *Effect of the damping function in dispersion corrected density functional theory.* Journal of Computational Chemistry, 2011. **32**(7): p. 1456-65.
46. Grimme, S., et al., *A consistent and accurate ab initio parametrization of density functional dispersion correction (DFT-D) for the 94 elements H-Pu.* The Journal of Chemical Physics, 2010. **132**(15): p. 154104.
47. Krack, M., *Pseudopotentials for H to Kr optimized for gradient-corrected exchange-correlation functionals.* Theoretical Chemistry Accounts, 2005. **114**: p. 145-152.
48. VandeVondele, J. and J. Hutter, *Gaussian basis sets for accurate calculations on molecular systems in gas and condensed phases.* The Journal of Chemical Physics, 2007. **127**(11): p. 114105.
49. Hartwigsen, C., S. Goedecker, and J. Hutter, *Relativistic separable dual-space Gaussian pseudopotentials from H to Rn.* Physical Review B, 1998. **58**(7): p. 3641-3662.
50. Goedecker, S., M. Teter, and J. Hutter, *Separable dual-space Gaussian pseudopotentials.* Physical Review B, 1996. **54**(3): p. 1703-1710.
51. Gupta, A., et al., *Object-oriented Programming Paradigms for Molecular Modeling.* Molecular Simulation, 2003. **29**(1): p. 29-46.
52. Wells, B.A. and A.L. Chaffee, *Ewald Summation for Molecular Simulations.* Journal of Chemical Theory and Computation, 2015. **11**(8): p. 3684-3695.
53. Wolf, D., et al., *Exact method for the simulation of Coulombic systems by spherically truncated, pairwise r−1 summation.* The Journal of Chemical Physics, 1999. **110**(17): p. 8254-8282.
54. Mayo, S.L., B.D. Olafson, and W.A. Goddard, *DREIDING: a generic force field for molecular simulations.* The Journal of Physical Chemistry, 1990. **94**(26): p. 8897-8909.
55. Rappe, A.K., et al., *UFF, a full periodic table force field for molecular mechanics and molecular dynamics simulations.* Journal of the American Chemical Society, 1992. **114**(25): p. 10024-10035.
56. Potoff, J.J. and J.I. Siepmann, *Vapor–liquid equilibria of mixtures containing alkanes, carbon dioxide, and nitrogen.* AIChE Journal, 2001. **47**(7): p. 1676-1682.
57. Peng, D.-Y. and D.B. Robinson, *A New Two-Constant Equation of State.* Industrial & Engineering Chemistry Fundamentals, 1976. **15**(1): p. 59-64.

58. Hoffmann, H.C., et al., *High-Pressure in Situ 129Xe NMR Spectroscopy and Computer Simulations of Breathing Transitions in the Metal–Organic Framework Ni2(2,6-ndc)2(dabco) (DUT-8(Ni)).* Journal of the American Chemical Society, 2011. **133**(22): p. 8681-8690.
59. Evans, J.D., et al., *Four-dimensional metal-organic frameworks.* Nature Communications, 2020. **11**(1): p. 2690.

Influence of particle size and external surface on adsorption and framework flexibility in DUT-8(Ni)

Supporting Information

Megan J. Thompson[¶], *Claire L. Hobday*[¶,†], *Irena Senkovska*[#], *Volodymyr Bon*[#], *Sebastian Ehrling*[#], *Mariia Maliuta*[#], *Stefan Kaskel*[#], *Tina Düren*[*,¶]

[¶] Centre for Advanced Separations Engineering, Department of Chemical Engineering, University of Bath, BA2 7AY, UK

[†] Current address: EaStChem School of Chemistry and Centre for Science at Extreme Conditions, University of Edinburgh, David Brewster Road, Joseph Black Building, Edinburgh, EH9 3FJ, UK

[#] Chair of Inorganic Chemistry, Department of Chemistry and Food Chemistry, TU Dresden, Bergstraße 66, 01069 Dresden, Germany

AUTHOR INFORMATION

* Prof. T. Düren, Centre for Advanced Separations Engineering, Department of Chemical Engineering, University of Bath, BA2 7AY, UK
E-mail: t.duren@bath.ac.uk

Section 1. Crystal morphology prediction

Bravais-Friedel-Donnay-Harker calculations were performed in Mercury to determine the equilibrium structures of DUT-8(Ni) (*op*) and DUT-8(Ni) (*cp*) [1, 2]. The CCCD number for the structures are 1056823 and 1034317 [3]). From this, the most dominant crystallographic planes could be determined to make the surfaces of the nanoparticle models. Figure S1 shows the resulting structures and relative surface areas that are inversely proportional to the growth rate of each Miller Plane.

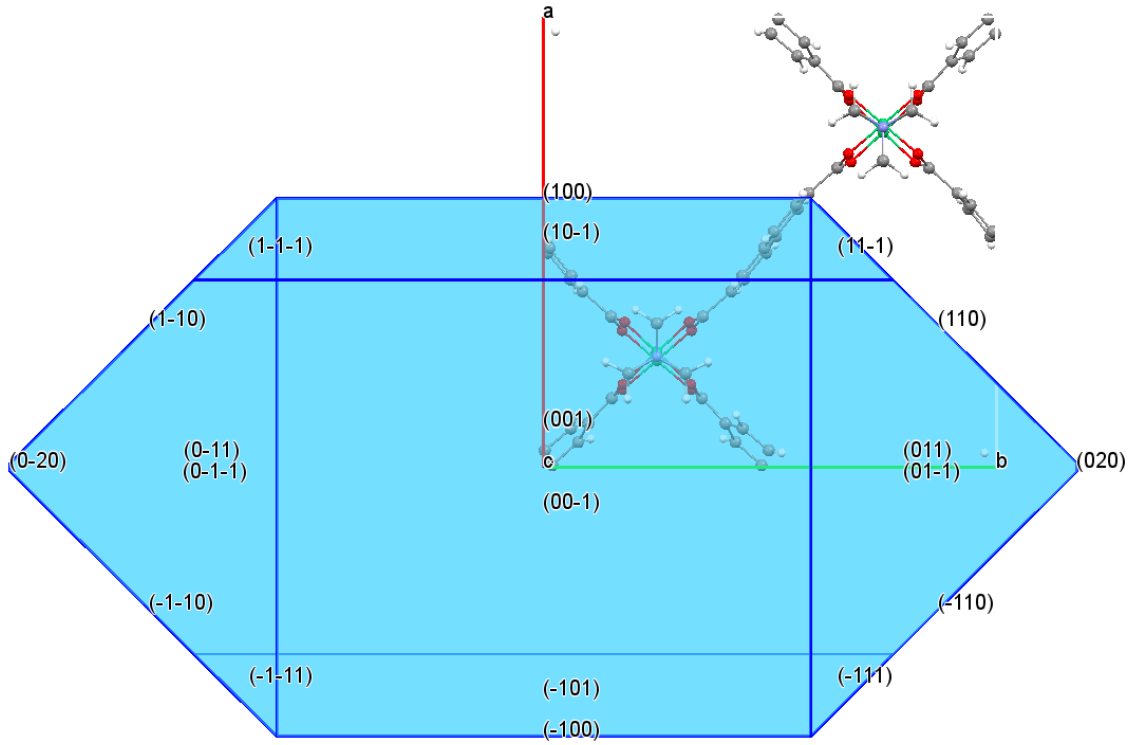

(a)

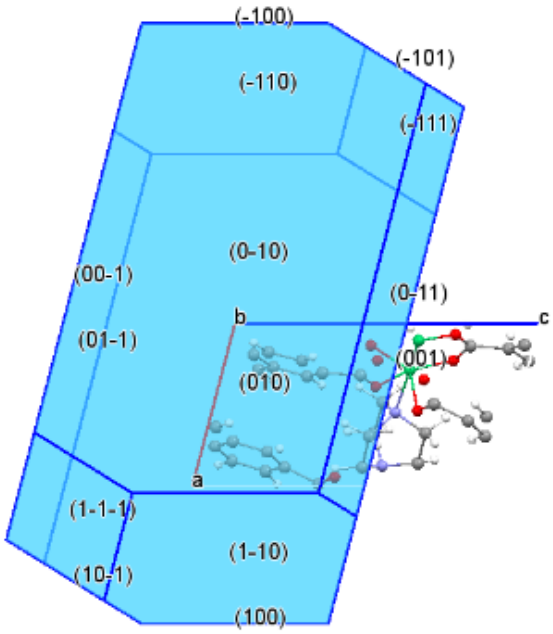

(b)

(c)

DUT-8 (*op*)		DUT-8 (*cp*)	
Miller plane	BFDH Area	Miller plane	BFDH Area
100	0.160	001	0.207
-100	0.160	00-1	0.207
110	0.102	010	0.118
-1-10	0.102	0-10	0.118
1-10	0.102	-100	0.055
-110	0.102	100	0.055
00-1	0.071	10-1	0.050
001	0.071	-101	0.050
011	0.022	1-10	0.034
0-11	0.022	-110	0.034
0-1-1	0.022	0-11	0.018
01-1	0.022	01-1	0.018
-101	0.013	1-1-1	0.015
10-1	0.013	-111	0.015
0-20	0.001	-	-
020	0.001	-	-

Figure S1. BFDH morphologies for (a) DUT-8 (op) and (b) DUT-8 (cp) with (c) relative BFDH surface areas for each plane

Section 2. Creation of models to represent DUT-8 microcrystals and nanoparticles

Microcrystals have negligible external surface area to volume ratios; therefore, the influence of the external surface was neglected by implementing the bulk unit cell in periodic boundaries. As the particle size decreases, the surface area to volume ratio increases, so the external surface becomes more influential on the adsorption mechanism. Therefore, infinite slabs were used to model the surface effects in DUT-8 nanoparticles (Figure S2).

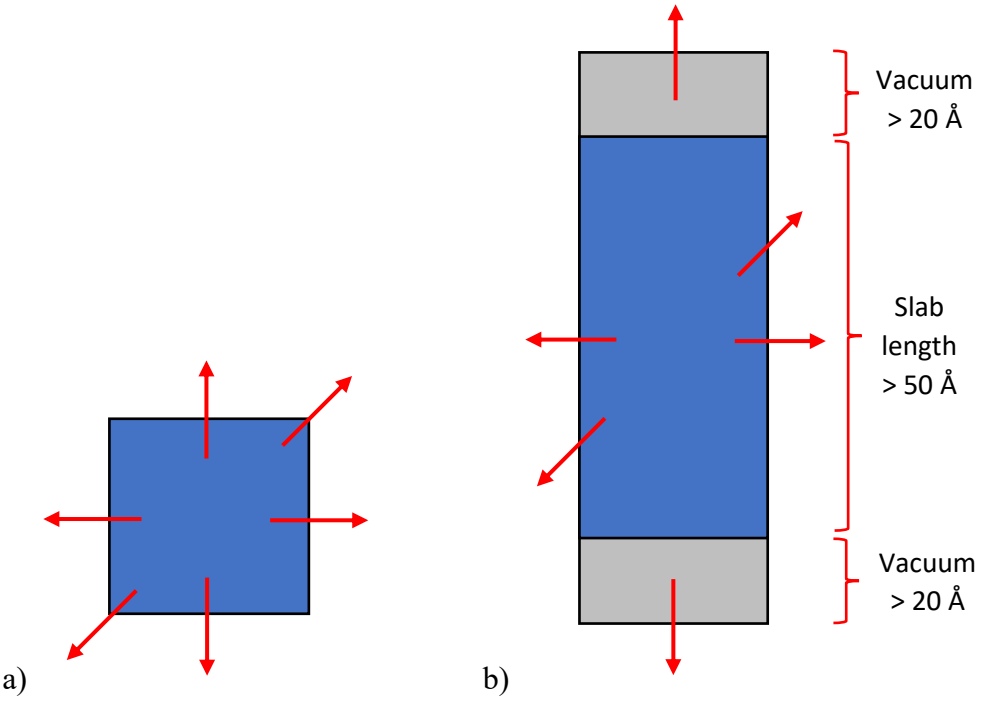

Figure S2. Schematic of (a) the bulk/microcrystal and (b) the slab/nanoparticle models. Red arrows indicate that periodic boundary conditions were applied in all three directions.

It was observed *via* face indexing single crystals that the (110) and (001) planes are most dominant, so slab models where cut with external faces along these planes. Coordination bonds between the nickel - nitrogen or nickel - oxygen atoms were cut, and uncoordinated metal sites were capped with either hydrogenated dabco, physisorbed DMF molecules, hydrogenated 2,6-ndc, or formate. These surfaces are shown in Figure S3.

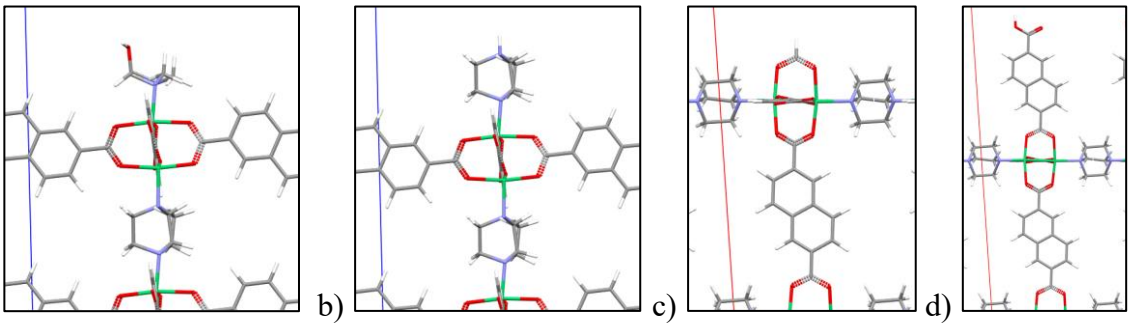

Figure S3. External surfaces of the slabs: (a) (001) DMF, (b) (001) dabco, (c) (110) formate, (d) (110) H(2,6-ndc).

Section 3. Isotherm normalization

Using the slab models results in inaccurate isotherms once the pores saturate due to extracrystalline adsorption in the vacuum gap leading to discrepancies between the experimental and simulated results. To account for this, a simple normalization can be applied to remove the influence of N_2 molecules in the vacuum gap: Figure S4 shows the difference in isotherms when normalized.

Firstly, the difference in volume due to the vacuum gap needs to be accounted for by introducing a ratio, R, that scales the volume of the slab (V_{slab}) to the total volume of the slab unit cell (V_{total}). Since the volume of the slab is arbitrary, it is much easier to calculate *R* as a ratio of the density of the complete slab unit cell ($\rho_{slab_{UC}}$) to the density of the bulk crystal (ρ_{bulk}).

$$R = \frac{V_{slab}}{V_{total}} \approx \frac{\rho_{slab_{UC}}}{\rho_{bulk}}$$

Up to the point where extracrystalline adsorption occurs, the change in the excess amount adsorbed, Δn_{ex}, is equal to the change in the total amount adsorbed, Δn_{total}:

$$\Delta n_{ex} = \Delta n_{total}$$

When extracrystalline adsorption begins, the ratio is used to calculate the actual excess adsorption whilst removing the influence of the vacuum gap:

$$\Delta n_{ex} = R \cdot \Delta n_{total}$$

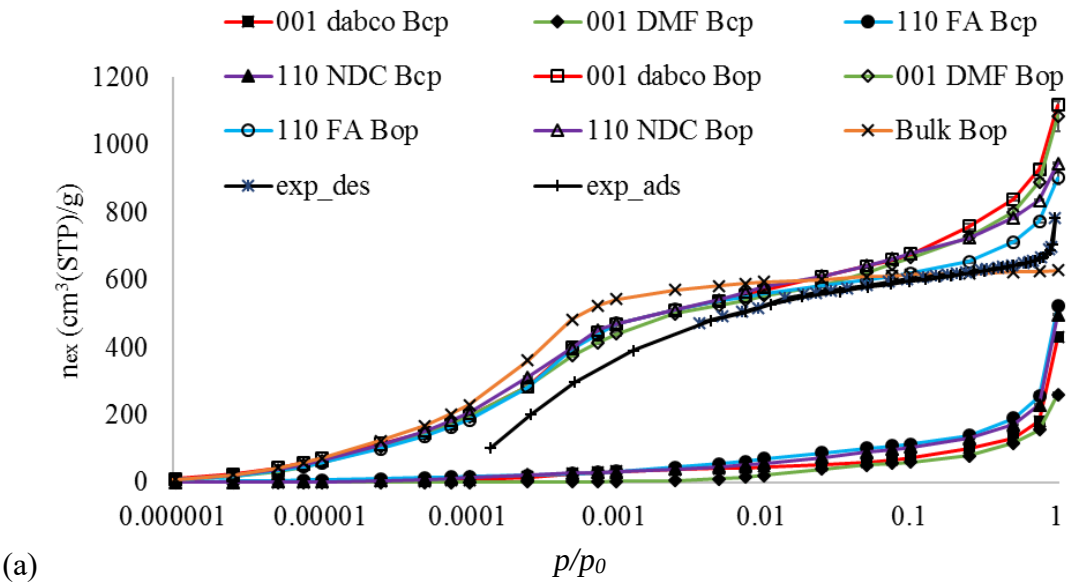

(a)

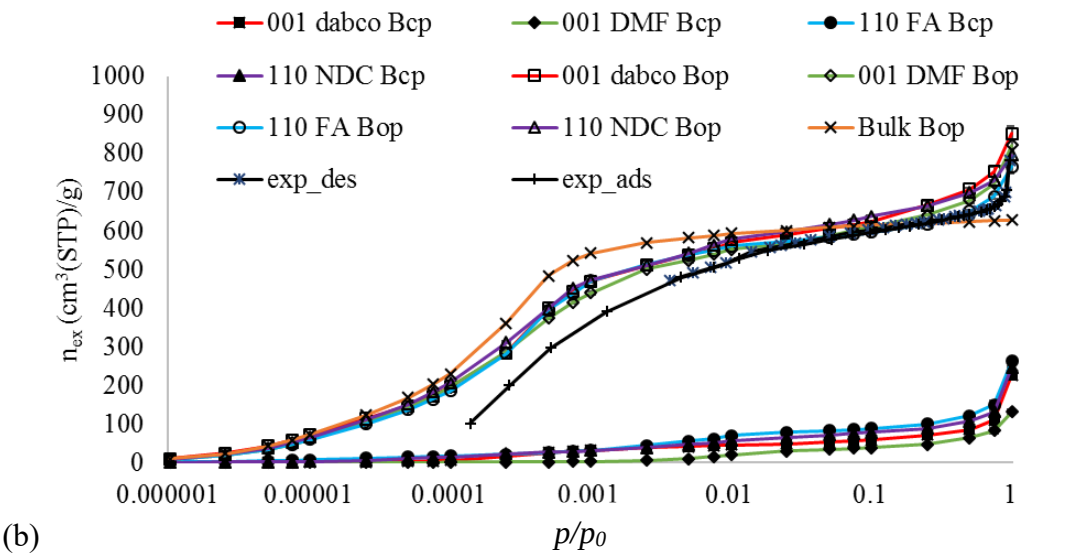

(b)

Figure S4. N_2 adsorption isotherms at 77 K in the slab models (and the experimental isotherm for comparison): a) original, and b) normalized to remove the influence of the vacuum gap.

Section 4. Phase transition prediction using osmotic framework adsorbed solution theory

To investigate the particle size dependence on phase transition, the osmotic framework adsorbed solution theory (OFAST) was used. In OFAST Equation S1 is used to determine the osmotic potential Ω_k of the closed and open pore structures [4].

$$\Omega_k = F_k + PV_k - RT\int_0^P \frac{n_k}{P} dP \qquad \text{Equation S1}$$

Here, F_k is the free energy of the empty structure in phase k (kJ/UC), P is the total external pressure (kPa), V_k is the unit cell volume of the empty framework (m^3/UC), R is the ideal gas constant (0.008314 kJ/mol K), T is the temperature (77 K), and n_k is the moles of gas

adsorbed in the unit cell (mol/UC). At the phase transition pressure, the osmotic potential of the closed and open pore structures should be equal, therefore at phase transition Equation S2 holds true [4]:

$$\Delta F = \Delta\left(\Omega_i(P) - \Omega_i(P=0)\right) = RT\int_0^P \frac{\Delta n}{P} dP - P\Delta V \qquad \text{Equation S2}$$

A Langmuir type isotherm was fitted to the bulk/microcrystal GCMC results to calculate the integral: $n = \frac{M \cdot K \cdot P}{1+K \cdot P}\left(\frac{mol}{UC}\right)$. The integral can be evaluated using Equation S3:

$$-RT\int_0^P \frac{n_k}{P} dP = -RTMLN(1+KP) \qquad \text{Equation S3}$$

The nanoparticles do not exhibit Langmuir isotherms because of the extracrystalline adsorption at high pressures. For this reason, a correction was added to fit the high pressure region of the isotherm: $n = \frac{M \cdot K \cdot P}{1+K \cdot P} + \alpha P^2\left(\frac{mol}{UC}\right)$ (where α is a fitted variable).

Section 5. Cyclic adsorption

Experimentally, cyclic adsorption of N_2 (amongst other guest molecules [5]) in the flexible DUT-8 microparticles causes their domain size to decrease, as shown in Figure S5. After seven cycles of N_2 adsorption at 77 K, the particle size decreases by over ten-fold, suggesting that the stress exerted on DUT-8(Ni) as it undergoes opening/closing causes the flexible crystals to undergo delamination.

a) 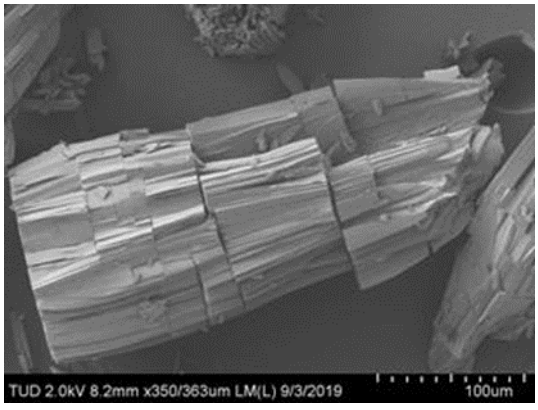

b) 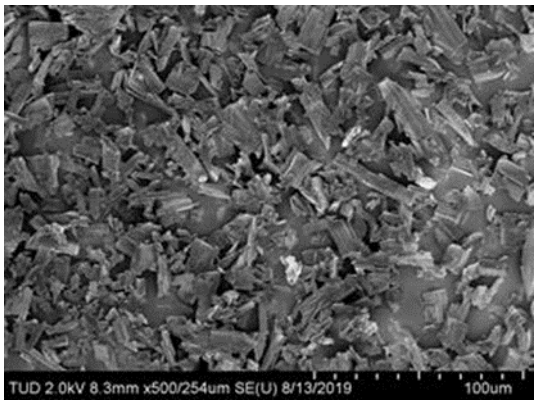

Figure S5. SEM images of flexible DUT-8(Ni) microparticles a) before and b) after seven cycles of N_2 adsorption at 77 K.

As the particle size decreases, the gate-opening/closing pressures increase because the cp structure becomes relatively more stable. Figure S6 shows that after each cycle, there is a marginal decrease in the maximum uptake as well as in the slope of the isotherm. Such trends are indicative of weaker N_2 – DUT-8(Ni) interaction energies.

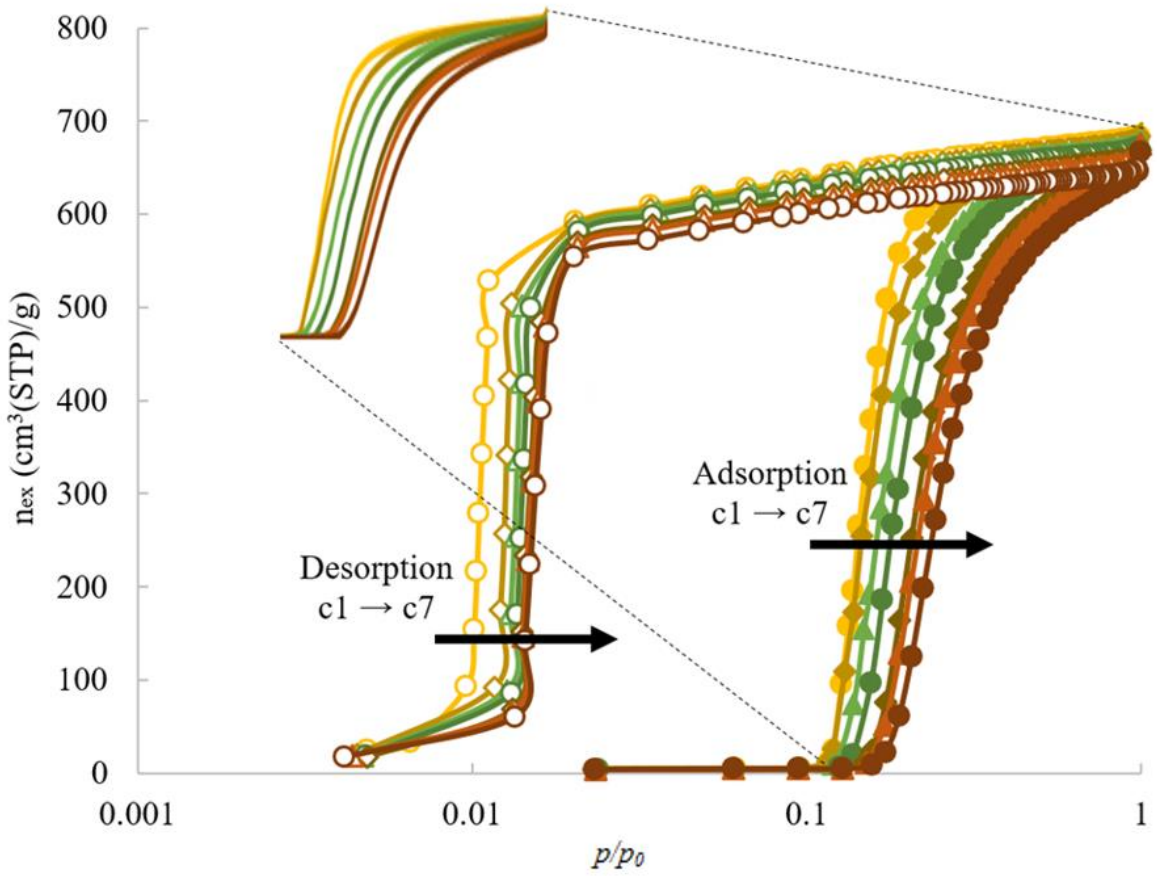

Figure S6. Experimental, cyclic adsorption of N_2 in the flexible microparticles at 77 K (showing seven cycles, c1 – c7)

Section 6. Boltzmann distributions

Figure S7 shows the Boltzmann distributions for N_2 adsorption in DUT-8, bulk conformer A*op* and B*op* at 77 K. There are no significant differences between the adsorption energy profiles in the two conformers

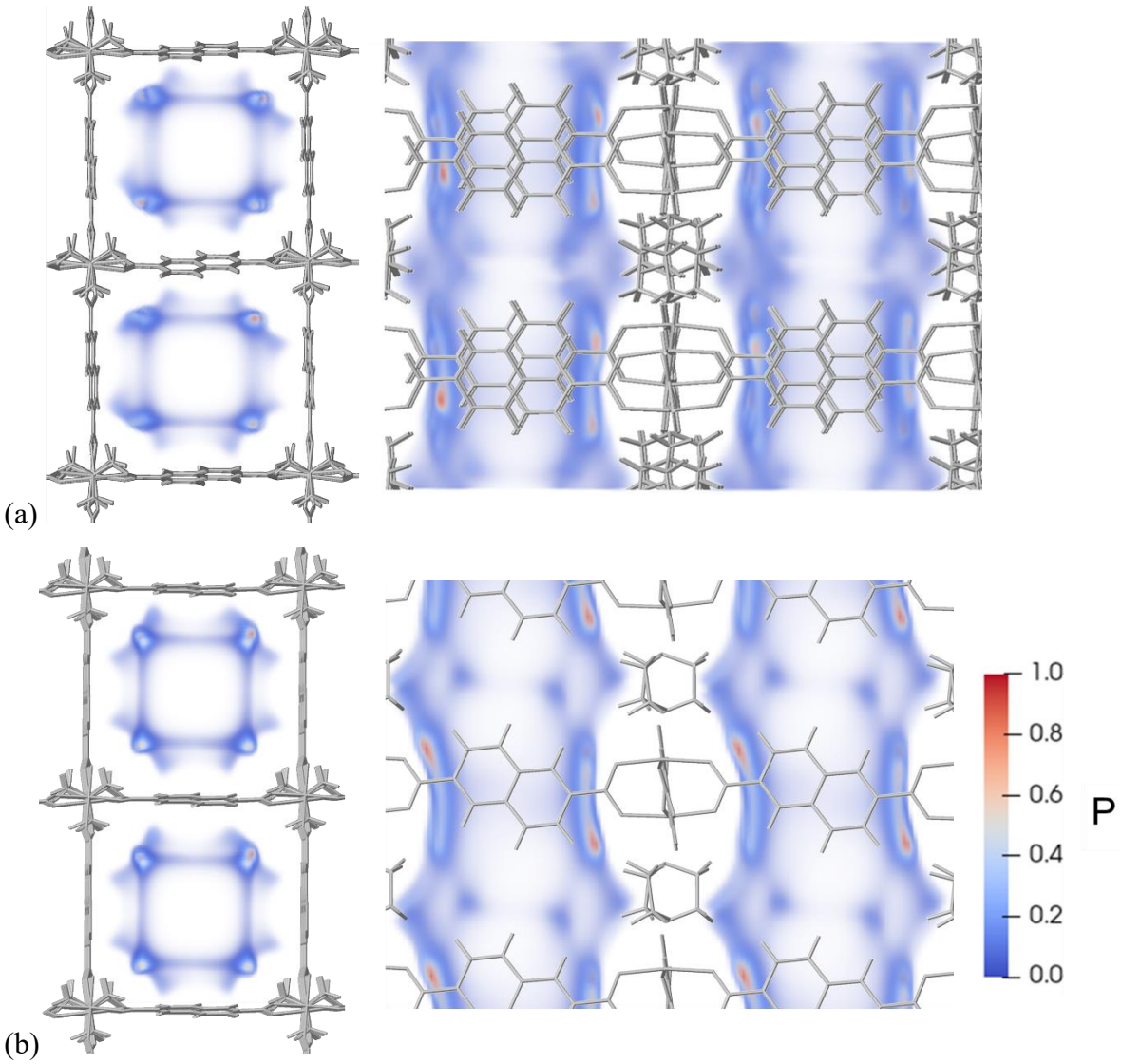

Figure S7. Boltzmann probability distribution for N_2 at 77 K inside the bulk conformer (a) A*op* and (b) B*op*.

Section 7. Why do the slabs models have a higher surface area to volume ratio than the experimental nanoparticles?

DUT-8(Ni) nanoparticles have a particle size of less than 500 nm. Assuming a spherical experimental nanoparticle of size equal to the thickness of the infinite slab models (i.e. 5 nm), the external surface area to volume ratio is:

$$\frac{4\pi\left(\frac{5}{2}\right)^2}{\frac{4}{3}\pi\left(\frac{5}{2}\right)^3} = 1.2\ \mathrm{nm^2/nm^3}$$

Considering the cuboidal slabs, the external surface area to volume ratio is approximately:

$$\frac{2(2 \times 2)}{2 \times 2 \times 5} = 2.5\ \mathrm{nm^2/nm^3}$$

Increasing the size of the real-life spherical nanoparticles decreases the external surface area to volume ratio since the surface area scales with r^2, whereas the volume scales with r^3. Therefore, the slabs always have a larger external surface area to volume ratio compared to the experimental crystals.

Section 8. OFAST gate-closing prediction for the bulk

Ab-initio minimisations were used to calculate the internal energy differences of the empty frameworks. Figure S8 shows that A*op* and B*op* have similar internal energies ($\Delta E_{Aop-Bop} = 6\ \mathrm{kJ\ mol^{-1}}$). The strain penalty associated with closing conformer A is greater than the change in dispersion interactions, and so A*op* cannot spontaneously close into A*cp* ($\Delta E_{Aop-Acp} = 37\ \mathrm{kJ\ mol^{-1}}$). B*cp* is more favourable than either *op* structure as the dispersion interactions dominate. The calculated energy difference between the conformer B structures ($\Delta E_{Bcp-Bop} = -76\ \mathrm{kJ\ mol^{-1}}$); is slightly smaller than the energy difference calculated by Petkov et al, ($\Delta E_{Bcp-Bop} = -102\ \mathrm{kJ\ mol^{-1}}$), who used different pseudopotentials and basis sets [6]). Both sets of results however are consistent with the experimental observation that "as-made" microparticles revert to B*cp* upon solvent removal [3, 7].

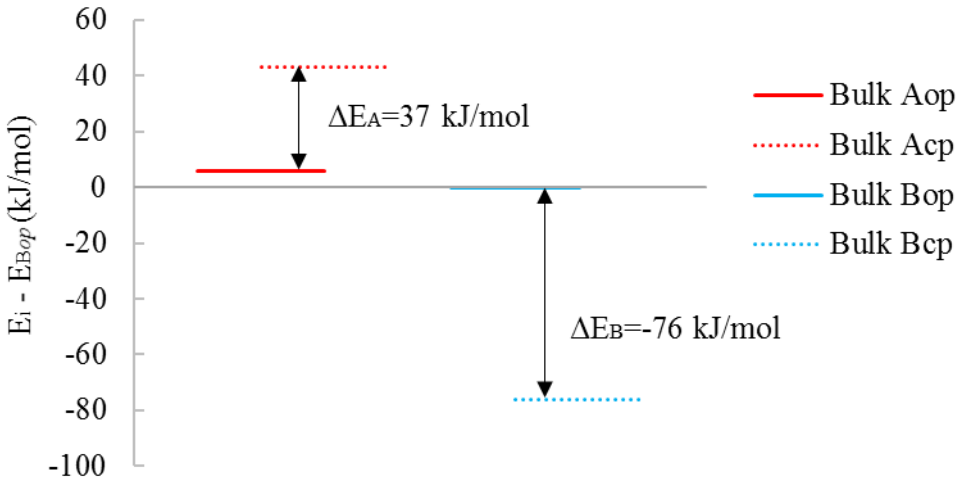

Figure S8. Relative internal energies of the empty bulk crystals

Figure S9 shows that the relative osmotic potentials of the conformer B structures overlap at a nitrogen pressure of $p/p_0 = 0.005$. This is the pressure at which the N_2-DUT-8 systems are

in equilibrium (i.e. the gate-closing pressure) [4]. Regardless of the pressure, Ω_{Aop} is always more favourable than Ω_{Acp}, and so the A*op* conformer of DUT-8 cannot transform into the A*cp* isomer.

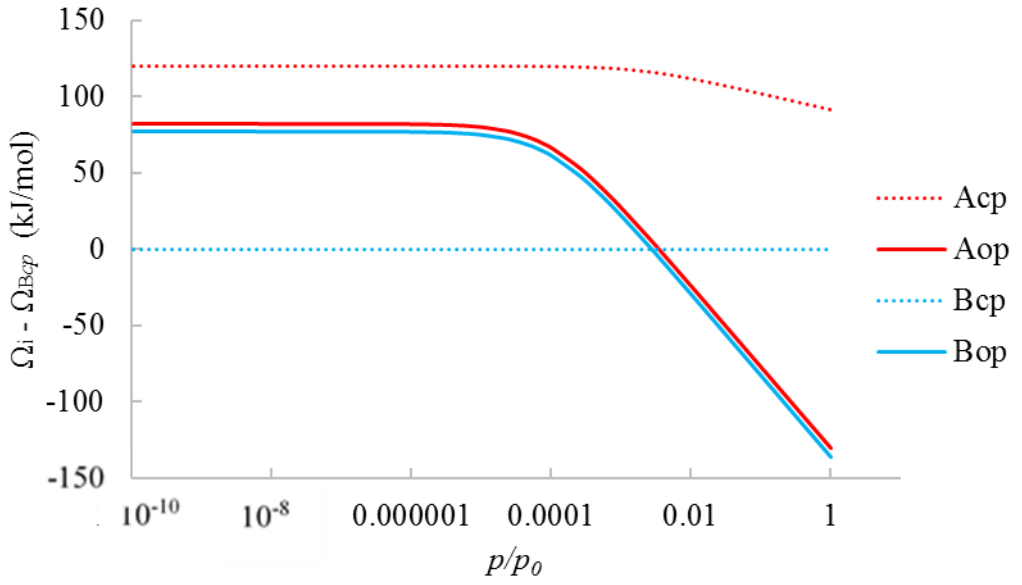

Figure S9. Relative osmotic potentials for N_2 adsorption at 77 K in the bulk framework

Section 9. Energy difference and gate closing pressures for different capping groups

OFAST was used to predict the gate-closing pressure in the bulk and slab models. Table S1 shows the internal energy differences and the gate-closing pressure for each system.

Table S1. Normalized (solvent free) B*cp* → B*op* energy differences and the gate closing pressures for each capping group

System	$E_{Bop\text{-}Bcp}$/Bulk (kJ/mol)	$p/p_0^{closing}$
001-DMF	33	0.003
110-FA	53	0.01
001-dabco	59	0.03
110-H(2,6-ndc)	69	0.05
Bulk	76	0.005

REFERENCES

1. Macrae, C.E., P; McCabe, P; Pidcock, E; Shields, G; Taylor, R; Towler, M; van de Streek, J, *Mercury.* Journal of Chemical Information and Modeling, 2006. **44**: p. 2133-2144.
2. Donnay, J.H., D, *A new law of crystal morphology extending the law of Bravais.* American Mineralogist, 1937. **22**(463): p. 446-467.
3. Bon, V., et al., *Exceptional adsorption-induced cluster and network deformation in the flexible metal–organic framework DUT-8(Ni) observed by in situ X-ray diffraction and EXAFS.* Physical Chemistry Chemical Physics, 2015. **17**(26): p. 17471-17479.
4. Coudert, F.-X., *The osmotic framework adsorbed solution theory: predicting mixture coadsorption in flexible nanoporous materials.* Physical Chemistry Chemical Physics, 2010. **12**(36): p. 10904-10913.
5. Bon, V., et al., *Tolerance of Flexible MOFs toward Repeated Adsorption Stress.* ACS Applied Materials & Interfaces, 2015. **7**(40): p. 22292-22300.
6. Petkov, P., et al., *Conformational isomerism controls collective flexibility in metal-organic framework DUT-8(Ni).* Physical Chemistry Chemical Physics, 2018.
7. Klein, N., et al., *Monitoring adsorption-induced switching by (129)Xe NMR spectroscopy in a new metal-organic framework Ni(2)(2,6-ndc)(2)(dabco).* Phys Chem Chem Phys, 2010. **12**(37): p. 11778-84.

CHAPTER 4. CISPLATIN UPTAKE AND RELEASE IN UiO-66 AND UiO-66(NH_2)

4.1. Motivation: test existing simulation techniques to model cisplatin uptake and release in MOFs

Existing computational studies on drug encapsulation in MOFs mainly use pure-component GCMC simulations [1-3], *ab-initio* simulations [4], or a combination of both [5-8]. However, very few of these studies account for water which is present both during drug molecule uptake and release, furthermore GCMC and DFT simulations can only provide limited information which is not directly relatable to experimentally derived release rates. In this chapter, a variety of classical and *ab-initio* simulation techniques are used to determine the uptake and release of cisplatin (CPT) in UiO-66 and a functionalised variant UiO-66(NH_2). These MOFs in particular were selected because of the available experimental data needed to validate the tested methodologies [9].

4.2. Summary: classical and *ab-initio* simulations with and without water

Cisplatin uptake was initially quantified using pure-component GCMC simulations. Due to the high packing density of water inside the pores of UiO-66 and UiO-66(NH_2), GCMC simulations could not be used to quantify mixed cisplatin + water adsorption. Instead, cisplatin adsorption in the solvated system was quantified using the BAR method (Section 2.3.4 [10]) at various cisplatin and water loadings. As discussed in Section 4.6, BAR was used to analyse the feasibility of cisplatin adsorption in the different pore types of each framework, by calculating the change in Gibbs free energy when decoupling cisplatin from bulk water and coupling it into the MOF + water + cisplatin system.

Release rates depend on cisplatin diffusivity through the framework. There are two methods of decreasing diffusivity: enhancing either the MOF – drug interaction energies that contribute to the intrapore diffusion, or the energy penalties associated with movement through the pore windows. Interaction energies calculated from GCMC simulations were compared to those calculated using *ab-initio* optimisations of various cisplatin configurations inside the pores. The interaction energies were also compared to rates of diffusion calculated using MD simulations with and without water, to investigate how much control over diffusion the interaction energies actually attain.

The interpore diffusivity cannot be quantified using normal MD simulations due to high energy barriers associated with cisplatin movement through the pore windows. Instead, a combination of SMD and the geometric analysis and simulation of polyhedra software (GASP [11]) were used to look at the individual contributions of the framework bonded interactions and cisplatin – framework interaction energies on the "pore-hop" energy barrier. Umbrella sampling (which allows the system to be equilibrated at each interval along the reaction coordinate) was also used for comparison.

4.3. Results: for polar guest molecules water plays a crucial role in uptake and release. The most suitable simulation tool depends on the required information

GCMC simulations can calculate the maximum achievable uptake (which is predominantly based on the pore volume); however, it is important to understand that when water is present this may not be the uptake achieved experimentally. BAR simulations indicate that the pore volume needs to be able to favourably accommodate both cisplatin and its solvation shell, else there is a driving force to displace cisplatin from the framework and back into solution. This substantially decreases the uptake compared to GCMC simulations. Compared to experimentally achieved uptake from solution [9], the BAR method is substantially closer to the experimentally observed loading, however it still overestimates results which is likely caused by diffusion limitations – something that neither BAR nor GCMC can capture.

Polar functional groups increase the MOF – CPT interaction energy (as calculated using pure-component GCMC or *ab-initio* simulations) which hypothetically reduces release rates. However, care must be taken as these results have no temporal aspect and they do not account for water, the presence of which decreases the MOF – CPT interaction energies. Instead, MD simulations show that water diffusivity decreases with polar groups, which in turn decreases cisplatin diffusivity.

Unbiased equilibrium techniques (such as normal MD simulations) are problematic in the case of MOFs with small window diameters because they cannot easily capture rare-events (i.e. pore-hopping). SMD simulations and umbrella sampling can capture the energy barriers associated with movement through the framework, however the limitations of each technique need to be considered when analysing results. In particular, SMD simulations do not let the system equilibrate, and hence potential energy barriers are only approximate. Umbrella simulations do let the system equilibrate, yet in this unique case (regardless of the

constraints used) equilibration results in an unphysical pathway through the framework which is described in depth in Section 4.6.

Overall, the work in this chapter helped aid the choice of simulation methods used in Chapters 5 and 6, which heavily depended on the information that needed to be gathered and what limitations were acceptable to draw meaningful conclusions. In Chapter 5 for instance, ideally diffusion data would have been gathered using normal MD simulations with water. However, small pore window diameters and reduced diffusivity in the presence of water requires unfathomably large simulation times to adequately sample the system. As a work around, non-solvated MD simulations could be used (with the limitation that there is no longer the influence of water which forms a solvation shell that affects the MOF – CPT interaction energies) or bias MD simulations could be used (with the limitation that equilibration cannot be obtained while retaining a sensible simulation path). Alternatively, by understanding the limitations of both techniques and comparing the results from each of them, it is possible to draw conclusions regardless of the short-comings because it was possible to see how much they actually influenced the results.

4.4. Errata

Not applicable as paper not yet submitted

4.5. Chapter 4 Preamble References

1. Liu, J.-Q., et al., *A combined experimental and computational study of novel nanocage-based metal–organic frameworks for drug delivery.* Dalton Transactions, 2015. **44**(44): p. 19370-19382.
2. Wang, J., et al., *Combined experimental and theoretical insight into the drug delivery of nanoporous metal–organic frameworks.* Royal Society of Chemistry Advances, 2015. **5**(104): p. 85606-85612.
3. Li, F., et al., *Encapsulation of pharmaceutical ingredient linker in metal–organic framework: combined experimental and theoretical insight into the drug delivery.* Royal Society Chemistry Advances, 2016. **6**(53): p. 47959-47965.
4. Filippousi, M., et al., *Biocompatible Zr-based nanoscale MOFs coated with modified poly(ε-caprolactone) as anticancer drug carriers.* International Journal of Pharmaceutics, 2016. **509**(1): p. 208-218.

5. Chalati, T., et al., *Porous metal organic framework nanoparticles to address the challenges related to busulfan encapsulation.* Nanomedicine, 2011. **6**(10): p. 1683-1695.
6. Ma, D.-Y., et al., *Hydrostable and Nitryl/Methyl-Functionalized Metal–Organic Framework for Drug Delivery and Highly Selective CO2 Adsorption.* Inorganic Chemistry, 2015. **54**(14): p. 6719-6726.
7. Kotzabasaki, M., et al., *OH-functionalization strategy in Metal-Organic Frameworks for drug delivery.* Chemical Physics Letters, 2017. **685**: p. 114-118.
8. Kotzabasaki, M. and G.E. Froudakis, *Review of computer simulations on anti-cancer drug delivery in MOFs.* Inorganic Chemistry Frontiers, 2018. **5**(6): p. 1255-1272.
9. Mocniak, K.A., et al., *Incorporation of cisplatin into the metal–organic frameworks UiO66-NH2 and UiO66 – encapsulation vs. conjugation.* Royal Society Chemistry Advances, 2015. **5**(102): p. 83648-83656.
10. Bennett, C.H., *Efficient estimation of free energy differences from Monte Carlo data.* Journal of Computational Physics, 1976. **22**(2): p. 245-268.
11. Wells, S.A. and A. Sartbaeva, *GASP: software for geometric simulations of flexibility in polyhedral and molecular framework structures.* Molecular Simulation, 2015. **41**(16-17): p. 1409-1421.

This declaration concerns the article entitled:			
Cisplatin uptake and release in UiO-66 and UiO-66(NH_2)			
Publication status (tick one) **Draft manuscript** [ ] **Submitted** [/] **In review** [ ] **Accepted** [ ] **Published** [ ]			
Publication details (reference)	Thompson, M. Wells, S. Düren, T. 2020. Molecular simulations of cisplatin uptake and release in UiO-66 and UiO-66(NH_2).		
Copyright status (tick the appropriate statement) I hold the copyright for this material [ ]		Copyright is retained by the publisher, but I have been given permission to replicate the material here [/]	
Candidate's contribution to the paper (provide details, and also indicate as a percentage)	The candidate contributed to / considerably contributed to / predominantly executed the… Formulation of ideas: The candidate predominantly formulated the detailed ideas (95 %). The idea to use GASP was formulated by S. A. Wells (5 %). Design of methodology: The candidate predominantly designed the method for the simulations (95 %). The idea to use GASP was formulated by S. A. Wells (5 %). Experimental work: The candidate predominantly conducted the simulations (95 %). GASP simulations were performed by S. A. Wells (5 %). Presentation of data in journal format: The candidate predominantly presented the work in a journal format (100 %)		
Statement from Candidate	This paper reports on original research I conducted during the period of my Higher Degree by Research candidature.		
Signed	Meyan Thompson	**Date**	01/09/2020

Molecular simulations of cisplatin uptake and release in UiO-66 and UiO-66(NH_2)

Megan J. Thompson, Stephen A. Wells, Tina Düren[*]

AUTHOR ADDRESS Prof. T. Düren, Centre for Advanced Separations Engineering, Department of Chemical Engineering, University of Bath, BA2 7AY, UK
E-mail: t.duren@bath.ac.uk

ABSTRACT

Metal-organic frameworks are highly promising drug delivery carriers for chemotherapy due to their tailorable properties. To design a MOF for drug delivery, we need to understand its drug loading capacity and whether it can retain cisplatin in healthy parts of the body and only release it in the vicinity of the tumour. In this paper, we investigate cisplatin delivery in biocompatible MOFs UiO-66 and UiO-66(NH_2) to determine whether standard molecular simulations used to screen potential chemotherapeutic drug carriers (pure-component GCMC and DFT simulations) are adequate, or if we need to change our methodology to better capture experimental conditions. Pure-component GCMC simulations capture the maximum uptake which predominantly depends on the pore volume, however this significantly exceeds the experimental loading. Alchemical simulations with implicit water molecules show that the solvation shell/pore size relationship is largely responsible for reduced uptake seen experimentally, and that at high enough water loading there is a driving force to push cisplatin out of the framework. Comparing this driving force to the interpore energy barrier, at a threshold water loading cisplatin will be displaced from both MOFs. As well as the interpore energy barrier, release rates can be quantified by intrapore diffusion coefficients, which significantly vary depending on the water loading. Stronger CPT-MOF interaction energies in UiO-66(NH_2) reduce diffusion rates at the optimal water loading compared to the parent structure. These results have been validated against experimental findings, hence the methodology can be used to screen MOFs for drug delivery.

Chemotherapy patients are typically treated by the intravenous administration of chemotherapeutics such as cisplatin (Figure 1), which is one of the most widely used chemotherapy drugs as it is effective against various types of cancer. It is a cytotoxic drug that cross-links with purine bases within DNA, preventing cell replication and growth, and inducing controlled self-destruction [1]. Unfortunately, the mechanism of cisplatin cytotoxicity is non-specific, and this causes the harmful side effects of chemotherapy [2]. Furthermore, indirect drug administration can reduce the dosage reaching the tumour, increasing its ability to develop a resistance to cisplatin [3].

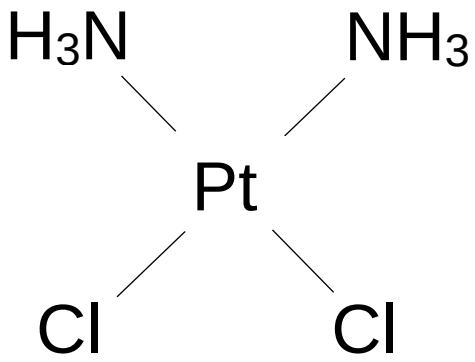

Figure 1. Structure of cisplatin (*cis*-diamminedichloroplatinum (II), $Pt(NH_3)_2Cl_2$)

Targeted chemotherapy can be accomplished using cancer-specific drugs or drug nanocarriers. For example, one of the primary differences between cancer and healthy cells are their mitochondrial functions, hence most cancer-specific drugs target these organelles [4] [5]. Alternatively, a non-toxic nanocarrier can be used to carry World Health Organisation approved cytotoxic drugs (such as cisplatin [6]) past healthy parts of the patient to the tumour. If the carrier can release the drug in the vicinity of the tumour whilst retaining it in healthy parts of the body, higher more localised doses can be achieved whilst reducing the harmful side effects of chemotherapy. Both cancer-targeting drugs and nanocarriers enable the accumulation of drugs in the vicinity of the tumour, enhancing the payload and reducing cytotoxic effects on healthy cells. Additionally, nanocarriers also increase the drug half-life, control release kinetics, and protect the drugs from degradation – further increasing the payload [7].

Nanocarriers that have been designed for targeted drug delivery include organic materials (such as nanostructured lipids [8], polymeric micelles [9], liposomes [10], peptides [11]), and inorganic materials (such as mesoporous silica [12] and oxide carriers [13]). Organic carriers have the advantage of being biocompatible, yet their storage capacity for drug molecules is limited. Inorganic carriers can offer enhanced storage capacity because of their larger specific surface areas and tuneable properties such as their porosity, interaction with guest molecules and external surface chemistry. However, they are often toxic and inert, making them non-biocompatible [14].

Metal-organic frameworks (MOFs) are hybrid materials which consist of metal nodes coordinated to organic ligands. These building units self-assemble into porous crystalline materials with well-defined internal surface areas, porosities and pore window sizes. By changing the primary building units or synthesis conditions, it is possible to fine-tune the properties of MOFs, such as their guest-host interactions [15], framework flexibility [16] and pore window sizes [17]. When scaled down from typical microcrystals to nanoparticles, surface functionalisation is also a feasible strategy to adjust the properties of the MOF such as its framework flexibility [18], to incorporate guest molecules onto the particle for example in combination therapy [19], or to improve the ease of incorporation of the MOF into the system of interest (for example, Chen et al incorporated nucleic acid polyacrylamide hydrogel onto the surface of UiO-68 to induce the release of an anthracycline, anticancer drug – doxorubicin – in the presence of adenosine triphosphate, ATP [20]). Such capabilities have resulted in the investigation of biocompatible MOFs as promising cisplatin carriers [19, 21]. Ideally a cisplatin carrier would be biodegradable, capable of large specific cisplatin uptake, retain cisplatin in healthy regions of the patient and release it only in the vicinity of the tumour. One method of achieving this would be to target the acidic microenvironment surrounding a tumour ($pH_e < 6.8$ compared to healthy cells $pH_e = 7.2$ [22]), resulting from higher glycolysis rates in cancer cells. As summarised in the review by Howarth et al, some MOFs such as members of the ZIF (=zeolitic imidazole framework) family are stable in pH>6.8 and will degrade in more acidic conditions [23]. This makes them promising candidates as cisplatin carriers. At the time of writing surprisingly few computational studies have been carried out to screen metal-organic frameworks for this purpose [24].

Previous computational studies include the use of *ab-initio* simulations to calculate host-guest interaction energies and the most favourable adsorption sites. For example, Filippousi et al used *ab-initio* molecular dynamics (AIMD) simulations to shed insight of cisplatin

uptake in UiO-66 and UiO-67 with missing ligand defects. In the case of UiO-66, they were able to depict the most favourable conformation of cisplatin uptake [25]. However, the accuracy of *ab-initio* calculations comes with the price that they are computationally very expensive. Alternatively, at an accuracy strongly determined by the forcefield parameters, classical forcefield approaches can be used to quickly screen MOF – drug behaviours at relatively low computational cost. As reported in the review by Kotzabasaki et al [24], several groups have used grand-canonical Monte Carlo and/or molecular docking simulations to investigate Fluorouracil (5-FU) drug delivery in various frameworks [26-28]. Research so far has focussed on the uptake and adsorption energies of pure drug molecules, concluding that the uptake mainly depends on the pore volume and that the rate of release mainly depends on the drug-MOF interaction energies. However, experimental studies of cisplatin uptake and release are usually carried out in an aqueous solution where cisplatin adsorption can be achieved using encapsulation (the passive diffusion of cisplatin from a solution to the MOF) or conjugation (similar to encapsulation, except using a functionalised ligand and pro-drug that can form CPT – MOF covalent bonds) [21].

In this paper, we explore whether the standard pure-component screening techniques (*ab-initio* optimisations and grand-canonical Monte Carlo simulations) used in previous research are good enough to model cisplatin drug delivery under experimental lab and ultimately physiological conditions, or whether we need to account for water to better mimic real-life conditions. We further investigate what types of simulation most efficiently capture the effects of water on cisplatin uptake and release. Because of the available experimental data [21, 29], the computational methods of characterising cisplatin delivery were validated using the biocompatible MOFs UiO-66 and UiO-66(NH_2), the structures of which are shown in Figure 2. Both MOFs have the same basic structure, namely 1,4-benzenedicarboxylate ligands coordinated to zirconium clusters into a framework consisting of 11 Å octahedral pores connected by triangular windows to 8 Å tetrahedral pores [30]. The structures differ because the ligands in UiO-66(NH_2) are functionalised with amine groups, which in turn will influence the interaction energy and/or binding strength to cisplatin and reduce the pore/pore-window size and hence void space and energy barrier associated with movement through the framework.

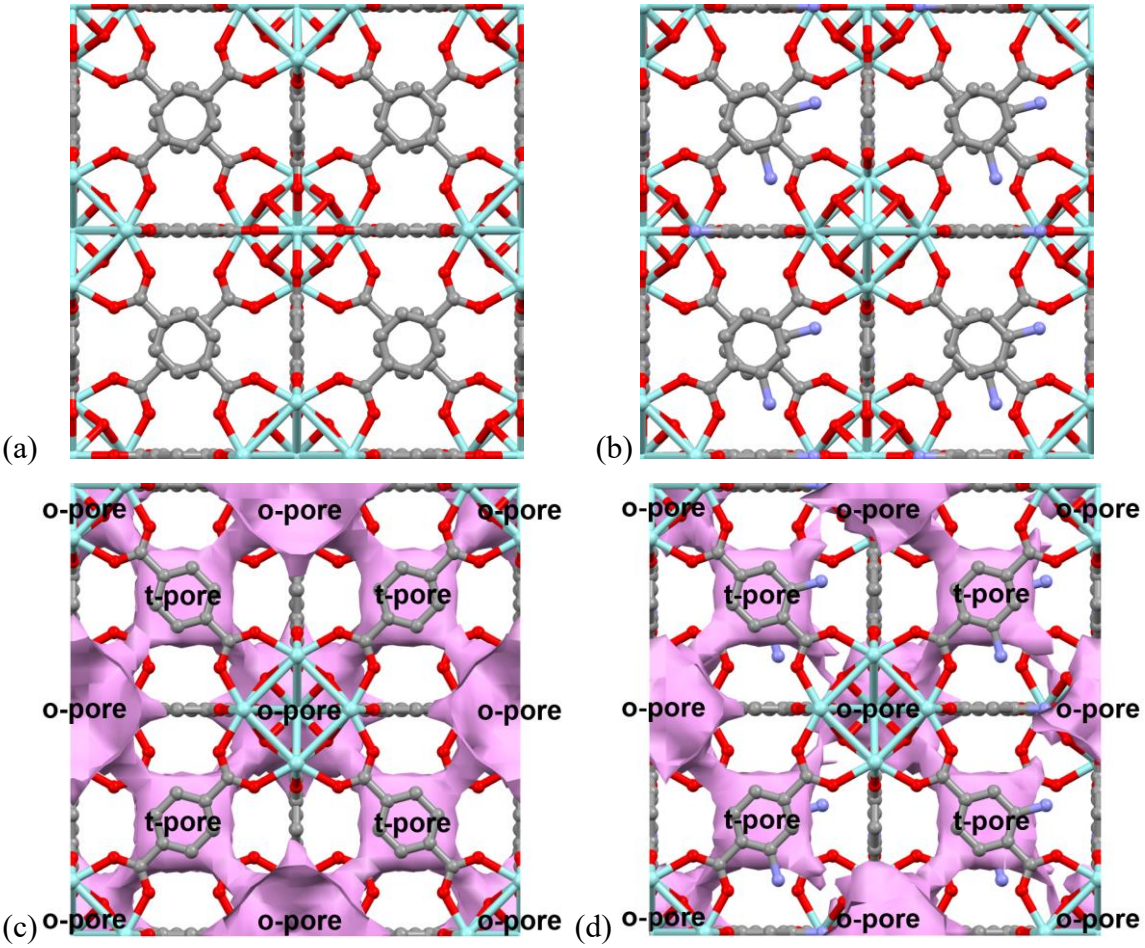

Figure 2. Crystal structures of (a) UiO-66 [$Zr_6O_4(OH)_4BDC_6$] and (b) UiO-66(NH_2) [$Zr_6O_4(OH)_4(BDC(NH_2))_6$]. Colour representations are: Zr=turquois, C=grey, O=red, N=blue. Hydrogens are omitted for clarity. Representation of the accessible pore volume for a 2 Å probe (pink) in (c) UiO-66 and (d) UiO-66(NH_2) generated using Mercury Software [31].

METHOD

Structural Models: The crystallographic structure of UiO-66 was obtained from literature [32], and an amine group was added to each BDC ligand to create UiO-66(NH_2). To represent the bulk crystal, periodic boundary conditions were used in all directions.

Classical Simulations: Classical simulations offer a relatively cheap method to model drug molecule uptake and delivery in MOFs, however the results depend on the forcefield used. In this work, the Lennard-Jones 12-6 potential and bonded parameters for the MOFs were taken from the Universal Force Field (UFF [33]). Partial charges were obtained as Mulliken charges from *ab-initio* static energy calculations on the initial structures (the validation for which is described in the SI, Section 1). Cisplatin (CPT) was modelled using the "standard

topology" developed by Yesylevskyy et al who used *ab-initio* methods [34]. Since this forcefield was tested with TIP3P, the same water model was also used in this research [35]. A cut-off radius of 12.5 Å was used to truncate all short-ranged interactions.

Most computational drug – MOF uptake studies are carried out using pure-component grand-canonical Monte Carlo (GCMC) simulations. We modelled pure-cisplatin uptake at 310 K (body temperature) using GCMC simulations as implemented in the multipurpose simulation code MuSiC [36]. During the GCMC simulations all cisplatin molecules and the MOFs were kept rigid. CPT-MOF Coulombic interaction energies were calculated using Ewald summation [37]. CPT-CPT Coulombic and Lennard-Jones interactions were calculated on-the-fly using the Wolf summation method [38] and the LJ 12-6 potential respectively. Microstates were generated using four GCMC moves: insertion, deletion, translation and rotation. 10 million iterations were used for each pressure point, and the first 40 % of microstates were discarded carefully ensuring that the ensemble averages are taken once the simulations have equilibrated.

Drug delivery carriers are normally modelled without accounting for water [25-28]. Experimentally however, cisplatin uptake and release are carried out in the presence of water or water-based simulated body fluids [21]. Due to the high loadings involved, GCMC simulations will not efficiently equilibrate water and cisplatin adsorbed in UiO-66/UiO-66(NH_2) at 1 bar, since the high loading will make insertion, deletion and ID-swap moves near impossible. Instead, molecular dynamics (MD) simulations were used.

All molecular dynamics (MD) simulations were carried out using the Groningen Machine for Chemical Simulations (GROMACS, 2019.2) code [39-44] keeping the MOF framework flexible. Topologies for the MOFs were generated by extending the orthogonal face-centred cell into a 2x2x2 supercell and using OBGMX which models all interactions using the Universal Force Field [33, 45]. No additional constraints were imposed on the framework. Long-ranged electrostatic interactions were calculated using the particle mesh Ewald algorithm [46, 47]. Long range dispersion corrections were applied to the energy and pressure terms. Prior to all MD simulations, the structures were pre-equilibrated using a steepest decent energy minimization followed by a 100 ps NVT equilibration. Separate temperature coupling baths were used for cisplatin and the framework, along with a modified Berendsen coupling method [48]. Depending on the ensemble used during production simulations a further 100 ps NPT equilibration was carried out. A Parrinello-Rahman

barostat was used for pressure coupling during equilibration. During the production simulations, temperature and (depending on the ensemble) pressure coupling was achieved using a Nosé-Hoover thermostat and a Parrinello-Rahman barostat [49, 50].

The Bennett's Acceptance Ratio (BAR) algorithm as implemented in GROMACS was used to calculate the equilibrium loading of cisplatin accounting for water [51]. At equilibrium there is no net transfer of cisplatin between System (a) (a = cisplatin in bulk water), and System (b) (b = MOF + cisplatin + water). Hence, the net change in Gibbs free energy when moving a cisplatin molecule between (a) and (b) is nil, as shown conceptually in Figure 3.

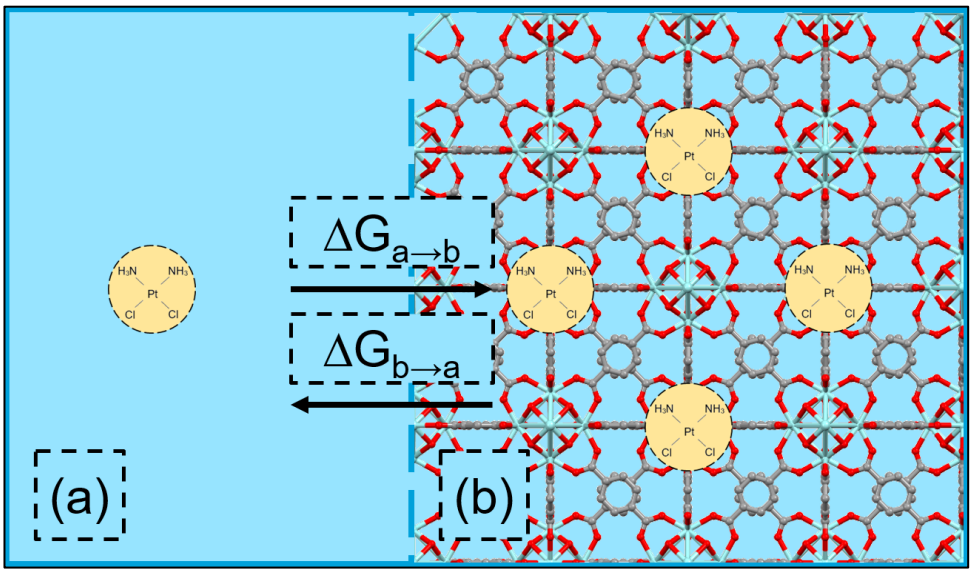

Figure 3. Schematic of models used in alchemical simulations (a = one cisplatin molecule in bulk water, b = varied number of cisplatin and water molecules in UiO-66/UiO-66(NH_2)). $\Delta G_{a\rightarrow b}$ and $\Delta G_{b\rightarrow a}$ are the changes in Gibbs free energies when moving one cisplatin molecule from a→b and b→a. At equilibrium $\Delta G_{a\rightarrow b} = \Delta G_{b\rightarrow a}$.

By gradually decoupling a single cisplatin molecule from Systems (a) and (b), it is possible to use the BAR method to calculate the free energy change associated with cisplatin uptake from solution using the Hess cycle in Figure 4.

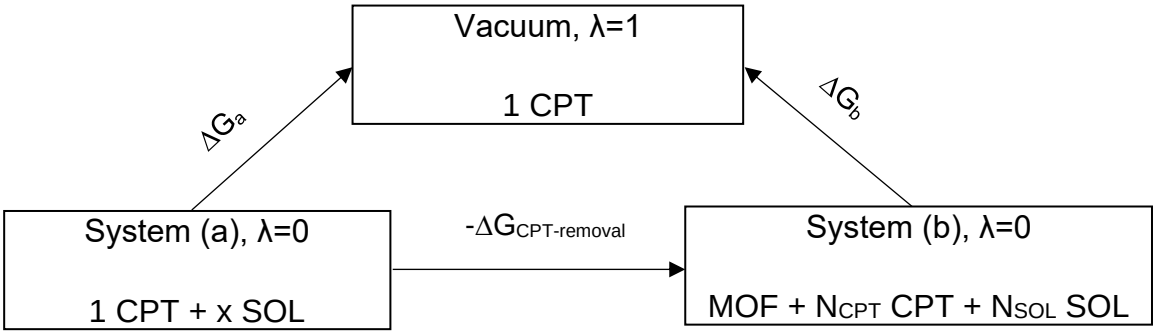

Figure 4. Hess cycle used to determine the equilibration loading of cisplatin and water in UiO-66 and UiO-66(NH_2). $\lambda = 0$ and $\lambda = 1$ refer to the beginning and end states of cisplatin during decoupling.

To decouple cisplatin, (corresponding to turning off all non-bonded interactions between cisplatin and the rest of the system), a series of configurations were generated between the fully coupled and decoupled states. The BAR algorithm [51] was then used to calculate the change in Gibbs free energy between the two states:

$$\Delta G = \int_0^1 d\lambda \left\langle \frac{dH(\lambda)}{d\lambda} \right\rangle \quad (1)$$

Where H is the parameterized Hamiltonian and λ refers to the position along an integration path between states 0 and 1. In this work, state 0 corresponds to a cisplatin molecule that fully interacts with the system, and state 1 corresponds to no interactions between cisplatin and the system [52]. To prevent molecules of opposite charge becoming trapped, the Coulombic interactions were decoupled before the LJ interactions. In total, 20 configurations were used to decouple the non-bonded interactions with varying λ between 0-1 in intervals of 0.1 to ensure each stage of decoupling shares part of the same phase space.

A single cisplatin molecule was decoupled from system (a), consisting of a 3 nm^3 box of water, and system (b), the MOF + water + cisplatin system at various water and cisplatin loadings. Each configuration was pre-equilibrated prior to a production run in the NPT ensemble for 1 ns at 298 K (encapsulation temperature [21]). The free energy difference was calculated using the BAR algorithm [51]. Adsorption energies for each water/cisplatin loading were calculated (for the fully coupled systems) as:

$$U_{ads} = U_{total} - U_{CPT}N_{CPT} - U_{SOL}N_{SOL} - U_{MOF} \quad (2)$$

Where U_{total} is the energy of the MOF + cisplatin + water system, U_{CPT} is the energy of a single cisplatin molecule in a 3 nm^3 box, N_{CPT} is the number of cisplatin molecules, U_{SOL} is the energy of a single water molecule in a 3 nm^3 box, N_{SOL} is the number of cisplatin molecules, and U_{MOF} is the energy of the empty framework. Each term was taken to be the average energy over a 1 ns MD simulation which was pre-equilibrated.

Normal (unbiased) MD simulations cannot capture movement through the pore windows which is a rare event due to the high associated energies. Instead, steered MD (SMD) and umbrella sampling simulations were used to quantify the energy barrier associated with moving one cisplatin molecule from an octahedral pore to the same chemical environment in another octahedral pore (from herein termed "pore-hopping"). It was assumed that the bulk of the crystal would confine a unit cell to a near constant volume, and that a single cisplatin molecule moving through the framework would not influence that volume significantly. For this reason, the SMD and umbrella sampling simulations were confined to the constant volume (NVT) ensemble.

A single cisplatin molecule was centred in the middle of one of the octahedral pores in UiO-66 and UiO-66(NH_2). Following pre-equilibration, SMD simulations were used to pull the cisplatin molecule into an adjacent octahedral pore along the [101] plane for 300 ps, using a pull rate of 0.01 nm/ps and a time step of 0.001 ps. A spring constant of 1,000 kJ mol^{-1} nm^{-2} was used to constrain cisplatin using a harmonic potential. Stronger spring constants and slower pull velocities were tested, however the simulation path and resulting energy barrier remained constant.

Sampling windows for the umbrella sampling simulations were collected every 0.1 nm along the SMD trajectories. As discussed with the results, individual windows were not pre-equilibrated but were subject to 10 ns MD simulations within the sampling window, bound by the same harmonic potential as used in the SMD simulations [53]. The final results were analysed using the weighted histogram analysis method (WHAM [54]). A total of eight pull and umbrella sampling simulations per MOF were carried out moving cisplatin in alternating directions through the framework. The starting configuration for each repeat was taken as the final position of the previous repeat's pull simulation.

Ab-initio simulations: SMD simulations can be used to calculate the potential energy barrier associated with pore-hopping, however for classical simulations the results strongly depend

on the forcefield. *Ab-initio* MD simulations remove the reliance on force fields, however they are expensive. Instead, the geometric analysis and simulation of polyhedra software (GASP [55]) was used investigate the intrinsic flexibility of UiO-66 and UiO-66(NH_2), and to determine whether such a technique can produce potential energy barriers associated with pore-hopping at relatively low cost whilst avoiding the dependency on forcefields. We used GASP to determine the intrinsic flexibility of UiO-66 and UiO-66(NH_2). In this approach, local atomic geometries (such as bond lengths and angles) are constrained using a series of superimposed templates whilst the unit cell parameters vary. The framework is within the limits of its "flexibility window" for any global variations in which the local geometry remains unaltered. The local geometry constraints in UiO-66 and UiO-66(NH_2) involved maintaining effectively rigid zirconium clusters whilst letting the carboxyl and aromatic groups rotate to different planes. All structures identified within the flexibility windows were analysed using PoreBlazer [56] to determine the pore-limiting diameter (PLD). The potential energy difference between each variant and the original structure were calculated based on the change in internal energy determined using relatively cheap *ab-initio* static energy calculations (as detailed in the SI, Section 2). By comparing the PLD at the time of pore-hopping (from the SMD simulations) to that of the structures generated within the flexibility window, we could compare the potential energy barriers calculated from classical SMD simulations and GASP/static energy calculations.

We performed static energy calculations on the GASP variants (to determine the potential energy barrier associated with opening the pore windows for cisplatin pore-hopping), and on the original UiO-66 and UiO-66(NH_2) structures (to determine the partial atomic charges used in classical simulations). During classical simulations, partial atomic charges of the framework and guest molecules are fixed despite their motion. To validate using static charges with polar guest molecules such as cisplatin and water, *ab-initio* geometry optimisations of cisplatin in UiO-66 and UiO-66(NH_2) were carried out. This allowed for the comparison of pre and post optimisation charges, framework charges with and without cisplatin, and cisplatin – MOF interaction energies calculating using DFT and GCMC simulations (see the SI, Section 1 for details).

RESULTS AND DISCUSSION

To date, the majority of MOF – drug simulation papers utilise pure component grand-canonical Monte Carlo simulations to determine the uptake [24]. Following this approach

Figure 5 shows the adsorption isotherms of pure CPT in UiO-66 and UiO-66(NH_2). For UiO-66 and UiO-66(NH_2), the maximum uptake is 0.67:1 and 0.56:1 CPT:Zr respectively. The uptake is lower in UiO-66(NH_2) because amine groups reduce the overall free volume from 0.46 cm^3/g to 0.42 cm^3/g (calculated using Poreblazer [56]).This ratio of free volumes of 1.11 to 1 for UiO-66 vs. UiO-66(NH_2) is the same as that reported by Zhang et al [57]. More specifically, due to the orientation of amine groups only one cisplatin molecule can fit into the octahedral pores (o-pore), whereas in UiO-66 two cisplatin molecules can fit into each o-pore. For both MOFs, one cisplatin molecule can fit into each 8 Å tetrahedral pore (t-pore) [58]. This makes sense as the molecular size of cisplatin is approximately 6 Å (see the SI, Section 3).

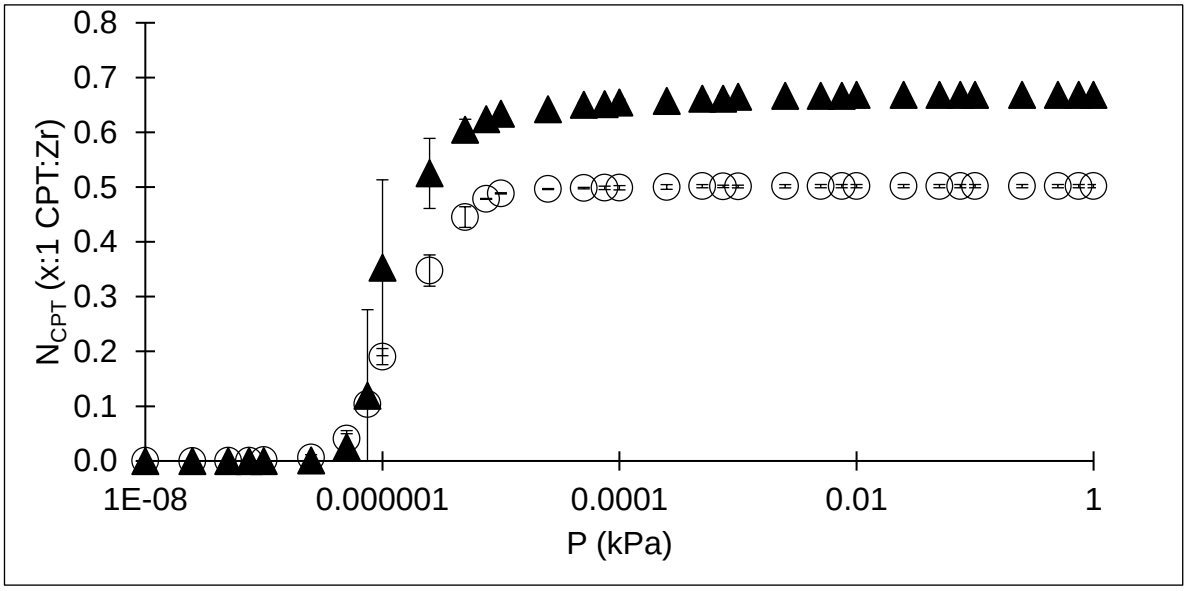

Figure 5. Adsorption isotherms of pure cisplatin in UiO-66 (▲) and UiO-66(NH_2) (○) at 310 K. Error bars show the standard deviation obtained from three independent repeat simulations.

The GCMC loadings are tenfold higher than the uptake achieved experimentally by encapsulation (cisplatin uptake via diffusion from solution ~ 0.06:1 CPT:Zr in UiO-66 and UiO-66(NH_2)). This suggests that water co-adsorption and diffusion limitations interfere. On the other hand, conjugation of a cisplatin pro-drug in UiO-66(NH_2) (i.e. the diffusion and covalent bonding of a functionalised, pre-activated cisplatin molecule into the MOF from solution) achieves a maximum loading that matches the simulated result (0.56:1 CPT:Zr) [21]. This implies that the maximum loading mainly depends on the available pore space, which is something that can be captured using GCMC simulations, as also shown in previous MOF – drug theoretical studies [24].

To capture the uptake via encapsulation where the co-adsorption of the solvent plays an important role, pure component GCMC simulations are therefore not appropriate and mixed water/cisplatin simulations are required. GCMC simulations of water/cisplatin mixtures will however not be efficient at capturing the effect of the solvent because most moves will be rejected due to the high loading of guest molecules. Alternatively, the Bennett's Acceptance Ratio algorithm [51] was used to get information about the mixed system.

To investigate the influence of water on cisplatin uptake, a single cisplatin molecule was decoupled from (a) the bulk water, and (b) the MOF + cisplatin + water system at different loadings of guest molecules. Figure 6 shows the change in Gibbs free energy ($\Delta G_{CPT\text{-}removal}$) when decoupling a single cisplatin molecule from the bulk water and the solvated MOFs. Based on the Hess cycle in Figure 4, if $(\Delta G_{CPT\text{-}removal})_{MOF} > (\Delta G_{CPT\text{-}removal})_{SOL}$, there is a driving force to move cisplatin from the solution into the framework, and vice versa.

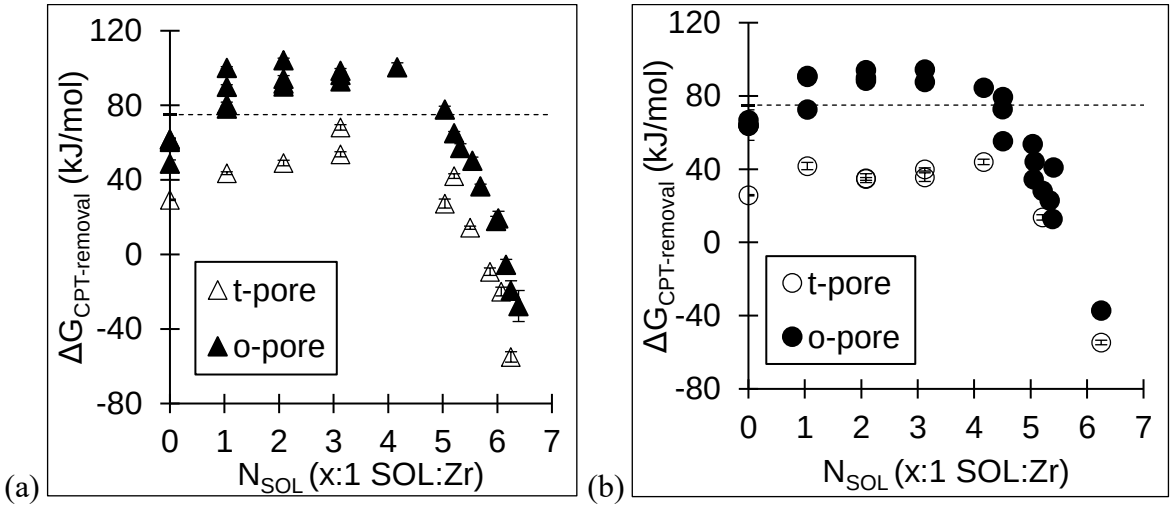

Figure 6. Change in Gibbs free energy as function of the number of water molecules (N_{SOL}) when decoupling a single cisplatin molecule from bulk water (dashed line), and solvated (a) UiO-66 and (b) UiO-66(NH_2) (T = 298 K, 0.005:1 CPT:Zr ≈ 0.54 wt%) for the two different types of pores present in both MOFs.

Both UiO-66 and UiO-66(NH_2) show similar trends in Figure 6: In the absence of water co-adsorption, cisplatin is more favourable in solution because of its solvation shell. For the larger o-pores, as the water loading (N_{SOL}) increases cisplatin is more favourable in the framework than in the bulk due to the combined interaction energies with water molecules in the solvation shell and the MOF. In contrast, the uptake into the smaller t-pores is never favourable (i.e. $(\Delta G_{CPT\text{-}removal})_{MOF} < (\Delta G_{CPT\text{-}removal})_{SOL}$) because there is not enough space in the t-pores for the solvation shell to establish demonstrating the importance of the solvation

shell and taking water into account. After a maximum, the framework begins to saturate which induces structural deformation of the framework. Therefore $(\Delta G_{CPT\text{-}removal})_{MOF}$ decreases and it becomes easier to decouple cisplatin at higher water loadings. The same trends are seen for higher cisplatin loading (N_{CPT}), except the framework starts to deform at a lower water uptake because of the reduced void space (as shown in the SI, Section 4).

Beyond the maxima in Figure 6, the frameworks distort considerably to accommodate more water molecules. In turn, as more water molecules are added the overall adsorption energy (U_{ads}) becomes more favourable because there are more interacting bodies. As shown in Figure 7, this is the case up to a minimum that is the water loading which achieves the most favourable overall adsorption energy for a given cisplatin uptake (at which $\sim \Delta G_{CPT\text{-}removal} =$ 0 kJ/mol). After the minimum it is unfavourable to add further guest molecules due to excessive framework distortions.

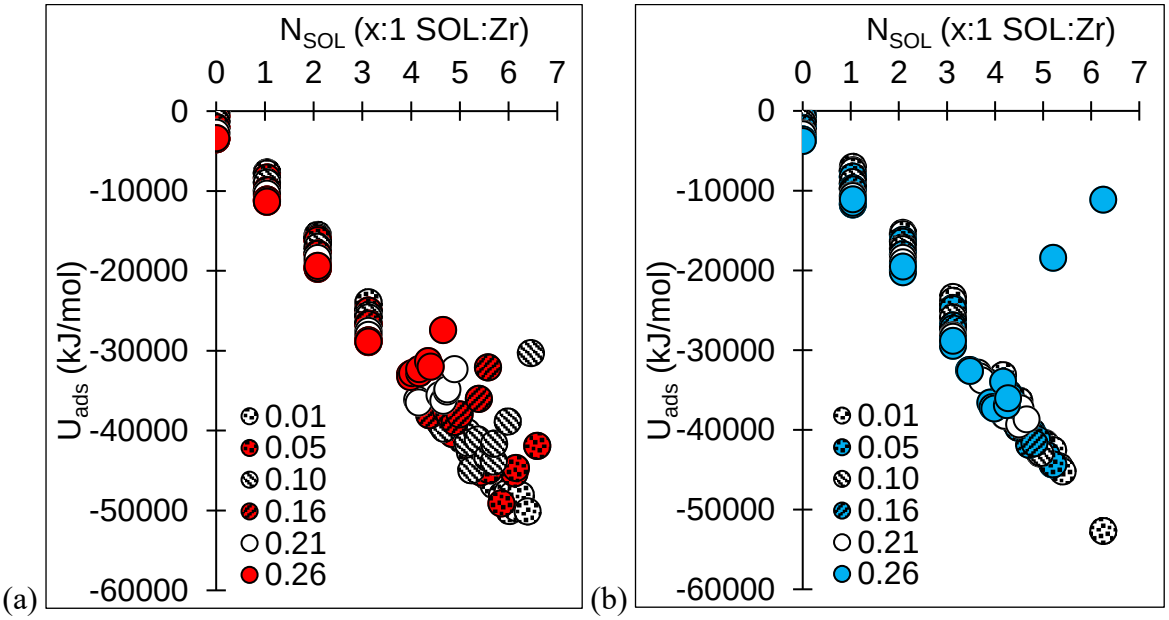

Figure 7. Overall adsorption energy (per unit cell – 192 Zr) as a function of water loading in (a) UiO-66 and (b) UiO-66(NH_2) at T=298 K (1:1 SOL:Zr = 6 $\%_{wt}$) for cisplatin loadings ranging from 0.01 CPT:Zr (1 $\%_{wt}$) to 0.26 CPT:Zr (28 $\%_{wt}$).

The maximum water loading that can be achieved before the framework starts to deform (i.e. the minima in Figure 7) increases with decreased cisplatin loading. Interpolation of these minima as a function of cisplatin loading indicates that in the absence of cisplatin, the equilibration loading of water is N_{SOL}=6.3:1 SOL:Zr (39 $\%_{wt}$) in both frameworks. This equilibrium water loading (39 $\%_{wt} \approx$ 21 mmol/g) is in close agreement with the experimental uptake of pure water (20 – 25 mmol/g [59-63]). Furthermore, the adsorption energies at the

minima become more negative (and adsorption more favourable) as the cisplatin loading decreases and hence the water loading increases. This suggests that water will displace all cisplatin molecules driving the system to a more energetically favourable state, which is the case for release experiments but in contrast to encapsulation during which the uptake of cisplatin is driven by equilibrium between cisplatin in solution and inside the framework. As captured by alchemical simulations (i.e. the crossover of lines shown in Figure 6 where $(\Delta G_{CPT\text{-}removal})_{MOF} = (\Delta G_{CPT\text{-}removal})_{SOL}$), equilibrium with cisplatin in solution occurs at relatively low water loadings, and only when cisplatin is situated inside the o-pores. Therefore, the theoretical loading at equilibrium is one cisplatin per o-pore or 0.17:1 CPT:Zr, which is about three times the experimental loading by encapsulation of 0.06:1 CPT:Zr [21]. The discrepancy between the simulated and experimental results is likely caused by other factors such as diffusion limitation, which is not captured by these simulations. Nevertheless, they paint a much more realistic picture than GCMC simulations of the uptake of pure cisplatin

For drug delivery, not only the uptake of the drug but also its release rate plays an important role. Experimentally, release rates are fourfold higher in UiO-66 compared to UiO-66(NH_2). It was speculated that this is due to enhanced interaction energies with the amine group and/or the energy barrier associated with interpore movement ("pore-hopping") [21], two aspects we will investigate next.

Figure 8 shows that CPT-MOF interaction energies, determined from pure component GCMC simulation, in UiO-66(NH_2) (average = - 60 kJ/mol) are stronger than those in UiO-66 (average = - 44 kJ/mol) because of enhanced electrostatic interactions between cisplatin and the amine groups ($[N\text{-}H^{\delta+}]_{MOF}$ - $[Cl^{\delta-}]_{CPT}$). This result agrees with the hypothesis that the difference in release rates between UiO-66 and UiO-66(NH_2) is caused by cisplatin anchoring to the functionalised BDC ligands. However, these pure component GCMC energies cannot provide information on how much the interaction energies will alter the release timing, nor how they will change when water is introduced to the system, as is the case during release experiments.

The alchemical simulations (Figure 6) showed that cisplatin adsorption is more favourable in the o-pores compared to the confined space in the t-pores, and therefore the interaction energies in the o-pores should be more favourable. On the other hand, potential energy maps generated from pure-cisplatin GCMC simulations (Figure 8a) show that this is not the case

in UiO-66, as the CPT-MOF interaction energies are less favourable in the o-pores compared to the t-pores. As illustrated in the potential energy histograms (Figure 8b), the pore types result in peaks at -10 - -40 kJ/mol in the o-pores compared to -40 - -80 kJ/mol in the t-pores. This is because Coulombic interactions between the $[N\text{-}H^{\delta+}]_{CPT}$ - $[Cl^{\delta-}]_{CPT}$ groups pull the two cisplatin molecules that share an o-pore further away from the framework atoms and closer to each other in UiO-66, as illustrated by the snapshot in Figure 8d.

Figure 8b shows that both the o-pores and t-pores in UiO-66(NH_2) contain (relatively) low energy adsorption sites, producing the first peak in the Figure 8c (-40 – -60 kJ/mol). As well as this, both pore types have strong adsorption sites depending on the position of the amine groups which form hydrogen bonds with cisplatin leading to the higher energy peaks in the histogram (-60 – -80 kJ/mol). As shown in Figure 8e, hydrogen bonds in the o-pores fix cisplatin in position. Combined with the reduced pore volume, this immobility makes it energetically favourable to only have one cisplatin in each o-pore, and therefore the grouping of cisplatin molecules witnessed in UiO-66 cannot occur in UiO-66(NH_2).

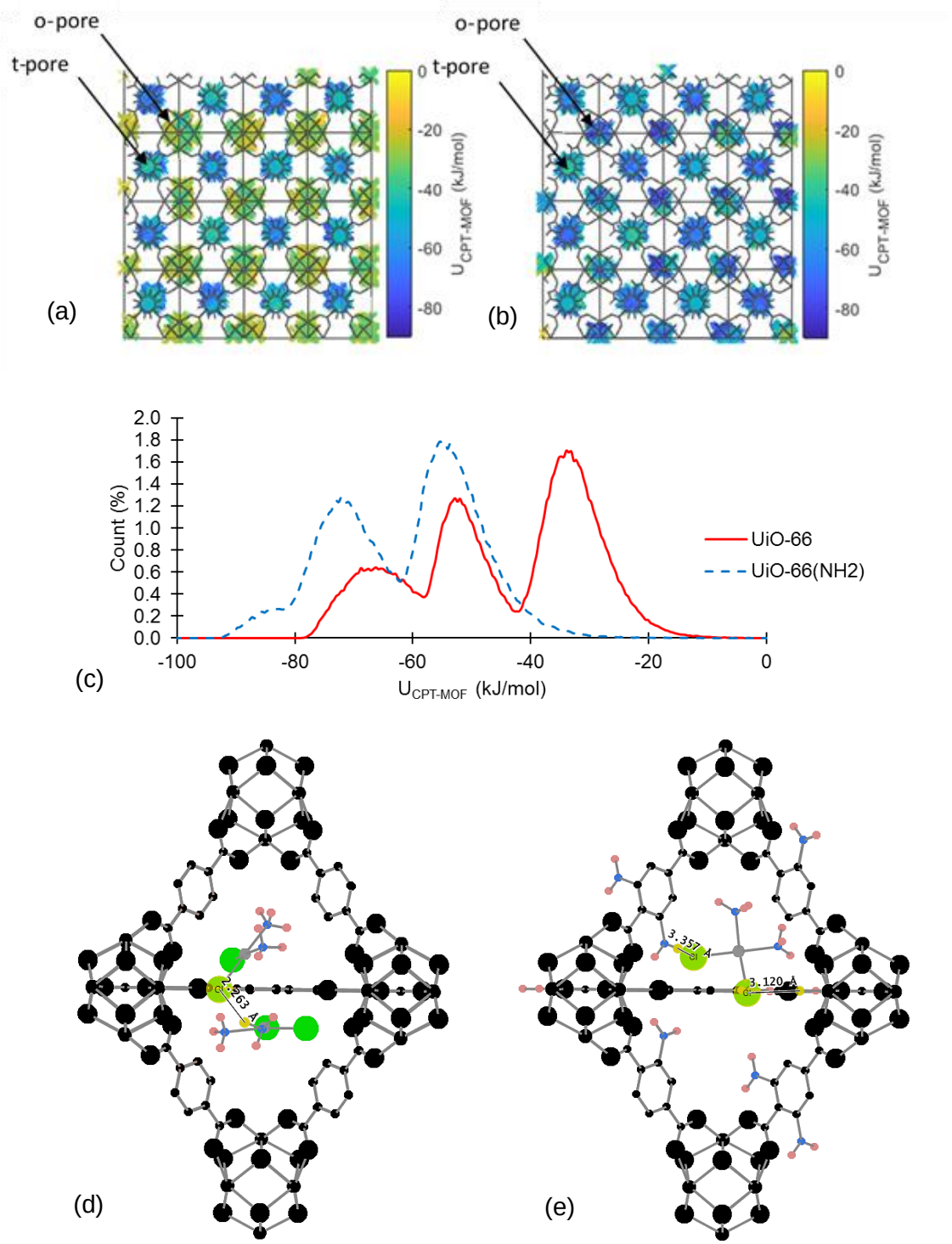

Figure 8. CPT-MOF interaction energy maps in UiO-66 (a) and UiO-66(NH_2) (b). CPT-MOF interaction energy histograms (c). Snapshots at maximum loading in UiO-66 (d) and UiO-66(NH_2) (e). (P=1 kPa, T=310 K)

Another, but computationally more expensive, method of determining the adsorption energy is to use *ab-initio* geometry optimisation. For this purpose, cisplatin molecules were randomly positioned into each pore type within a primitive unit cell (that consists of 1 o-

pore and 2 t-pore), and each configuration was optimised. Figure 9 shows the adsorption energy normalised per cisplatin molecule.

The average adsorption energy increases with more cisplatin molecules due to enhanced non-bonded interactions. In UiO-66, the lowest adsorption energy occurs at the maximum loading (two cisplatin molecules in the o-pore and two in the t-pore, 2o2t). In UiO-66(NH_2), the lowest adsorption energy occurs at a loading 2o1t because the addition of a further cisplatin molecule results in unfavourable framework distortions that outweigh the energy gained by addition of a fourth molecule. In both MOFs, the o-pores are a more favourable adsorption site compared to the smaller t-pores. Considering a single cisplatin molecule travelling through the framework, it needs to pass between the favourable o-pores and less favourable t-pores. To do so, the energy difference that cisplatin needs to overcome is 9 kJ/mol and 49 kJ/mol in UiO-66 and UiO-66(NH_2) respectively (corresponding to going from 1o to 1t, Figure 9). This difference in energy is a barrier to pore-hopping corresponding to a ratio of 1:5.4 (UiO-66:UiO-66(NH_2)). This is consistent with the four-fold faster release rate from the parent compared to the amine structure [21].

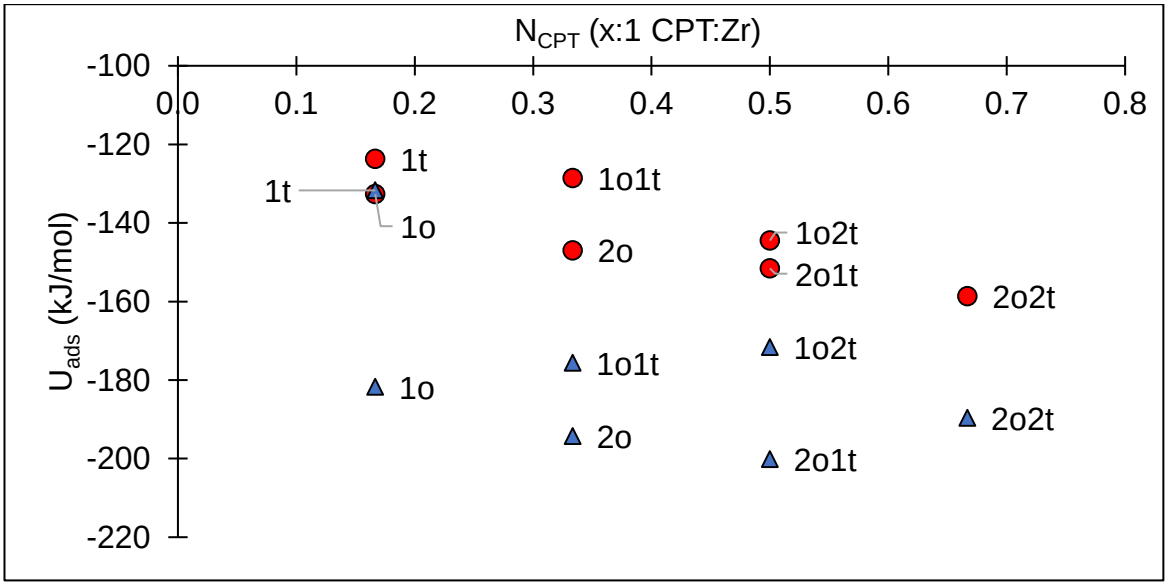

Figure 9. Total (bonded + non-bonded), average adsorption energy for cisplatin in UiO-66 (●) and UiO-66(NH_2) (▲). XoYt refers to X cisplatin molecules in the single o-pore and Y molecules per two t-pores (note that each unit cell consists of one o-pore and two t-pores).

Using *ab-initio* simulations, we can carefully place a single cisplatin molecule in the adsorption site of interest thus determining the energy difference associated with the o-pores and t-pores, whereas in the GCMC simulations these energies are influenced by the presence of other CPT molecules in the same or adjacent pores. The adsorption energies from GCMC

simulations (Figure 8) and *ab-initio* optimisations (Figure 9) are not directly comparable as the latter allows the framework to relax around cisplatin molecules revealing more favourable adsorption sites. On the other hand, Equation 2 can be used to directly compare the adsorption energies calculated from *ab-initio* optimisations and forcefield-based MD simulations in a non-solvated system but fully flexible system. There is a 40 % difference between the calculated energies (shown in Table 1), yet both levels of theory show the same trend: stronger adsorption energies in UiO-66(NH_2) compared to UiO-66. *Ab-initio* optimisations are a higher level of theory, however they are expensive and hence not suitable to model solvated frameworks (at the equilibrium loading ~ 6.3 SOL:Zr would be needed). Furthermore, they are run at 0 K and do not account for the temperature of the system. Therefore, when screening large numbers of MOFs as drug delivery carriers, classical simulations are the more effective tool.

Table 1. Cisplatin adsorption energies in UiO-66 and UiO-66(NH_2) from classical MD simulations (T=298 K) and *ab-initio* geometry optimisations (T=0 K). Calculated at loadings of N_{CPT} = 0.2:1 CPT:Zr, N_{SOL} = 0:1 SOL:Zr.

System	U_{ads} (kJ/mol)		
	ab-initio	MD	% difference
UiO-66	-133	-90	39
UiO-66(NH_2)	-182	-126	36

So far, analysis of the interaction energies has clearly shown that $U_{CPT\text{-}MOF}$ is more favourable in UiO-66(NH_2) compared to UiO-66. But how does this influence the release rate of cisplatin? MD simulations were used to calculate the intrapore diffusivity of cisplatin in UiO-66 and UiO-66(NH_2) at different water loadings and at a constant cisplatin loading of one CPT molecule per o-pore (which corresponds to the loading predicted by alchemical simulations discussed previously). As shown in Figure 10, water molecules significantly influence the diffusivity of cisplatin and the intrapore diffusivity decreases as the water loading increases in both MOFs, because water limits the motion of cisplatin in the confined pore space. For a given water loading, cisplatin movement is lower in UiO-66(NH_2) compared to UiO-66. Note that as shown in Figure 7, the optimal water loading for a given cisplatin uptake is approximately the same in both frameworks due to their similar free volumes (UiO-66=0.46 cm^3/g and UiO-66(NH_2)=0.42 cm^3/g). If this was not the case, it would not be fair to compare diffusivities based on a constant water loading because of confinement effects in smaller pores. Instead, the diffusivities should be compared at the

optimal water loading in each framework. The restricted movement of cisplatin in UiO-66(NH_2) is due to the stronger cisplatin/framework interaction energies and a series of cisplatin – water – BDC(NH_2) hydrogen bonds that anchor it in position. This anchoring to amine groups provides a further reason for the slower cisplatin release from UiO-66(NH_2) [21].

(a)

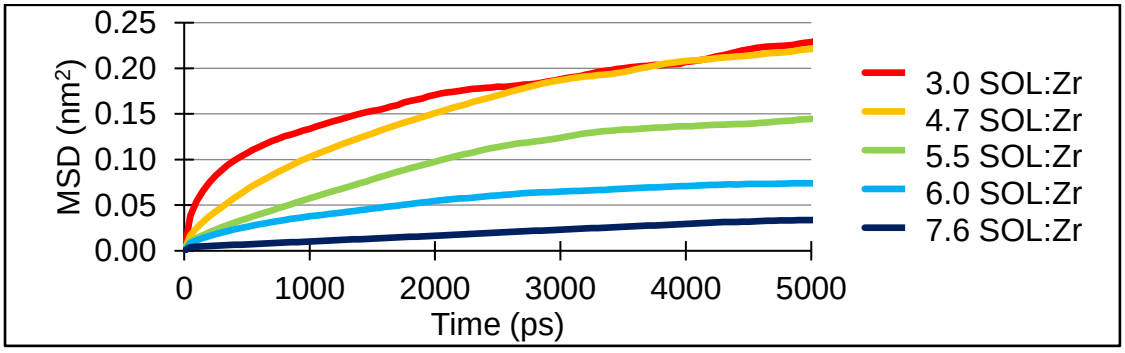

(b)

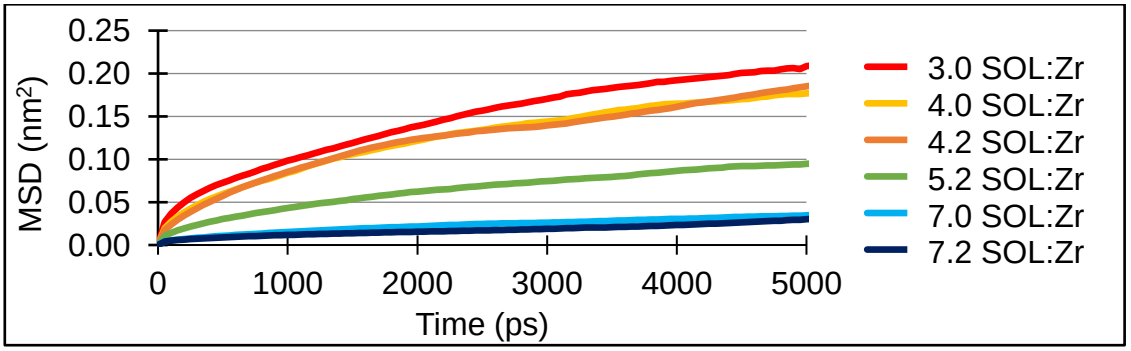

(c)

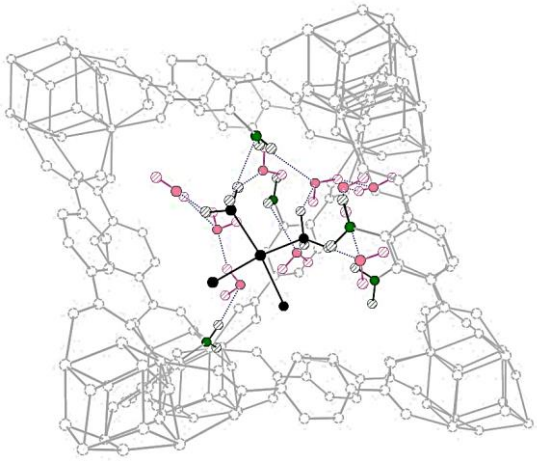

Figure 10. MSD for cisplatin (1 CPT / o-pore) at different water loadings in (a) UiO-66 and (b) UiO-66(NH_2). Individual repeats are shown in the SI, Section 5. (c) Snapshot of cisplatin (black) anchoring in UiO-66(NH_2) (grey) via hydrogen bonding (dotted lines) between water molecules (pink) and NH_2 (green) functionalised BDC ligands. Heavy atoms are filled, hydrogens are dashed.

The previous techniques used (GCMC, *ab-initio* optimisations, MD simulations) can capture the variation of behaviour in the different pores, but they cannot provide information regarding energy barriers during interpore movement. Although MD simulations can be used to determine intrapore diffusion rates, pore-hopping is a rare event due to the unfavourable energies when cisplatin is passing through the narrow pore windows. Instead, the interpore movement of cisplatin was quantified by calculating the total potential energy barrier (= non-bonded + bonded) associated with its movement through the triangular pore windows of UiO-66 and UiO-66(NH_2) using steered MD (SMD) simulations. The total potential energy barrier was calculated as the difference between the least favourable and average energies over the course of the trajectories.

Of course, the energy barriers obtained from classical SMD simulations heavily depend on the forcefield. *Ab-initio* SMD could be used instead, yet this would be computationally prohibitively expensive especially for cisplatin in the presence of water molecules. Instead, classical SMD energy barriers were compared to those calculated using *ab-initio* static energy calculations on structures within their "flexibility window" (i.e. the limit to which the unit cell parameters can be varied without compromising the local geometry) generated using the software GASP which allows us to identify the intrinsic flexibility of UiO-66 and UiO-66(NH_2) [55]. Not only does this provide a relatively computationally cheap sanity check for our forcefield generated energy barriers, but it also allows us to determine without breaking bonds in our framework or imposing large artificial forces (as in SMD) how far the pore windows can open and whether they can open far enough for cisplatin diffusion. We carried out *ab-initio* static energy calculations on the GASP structures to determine the relative potential energy of each structure compared to the lowest energy variant. As there are no cisplatin molecules present in the GASP structures, we considered this energy difference to be the bonded contribution to the pore-hopping energy barrier. PoreBlazer [56] was used to determine the pore-limiting diameter of the frameworks from the SMD simulations (at the time of pore-hopping), and for each GASP variant.

Figure 11 shows the total potential energy barrier as a function of the pore limiting diameter in the highest energy SMD configuration and the bonded potential energy difference to achieve each GASP variant. Firstly, the pore-limiting diameter calculated from SMD simulations at the time of pore-hopping is within the bounds set by the flexibility window (i.e. GASP simulations show that the window size can be further expanded whilst maintaining the local geometry). Secondly, SMD simulations show that the overall change

in potential energy is dominated by bonded interactions within the framework, and since the total SMD barrier agrees with the GASP / *ab-initio* energy differences, both methods can be used to obtain the bonded contribution to the intercell energy barrier.

Based on Figure 11, the bonded potential energy barrier is higher in UiO-66 because electrostatic repulsion between amine groups and the carboxyl groups aids ligand rotation in UiO-66(NH_2). This is in line with the trend observed by Pakhira *et al.* who argued that the energy barrier to rotate polar ligands is lower due to electrostatic repulsion [64]. Experimentally, release rates from UiO-66 are faster than from UiO-66(NH_2), suggesting that the bonded barriers are not the primary reason for the differences seen between the release rate of cisplatin in the two frameworks. However, by comparing the pore-limiting diameter at the time of pore-hopping to the maximum diameter determined within the flexibility window, these simulations can inform us whether (or not) structural deformation (i.e. compromising the local geometry) is required for interpore movement of cisplatin.

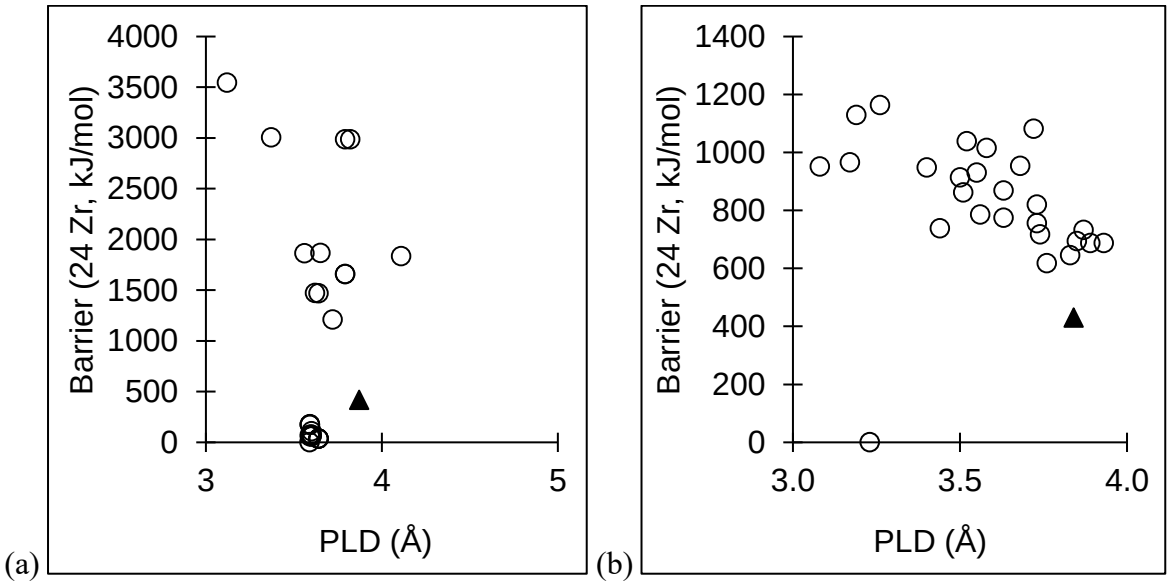

Figure 11. Bonded potential energy barrier of the frameworks as a function of the pore-limiting diameter (PLD). Shown for the GASP structures generated within the flexibility window (○) and an average across seven repeated SMD simulations (▲– error bars showing standard deviation are within the symbol size). (a) UiO-66 and (b) UiO-66(NH_2).

A more meaningful approach to compare release rates is by looking at the change in CPT-MOF non-bonded interaction energies during pore-hopping as determined by the SMD simulations. As with the total potential energy barrier (= non-bonded + bonded), the CPT-MOF non-bonded barriers were calculated as the difference between the least favourable CPT-MOF energy and the average CPT-MOF energy over the course of the simulation. For

UiO-66 and UiO-66(NH_2), the average non-bonded barriers (and standard deviations across seven repeat simulations) are 34(±6) kJ/mol and 48(±4) kJ/mol respectively. Stronger interaction energies between the polar arms of cisplatin and the amine groups in UiO-66(NH_2) result in higher non-bonded CPT-MOF energy barriers compared to the parent structure. Unlike the bonded contribution to the total energy barrier, this is in agreement with the higher release rates from UiO-66 [21]. This again emphasises the importance of including water molecules in the simulation as they provide the energy to open pore windows in the MOF to the extent needed for pore-hopping. In this case, the CPT-MOF interaction energies are more important than the bonded contribution to the pore-hop energy barrier and hence the release rate.

As opposed to the potential energy barrier discussed so far, the total Helmholtz free energy barrier ($\Delta A_{porehop}$) takes into consideration entropic contributions to the pore-hop energy barrier. To compare the pore-hop free energy barrier to the driving force to displace cisplatin from the framework back into solution ($\Delta G_{CPT\text{-}removal}$ calculated using alchemical simulations, Figure 6), umbrella sampling pull simulations were used. Figure 12 shows the potential mean force (PMF) for cisplatin movement through UiO-66 and UiO-66(NH_2) after 1 ns of simulation time. Peaks in the PMF are indicative of unfavourable MOF – CPT energies as cisplatin passes through the narrow pore windows. Troughs designate more favourable energies as cisplatin passes through the o-pores and t-pores, as labelled on Figure 12. The pore-hop energy barrier is the change in energy as cisplatin moves from a pore (trough) through an adjacent window (peak).

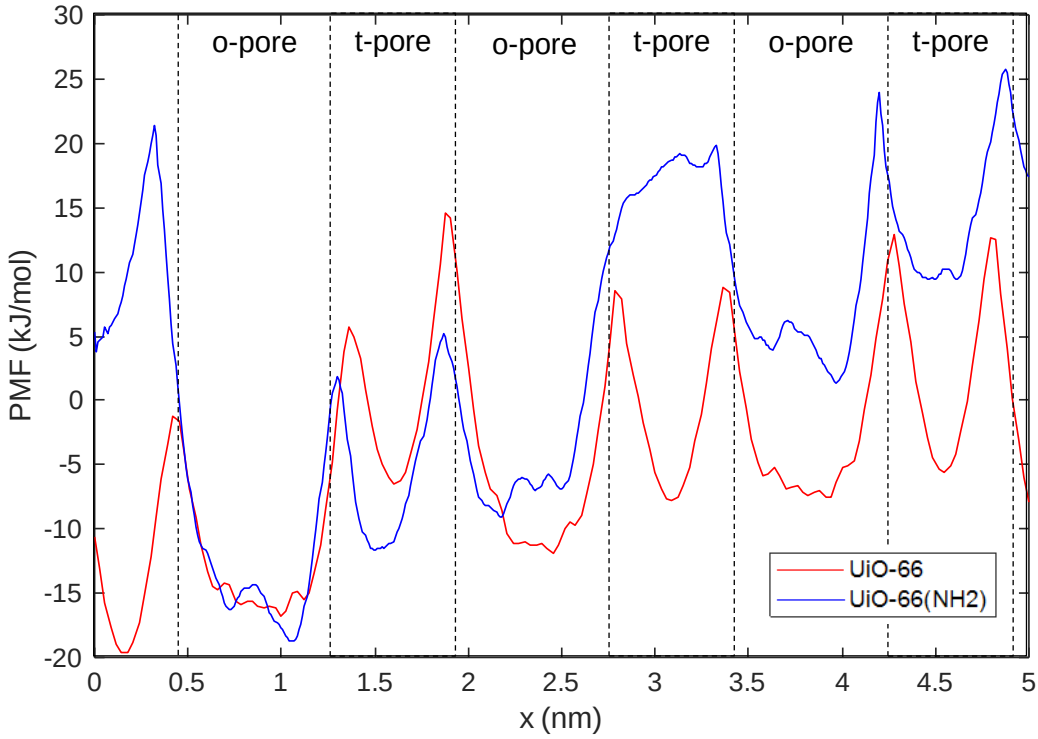

Figure 12. PMF for a cisplatin molecule moving through empty UiO-66 and UiO-66(NH_2) structures.

During the pull simulations used to generate configurations for the umbrella sampling in Figure 12, pore-hopping induces structural deformations in the framework, resulting in increasingly less favourable energies with more pore-hops. Clearly, the pore-hopping phenomena is energetically unfavourable (as expected from the previous discussion). After moving from the o-pore to the t-pore, there are significant deformations in the framework, and so if the system equilibrates cisplatin moves out of the deformed t-pore into an o-pore within the same sampling window. This results in an unphysical pathway through the framework which cannot be analysed as a PMF (see the SI, Section 6 for detail). Therefore, a shorter simulation time was used to analyse the PMF.

While after 1 ns of simulation time cisplatin has not equilibrated in the adsorption sites (within the o-pores and t-pores) and therefore the energy difference between adsorption sites cannot be directly compared to equilibration simulations such as GCMC and geometry optimisations, the simulation path remains sensible and therefore, we can estimate pore-hopping energy barriers from the PMF.

As shown in Figure 2, in UiO-66(NH_2) some but not all of the pore windows are narrowed by the presence of amine groups. Considering the larger windows in the amine structure, the

pore-hop energy barrier is approximately 10 – 20 kJ/mol in both UiO-66 and UiO-66(NH_2). If cisplatin attempts to move through the smaller window in UiO-66(NH_2), the energy barrier is significantly higher (~ 30 kJ/mol). These values compare well to the π-flip energy barrier of empty UiO-66 calculated using nuclear magnetic resonance experiments reported by Kolokolov et al (~30 kJ/mol per BDC [65]). The larger energy barrier in the amine structure indicates reduced movement through UiO-66(NH_2) compared to UiO-66.

At an energy barrier of $\Delta A_{porehop}$ = 20 kJ/mol, cisplatin is highly unlikely to pass through one of the triangular pore windows (P = 0.04 %) and so cisplatin cannot pass through an otherwise empty framework. As seen experimentally [21], at sufficient water loading there is enough of a driving force to overcome the pore-hopping energy barrier in both MOFs. Therefore, water must provide the activation energy for the MOF windows to open wide enough and based on the alchemical simulations, enough activation energy ($\Delta G_{CPT\text{-}removal}$ > 20 kJ/mol) is provided to push cisplatin through the framework at a loading > 5.21:1 SOL:Zr.

CONCLUSION

A variety of computational methods have been assessed for their suitability to model cisplatin uptake and release in biocompatible MOFs, UiO-66 and UiO-66(NH_2). All simulations make use of standardised methods, and the methods that we recommend should be applicable to predict the uptake and release properties of other MOF - drug delivery systems.

Pure-component GCMC simulations (often used in computational screening papers) can provide the maximum theoretical loading of cisplatin as well as the adsorption energies at the maximum loading. However, such information can be misleading because they do not account for the presence of water. In contrast, BAR simulations with water show that there is a net driving force to displace cisplatin from the smaller pores within the frameworks (otherwise shown during GCMC simulations to be a favourable adsorption site), indicating the importance of the solvation shell when predicting the experimental loading. The impact of water is often overlooked in computational drug screening papers; however, where highly polar guest molecules are being adsorbed from solution, it plays an integral role in the uptake.

Insight into cisplatin release rates were gained from the variation in intrapore and interpore energies. Pure component GCMC and *ab-initio* simulations show stronger CPT-MOF interaction energies and a higher o-pore to t-pore energy difference in UiO-66(NH_2) compared to UiO-66, both of which are indicative of a slower release rate. However, they provide limited information on how these interaction energies are influenced by water, nor to what extent they will influence the release rate as they sample energies at the minima / equilibrium and provide no concept of time dependent movement. MD simulations highlight the decrease in intrapore diffusion with increased water loading, and that (in agreement with experimental results) at the optimal water loading cisplatin diffusivity is higher in UiO-66 compared to UiO-66(NH_2). The interpore diffusivity cannot be quantified using equilibrium techniques such as unbiased MD because pore-hopping is a rare event, however the pore-hop energy barrier determined using steered MD/GASP or umbrella sampling simulations indicates whether diffusion through the system is possible without structural deformations. By comparison of the energy barrier and driving force to displace cisplatin, it can also be inferred that cisplatin will not be released from either framework until a threshold water loading is achieved.

ASSOCIATED CONTENT

Details of the partial atomic charges, *ab-initio* simulation details, cisplatin size approximations, additional BAR simulation results at higher cisplatin loadings, MSD repeats and time-dependent free energy landscapes can be found in the Supporting Information.

ACKNOWLEDGEMENTS

This work was supported by funding from the European Research Council (ERC) under the European Union's Horizon 2020 research and innovation programme (grant agreement No 648283 "GROWMOF"). It made use of the Balena High Performance Computing (HPC) Service at the University of Bath.

ABBREVIATIONS

MOF, Metal-organic framework; CPT, cisplatin; UiO, Universitetet i Oslo; SOL, solvent

REFERENCES

1. Kelland, L., *The resurgence of platinum-based cancer chemotherapy.* Nature Reviews Cancer, 2007. **7**(8): p. 573-584.
2. Astolfi, L., et al., *Correlation of adverse effects of cisplatin administration in patients affected by solid tumours: a retrospective evaluation.* Oncology reports, 2013. **29**(4): p. 1285-1292.
3. Dasari, S. and P.B. Tchounwou, *Cisplatin in cancer therapy: molecular mechanisms of action.* European journal of pharmacology, 2014. **740**: p. 364-378.
4. Fulda, S., L. Galluzzi, and G. Kroemer, *Targeting mitochondria for cancer therapy.* Nature Reviews Drug Discovery, 2010. **9**(6): p. 447-464.
5. Kalyanaraman, B., *Teaching the basics of cancer metabolism: Developing antitumor strategies by exploiting the differences between normal and cancer cell metabolism.* Redox Biology, 2017. **12**: p. 833-842.
6. *The selection and use of essential medicines.* World Health Organisation Technical Report Series, 2008(950): p. backcover, vii-174.
7. Pérez-Herrero, E. and A. Fernández-Medarde, *Advanced targeted therapies in cancer: Drug nanocarriers, the future of chemotherapy.* European Journal of Pharmaceutics and Biopharmaceutics, 2015. **93**: p. 52-79.
8. Di, H., et al., *Doxorubicin- and cisplatin-loaded nanostructured lipid carriers for breast cancer combination chemotherapy.* Drug Development and Industrial Pharmacy, 2016. **42**(12): p. 2038-2043.
9. Zhuang, W., et al., *A fully absorbable biomimetic polymeric micelle loaded with cisplatin as drug carrier for cancer therapy.* Regenerative Biomaterials, 2017. **5**(1): p. 1-8.
10. Catanzaro, D., et al., *Cisplatin liposome and 6-amino nicotinamide combination to overcome drug resistance in ovarian cancer cells.* Oncotarget, 2018. **9**(24): p. 16847-16860.
11. Lai, Y., et al., *An effective peptide cargo carrier for the delivery of cisplatin in ovarian cancer cells.* Dyes and Pigments, 2017. **143**: p. 342-347.
12. Park, S.S., et al., *Functionalised mesoporous silica nanoparticles with excellent cytotoxicity against various cancer cells for pH-responsive and controlled drug delivery.* Materials & Design, 2019. **184**: p. 108187.
13. Rosli, N.F., et al., *Graphene Oxide Nanoplatelets Potentiate Anticancer Effect of Cisplatin in Human Lung Cancer Cells.* Langmuir, 2019. **35**(8): p. 3176-3182.

14. Sheikh Tanzina, H. and C. Ezharul Hoque, *Recent Progress in Delivery of Therapeutic and Imaging Agents Utilizing Organic-Inorganic Hybrid Nanoparticles.* Current Drug Delivery, 2018. **15**(4): p. 485-496.
15. Ploskonka, A.M. and J.B. DeCoste, *Tailoring the Adsorption and Reaction Chemistry of the Metal–Organic Frameworks UiO-66, UiO-66-NH2, and HKUST-1 via the Incorporation of Molecular Guests.* ACS Applied Materials & Interfaces, 2017. **9**(25): p. 21579-21585.
16. Miura, H., et al., *Tuning the gate-opening pressure and particle size distribution of the switchable metal–organic framework DUT-8(Ni) by controlled nucleation in a micromixer.* Dalton Transactions, 2017. **46**(40): p. 14002-14011.
17. Deng, H., et al., *Large-Pore Apertures in a Series of Metal-Organic Frameworks.* Science, 2012. **336**(6084): p. 1018-1023.
18. Wannapaiboon, S., et al., *Control of structural flexibility of layered-pillared metal-organic frameworks anchored at surfaces.* Nature Communications, 2019. **10**(1): p. 346.
19. He, C., et al., *Nanoscale Metal–Organic Frameworks for the Co-Delivery of Cisplatin and Pooled siRNAs to Enhance Therapeutic Efficacy in Drug-Resistant Ovarian Cancer Cells.* Journal of the American Chemical Society, 2014. **136**(14): p. 5181-5184.
20. Chen, W.-H., et al., *Stimuli-Responsive Nucleic Acid-Based Polyacrylamide Hydrogel-Coated Metal–Organic Framework Nanoparticles for Controlled Drug Release.* Advanced Functional Materials, 2018. **28**(8): p. 1705137.
21. Mocniak, K.A., et al., *Incorporation of cisplatin into the metal–organic frameworks UiO66-NH2 and UiO66 – encapsulation vs. conjugation.* Royal Society Chemistry Advances, 2015. **5**(102): p. 83648-83656.
22. Sun, H., et al., *Warburg Effects in Cancer and Normal Proliferating Cells: Two Tales of the Same Name.* Genomics, Proteomics & Bioinformatics, 2019. **17**(3): p. 273-286.
23. Howarth, A.J., et al., *Chemical, thermal and mechanical stabilities of metal–organic frameworks.* Nature Reviews Materials, 2016. **1**(3): p. 15018.
24. Kotzabasaki, M. and G.E. Froudakis, *Review of computer simulations on anti-cancer drug delivery in MOFs.* Inorganic Chemistry Frontiers, 2018. **5**(6): p. 1255-1272.
25. Filippousi, M., et al., *Biocompatible Zr-based nanoscale MOFs coated with modified poly(ε-caprolactone) as anticancer drug carriers.* International Journal of Pharmaceutics, 2016. **509**(1): p. 208-218.

26. Liu, J.-Q., et al., *A combined experimental and computational study of novel nanocage-based metal–organic frameworks for drug delivery.* Dalton Transactions, 2015. **44**(44): p. 19370-19382.
27. Wang, J., et al., *Combined experimental and theoretical insight into the drug delivery of nanoporous metal–organic frameworks.* Royal Society of Chemistry Advances, 2015. **5**(104): p. 85606-85612.
28. Li, F., et al., *Encapsulation of pharmaceutical ingredient linker in metal–organic framework: combined experimental and theoretical insight into the drug delivery.* Royal Society Chemistry Advances, 2016. **6**(53): p. 47959-47965.
29. Lin, S.-X., et al., *Effective loading of cisplatin into a nanoscale UiO-66 metal–organic framework with preformed defects.* Dalton Transactions, 2019. **48**(16): p. 5308-5314.
30. Zhu, X., et al., *Inherent anchorages in UiO-66 nanoparticles for efficient capture of alendronate and its mediated release.* Chemical Communications, 2014. **50**(63): p. 8779-8782.
31. Macrae, C., et al., *Mercury 4.0: from visualization to analysis, design and prediction.* Journal of Applied Crystallography, 2020. **53**: p. 226-235.
32. Trickett, C.A., et al., *Definitive Molecular Level Characterization of Defects in UiO-66 Crystals.* Angewandte Chemie International Edition, 2015. **54**(38): p. 11162-11167.
33. Rappe, A.K., et al., *UFF, a full periodic table force field for molecular mechanics and molecular dynamics simulations.* Journal of the American Chemical Society, 1992. **114**(25): p. 10024-10035.
34. Yesylevskyy, S., et al., *Empirical force field for cisplatin based on quantumdynamics data: case study of new parameterization scheme for coordinationcompounds.* Journal of Molecular Modeling, 2015. **21**(10): p. 268.
35. Jorgensen, W.L., et al., *Comparison of simple potential functions for simulating liquid water.* The Journal of Chemical Physics, 1983. **79**(2): p. 926-935.
36. Gupta, A., et al., *Object-oriented Programming Paradigms for Molecular Modeling.* Molecular Simulation, 2003. **29**(1): p. 29-46.
37. Wells, B.A. and A.L. Chaffee, *Ewald Summation for Molecular Simulations.* Journal of Chemical Theory and Computation, 2015. **11**(8): p. 3684-3695.
38. Wolf, D., et al., *Exact method for the simulation of Coulombic systems by spherically truncated, pairwise r−1 summation.* The Journal of Chemical Physics, 1999. **110**(17): p. 8254-8282.

39. Berendsen, H.J.C., D. van der Spoel, and R. van Drunen, *GROMACS: A message-passing parallel molecular dynamics implementation.* Computer Physics Communications, 1995. **91**(1): p. 43-56.
40. Bekker, H., et al., *Gromacs - a Parallel Computer for Molecular-Dynamics Simulations.* Physics Computing '92, 1993: p. 252-256.
41. Lindahl, E., B. Hess, and D. van der Spoel, *GROMACS 3.0: a package for molecular simulation and trajectory analysis.* Molecular modeling annual, 2001. **7**(8): p. 306-317.
42. Van Der Spoel, D., et al., *GROMACS: Fast, flexible, and free.* Journal of Computational Chemistry, 2005. **26**(16): p. 1701-1718.
43. Hess, B., et al., *GROMACS 4: Algorithms for Highly Efficient, Load-Balanced, and Scalable Molecular Simulation.* Journal of Chemical Theory and Computation, 2008. **4**(3): p. 435-447.
44. Pronk, S., et al., *GROMACS 4.5: a high-throughput and highly parallel open source molecular simulation toolkit.* Bioinformatics, 2013. **29**(7): p. 845-54.
45. Garberoglio, G., *OBGMX: A web-based generator of GROMACS topologies for molecular and periodic systems using the universal force field.* Journal of Computational Chemistry, 2012. **33**(27): p. 2204-2208.
46. Darden, T., D. York, and L. Pedersen, *Particle mesh Ewald: An N·log(N) method for Ewald sums in large systems.* The Journal of Chemical Physics, 1993. **98**(12): p. 10089-10092.
47. Essmann, U., et al., *A smooth particle mesh Ewald method.* The Journal of Chemical Physics, 1995. **103**(19): p. 8577-8593.
48. Bussi, G., D. Donadio, and M. Parrinello, *Canonical sampling through velocity rescaling.* The Journal of Chemical Physics, 2007. **126**(1): p. 014101.
49. Nosé, S., *A unified formulation of the constant temperature molecular dynamics methods.* The Journal of Chemical Physics, 1984. **81**(1): p. 511-519.
50. Hoover, W.G., *Canonical dynamics: Equilibrium phase-space distributions.* Physical Review A, 1985. **31**(3): p. 1695-1697.
51. Bennett, C.H., *Efficient estimation of free energy differences from Monte Carlo data.* Journal of Computational Physics, 1976. **22**(2): p. 245-268.
52. Shirts, M.R., et al., *Extremely precise free energy calculations of amino acid side chain analogs: Comparison of common molecular mechanics force fields for proteins.* The Journal of Chemical Physics, 2003. **119**(11): p. 5740-5761.

53. Torrie, G.M. and J.P. Valleau, *Nonphysical sampling distributions in Monte Carlo free-energy estimation: Umbrella sampling.* Journal of Computational Physics, 1977. **23**(2): p. 187-199.
54. Kumar, S., et al., *THE weighted histogram analysis method for free-energy calculations on biomolecules. I. The method.* Journal of Computational Chemistry, 1992. **13**(8): p. 1011-1021.
55. Wells, S.A. and A. Sartbaeva, *GASP: software for geometric simulations of flexibility in polyhedral and molecular framework structures.* Molecular Simulation, 2015. **41**(16-17): p. 1409-1421.
56. Sarkisov, L. and A. Harrison, *Computational structure characterisation tools in application to ordered and disordered porous materials.* Molecular Simulation, 2011. **37**(15): p. 1248-1257.
57. Zhang, W., et al., *Cooperative effect of temperature and linker functionality on CO2 capture from industrial gas mixtures in metal–organic frameworks: a combined experimental and molecular simulation study.* Physical Chemistry Chemical Physics, 2012. **14**(7): p. 2317-2325.
58. Cavka, J.H., et al., *A New Zirconium Inorganic Building Brick Forming Metal Organic Frameworks with Exceptional Stability.* Journal of the American Chemical Society, 2008. **130**(42): p. 13850-13851.
59. Wiersum, A.D., et al., *An evaluation of UiO-66 for gas-based applications.* Chemistry – An Asian Journal, 2011. **6**(12): p. 3270-80.
60. Schoenecker, P.M., et al., *Effect of Water Adsorption on Retention of Structure and Surface Area of Metal–Organic Frameworks.* Industrial & Engineering Chemistry Research, 2012. **51**(18): p. 6513-6519.
61. Furukawa, H., et al., *Water Adsorption in Porous Metal–Organic Frameworks and Related Materials.* Journal of the American Chemical Society, 2014. **136**(11): p. 4369-4381.
62. Ghosh, P., Y.J. Colón, and R.Q. Snurr, *Water adsorption in UiO-66: the importance of defects.* Chemical Communications, 2014. **50**(77): p. 11329-11331.
63. Canivet, J., et al., *Water adsorption in MOFs: fundamentals and applications.* Chemical Society Reviews, 2014. **43**(16): p. 5594-5617.
64. Pakhira, S., *Rotational dynamics of the organic bridging linkers in metal–organic frameworks and their substituent effects on the rotational energy barrier.* Royal Society of Chemistry Advances, 2019. **9**(65): p. 38137-38147.

65. Kolokolov, D.I., et al., *Probing the Dynamics of the Porous Zr Terephthalate UiO-66 Framework Using 2H NMR and Neutron Scattering.* The Journal of Physical Chemistry C, 2012. **116**(22): p. 12131-12136.

TOC GRAPHIC

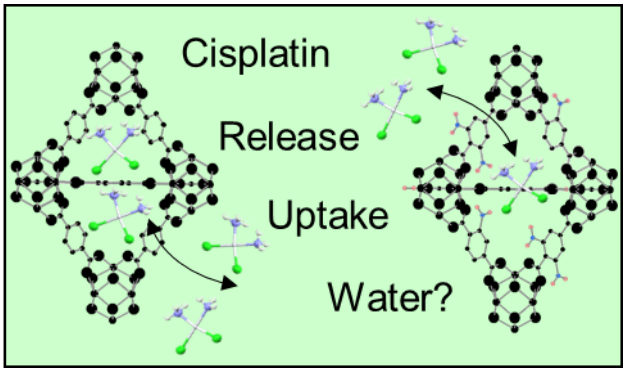

Molecular simulations of cisplatin uptake and release in UiO-66 and UiO-66(NH_2)

Supporting Information

Megan J. Thompson, Stephen A. Wells, Tina Düren[*]

AUTHOR ADDRESS Prof. T. Düren, Centre for Advanced Separations Engineering, Department of Chemical Engineering, University of Bath, BA2 7AY, UK
E-mail: t.duren@bath.ac.uk

Section 1. Partial atomic charges

Labels were used to classify framework atoms into different groups based on their chemical surroundings (Figure S1). The partial atomic charges used in the classical simulations were the group averages shown in Table S1:

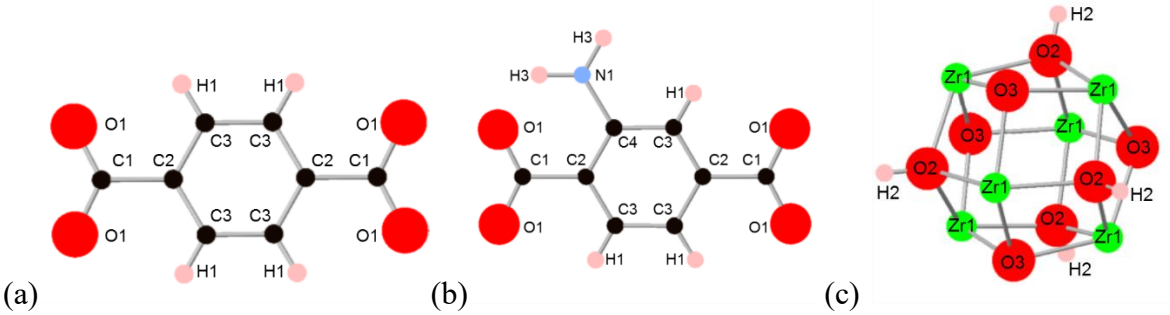

Figure S1. Groups used to average the partial atomic charges in (a) BDC, (b) BDC(NH_2), and (c) $Zr_6O_4(OH)_4$

Table S1. Partial atomic charges used in the classical simulations

Atom Type	MOF	
	UiO-66	UiO-66(NH_2)
C1	0.253	0.250
C2	-0.013	-0.020
C3	-0.104	-0.105
C4	-	0.077
H1	0.145	0.133
H2	0.396	0.399

Atom Type	MOF	
	UiO-66	UiO-66(NH_2)
H3	-	0.132
N1	-	-0.222
O1	-0.288	-0.293
O2	-0.580	-0.581
O3	-0.543	-0.538
Zr1	0.990	0.986

The purpose of this paper was to compare and validate the methods used to screen metal-organic frameworks for cisplatin uptake and release. For screening purposes, it is important to reduce the computational cost, and therefore the partial atomic charges were obtained from static energy calculations on the initial (non-optimised) primitive unit cells.

Charges in the framework will be influenced by subtle changes in the atomic arrangement. Furthermore, cisplatin itself has highly electronegative groups, and therefore its position inside the framework could influence the charge distribution. To determine if these issues will influence the classical simulations that make use of the partial atomic charges, *ab-initio* optimisations were carried out on UiO-66 and UiO-66(NH_2) at different cisplatin loadings.

a)

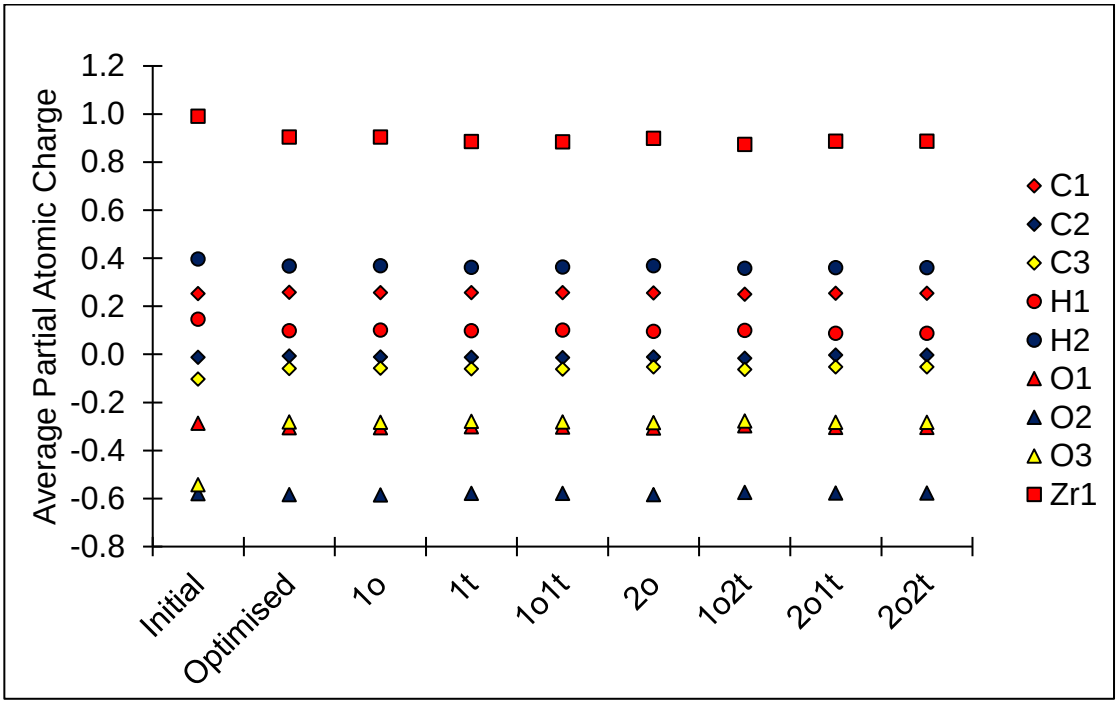

b)

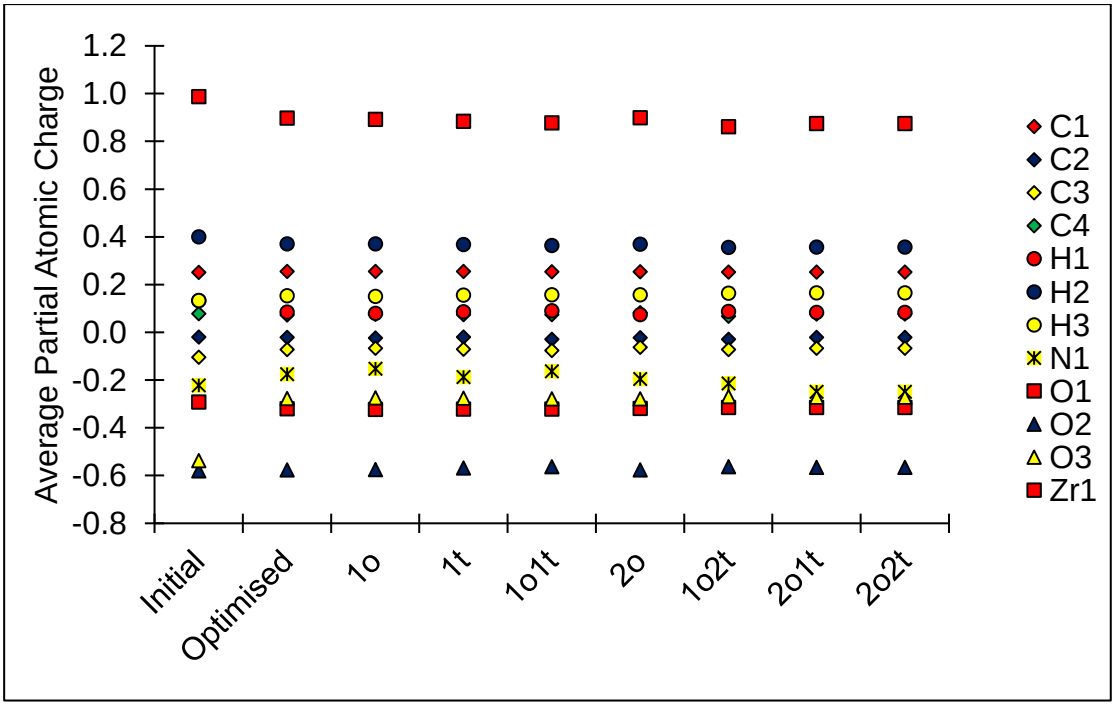

Figure S2. Comparison of partial atomic charges in (a) UiO-66 and (b) UiO-66(NH_2) calculated using different methods and conformations of cisplatin: Initial=static energy of empty structure, optimised=minimisation of empty structure, XoYt = X cisplatin/1 o-pore, Y cisplatin/2 t-pores.

Overall there are no significant changes in the partial atomic charges calculated for the optimised structures with different loadings of cisplatin. When comparing the static energy and minimised charges of the empty structures, there are insignificant differences for all atoms except for O3 for which the charges are -0.5 compared to -0.3 in the initial and final

structures respectively. Though Coulombic interactions between O3 and cisplatin will be influenced by this discrepancy, the charge is the same sign as in the optimised structure and the overall charge of the zirconium nodes are the same (3.04 and 3.03 in the optimised and initial structures respectively). Therefore, it is highly unlikely that this will significantly influence the classical simulation results.

Section 2. *Ab-initio* simulation details

The Quickstep module in CP2K [1-6] was used for both the static energy calculations and the geometry optimisations. Quickstep uses an efficient Gaussian and Planewave approach in which the electron density and wavefunctions are represented by planewaves and Gaussian orbitals respectively. Planewave cutoff and relative cutoff values of 500 Ry and 50 Ry were used respectively. Exchange correlation energies were approximated using the Perdew-Burke-Ernzerhof functional [7] with DFT-D3 dispersion corrections [8, 9]. Goedecker, Teter and Hutter (GTH) pseudopotentials were used to model core electrons [2]. Triple-zeta Gaussian type basis sets were used to describe all atoms with the exception of zirconium and platinum which were described using double-zeta functions [10]. As with the planewaves, core electrons were described by GTH pseudopotentials [11, 12]. A tolerance of 10^{-6} was used for the convergence of the wavefunction in both types of *ab-initio* simulation. For the optimization, convergence tolerances were set to 0.003 and 0.0015 Bohr for the maximum and root-mean-square of atomic displacements, and 0.0004 and 0.0003 Bohr/Ha for the maximum and root-mean-square of the atomic forces.

Section 3. Size of cisplatin

As a “back of the envelope” calculation, the cisplatin uptake in a pore of a given size can be determined based on its the collision diameter. As shown in Figure S3, this was approximated as 6 Å using the LJ sigma values presented by Yesylevskyy et al [13].

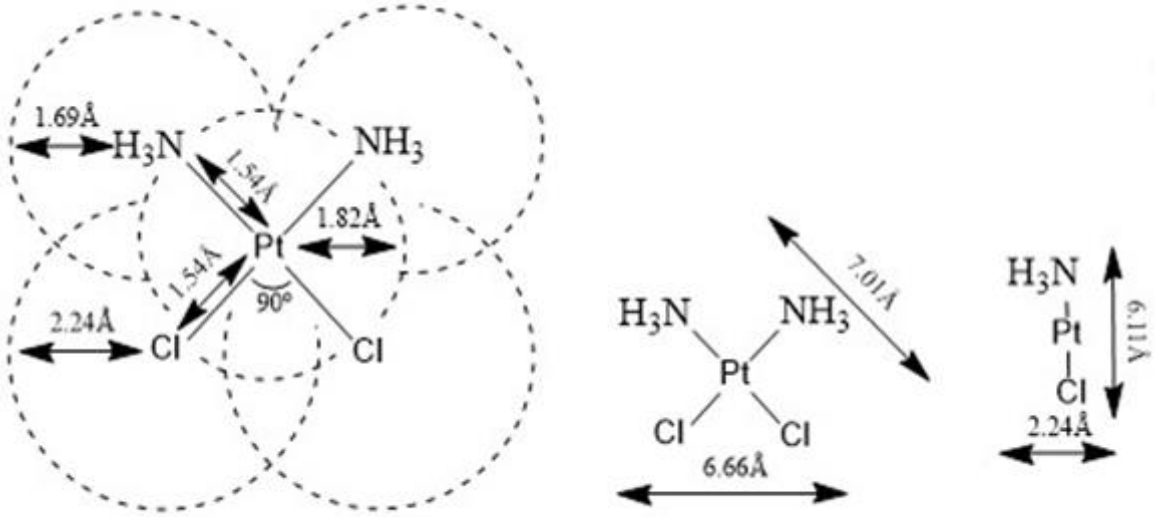

Figure S3. Approximation for cisplatin collision diameter using the LJ sigma values presented by Yesylevskyy et al [13].

Section 4. BAR simulations for various cisplatin loadings

During encapsulation, the co-adsorption of water (as well as diffusion limitations) will decrease cisplatin uptake. Alchemical simulations were used to predict the uptake whilst accounting for the influence of water. Figure S4 and Figure S5 show that the overall trends between solvation and the Gibbs free energy are the same as those described in the main text regardless of the cisplatin loading.

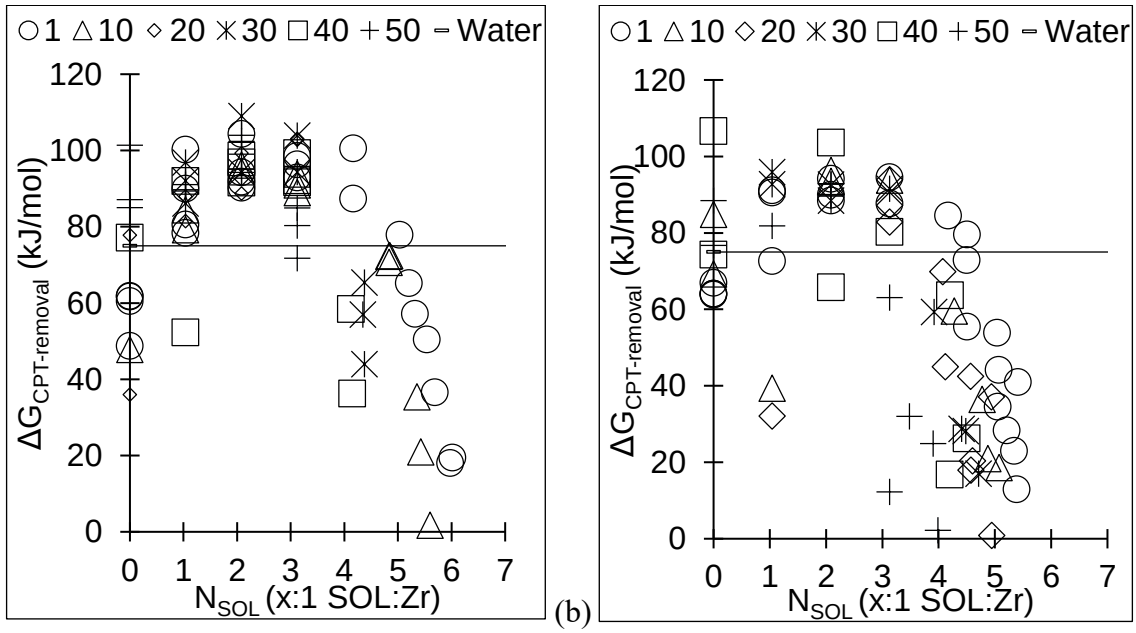

Figure S4. Gibbs free energy of decoupling one cisplatin molecule from an o-pore in (a) UiO-66 and (b) UiO-66(NH_2) at different loadings of water and cisplatin (T=298 K)

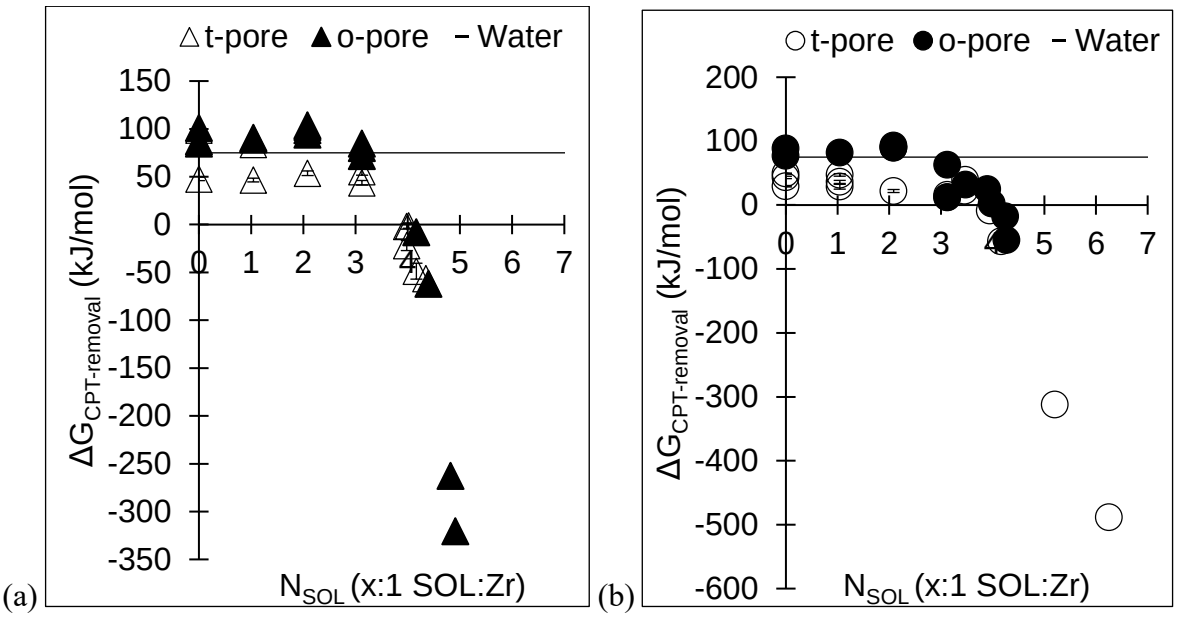

Figure S5. Gibbs free energy of decoupling one cisplatin molecule from solvated (a) UiO-66 and (b) UiO-66(NH_2) at various solvent loadings and a cisplatin loading of 0.26 CPT:Zr

Section 5. Individual repeats for cisplatin MSD at various water loadings

(a)

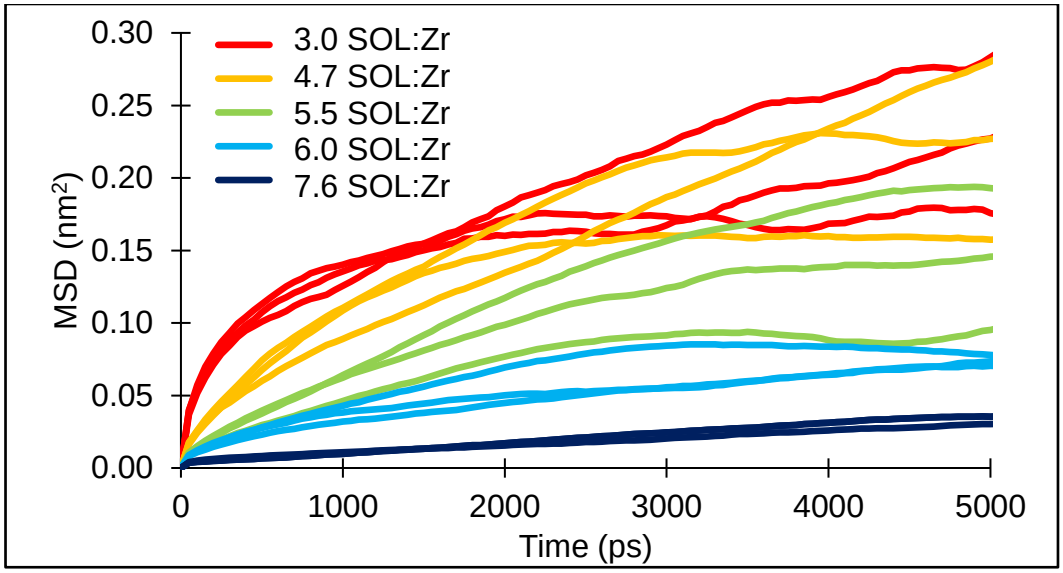

(b)

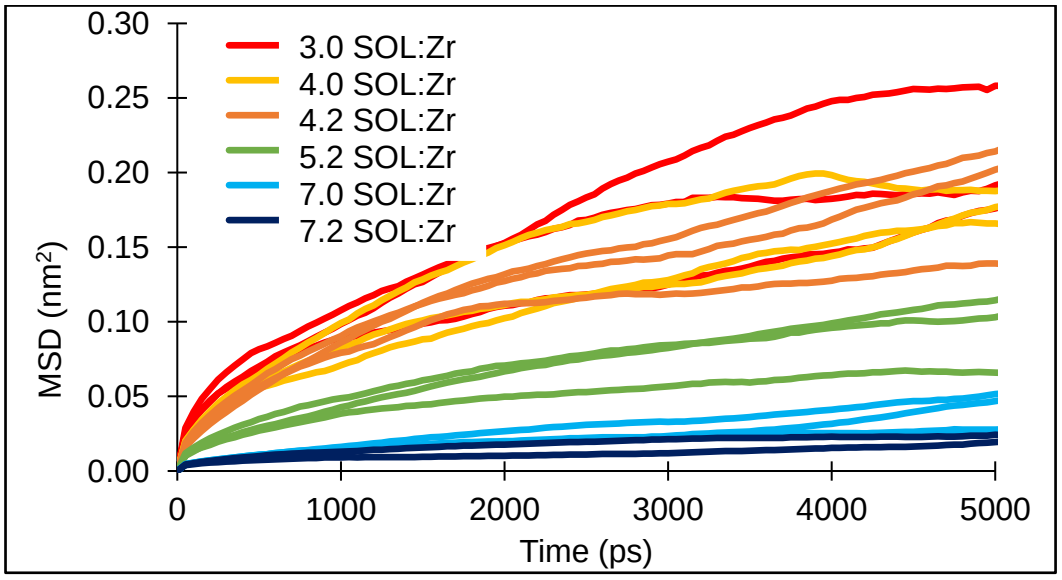

Figure S6. Mean square displacement for cisplatin at different water loadings in (a) UiO-66 and (b) UiO-66(NH_2). Different lines of the same colour represent independent repeats with the same water loading

Section 6. Time-dependent free energy profiles

Figure S7 shows time-dependent PMFs for cisplatin being dragged through UiO-66 and UiO-66(NH_2).

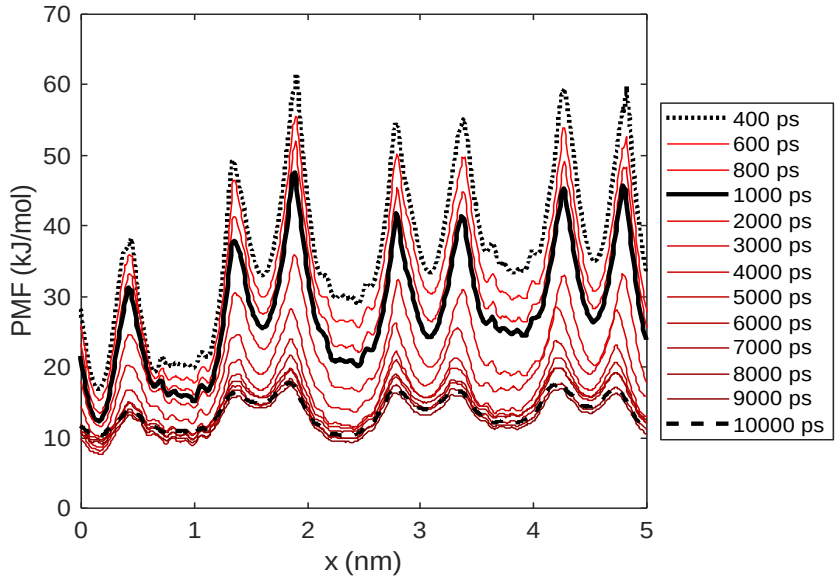

(a)

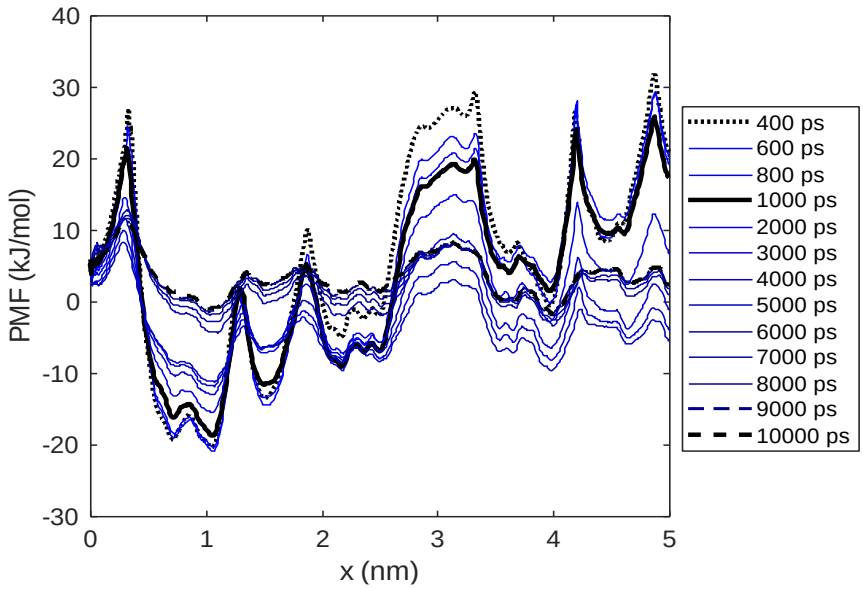

(b)

Figure S7. Simulation time dependent PMFs of cisplatin moving through (a) UiO-66 and (b) UiO-66(NH_2) at T=310 K.

Pull simulations were used to generate the configurations for umbrella sampling. During these simulations, the framework distorts due to the high energy associated with cisplatin movement through the pore windows. This means that after 1 ns of simulation time, the system is not fully equilibrated. If allowed to equilibrate, cisplatin in distorted t-pores will move into adjacent o-pores within the same sampling window. This results in a non-physical

trajectory which cannot be analysed as a PMF. For this reason, the PMFs shown in the main body of the text were analysed prematurely. Although the sampling windows are not fully equilibrated after 1 ns, the trajectories show a physical path, and therefore despite not being accurate, they provide a reasonable estimate for the energy barriers.

References

1. Hutter, J., et al., *cp2k: atomistic simulations of condensed matter systems.* Wiley interdisciplinary reviews. Computational molecular science, 2014. **4**: p. 25.
2. VandeVondele, J., et al., *Quickstep: Fast and accurate density functional calculations using a mixed Gaussian and plane waves approach.* Computer Physics Communications, 2005. **167**(2): p. 103-128.
3. Borštnik, U., et al., *Sparse matrix multiplication: The distributed block-compressed sparse row library.* Parallel Computing, 2014. **40**(5): p. 47-58.
4. Frigo, M. and S.G. Johnson, *The Design and Implementation of FFTW3.* Proceedings of the Institute of Electrical and Electronics Engineers, 2005. **93**(2): p. 216-231.
5. VandeVondele, J. and J. Hutter, *An efficient orbital transformation method for electronic structure calculations.* The Journal of Chemical Physics, 2003. **118**(10): p. 4365-4369.
6. Lippert, B.G., J.H. Parrinello, and Michele, *A hybrid Gaussian and plane wave density functional scheme.* Molecular Physics, 1997. **92**(3): p. 477-488.
7. Perdew, J.P., K. Burke, and M. Ernzerhof, *Generalized Gradient Approximation Made Simple.* Physical Review Letters, 1996. **77**(18): p. 3865-3868.
8. Grimme, S., S. Ehrlich, and L. Goerigk, *Effect of the damping function in dispersion corrected density functional theory.* Journal of Computational Chemistry, 2011. **32**(7): p. 1456-65.
9. Grimme, S., et al., *A consistent and accurate ab initio parametrization of density functional dispersion correction (DFT-D) for the 94 elements H-Pu.* The Journal of Chemical Physics, 2010. **132**(15): p. 154104.
10. VandeVondele, J. and J. Hutter, *Gaussian basis sets for accurate calculations on molecular systems in gas and condensed phases.* The Journal of Chemical Physics, 2007. **127**(11): p. 114105.
11. Hartwigsen, C., S. Goedecker, and J. Hutter, *Relativistic separable dual-space Gaussian pseudopotentials from H to Rn.* Physical Review B, 1998. **58**(7): p. 3641-3662.

12. Goedecker, S., M. Teter, and J. Hutter, *Separable dual-space Gaussian pseudopotentials.* Physical Review B, 1996. **54**(3): p. 1703-1710.
13. Yesylevskyy, S., et al., *Empirical force field for cisplatin based on quantumdynamics data: case study of new parameterization scheme for coordinationcompounds.* Journal of Molecular Modeling, 2015. **21**(10): p. 268.

CHAPTER 5. TAILORING DEFECTS OR BUILDING UNITS FOR CONTROLLED CISPLATIN DRUG DELIVERY

5.1. Motivation: narrow down the better method of tailoring MOFs to reduce release rates while increasing uptake

If a framework is promising for drug delivery, it makes sense to tailor that framework to enhance its uptake and retention. This can be done using reticular synthesis (i.e. using different building blocks and similar synthesis conditions to achieve predetermined structures based on a prototype [1]), or by incorporating defects into the framework [2]. However, the current literature does not indicate which method produces better drug delivery carriers.

This section addresses the aforementioned gap using the biocompatible UiO-66 with and without missing ligand defects, mainly because of the well-established literature and experimental data [3-6]. For comparison, non-functionalised and NH_2 functionalised defect free variants of UiO-66 with larger pore sizes (UiO-67 and UiO-68) were also used and compared to the defective structures. Particular attention was attributed to the level of control over cisplatin diffusion each structure could provide. Based on the calculated diffusivities, the aim of this work was to recommend whether it is better to tailor MOF drug delivery carriers using defects or different building units.

5.2. Summary: MD simulations without water and SMD with water to look at diffusion mechanisms

Since pore volume is the determining factor for cisplatin uptake (see Chapter 4), this was calculated using Poreblazer [7]. In the non-solvated systems, MD simulations were used to produce mean-square displacement (MSD) curves of cisplatin from which the diffusivity could be calculated (Section 2.3.4). Diffusivities calculated at various temperatures were used to determine activation energies associated with diffusion in each system. As discussed in Chapter 4, water has a large impact on the MOF-CPT interaction energies as well as the diffusivities, however when water is present the rate of diffusion is too slow to witness interpore movement. For this reason, the non-solvated energy barriers were compared to the solvated energy barriers calculated using SMD simulations to determine how well each structure performs at cisplatin retention.

5.3. Results: defect-free MOFs with polar functional groups are recommended as opposed to defects

Both the MD and SMD results (with and without water) show that cisplatin retention is equally achievable in frameworks with larger functionalised pores (i.e. UiO-68(NH_2)) as it is in the defective UiO-66 models. Cisplatin diffusion in the defective UiO-66 structures is usually predictable: namely if the modulator size decreases or if polar modulators are used diffusion decreases. However, there are unexpected results which are not intuitive, for example larger step sizes between favourable adsorption sites caused by specific positions of modulators and ligands significantly decreases diffusivity. These simulations indicate that defect free, functionalised structures are a better way forward to derive an ideal drug delivery carrier.

5.4. Errata

Not applicable as paper not yet submitted

5.5. Chapter 5 Preamble References

1. Eddaoudi, M., et al., *Systematic design of pore size and functionality in isoreticular MOFs and their application in methane storage.* Science, 2002. **295**(5554): p. 469-72.
2. Lin, S.-X., et al., *Effective loading of cisplatin into a nanoscale UiO-66 metal–organic framework with preformed defects.* Dalton Transactions, 2019. **48**(16): p. 5308-5314.
3. Wu, H., et al., *Unusual and Highly Tunable Missing-Linker Defects in Zirconium Metal–Organic Framework UiO-66 and Their Important Effects on Gas Adsorption.* Journal of the American Chemical Society, 2013. **135**(28): p. 10525-10532.
4. Trickett, C.A., et al., *Definitive Molecular Level Characterization of Defects in UiO-66 Crystals.* Angewandte Chemie International Edition, 2015. **54**(38): p. 11162-11167.
5. Hu, Z., et al., *Modulator Effects on the Water-Based Synthesis of Zr/Hf Metal–Organic Frameworks: Quantitative Relationship Studies between Modulator,*

Synthetic Condition, and Performance. Crystal Growth & Design, 2016. **16**(4): p. 2295-2301.

6. Mocniak, K.A., et al., *Incorporation of cisplatin into the metal–organic frameworks UiO66-NH2 and UiO66 – encapsulation vs. conjugation.* Royal Society Chemistry Advances, 2015. **5**(102): p. 83648-83656.
7. Sarkisov, L. and A. Harrison, *Computational structure characterisation tools in application to ordered and disordered porous materials.* Molecular Simulation, 2011. **37**(15): p. 1248-1257.

5.6. Paper

This declaration concerns the article entitled:								
Tailoring defects or building units for controlled cisplatin drug delivery								
Publication status (tick one)								
Draft manuscript	/	**Submitted**		**In review**		**Accepted**		**Published**
Publication details (reference)	Thompson, M. Düren, T. 2020. Tailoring defects or building units for controlled cisplatin drug delivery.							
Copyright status (tick the appropriate statement)								
I hold the copyright for this material	/	Copyright is retained by the publisher, but I have been given permission to replicate the material here						
Candidate's contribution to the paper (provide details, and also indicate as a percentage)	The candidate contributed to / considerably contributed to / predominantly executed the… Formulation of ideas: The candidate predominantly formulated the detailed ideas (100 %). Design of methodology: The candidate predominantly designed the method for the simulations (100 %). Experimental work: The candidate predominantly conducted the simulations (100 %). Presentation of data in journal format: The candidate predominantly presented the work in a journal format (100 %)							
Statement from Candidate	This paper reports on original research I conducted during the period of my Higher Degree by Research candidature.							
Signed				**Date**	01/09/2020			

Tailoring defects or building units for controlled cisplatin drug delivery

Megan J. Thompson, Tina Düren[*]

AUTHOR ADDRESS Prof. T. Düren, Centre for Advanced Separations Engineering, Department of Chemical Engineering, University of Bath, BA2 7AY, UK
E-mail: t.duren@bath.ac.uk

ABSTRACT

One third of the worldwide population will be diagnosed with cancer at some point in their lives, yet it remains one of the hardest diseases to combat because of the non-specificity of treatment. Targeted chemotherapy using nanocarriers is a promising method for improving the welfare of cancer patients, yet the hunt for an ideal nanocarrier continues. In this work we compare two methods for tailoring a highly promising category of nanocarriers – metal-organic frameworks, MOFs, to achieve good drug loading and retention properties, namely incorporation of defects and altering building units. Focussing on a well-known series of biocompatible MOFs (UiO-66, UiO-67 and UiO-68), we use molecular simulations to highlight the complex interplay between different structural characteristics such as variations in host-guest energies throughout the framework, pore size, and pore window diameter. Our simulations show that similar levels of cisplatin retention can be achieved in the wider pores of functionalised UiO-67 and UiO-68 compared to the defective UiO-66 structures. Furthermore, it is not possible to finely tune defects, yet their precise configuration has a major influence on cisplatin diffusivity. Our recommendation is that further studies involving MOFs as nanocarriers should focus on functionalising frameworks with wider pores (to enhance uptake and encapsulation rates) as opposed to tailoring defects which is something that gives us significantly less control.

INTRODUCTION

Cancer is a disease whereby abnormal cells rapidly mutate into tumours, which can continually invade and damage other healthy areas of the body via metastasis, and one in three people are diagnosed with cancer in their lifetime. Unfortunately, cancer is extremely difficult to treat for a variety of reasons, including the issue of metastasis, a lack of biomarkers and drug resistance abilities [1]. One of the most common forms of treatment to date is chemotherapy during which chemotherapeutics are injected into the patient. Often the chemotherapeutics are cytotoxic drugs

which interfere with DNA causing apoptosis (programmed cell death) which mainly effects rapidly growing cells such as those in a tumour. However, the majority of World Health Organisation approved chemotherapeutics are non-specific and also very damaging to rapidly growing normal healthy cells causing severe side effects [2, 3]. To reduce toxicity to normal healthy cells and improve dosage in the vicinity of a tumour, targeted drug delivery has become a popular area of research. The idea is that the subtle physiochemical properties specific to tumours (for instance changes in the extracellular pH [4, 5] or antigens that are overexpressed by tumours [6]) are targeted for instance using a drug delivery carrier.

Existing nanocarriers can be subcategorised into inorganic carriers (e.g. quantum dots or carbon nanotubes) and organic carriers (e.g. micelles or liposomes). Typically however there is a trade-off between the drug loading capacity and nanocarrier biocompatibility / biodegradability [7]. Metal-organic frameworks are hybrid materials that can be tailored to avoid such a trade-off. They consist of metal nodes coordinated by organic ligands resulting in porous crystalline materials which typically have large pore volumes and internal surface areas. Furthermore by changing the building units, we can strategically tailor properties such as the pore window size, cavity volume, and MOF – guest molecule interaction energies in order to enhance uptake or control guest molecule diffusivity [8]. Depending on their building units, MOFs can be biocompatible, and some MOFs are only stable within a given pH range. This property can be exploited for drug delivery where the MOF nanocarrier is stable in normal healthy parts of the body and but unstable in the acidic extracellular area surrounding a tumour [9]. As well as this, it is possible to conjugate antibodies onto the external surface of MOFs allowing them to target antigens that are specifically overexpressed by tumours [10].

An ideal MOF for drug delivery will have a high loading capacity coupled with a fast uptake rate as well as a slow release rate. Unfortunately, most studies show that high loading is mainly governed by the accessible pore volume [11-13] which often equates to larger window apertures and faster release rates. To overcome this, it is possible tune MOF – guest interactions to increase retention time as well as the loading. For example, Rojas et al found that the release rate of ibuprofen (which is hydrophobic) is slower than the release rate of aspirin (which is hydrophilic) in UiO-66 (hydrophobic) [12].

As summarised in the extensive review by Kotzabasaki et al [14], most theoretical studies on drug delivery quantify uptake using grand-canonical Monte Carlo simulations, arriving at a common conclusion that the loading is governed by the pore volume [15, 16]. However, when we applied the same technique to quantify cisplatin uptake in UiO-66 [17], the loading was significantly higher than that reported experimentally [18], indicating the importance of water coadsorption and diffusion hinderance during encapsulation. Release rates are normally quantified based on the use of non-

temporal simulations (e.g. geometry optimisations or GCMC) to derive MOF – drug interaction energies [15, 16, 19]. However, the lack of temporal aspect could result in unforeseen discrepancies between the interaction energy and experimental release rates. To the best of our knowledge, the only group to use time-averaged molecular dynamics (MD) simulations to determine chemotherapeutic release rates in MOFs is Kotzabasaki et al who performed MD simulations of gemcitabine diffusion in solvated mesoporous IRMOF-74-III (with and without polar functional groups). They found a slight reduction in diffusivity when polar functional groups are used, and that diffusivity decreases at higher loadings due to the formation of drug aggregates [20].

In this work we focus on characterising and controlling diffusion of one of the main cytotoxic drugs used in chemotherapy – cisplatin (*cis*-diamminedichloridoplatinum (II) shown in Figure 1), in variations of one of the most widely studied microporous MOFs – UiO-66. UiO-66 is a biocompatible MOF [21] that consists of zirconium clusters ($Zr_6O_4(OH)_4$) coordinated by the carboxyl groups of twelve BDC ligands (BDC=benzenedicarboxylic acid) per cluster [22]. It is arranged into larger octahedral pores (1.1 nm) and smaller tetrahedral pores (0.8 nm), which are connected by narrow triangular windows with 0.36 nm diameter. Depending on the synthesis conditions (e.g. modulators used to slow down crystallisation), UiO-66 normally has 1 – 4 missing BDC ligands per cluster [23], and the maximum concentration of defects reported in crystalline structures experimentally is 4.3 monocarboxylate acids per node, (though up to 6 defects/node can be achieved in the crystalline structure using different types of modulators [24]) [25]. Missing ligand defects can be systematically tuned to alter the structural and chemical properties [26]. For drug delivery applications, defects can be advantageous, as they increase the free volume (hence loading capacity) and the defective sites can be used for anchorage to prevent premature drug release [27, 28]. Another strategy to increase the free volume is to use larger ligands, for example in isoreticular MOFs UiO-67 and UiO-68 which differ from UiO-66 in that larger biphenyldicarboxylate (BPDC) and t*erphenyl*dicarboxylate (TPDC) ligands connect $Zr_6O_4(OH)_4$ nodes [22]. The larger ligands increase the tetrahedral and octahedral pore sizes to 1.0 and 1.2 nm in UiO-67, and 1.2 and 1.4 nm in UiO-68 (calculated using PoreBlazer [29]). Compared to UiO-66, these frameworks are less likely to have missing ligand defects [30, 31]. In this work, we investigate the level of cisplatin retention achievable in defective UiO-66 and the defect free isoreticular structures.

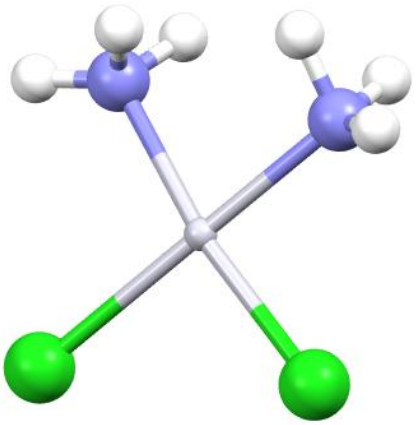

Figure 1. Structure of the polar drug, cisplatin. Colour scheme: green = chlorine, grey = platinum, blue = nitrogen, white = hydrogen.

Our aims are to understand how the properties of these microporous frameworks (e.g. pore volume, window diameter, and polar functionality) influence cisplatin diffusion and to determine which property dominates retention under different circumstances. For example, if the pore window diameter is larger than the diameter of cisplatin, then how do other properties such as the pore volume influence diffusivity? We also look at the influence of polar functional groups by comparing cisplatin diffusion in non-functionalised structures compared to frameworks with NH_2 functionalised ligands. Furthermore, we investigate what route (e.g. incorporating defects, adding functional groups, or varying ligand size) results in the best control of achieving slow release rates whilst retaining a large pore volume to enhance loading capacity.

METHOD

Structural Models: Structures of defect-free UiO-66, UiO-67, and UiO-68 were taken from the Cambridge Structural Database [32-34], and amine groups were added to the ligands using Mercury [35]. Missing ligand defects in UiO-66 were modelled by removing 2, 4, and 6 BDC/node and coordinating the metal sites using the carboxyl groups of methanoic acid (MA), ethanoic acid (EA) or trifluoroethanoic acid (TFA). We will denote the missing linker defects as XMA, XEA, XTFA where X represents the number of missing BDC linkers per node, and MA, EA and TFA stands for the node capped with methanoic acid, ethanoic acid or trifluoroethanoic acid, respectively. For example, 2MA stands for two missing ligands per node capped with methanoic acid. When creating defects, adjacent BDC were removed (Figure 2) to emphasize the change in pore window diameter as the concentration of defects increases.

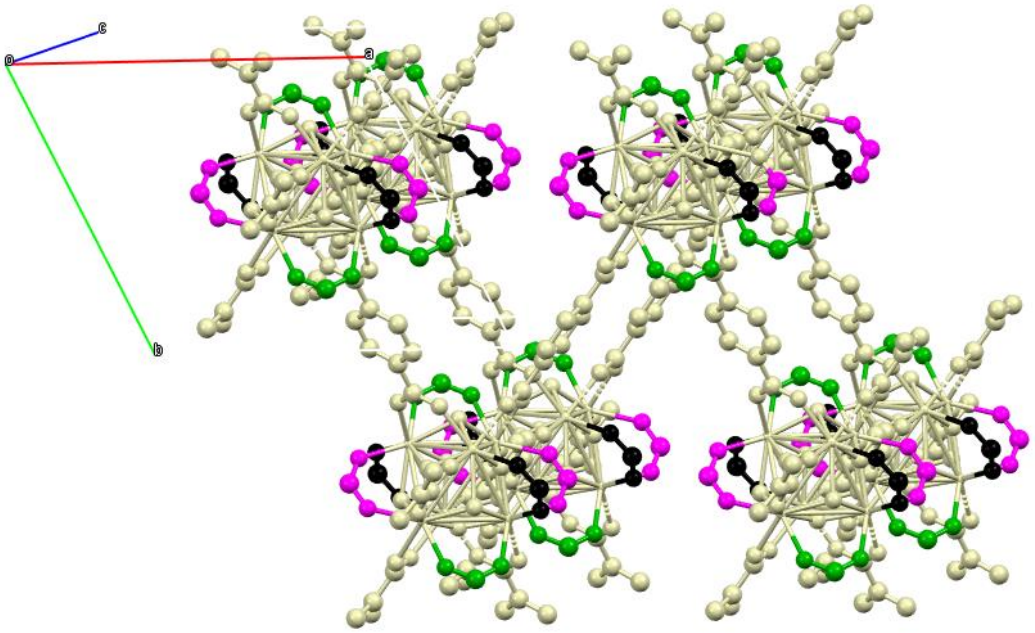

Figure 2. UiO-66 defect model, showing the order of BDC ligands removed: 2, 4, 6 defect/node = black, pink, green. For clarity, MA modulators have been used as an example and hydrogen atoms have been omitted.

Molecular dynamics simulations: Bias and unbiased MD simulations were used to determine the interpore and intrapore diffusion behaviours of cisplatin in each framework. For all MD simulations, the forcefield parameters for cisplatin were taken from the work of Yesylevskyy et al [36] and for water the TIP3P was used [37]. Mulliken charges for each framework were obtained using static energy calculations in CP2K (see below), and Lennard Jones / bonded interaction parameters were taken from the Universal Forcefield [38] using the topology builder OBGMX [39]. To model "perfect defects", the structures used to build topologies were not optimised prior to use in OBGMX. This is discussed in more detail with the results, however in brief when optimised some of the structures closed (though the bonding remained intact). It is unlikely that such structures would close when exposed to water because favourable host-guest interaction energies would mean that the lowest energy state would enhance the loading (hence the structure should reopen) [40]. For this reason, we modelled diffusion in the open pore (non-optimised) structures only. Either a single cisplatin molecule was randomly inserted into the frameworks, or they were carefully positioned to achieve a loading of one cisplatin molecule per octahedral pore. Details for obtaining the optimal water loading can be found in the SI, Section S1.

MD and SMD simulations were carried out using the Groningen Machine for Chemical Simulations (GROMACS) [41-46]. Under the assumption that the bulk crystal would confine a unit cell to constant volume, the NVT ensemble was employed during all simulations. The framework and guest

molecules were treated as fully flexible. Electrostatic interactions were modelled using the particle mesh Ewald algorithm [47, 48], and the 12-6 Lennard Jones potential was used to model non-Coulombic interactions. A Verlet cutoff scheme was used in the neighbour search and cutoff values for the Coulombic and Van der Waals terms were set to 1.25 nm. Dispersion corrections were applied to the energy and pressure terms, and the temperature was set to 298 K. Periodic boundary conditions were employed in all directions.

Normal MD simulations have the advantage that they can sample an equilibrated system, however when water is present the rate of cisplatin diffusion is too slow to witness interpore movement within reasonable simulation times. Instead, steered-MD (SMD) simulations were used. SMD allows us to look at the process of interpore movement in the presence of water, though these simulations are only equilibrated in the limit of infinitely slow pull velocities. Therefore, the SMD results can only provide an initial estimate for how the interaction energies will vary along the coordinate path when water is present. Based on these pros and cons, for the non-solvated systems we calculated the diffusivity (D_{NoSol}) and considered the activation energy (Q^{EQ}) based on the gradient of diffusivities as a function of temperature, calculated using more reliable equilibrium MD simulations. For the solvated system, we considered the maximum diffusion energy barrier (Q^{SMD}), estimated from the change in interaction energies calculated using steered-MD simulations. If water does not influence the conclusions then the diffusivity in the absence of water, D_{NoSol} should be inversely proportional to the energy barrier, Q^{SMD}.

For all MD simulations, each system was energy minimised and pre-equilibrated prior to the collection of data. A steepest decent minimisation was initially carried out using a tolerance of 1,000 kJ mol^{-1} nm^{-2} and a step size of 0.01 nm. Next, the systems were pre-equilibrated for 200 ps using a timestep of 1 fs and a modified Berendsen thermostat to regulate the temperature [49]. For the 20 ns normal MD production runs, Nose-Hoover temperature coupling was employed [50, 51]. This 20 ns timescale was deemed appropriate since mean-square displacement (MSD) plots were linear and frequent interpore movement was witnessed. Based on the gradients of MSD plots, the diffusion coefficient (D_{NoSol}) was calculated as D_{NoSol}=MSD/6t (where t is the simulation time). By calculating the diffusion coefficient at various temperatures (T = 298 K – 798 K), Arrhenius plots were generated and used to calculate the activation energy (Q^{EQ}) and pre-exponent (D_0, which is a function of successiveness of atom jumps, the jump frequency, and the characteristic diffusion length) [52].

For the solvated SMD simulations, cisplatin was pulled along the [0 -1 1] plane for 10 ns (that is the plane in which a moveable path is created in the 2 defects/node model, Figure 2). A harmonic spring constant of 5,000 kJ mol^{-1} nm^{-2} was used to constrain cisplatin to the auxiliary pull atom which moved along the coordinate path at a velocity of 0.0025 nm/ps (the choice of these parameters is

justified in the SI, Section S2). The activation energy, Q^{SMD}, was approximated from the change in interaction energy as cisplatin moves through the framework.

Ab-initio simulations: CP2K was used to carry out static energy and optimisation simulations. Static energy calculations of the non-optimised structures yielded the Mulliken charges used in the MD and SMD simulations while each structure was also optimised to determine how defects will influence the structure (compared to the idealised defect models). In both cases, the Gaussian and Planewave approach as implemented in the Quickstep module was used [53-58]. Goedecker, Teter and Hutter (GTH) pseudopotentials were used to model the core electrons [54, 59, 60], and all atoms were modelled using triple-zeta Gaussian basis sets except for zirconium for which double-zeta functions were used [61]. Cutoff and relative cutoffs of 600 Ry and 50 Ry were used, and exchange correlation terms were approximated using the Perdew-Burke-Ernzerhof functional [62] with DFT-D3 dispersion corrections [63, 64]. Convergence of the wavefunction was set to a tolerance of 10^{-6} and optimisation tolerances were set to: maximum atomic displacement = 0.003 Bohr, root-mean square atomic displacement = 0.0015 Bohr, maximum atomic force = 0.0004 Bohr/Ha, and root-mean square atomic force = 0.0003 Bohr/Ha.

RESULTS AND DISCUSSION

To understand the interplay between cisplatin diffusion and different MOF properties, we initially simulated single cisplatin molecules in otherwise empty frameworks. This removes all other influences on the rate of diffusion (e.g. guest – guest molecule interactions), so we can focus solely on the framework properties. At 298 K, all structures except for defect-free UiO-66 and 4TFA show normal diffusivity (as shown by MSD plots in the SI, Section S3). In UiO-66, comparatively rigid BDC ligands form a pore window diameter of 0.36 nm which is smaller than the collision diameter of cisplatin (≈ 0.5 nm). The causes of sub-diffusivity in 4TFA at 298 K are discussed in more detail below, but it is worth pointing out that normal diffusion is seen in 4TFA as the temperature increases (≥ 398 K).

Figure 3a compares cisplatin diffusivity in the defective UiO-66 structures. In general, cisplatin diffusivity is slower (hence retention is better) if larger modulators are used (comparing EA to MA), or if modulators derived from stronger acids are used (comparing similarly sized TFA and EA). Surprisingly the rate of diffusivity at 298 K decreases going from 2 → 6 → 4 defects/node for all capping types at 298 K. It should be noted however that (as shown in the SI, Section S3) at higher temperatures diffusivity decreases going from 6 → 4 → 2 defects/node as expected. The decrease in diffusivity with modulators derived from stronger acids or larger modulators are still observable at higher temperatures. The diffusivity is inversely proportional to the activation energy (Figure 3b) and directly proportional to the pre-exponential factor (Figure 3c).

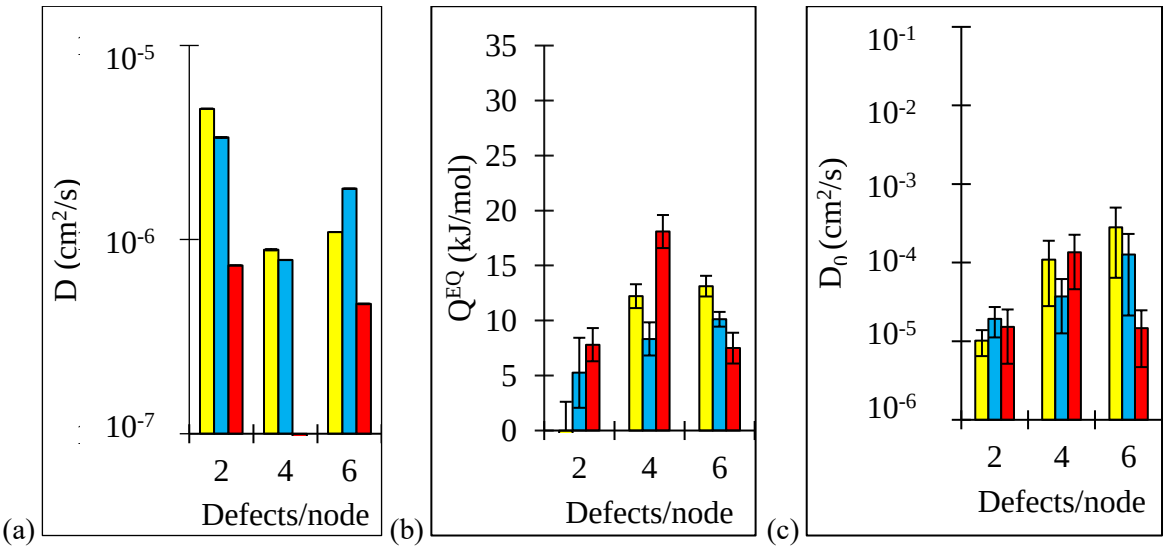

Figure 3. Diffusivity of a single cisplatin molecule at 298 K inside non-solvated UiO-66 defective structures (a). No diffusivity is shown for 4TFA as normal diffusion was not observed. Arrhenius-based diffusion activation energies (Q^{EQ}) and pre-exponential factors (D_0) for a single cisplatin molecule in the non-solvated structures (b/c). For 2MA, the activation energy is ~ 0 kJ/mol, hence no bar can be seen in (b). Colour scheme: yellow = MA, blue = AA, red = TFA modulated UiO-66.

The diffusivities in Figure 3a can be explained in terms of the activation energies in Figure 3b. Firstly, it should be noted that the diffusion activation energy is associated with the variation in energy as cisplatin moves between favourable adsorption sites via less favourable sites in the framework (such as the pore windows). As shown in the SI, Section 4, the most favourable adsorption sites are associated with the aromatic and carboxyl groups of the BDC ligands (hence to maximise the adsorption energy, cisplatin adsorbs in the pore corners). At 2 defects/node, there is zero activation energy in 2MA (hence high diffusivities) because the short alkyl chains do not intrude the pore window and weak interaction energies with the modulators equate to less anchorage in the pore corners. The activation energy is higher (hence the diffusivity is lower) in 2TFA compared to 2EA because cisplatin interacts more favourably with the carboxyl group associated with the TFA modulators (as it is a stronger acid the oxygen atoms are less negatively charged and so the electronegative atoms in cisplatin experience less Coulombic repulsion).

As the number of defects increase, interaction energies associated with the modulator chain (MA = H atom, EA = methyl group, TFA = trifluoromethyl group) become more influential on the activation energy. For example, a high density of unfavourable groups pertaining to the modulators will increase the variation in energy (hence the activation energy) associated with cisplatin movement through the framework. At 4 defects/node, the activation energy in the TFA structure remains the highest out of the modulators used because of strong interactions with the carboxyl group and weak

interaction energies with the chain (fluorine atoms repel the electronegative atoms in cisplatin). The activation energy is higher in 4MA compared to 4EA because in the former there are weak interaction energies associated with the modulator chain, and in the latter, there are relatively strong interaction energies with the chain (as methyl groups are larger, the interaction energies are more favourable, and this reduces the variation in activation energy that cisplatin must overcome). At 6 defects/node, the same trend is seen in the MA and EA structures. 6TFA however has a surprisingly low activation energy, which arises from opposing interaction energies from the modulators and ligands. More specifically, when cisplatin is in the pore corners next to the ligands, it experiences unfavourable interaction energies with the electronegative groups of the TFA modulators (see the SI, Section 4).

Figure 4 shows the cisplatin diffusivity and Arrhenius based diffusion constants inside defect-free UiO-67 and UiO-68 (defect-free UiO-66 was excluded from these results because sub-diffusion was observed). As seen in Figure 4, cisplatin diffusivity is slower in non-functionalised UiO-67 compared to UiO-68 (the phenomena of larger pores and enhanced diffusivity is commonly seen in various other systems [65, 66]), yet both defect-free structures show a similar magnitude of cisplatin diffusivity as the defective UiO-66 structures (~ 10^{-6} cm^2/s). As in the experimental work by Mocniak et al [18], if polar NH_2 functional groups are added to the defect free structures we can significantly reduce diffusivity (hence control release rates) compared to the majority of defective UiO-66 structures due to enhanced interaction energies with cisplatin (UiO-67 = 66 $\%_{decrease}$, UiO-68 = 91 $\%_{decrease}$). In the amine functionalised variants, diffusivity is slower in UiO-68(NH_2) compared to UiO-67(NH_2).

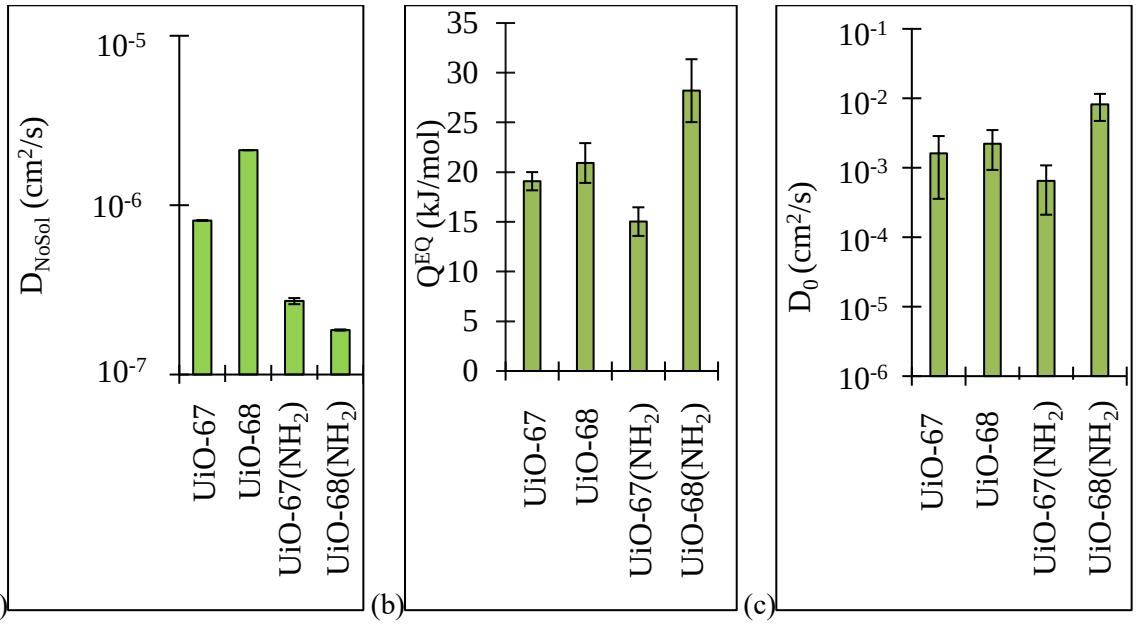

Figure 4. Diffusivity of a single cisplatin molecule at 298 K inside non-solvated UiO-67 and UiO-68 structures with and without NH_2 functionalised ligands (a). Arrhenius-based diffusion activation energy (Q^{EQ}) and pre-exponential factors (D_0) for a single cisplatin molecule in the non-solvated structures (b/c).

Diffusivities in non-functionalised UiO-67 and UiO-68 are on par with those in the defective UiO-66 structures (Figure 3). As shown in Figure 3b/c and Figure 4b/c, they have higher activation energies than the defective structures (because larger pores increase the distance between favourable adsorption sites resulting in a larger variation in energy), but they also have larger D_0 values (because the distances moved in successive steps are larger). If amine groups are added, the activation energy further increases resulting in lower diffusivities. This is more pronounced in UiO-68(NH_2) because the larger pore size creates bigger gaps between the favourable NH_2 sites.

Figure 5 summarises how the properties of MOFs are linked to D_0 and Q^{EQ}. If the window diameter is less than 4 Å (i.e. as in 2 – 4 EA and TFA), there is a sharp increase in the activation energy because interpore movement requires the displacement of framework atoms. At such small window diameters, the activation energy significantly increases if the number of defects increase (because as mentioned, there is a high density of unfavourable modulator – cisplatin interactions) or if the modulators are derived from TFA (because of the anchoring/repulsion caused by polar groups). In other words, the release rates decrease if cisplatin has to pass through highly unfavourable regions of the framework (i.e. large concentrations of unfavourable modulators). Slower release rates in TFA modulated structures are expected as similar phenomena have been seen experimentally, namely hydrophilic drug release decreases significantly in frameworks with hydrophilic groups [12, 18]. However, the decrease in release rates going from 2 to 4 defects/node at 298 K is not intuitive.

If the window size increases beyond 4 Å, both the preexponential factor and activation energy increase because the pore size (hence distance between favourable adsorption sites) increases. This increase is particularly enhanced when polar functional groups are added to the ligands. As shown by the diffusivities in Figures 3 and 4, this indicates that we can achieve the same controlled release rates using functionalised MOFs with larger pore sizes as we can using MOFs with small pore sizes. Such a finding would be important as it may enable us to achieve a higher loading of cisplatin, faster encapsulation rates as well as good retention of the drug. The validity of this conclusion is further analysed in the following sections where more realistic systems are simulated.

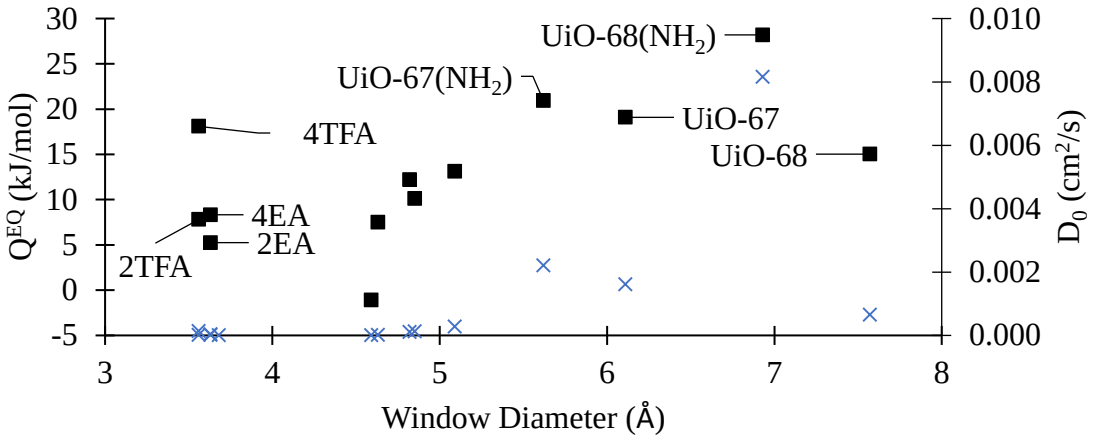

(a)

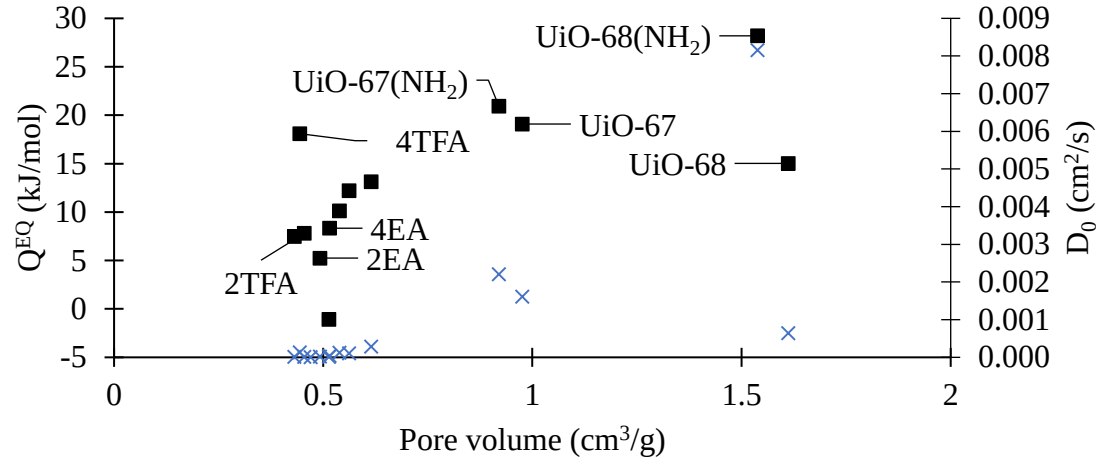

(b)

Figure 5. Diffusion activation energy, Q^{EQ}, (■) and preexponential factor, D_0, (×) as a function of (a) the window diameter and (b) the pore volume. Results gathered from non-solvated simulations of a single cisplatin molecule in each structure, at temperatures ranging from 298 – 798 K, with seven repeats at each temperature

So far, single cisplatin molecules have been modelled inside otherwise empty frameworks to solely investigate the influence of MOF properties on cisplatin mobility. However, experimentally cisplatin loadings of 5 – 26 $\%_{wt}$ are achievable in UiO-66 (depending on the uptake method and defect concentration), and release/uptake experiments are carried out in aqueous solutions [18, 28].

When modelling a single cisplatin molecule, all structures (except for UiO-66) permit interpore movement, and normal diffusion regimes are generally observed. When the loading increases from 1:8 to 1:1 CPT:octahedral pore, clusters of cisplatin molecules form inside the pores due to strong electrostatic interactions between the chlorine and amine groups (snapshots are available in the SI, Section S5). As shown in Figure 6, this hinders mobility and changes the diffusion regime from normal ($\langle r^2 \rangle \propto t^{\alpha}$ where $\alpha = 1$), to a combination of normal/sub-diffusive ($\langle r^2 \rangle \propto t^{\alpha}$ where $\alpha < 1$), because either a large cluster has to pass through the pore windows, or a single cisplatin molecule

needs to break away from the clusters to achieve interpore movement. These results indicate that the release rate per cisplatin molecule decreases at higher loadings. Steric hinderance caused by guest molecule grouping is a well-known effect that increases with loading [67] [68], and the clustering effect is also seen in other MOF – drug systems [20].

For both high and low cisplatin loadings, diffusion increases with pore window diameter (UiO-66 → TFA/EA → MA → UiO-67 → UiO-68). In contrast to the simulations with just one CPT molecule, changing the modulator polarity or the number of defects does not have an effect at a loading of one CPT:octahedral pore, suggesting the window diameter is the rate-limiting factor for the diffusion at higher loading.

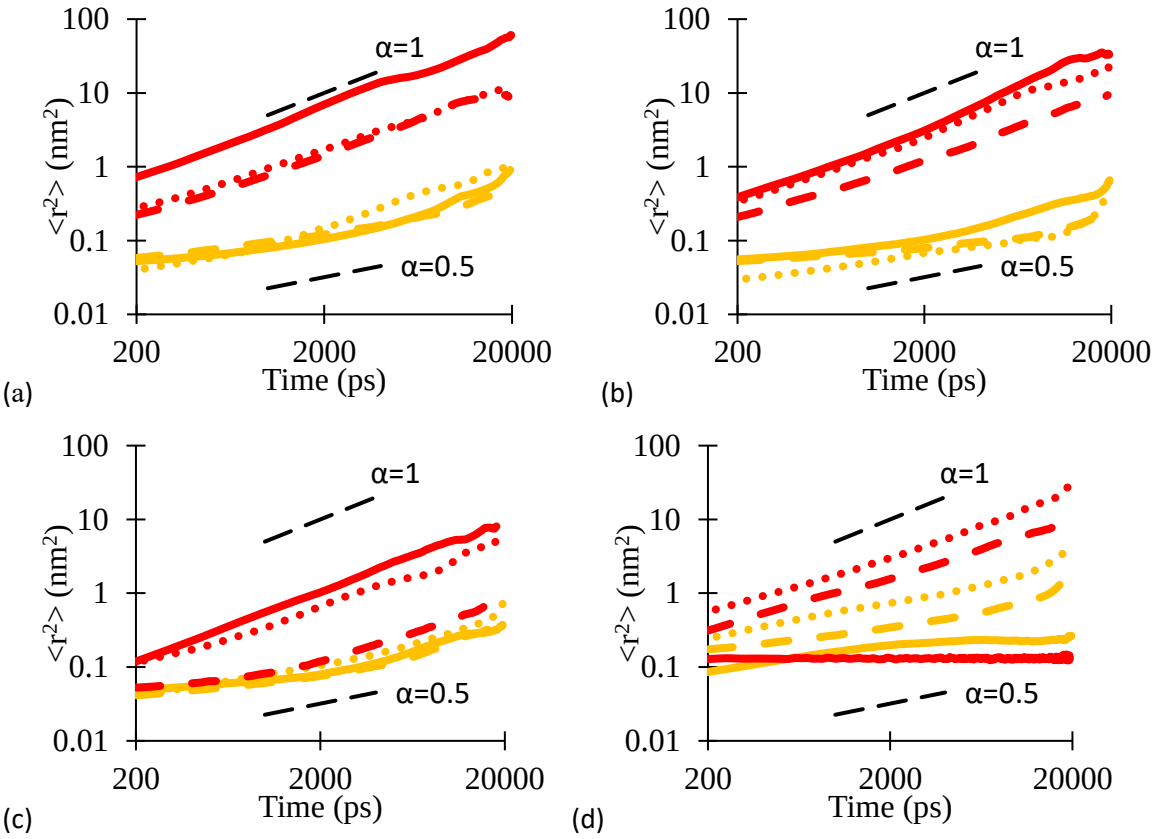

Figure 6: Comparison of MSD for cisplatin loadings of 1CPT/8 octahedral pores (red) and 1CPT/1 octahedral pore (purple) at 298 K in the defective UiO-66 structures modulated with (a) MA, (b) EA, (c) TFA (solid line 2 defects / node, dashed line 4 defects / node, dotted line 6 defects/node) and (d) defect free UiO-66 (solid line), UiO-67 (dashed line) and UiO-68 (dotted line). The expected gradients for normal and sub diffusion are represented by the black dotted lines, where $\langle r^2 \rangle$ is proportional to t^{α} ($\alpha = 1$ and $\alpha = 0.5$ respectively).

As release and uptake experiments are typically carried out in aqueous solution, we added explicit water molecules to the system to look at the influence of water on the rate of cisplatin diffusivity. Compared to the non-solvated system, Figure 7 shows that cisplatin diffusivity decreases by several orders of magnitude when water molecules are present due to tighter packing in the pores. In

agreement with the solvent-free results, smaller cavities (UiO-68 → UiO-67 → UiO-66) and smaller pore window sizes (MA → EA) decrease diffusion and hence the release rates. Diffusivity also decreases with modulator polarity (EA → TFA), though this is more likely due to MOF – water interaction energies as opposed to $U_{MOF\text{-}CPT}$ (which is significantly reduced in all systems due to the formation of a solvation shell, see the SI, Section S6). Figure 7 also shows that there is a strong correlation between water and cisplatin diffusivity, caused by hydrogen bonding between the cisplatin and water molecules – namely cisplatin is "carried" through the system by water. The outlier, UiO-68(NH_2), has particularly low cisplatin diffusivity compared to water which is caused by strong NH_2 – CPT interaction energies (evident from the energy landscapes shown in the SI, Section 7) and a relatively large free volume for water molecules (that are not part of the solvation shell) to move.

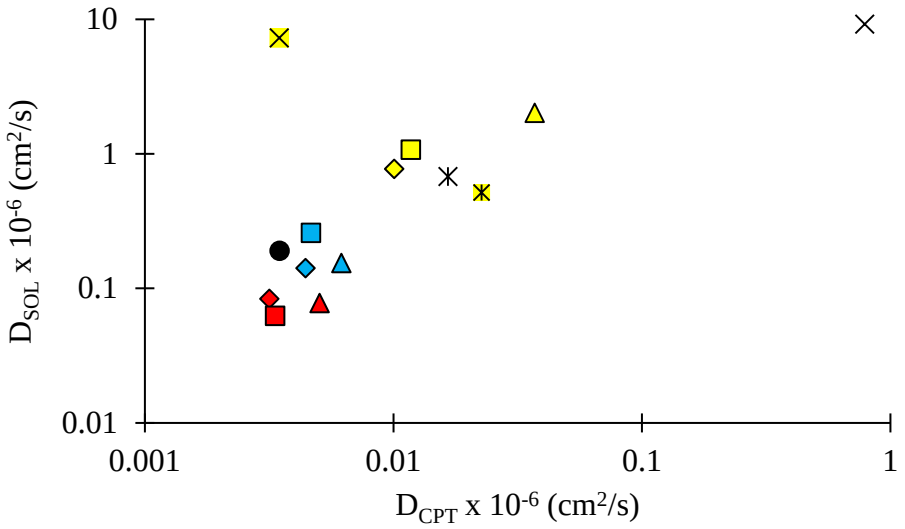

Figure 7. Diffusivity of cisplatin and water at 298 K in each system at a loading of one cisplatin molecule per octahedral pore. Marker scheme (defect free): ● UiO-66, ✳ UiO-67, ✳ UiO-67(NH_2), × UiO-68, × UiO-68(NH_2). Marker scheme (UiO-66 defect structures): diamond, triangle, square = 2, 4, 6 defects/node respectively. Colour scheme (UiO-66 defect structures): yellow, blue, red = MA, AA, TFA modulated nodes respectively.

When water is present, interpore diffusion cannot be quantified within reasonable MD time scales because of reduced cisplatin mobility. Instead, SMD simulations were used to determine the interpore energy barrier of the solvated system. Energy barriers calculated in the solvated system (Q^{SMD}, Figure 8) are overall inversely proportional to the diffusivity of a single cisplatin molecule in the non-solvated system (D_{NoSol}). We therefore draw the same conclusions as in the non-solvated equilibrium MD simulations, namely cisplatin diffusivity decreases with the modulator size and polarity. UiO-67 and UiO-68 offer an energy barrier similar to those seen in the non-polar defect models, particularly so when functionalised with NH_2 groups. By having a larger distance between favourable adsorption sites (UiO-68 compared to UiO-67), the energy barrier increases (a phenomenon which was also seen by Amirjalayer et al [65]). As before, this indicates that we can achieve similar energy

barriers to the frameworks with small pore-window diameters by manipulating the MOF-CPT interaction energies in MOFs with larger pores. (See energy landscapes in the SI, Section S2).

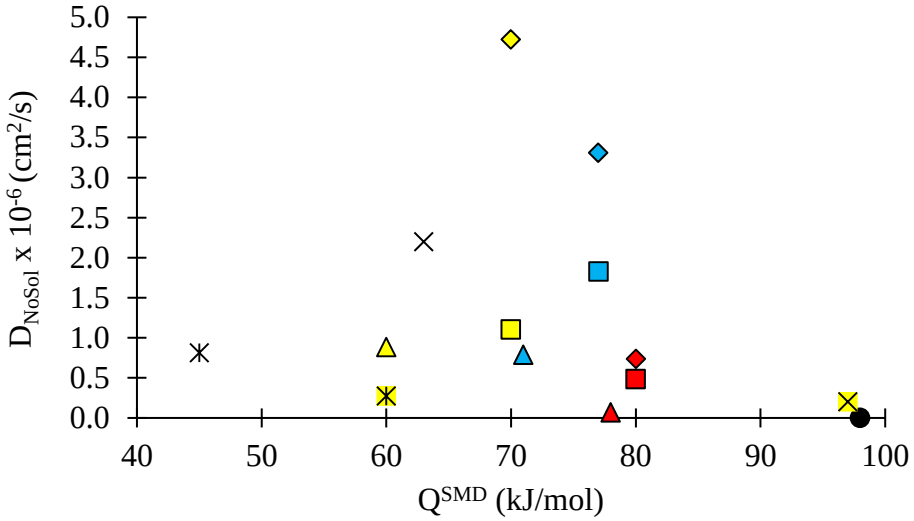

Figure 8. Comparison at 298 K of the cisplatin diffusivity in non-solvated systems (D_{NoSol}, calculated from equilibrium MD simulations) and the energy barrier associated with cisplatin movement through the solvated frameworks (Q^{SMD}, calculated from SMD simulations). Marker scheme (defect free): ● UiO-66, ✳ UiO-67, ✳ UiO-67(NH_2), × UiO-68, × UiO-68(NH_2). Marker scheme (UiO-66 defect structures): diamond, triangle, square = 2, 4, 6 defects/node respectively. Colour scheme (UiO-66 defect structures): yellow, blue, red = MA, AA, TFA modulated nodes respectively.

We have shown that the influence of defects on release rates depends substantially on their relative positions in the crystal as well as more controllable factors such as the size and chemical functionality of capping modulator. Due to the lack of controllability, it is much easier to achieve the same level of retention (and most likely a better uptake and encapsulation rate) using functionalised defect free MOFs with larger pore volumes such as UiO-68(NH_2). Furthermore, we have modelled ideal structures with defects (i.e. taking the defect-free UiO-66 structure and removing *n* ligand per node which are then capped with different modulator). While it may be intuitive that adding defects will increase the pore size hence enhance drug loading, *ab-initio* geometry optimisations shows that the pores of 4MA and 6MA close (although it should be noted that the bonds stay intact, as seen in the SI, Section S8). Non of the other structures close upon optimisation. Comparing the pore window diameters and volumes before and after optimisation (non-optimised → optimised | pore window diameters: 4MA: 4.82 → 2.98 Å, 6MA: 5.09 → 2.87 Å | pore volumes: 4MA: 0.562 → 0.256 cm^3/g, 6MA: 0.615 → 0.206 cm^3/g) this would lead to significantly lower diffusivity but also significantly lower cisplatin uptake than otherwise anticipated.

CONCLUSIONS

In this work we have contrasted the main methods of increasing the pore volume and hence drug loading (the use of defects and variable building units) in a set of isoreticular, hydrophobic MOFs (UiO-66, UiO-67, and UiO-68) for their influence on release rates.

Defects allow to tailor the diffusion of cisplatin. For example by increasing the modulator's polarity the interaction energies with polar drug molecules (such as cisplatin) increase, thus decreasing the rate of diffusion and drug release. By increasing the size of modulator, the pore window diameter decreases thus forming a barrier to drug molecule diffusion and hence release rates. However, release rates also depend on effects that we have less control over – such as the defect/ligand arrangement. As well as this, *ab-initio* optimisations show that even if we are able to fine tailor defects, unexpected structural changes (such as pore closing) may lead to unexpected results.

Another strategy to tailor the diffusion of cisplatin is to use structures with larger or functionalised linkers. Defect-free isoreticular MOFs with larger pore sizes (hence drug molecule capacity) and larger pore window sizes (which should equate to easier movement through the framework) lead to faster drug molecule diffusivities. However, when the MOFs are functionalised with polar NH_2 groups, the polar drug molecule diffusivities are on par with those in the structures where the diffusivity is limited by the pore window sizes due to enhanced framework – guest interaction energies which anchor the polar drug molecules.

To achieve enhanced uptake and retention times, it is overall more promising to focus on using functionalising defect-free MOFs as opposed to trying to fine tune defects, as it is more predictable, can offer similar retention rates using the MOF-guest interactions as opposed to the pore window size, and therefore we can get away with using larger pore volumes which would enhance loading and the encapsulation rates.

ASSOCIATED CONTENT

Details of the optimal water loading, spring constant and SMD pull velocity, raw data (including energy landscapes and MSD plots), interaction energies and snapshots can be found in the Supporting Information.

ACKNOWLEDGEMENTS

This work was supported by funding from the European Research Council (ERC) under the European Union's Horizon 2020 research and innovation programme (grant agreement No 648283 "GROWMOF"). It made use of the Balena High Performance Computing (HPC) Service at the University of Bath.

ABBREVIATIONS

MOF, Metal-organic framework; CPT, cisplatin; UiO, Universitetet i Oslo; MA, methanoic acid; EA, ethanoic acid; TFA, trifluoroacetic acid

REFERENCES

1. Chakraborty, S. and T. Rahman, *The difficulties in cancer treatment.* Ecancermedicalscience, 2012. **6**: p. ed16-ed16 DOI: 10.3332/ecancer.2012.ed16
2. Liu, B., et al., *Protecting the normal in order to better kill the cancer.* Cancer medicine, 2015. **4**(9): p. 1394-1403 DOI: 10.1002/cam4.488
3. *The selection and use of essential medicines.* World Health Organisation Technical Report Series, 2008(950): p. backcover, vii-174
4. Sun, H., et al., *Warburg Effects in Cancer and Normal Proliferating Cells: Two Tales of the Same Name.* Genomics, Proteomics & Bioinformatics, 2019. **17**(3): p. 273-286 DOI: https://doi.org/10.1016/j.gpb.2018.12.006
5. Tian, L. and Y.H. Bae, *Cancer nanomedicines targeting tumor extracellular pH.* Colloids and surfaces. B, Biointerfaces, 2012. **99**: p. 116-126 DOI: 10.1016/j.colsurfb.2011.10.039
6. Marques, A.C., et al., *Functionalizing nanoparticles with cancer-targeting antibodies: A comparison of strategies.* Journal of Controlled Release, 2020. **320**: p. 180-200 DOI: https://doi.org/10.1016/j.jconrel.2020.01.035
7. Senapati, S., et al., *Controlled drug delivery vehicles for cancer treatment and their performance.* Signal Transduction and Targeted Therapy, 2018. **3**(1): p. 7 DOI: 10.1038/s41392-017-0004-3
8. Yaghi, O., et al., *Reticular Synthesis and the Design of New Materials.* Nature, 2003. **423**: p. 705-714 DOI: 10.1038/nature01650

9. Howarth, A.J., et al., *Chemical, thermal and mechanical stabilities of metal–organic frameworks.* Nature Reviews Materials, 2016. **1**(3): p. 15018 DOI: 10.1038/natrevmats.2015.18
10. Cai, M., et al., *Metal Organic Frameworks as Drug Targeting Delivery Vehicles in the Treatment of Cancer.* Pharmaceutics, 2020. **12**(3): p. 232 DOI: 10.3390/pharmaceutics12030232
11. Bhattacharjee, A., M.K. Purkait, and S. Gumma, *Doxorubicin Loading Capacity of MIL-100(Fe): Effect of Synthesis Conditions.* Journal of Inorganic and Organometallic Polymers and Materials, 2020 DOI: 10.1007/s10904-020-01456-2
12. Rojas, S., et al., *Toward Understanding Drug Incorporation and Delivery from Biocompatible Metal-Organic Frameworks in View of Cutaneous Administration.* ACS omega, 2018. **3**(3): p. 2994-3003 DOI: 10.1021/acsomega.8b00185
13. Keskin, S. and S. Kızılel, *Biomedical Applications of Metal Organic Frameworks.* Industrial & Engineering Chemistry Research, 2011. **50**(4): p. 1799-1812 DOI: 10.1021/ie101312k
14. Kotzabasaki, M. and G.E. Froudakis, *Review of computer simulations on anti-cancer drug delivery in MOFs.* Inorganic Chemistry Frontiers, 2018. **5**(6): p. 1255-1272 DOI: 10.1039/C7QI00645D
15. Liu, J.-Q., et al., *A combined experimental and computational study of novel nanocage-based metal–organic frameworks for drug delivery.* Dalton Transactions, 2015. **44**(44): p. 19370-19382 DOI: 10.1039/C5DT02171E
16. Kotzabasaki, M., et al., *OH-functionalization strategy in Metal-Organic Frameworks for drug delivery.* Chemical Physics Letters, 2017. **685**: p. 114-118 DOI: https://doi.org/10.1016/j.cplett.2017.07.053
17. Thompson, M., S. Wells, and T. Düren, *Molecular simulations of cisplatin uptake and release in UiO-66 and UiO-66(NH2)*. 2020, University of Bath.
18. Mocniak, K.A., et al., *Incorporation of cisplatin into the metal–organic frameworks UiO66-NH2 and UiO66 – encapsulation vs. conjugation.* Royal Society Chemistry Advances, 2015. **5**(102): p. 83648-83656 DOI: 10.1039/C5RA14011K
19. Li, F., et al., *Encapsulation of pharmaceutical ingredient linker in metal–organic framework: combined experimental and theoretical insight into the drug delivery.* Royal Society Chemistry Advances, 2016. **6**(53): p. 47959-47965 DOI: 10.1039/C6RA06178H

20. Kotzabasaki, M., et al., *Multiscale simulations reveal IRMOF-74-III as a potent drug carrier for gemcitabine delivery.* Journal of Materials Chemistry B, 2017. **5**(18): p. 3277-3282 DOI: 10.1039/C7TB00220C
21. Abánades Lázaro, I. and R.S. Forgan, *Application of zirconium MOFs in drug delivery and biomedicine.* Coordination Chemistry Reviews, 2019. **380**: p. 230-259 DOI: https://doi.org/10.1016/j.ccr.2018.09.009
22. Cavka, J.H., et al., *A New Zirconium Inorganic Building Brick Forming Metal Organic Frameworks with Exceptional Stability.* Journal of the American Chemical Society, 2008. **130**(42): p. 13850-13851 DOI: 10.1021/ja8057953
23. Svane, K.L., et al., *Vacancy defect configurations in the metal–organic framework UiO-66: energetics and electronic structure.* Journal of Materials Chemistry A, 2018. **6**(18): p. 8507-8513 DOI: 10.1039/C7TA11155J
24. Feng, X., et al., *Engineering a Highly Defective Stable UiO-66 with Tunable Lewis-Brønsted Acidity: The Role of the Hemilabile Linker.* Journal of the American Chemical Society, 2020. **142**(6): p. 3174-3183 DOI: 10.1021/jacs.9b13070
25. Bueken, B., et al., *Tackling the Defect Conundrum in UiO-66: A Mixed-Linker Approach to Engineering Missing Linker Defects.* Chemistry of Materials, 2017. **29**(24): p. 10478-10486 DOI: 10.1021/acs.chemmater.7b04128
26. Wu, H., et al., *Unusual and Highly Tunable Missing-Linker Defects in Zirconium Metal–Organic Framework UiO-66 and Their Important Effects on Gas Adsorption.* Journal of the American Chemical Society, 2013. **135**(28): p. 10525-10532 DOI: 10.1021/ja404514r
27. Filippousi, M., et al., *Biocompatible Zr-based nanoscale MOFs coated with modified poly(ε-caprolactone) as anticancer drug carriers.* International Journal of Pharmaceutics, 2016. **509**(1): p. 208-218 DOI: https://doi.org/10.1016/j.ijpharm.2016.05.048
28. Lin, S.-X., et al., *Effective loading of cisplatin into a nanoscale UiO-66 metal–organic framework with preformed defects.* Dalton Transactions, 2019. **48**(16): p. 5308-5314 DOI: 10.1039/C9DT00719A
29. Sarkisov, L. and A. Harrison, *Computational structure characterisation tools in application to ordered and disordered porous materials.* Molecular Simulation, 2011. **37**(15): p. 1248-1257 DOI: 10.1080/08927022.2011.592832
30. Øien, S., et al., *Detailed Structure Analysis of Atomic Positions and Defects in Zirconium Metal–Organic Frameworks.* Crystal Growth & Design, 2014. **14**(11): p. 5370-5372 DOI: 10.1021/cg501386j

31. Gutov, O.V., et al., *Metal–Organic Framework (MOF) Defects under Control: Insights into the Missing Linker Sites and Their Implication in the Reactivity of Zirconium-Based Frameworks.* Inorganic Chemistry, 2015. **54**(17): p. 8396-8400 DOI: 10.1021/acs.inorgchem.5b01053
32. Groom, C.R., *The Cambridge Structural Database*, A. Crystallographica, Editor. 2016.
33. Yang, Q., et al., *CH4 storage and CO2 capture in highly porous zirconium oxide based metal–organic frameworks.* Chemical Communications, 2012. **48**(79): p. 9831-9833 DOI: 10.1039/C2CC34714H
34. Trickett, C.A., et al., *Definitive Molecular Level Characterization of Defects in UiO-66 Crystals.* Angewandte Chemie International Edition, 2015. **54**(38): p. 11162-11167 DOI: 10.1002/anie.201505461
35. Macrae, C., et al., *Mercury 4.0: from visualization to analysis, design and prediction.* Journal of Applied Crystallography, 2020. **53**: p. 226-235
36. Yesylevskyy, S., et al., *Empirical force field for cisplatin based on quantumdynamics data: case study of new parameterization scheme for coordinationcompounds.* Journal of Molecular Modeling, 2015. **21**(10): p. 268 DOI: 10.1007/s00894-015-2812-0
37. Jorgensen, W.L., et al., *Comparison of simple potential functions for simulating liquid water.* The Journal of Chemical Physics, 1983. **79**(2): p. 926-935 DOI: 10.1063/1.445869
38. Rappe, A.K., et al., *UFF, a full periodic table force field for molecular mechanics and molecular dynamics simulations.* Journal of the American Chemical Society, 1992. **114**(25): p. 10024-10035 DOI: 10.1021/ja00051a040
39. Garberoglio, G., *OBGMX: A web-based generator of GROMACS topologies for molecular and periodic systems using the universal force field.* Journal of Computational Chemistry, 2012. **33**(27): p. 2204-2208 DOI: 10.1002/jcc.23049
40. Coudert, F.-X., *The osmotic framework adsorbed solution theory: predicting mixture coadsorption in flexible nanoporous materials.* Physical Chemistry Chemical Physics, 2010. **12**(36): p. 10904-10913 DOI: 10.1039/C003434G
41. Berendsen, H.J.C., D. van der Spoel, and R. van Drunen, *GROMACS: A message-passing parallel molecular dynamics implementation.* Computer Physics Communications, 1995. **91**(1): p. 43-56 DOI: https://doi.org/10.1016/0010-4655(95)00042-E

42. Bekker, H., et al., *Gromacs - a Parallel Computer for Molecular-Dynamics Simulations.* Physics Computing '92, 1993: p. 252-256
43. Lindahl, E., B. Hess, and D. van der Spoel, *GROMACS 3.0: a package for molecular simulation and trajectory analysis.* Molecular modeling annual, 2001. **7**(8): p. 306-317 DOI: 10.1007/s008940100045
44. Van Der Spoel, D., et al., *GROMACS: Fast, flexible, and free.* Journal of Computational Chemistry, 2005. **26**(16): p. 1701-1718 DOI: 10.1002/jcc.20291
45. Hess, B., et al., *GROMACS 4: Algorithms for Highly Efficient, Load-Balanced, and Scalable Molecular Simulation.* Journal of Chemical Theory and Computation, 2008. **4**(3): p. 435-447 DOI: 10.1021/ct700301q
46. Pronk, S., et al., *GROMACS 4.5: a high-throughput and highly parallel open source molecular simulation toolkit.* Bioinformatics, 2013. **29**(7): p. 845-54 DOI: 10.1093/bioinformatics/btt055
47. Darden, T., D. York, and L. Pedersen, *Particle mesh Ewald: An N·log(N) method for Ewald sums in large systems.* The Journal of Chemical Physics, 1993. **98**(12): p. 10089-10092 DOI: 10.1063/1.464397
48. Essmann, U., et al., *A smooth particle mesh Ewald method.* The Journal of Chemical Physics, 1995. **103**(19): p. 8577-8593 DOI: 10.1063/1.470117
49. Bussi, G., D. Donadio, and M. Parrinello, *Canonical sampling through velocity rescaling.* The Journal of Chemical Physics, 2007. **126**(1): p. 014101 DOI: 10.1063/1.2408420
50. Nosé, S., *A unified formulation of the constant temperature molecular dynamics methods.* The Journal of Chemical Physics, 1984. **81**(1): p. 511-519 DOI: 10.1063/1.447334
51. Hoover, W.G., *Canonical dynamics: Equilibrium phase-space distributions.* Physical Review A, 1985. **31**(3): p. 1695-1697 DOI: 10.1103/PhysRevA.31.1695
52. Freyss, M., *Atomic transport properties*. 2015: Nuclear Energy Agency of the OECD (NEA). p. 187-198.
53. Hutter, J., et al., *cp2k: atomistic simulations of condensed matter systems.* Wiley interdisciplinary reviews. Computational molecular science, 2014. **4**: p. 25 DOI: 10.1002/wcms.1159
54. VandeVondele, J., et al., *Quickstep: Fast and accurate density functional calculations using a mixed Gaussian and plane waves approach.* Computer Physics Communications, 2005. **167**(2): p. 103-128 DOI: https://doi.org/10.1016/j.cpc.2004.12.014

55. Borštnik, U., et al., *Sparse matrix multiplication: The distributed block-compressed sparse row library.* Parallel Computing, 2014. **40**(5): p. 47-58 DOI: https://doi.org/10.1016/j.parco.2014.03.012

56. Frigo, M. and S.G. Johnson, *The Design and Implementation of FFTW3.* Proceedings of the Institute of Electrical and Electronics Engineers, 2005. **93**(2): p. 216-231 DOI: 10.1109/JPROC.2004.840301

57. VandeVondele, J. and J. Hutter, *An efficient orbital transformation method for electronic structure calculations.* The Journal of Chemical Physics, 2003. **118**(10): p. 4365-4369 DOI: 10.1063/1.1543154

58. Lippert, B.G., J.H. Parrinello, and Michele, *A hybrid Gaussian and plane wave density functional scheme.* Molecular Physics, 1997. **92**(3): p. 477-488 DOI: 10.1080/002689797170220

59. Hartwigsen, C., S. Goedecker, and J. Hutter, *Relativistic separable dual-space Gaussian pseudopotentials from H to Rn.* Physical Review B, 1998. **58**(7): p. 3641-3662 DOI: 10.1103/PhysRevB.58.3641

60. Goedecker, S., M. Teter, and J. Hutter, *Separable dual-space Gaussian pseudopotentials.* Physical Review B, 1996. **54**(3): p. 1703-1710 DOI: 10.1103/PhysRevB.54.1703

61. VandeVondele, J. and J. Hutter, *Gaussian basis sets for accurate calculations on molecular systems in gas and condensed phases.* The Journal of Chemical Physics, 2007. **127**(11): p. 114105 DOI: 10.1063/1.2770708

62. Perdew, J.P., K. Burke, and M. Ernzerhof, *Generalized Gradient Approximation Made Simple.* Physical Review Letters, 1996. **77**(18): p. 3865-3868 DOI: 10.1103/PhysRevLett.77.3865

63. Grimme, S., S. Ehrlich, and L. Goerigk, *Effect of the damping function in dispersion corrected density functional theory.* Journal of Computational Chemistry, 2011. **32**(7): p. 1456-65 DOI: 10.1002/jcc.21759

64. Grimme, S., et al., *A consistent and accurate ab initio parametrization of density functional dispersion correction (DFT-D) for the 94 elements H-Pu.* The Journal of Chemical Physics, 2010. **132**(15): p. 154104 DOI: 10.1063/1.3382344

65. Amirjalayer, S. and R. Schmid, *Influence of Pore Dimension on the Host–Guest Interaction in Metal–Organic Frameworks.* The Journal of Physical Chemistry C, 2016. **120**(48): p. 27319-27327 DOI: 10.1021/acs.jpcc.6b08609

66. Forse, A.C., et al., *Influence of Pore Size on Carbon Dioxide Diffusion in Two Isoreticular Metal–Organic Frameworks.* Chemistry of Materials, 2020. **32**(8): p. 3570-3576 DOI: 10.1021/acs.chemmater.0c00745
67. Skoulidas, A.I. and D.S. Sholl, *Molecular Dynamics Simulations of Self-Diffusivities, Corrected Diffusivities, and Transport Diffusivities of Light Gases in Four Silica Zeolites To Assess Influences of Pore Shape and Connectivity.* The Journal of Physical Chemistry A, 2003. **107**(47): p. 10132-10141 DOI: 10.1021/jp0354301
68. Erucar, I. and S. Keskin, *Computational investigation of metal organic frameworks for storage and delivery of anticancer drugs.* Journal of Materials Chemistry B, 2017. **5**(35): p. 7342-7351 DOI: 10.1039/C7TB01764B

Tailoring defects or building units for controlled cisplatin drug delivery

Supporting information

Megan J. Thompson, Tina Düren[*]

AUTHOR ADDRESS Prof. T. Düren, Centre for Advanced Separations Engineering, Department of Chemical Engineering, University of Bath, BA2 7AY, UK
E-mail: t.duren@bath.ac.uk

Table of Contents

Section S1. Optimal water loading

To determine the optimal water loading, cisplatin molecules were initially positioned in each system to achieve a loading of 1CPT/octahedral pore. Next, GROMACS was used to solvate the system, and this was followed by a 200 ps NVT equilibration. These steps of solvation – equilibration were carried out over 20 times for each system, and plots of the system potential energy against solvation were used to determine the water loading which achieves the optimal energy (Figure S1). For most systems, the optimal loading was taken to be when the average energy per water molecule is at its minima. The loading in UiO-66 is in agreement with experimental results (7CPT/Zr = 25 mmol/g as opposed to experimental results of 20 – 25 mmol/g [58-62]).

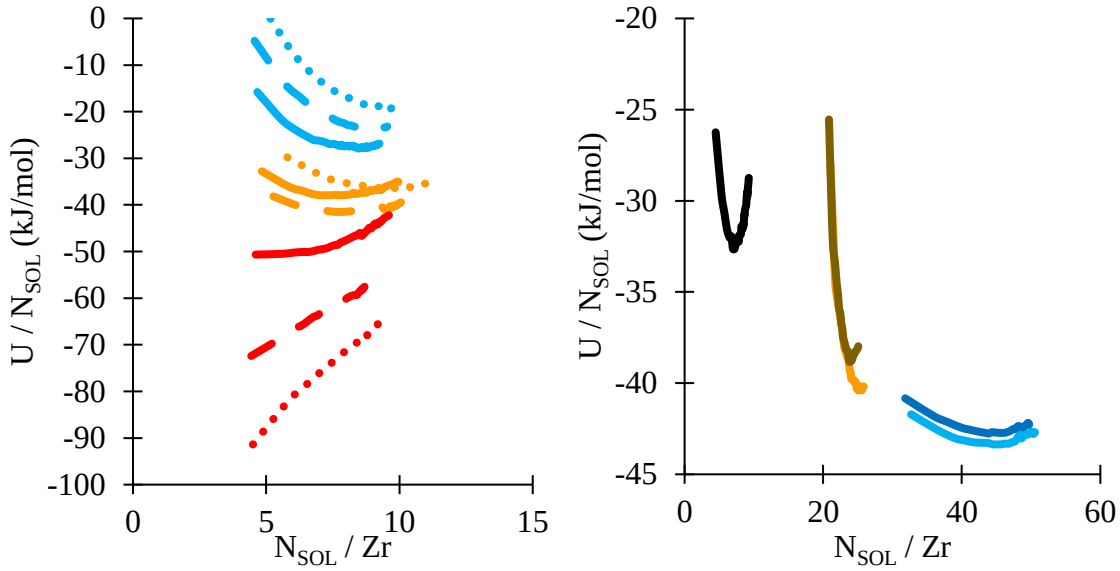

Figure S1. Average potential energy normalised with respect to the number of water molecules as a function of the number of water molecules. Shown for (a) defective UiO-66 structures (yellow=MA, blue=EA, red=TFA), and (b) defect-free UiO-66 (black), UiO-67 (brown, NH_2 variant = gold), and UiO-68 (blue, NH_2 variant = light blue)

In the case of TFA, no such equilibrium point is seen due to strong energy sites within the framework caused by the TFA groups. Instead, the average energy per water molecule gradually becomes less favourable with increased loading. As a best estimate, we used the maximum achievable loading (which is also the minima for the average potential energy not normalised with respect to the number of water molecules). This may reduce the cisplatin movement in each TFA model compared to the other systems, however the conclusions drawn from this paper would remain the same.

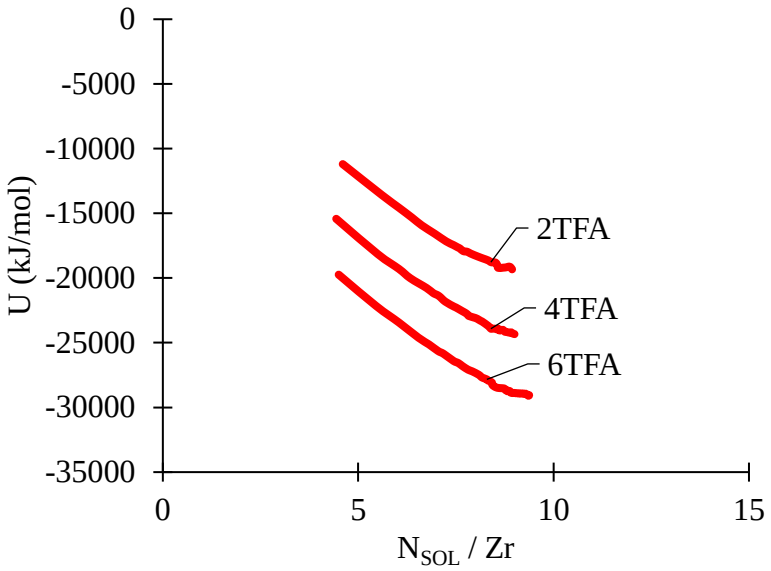

Figure S2. Average potential energy as a function of the number of water molecules in the TFA modulated UiO-66 structures.

Section S2. Spring constants and pull velocity

For a fair analysis, the spring constant (which determines the strength of the Harmonic potential acting on the SMD atoms) was kept constant across all systems. Its value was chosen based on the optimal for UiO-66, which based on its small and comparatively rigid pore-windows would have the highest pore-hopping energy barrier and would also require the tightest constraint (Table S1). The pull velocity was also kept constant across all systems, however due to the variation in channel sizes multiple values were tested for each framework to check that reproduceable paths were formed (which are shown in Figure S3).

Table S1. Energy barriers for UiO-66 obtained using a variety of spring constants and pull velocities

v (nm/ps) / k (kJ/mol.nm^2)	0.0025	0.005	0.01	0.05
1000	70	70	70	70
2000	90	90	90	90
3000	100	90	90	90
4000	80	100	100	100
5000	100	100	100	100

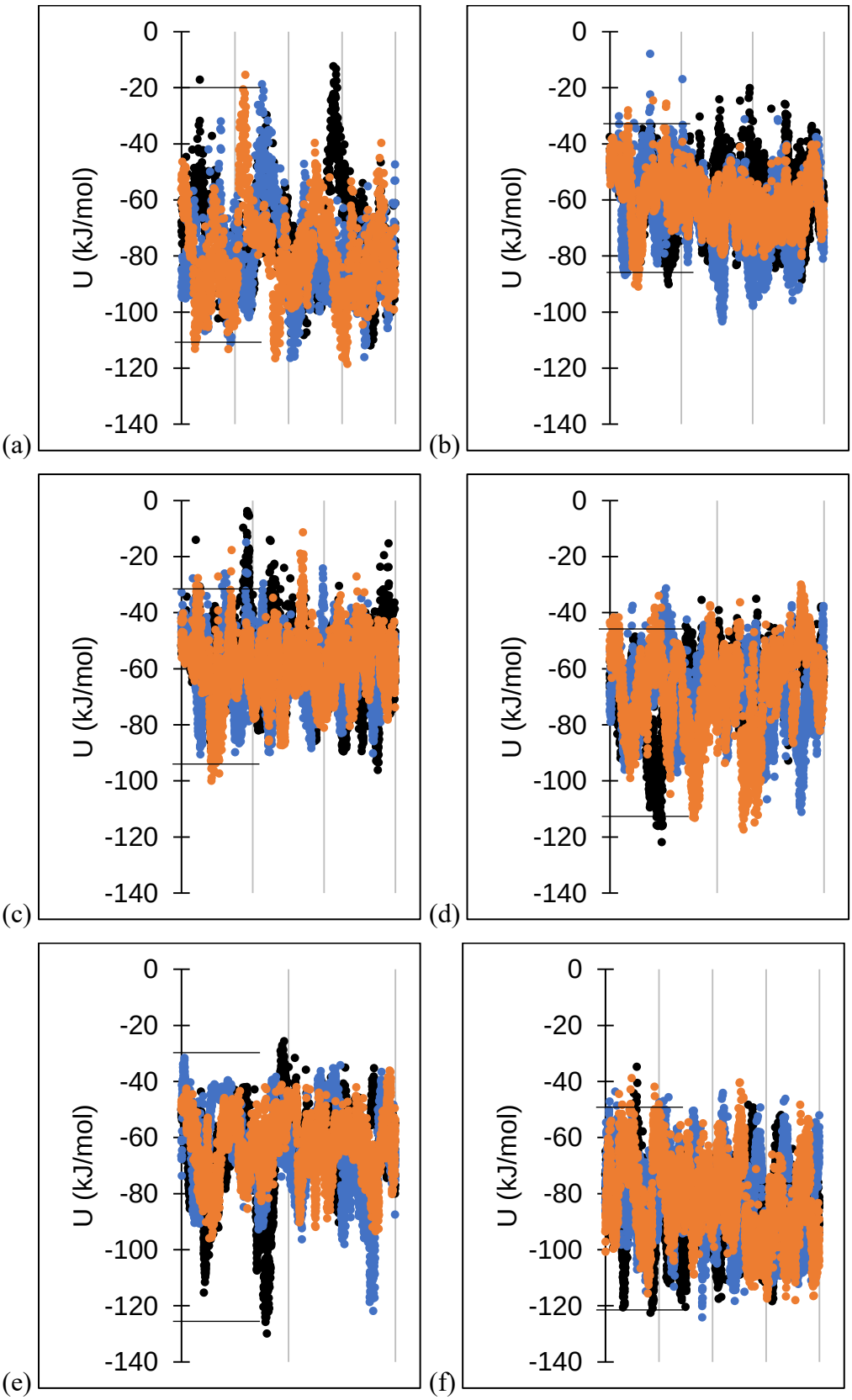
(a)
(b)
(c)
(d)
(e)
(f)
U (kJ/mol)
0
-20
-40
-60
-80
-100
-120
-140

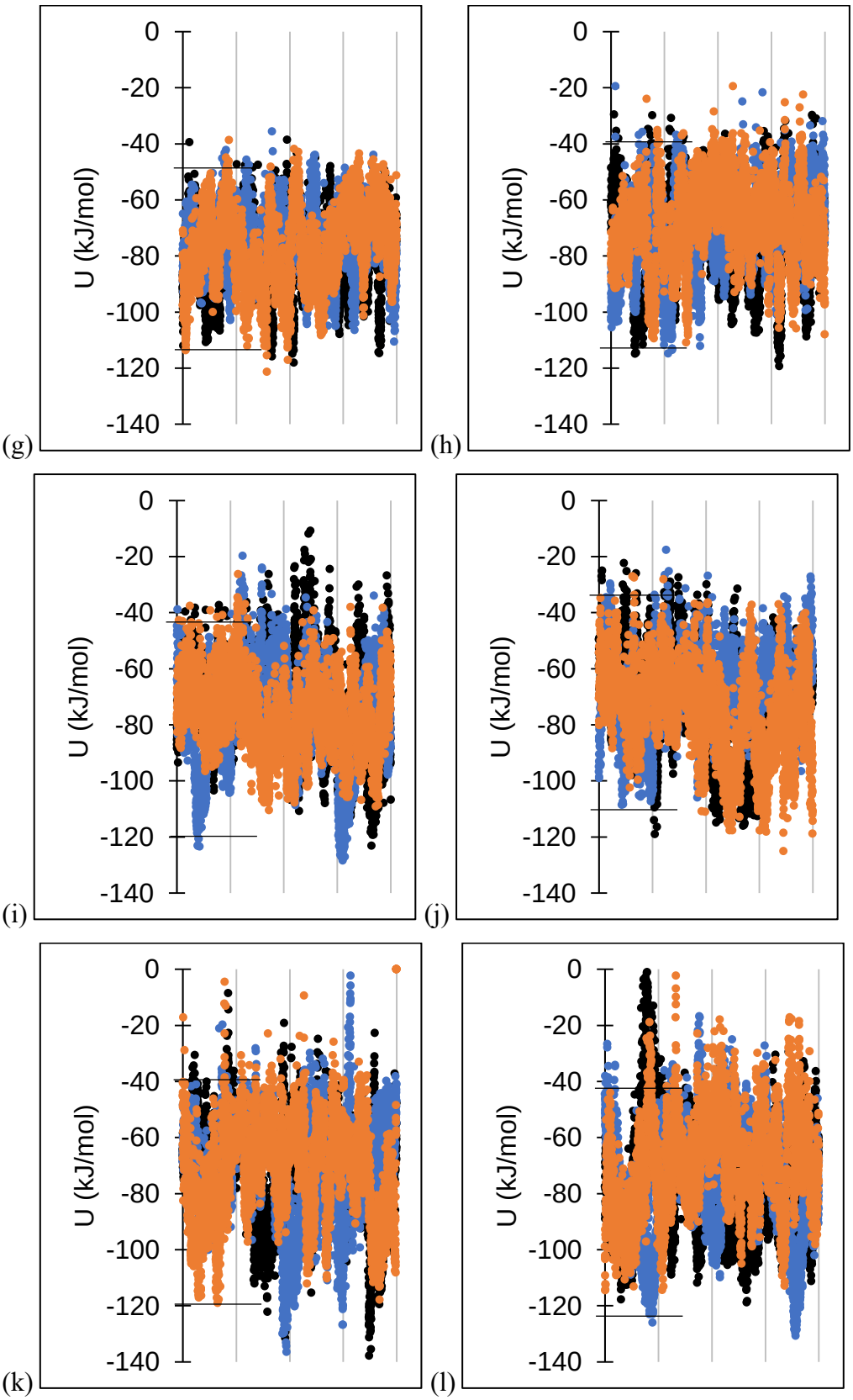
(g)
(h)
(i)
(j)
(k)
(l)
U (kJ/mol)
0
-20
-40
-60
-80
-100
-120
-140

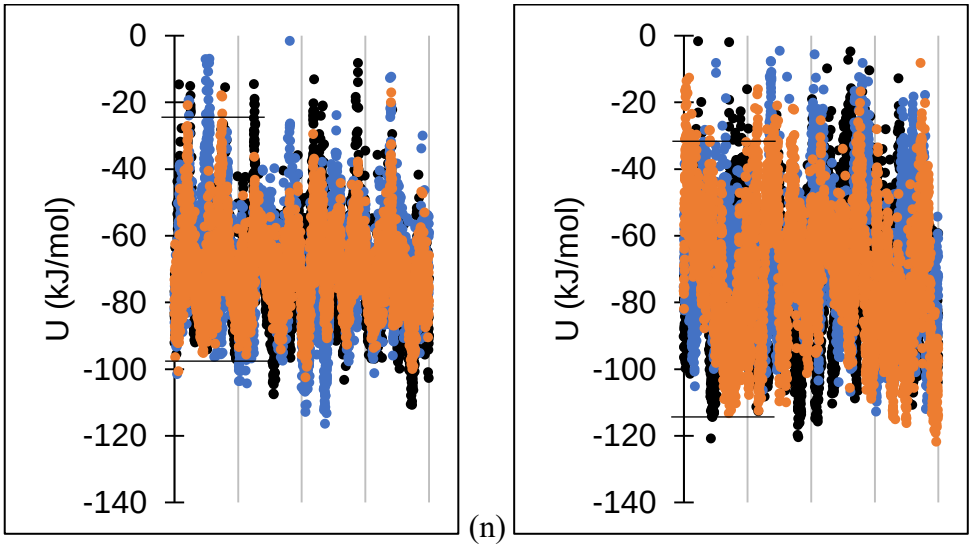

Figure S3. Non-bonded potential energy barrier (consists of $U_{MOF-CPT}$, $U_{MOF-SOL}$, $U_{SOL-SOL}$, $U_{CPT-SOL}$) along the coordinate path of the pull simulations. Shown for (a) UiO-66, (b) UiO-67, (c) UiO-67(NH_2), (d) UiO-68, (e) UiO-68(NH_2), (f) 2MA, (g) 4MA, (h) 6MA, (i) 2EA, (j) 4EA, (k) 6EA, (l) 2TFA, (m) 4TFA, and (n) 6TFA. (k=5,000 kJ/mol.nm^2, v=0.0025 nm/ps). Black horizontal lines show the maximum energy barrier observed. Different coloured series are independent SMD simulations.

Section S3. Cisplatin MSD (no solvent, 1CPT/unit cell)

All figures in this section of the SI refer to the systems whereby a single cisplatin molecule is simulated in an otherwise empty structure. At least seven repeats were carried out for each dataset. Figure S4 shows the MSD plots for a single cisplatin molecule inside each non-solvated structure at 298 K. Figure S5 shows the MSD plots for a single cisplatin molecule inside each non-solvated structure at temperatures ranging from 348 K – 798 K. Figure S6 shows the resulting cisplatin diffusivities as a function of temperature.

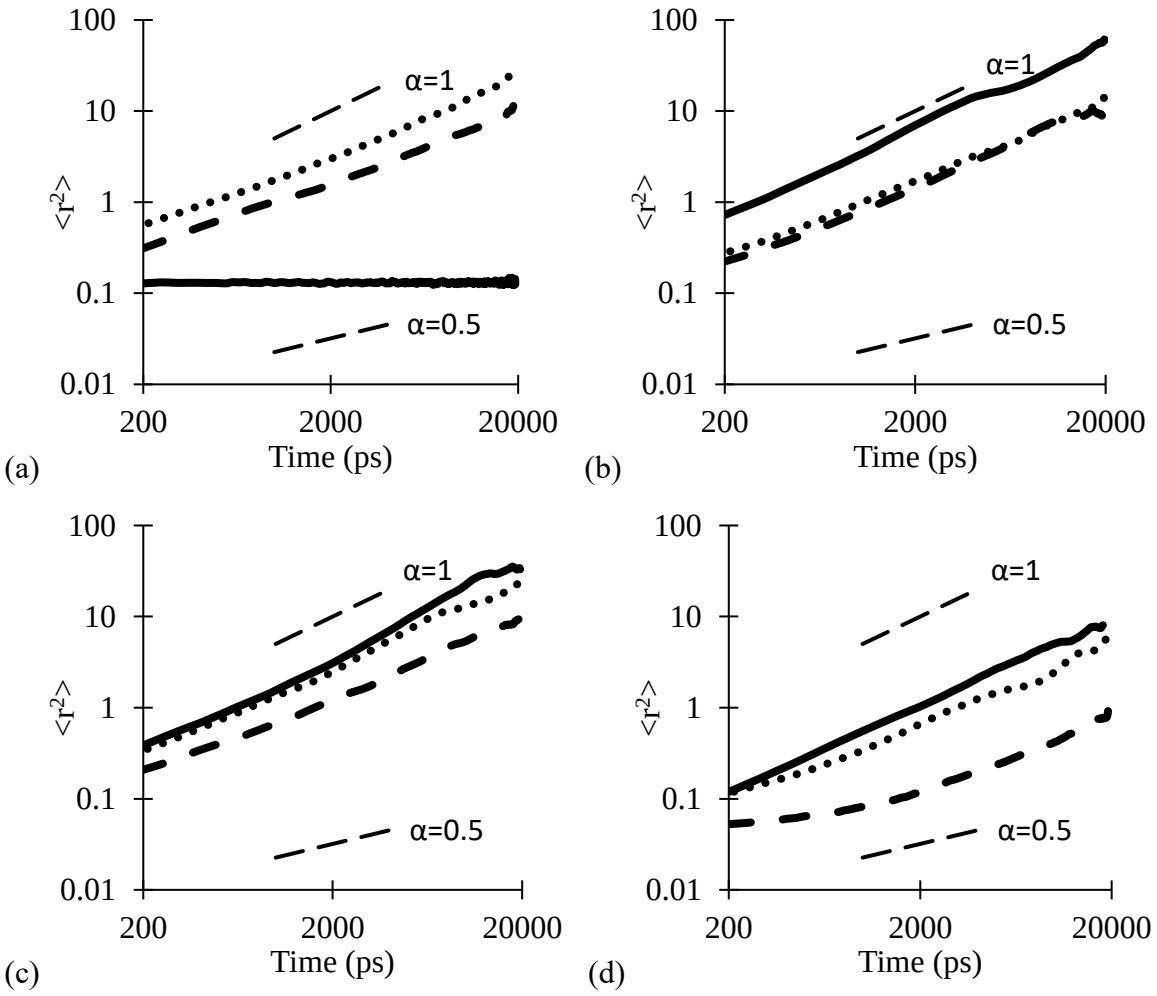

Figure S4. MSD plots of cisplatin in each structure at 298 K in (a) UiO-66, UiO-67, UiO-68, (b) 2MA, 4MA, 6MA, (c) 2AA, 4AA, 6AA, and (d) 2TFA, 4TFA, 6TFA. Line style for each series in order as given = solid, dashed, dotted. The expected gradients for normal and sub diffusion are represented by the black dotted lines, where $\langle r^2 \rangle$ is proportional to t^{α} (α = 1 and α = 0.5 respectively).

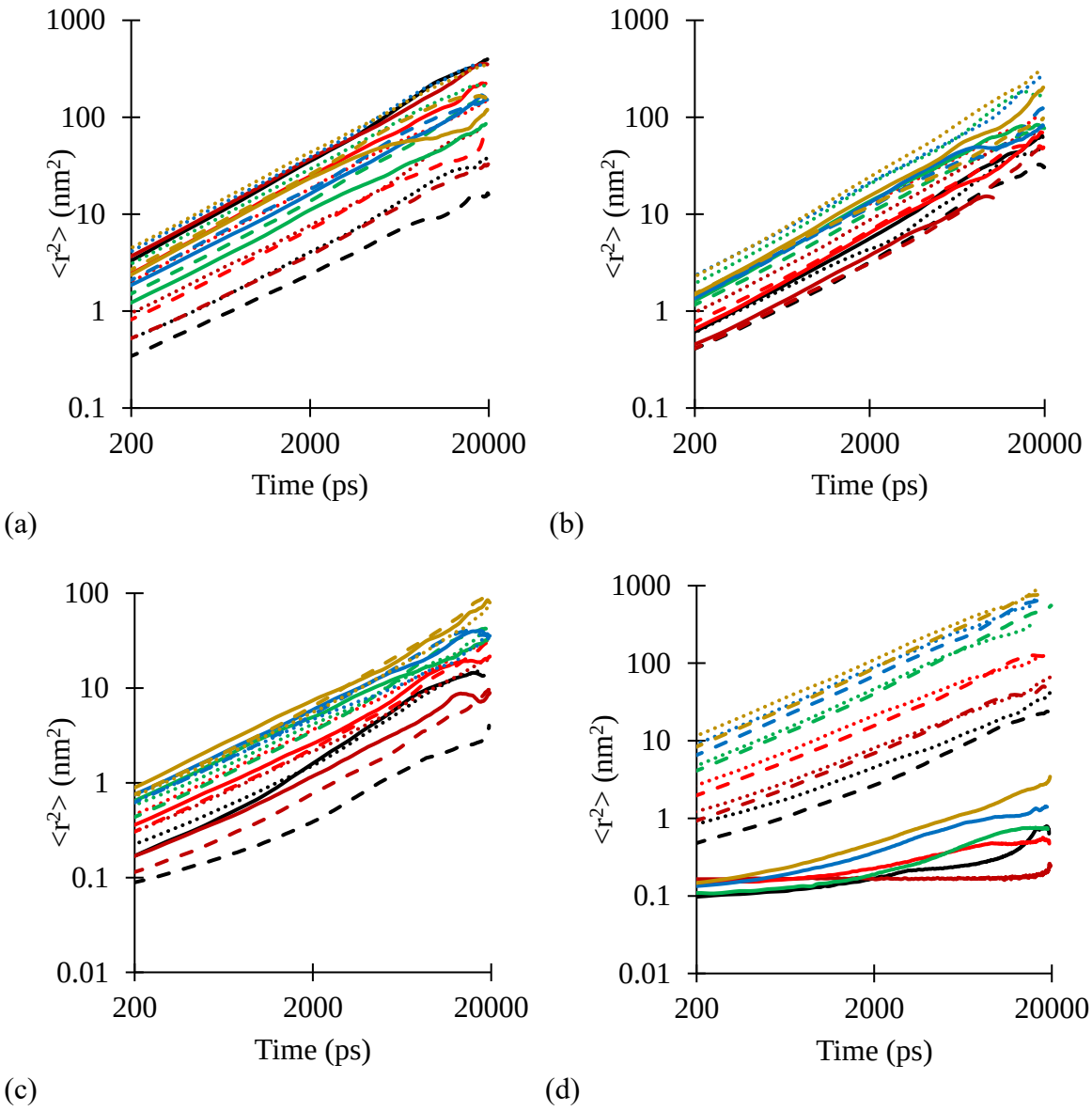

Figure S5. MSD for a single cisplatin molecule in (a) 2MA, 4MA, 6MA, (b) 2AA, 4AA, 6AA, (c) 2TFA, 4TFA, 6TFA, and (d) UiO-66, UiO-67, and UiO-68, averaged over at least seven repeats. Line style for each series in order as given = solid, dashed, dotted. Colours: black=348 K, dark red = 398 K, red = 498 K, green = 598 K, blue = 698 K, gold = 798 K.

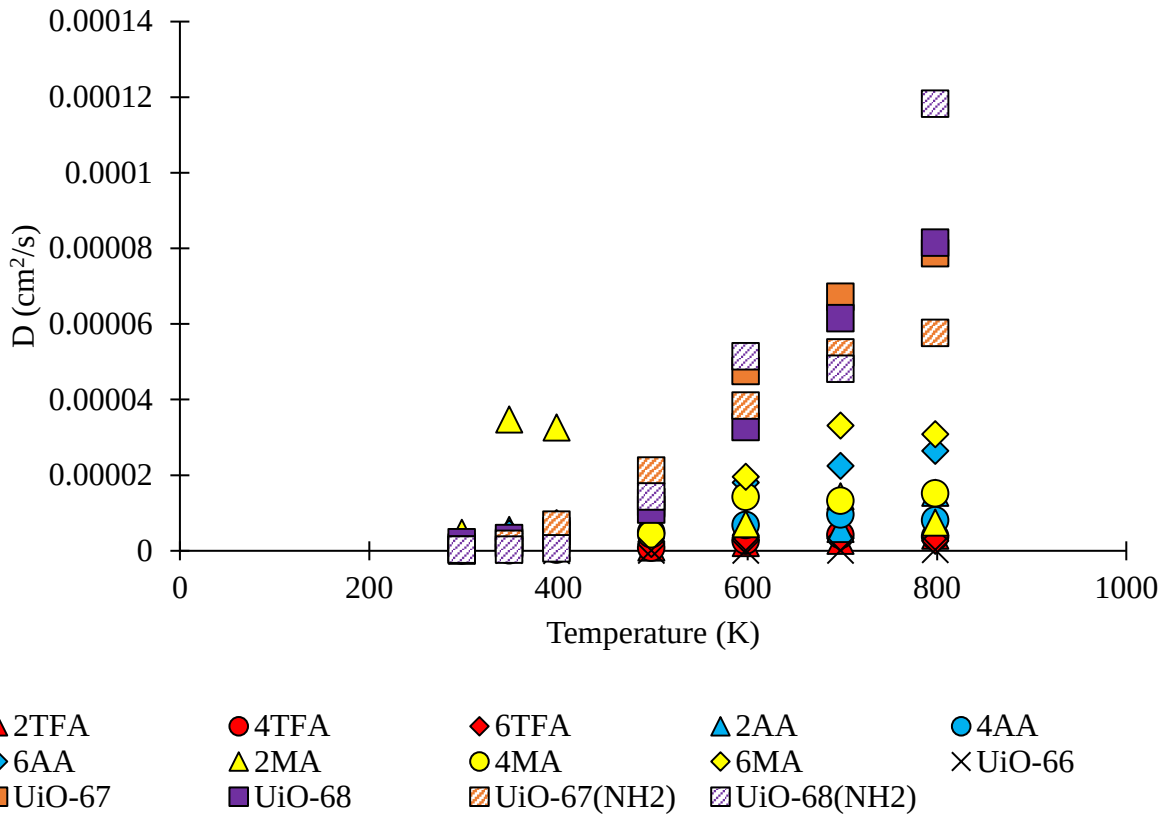

Figure S6. Diffusivities of a single cisplatin molecule inside otherwise empty structures at temperatures between 298 K and 798 K.

Section S4. Cisplatin – modulator & cisplatin – ligand interaction energies in empty frameworks

All of the interaction energies in this section refer to the systems in which a single cisplatin molecule is in an otherwise empty framework at 298 K. Figure S7 shows average cisplatin interaction energies with the functional groups of the modulators and ligands. Figure S8 shows the relationship (described in the main text) between cisplatin CPT – $[COO^-]_{modulator}$, CPT – $[chain]_{modulator}$ and the activation energy. Figure S9 shows an example of the variation in interaction energies between the TFA modulators and BDC ligands in 6TFA.

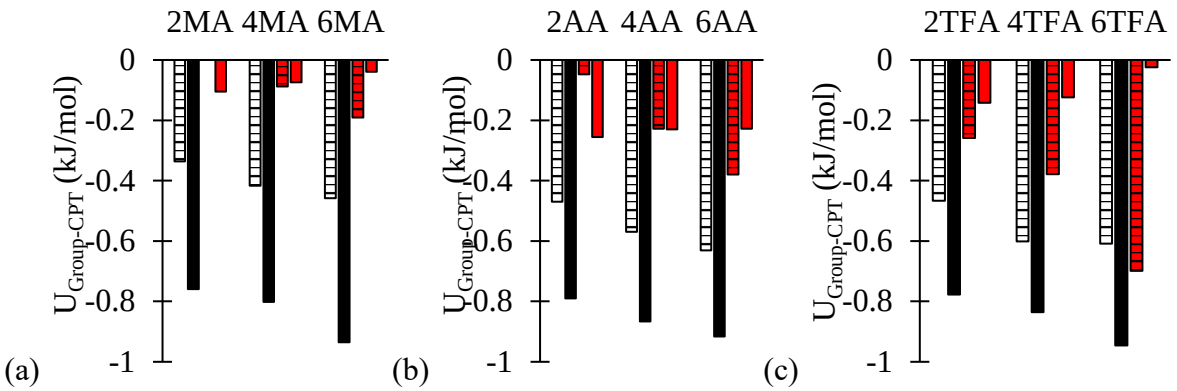

Figure S7. Normalised, average cisplatin interaction energies with the functional groups in the BDC ligands and modulators in defective UiO-66 structures. (Group colour scheme: white/black stripes = $[COO^-]_{BDC}$, black fill = $[C_6H_4]_{BDC}$, red/black stripes = $[COO^-]_{modulator}$, red fill = $[C_6H_4]_{modulator}$).

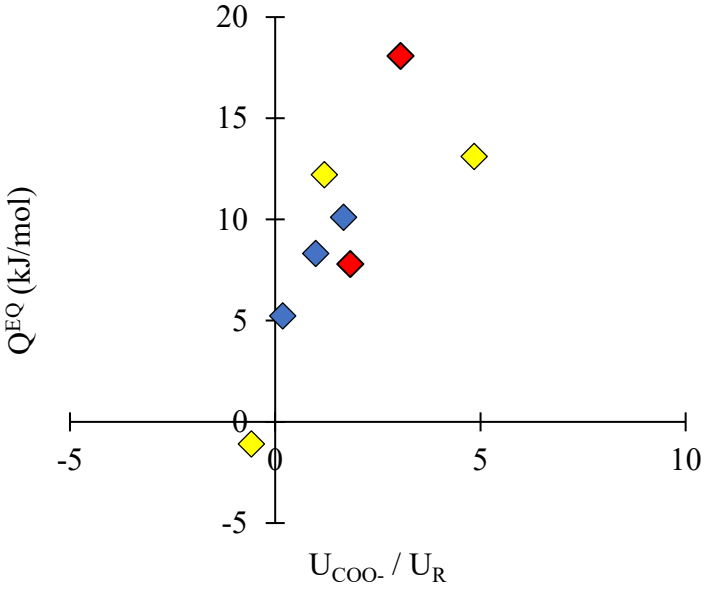

Figure S8. Activation energy as a function of the ratio of CPT – $[COO^-]_{modulator}$ and CPT – $[chain]_{modulator}$ energies. 6TFA has been excluded (for reasons explained in the main text). (Colour scheme: yellow = MA, blue = EA, red = TFA).

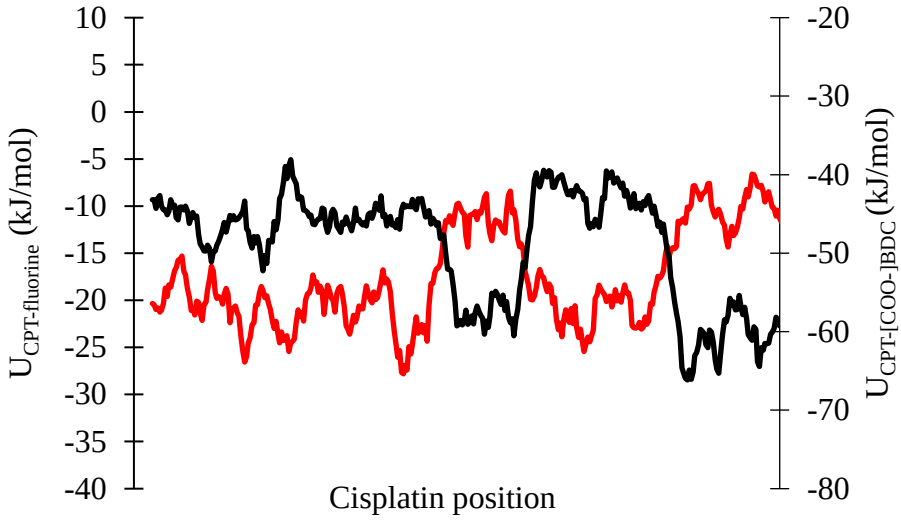

Figure S9. Example of variation in interaction energies between CPT – $[F]_{modulator}$ and CPT – $[COO^-]_{BDC}$ in 6TFA.

Section S5. Cisplatin agglomeration snapshots

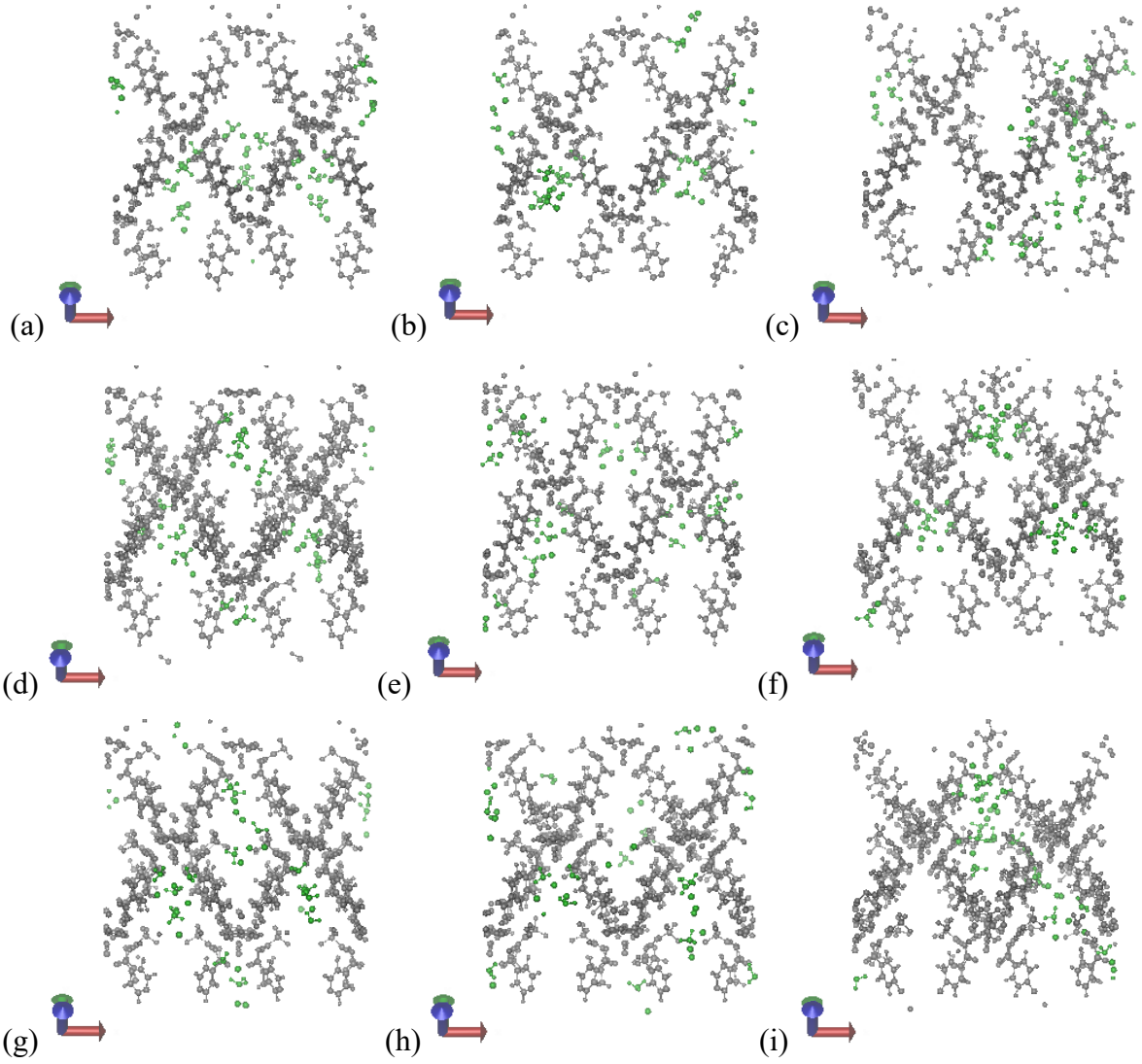

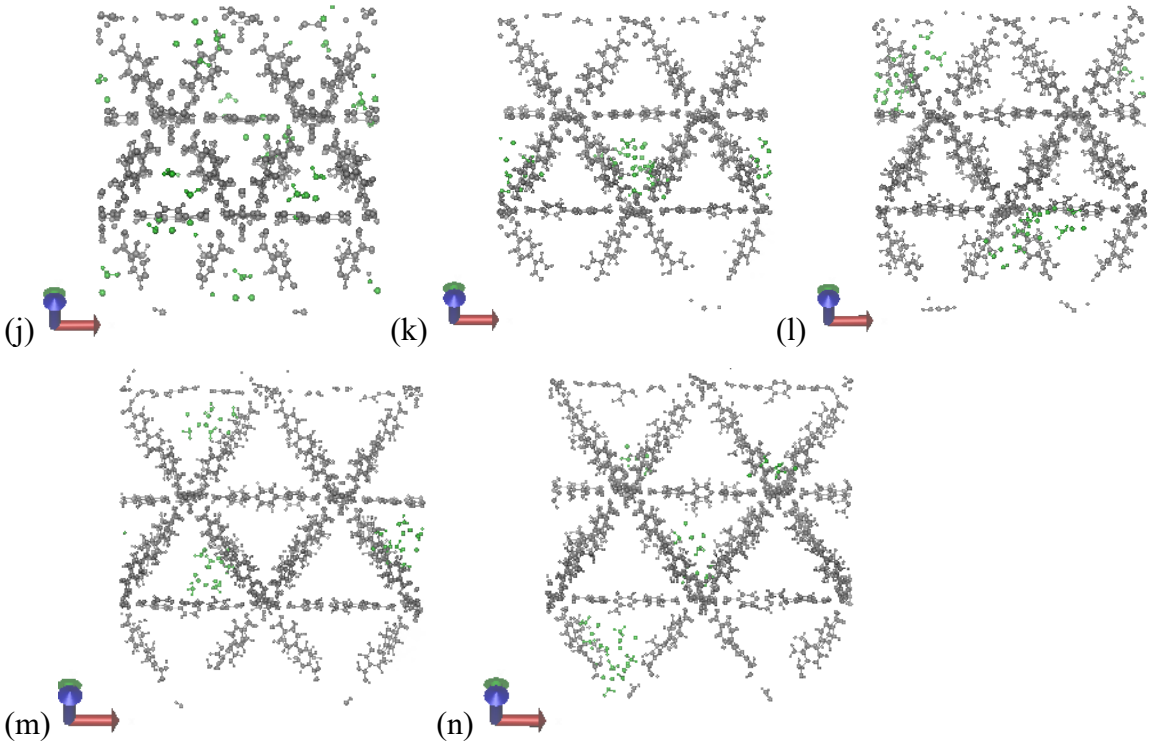

Figure S10. Equilibrated snapshots of cisplatin (green) at 298 K in non-solvated (a-n) 2MA, 4MA, 6MA, 2AA, 4AA, 6AA, 2TFA, 4TFA, 6TFA, UiO-66, UiO-67, UiO-67(NH_2), UiO-68, and UiO-68(NH_2) respectively (grey). Loading of 1CPT per octahedral pore

Section S6. MOF – cisplatin interaction energies with and without water

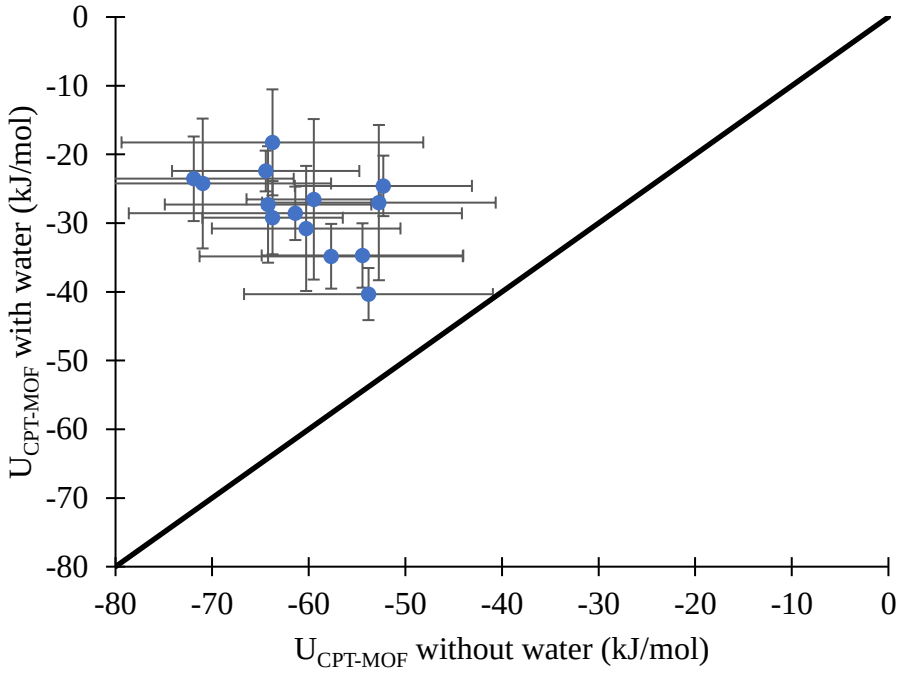

Figure S11: Average CPT-MOF interaction energy with and without water from equilibrium MD simulations at 298 K.

Section S7. MOF – cisplatin only potential energy landscapes

Figure S12 shows the potential energy variation as cisplatin is pulled through each solvated structure. Compared to Figure S3 (which was generated using the same solvated SMD simulations at 298 K) Figure S12 shows only the MOF – CPT interaction energies (as opposed to the full non-bonded potential energies).

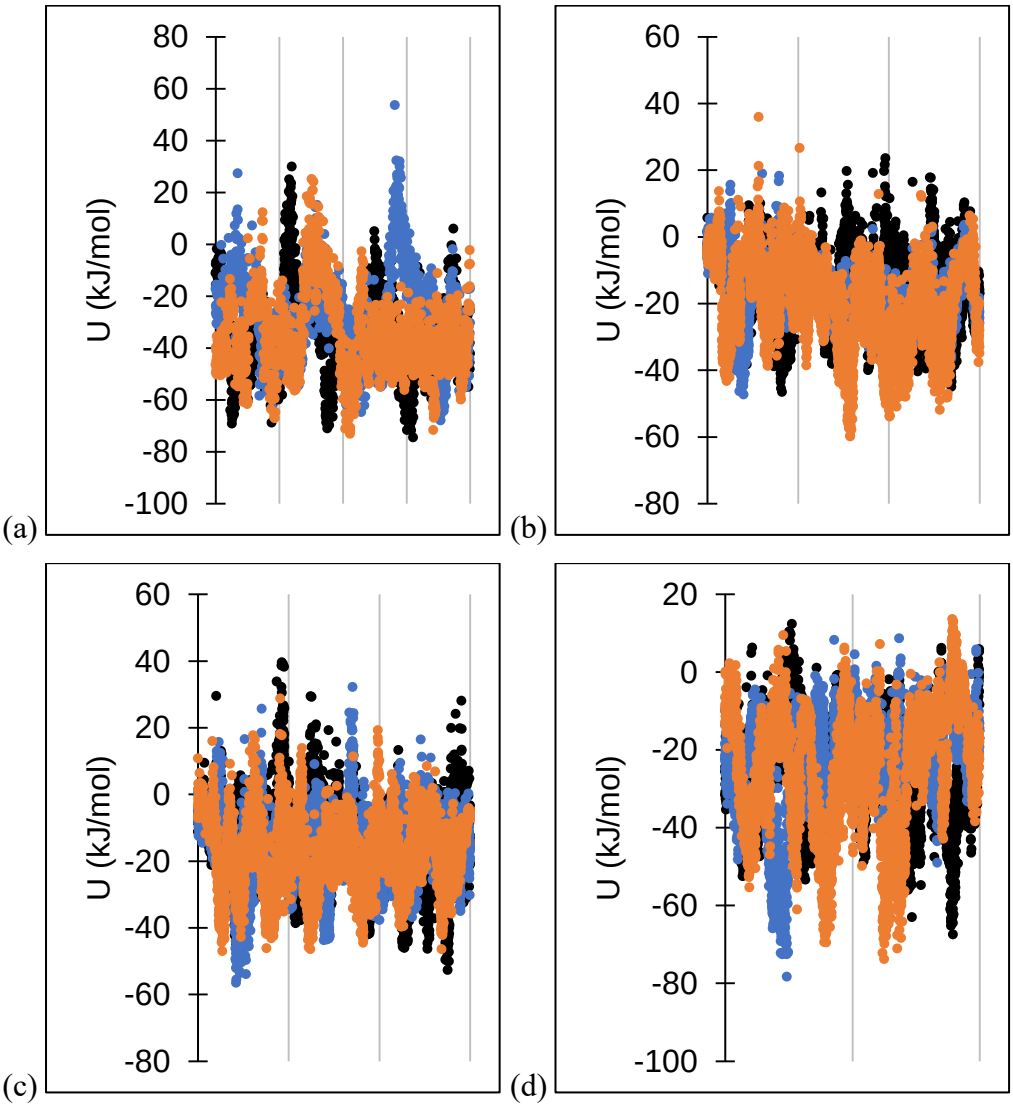

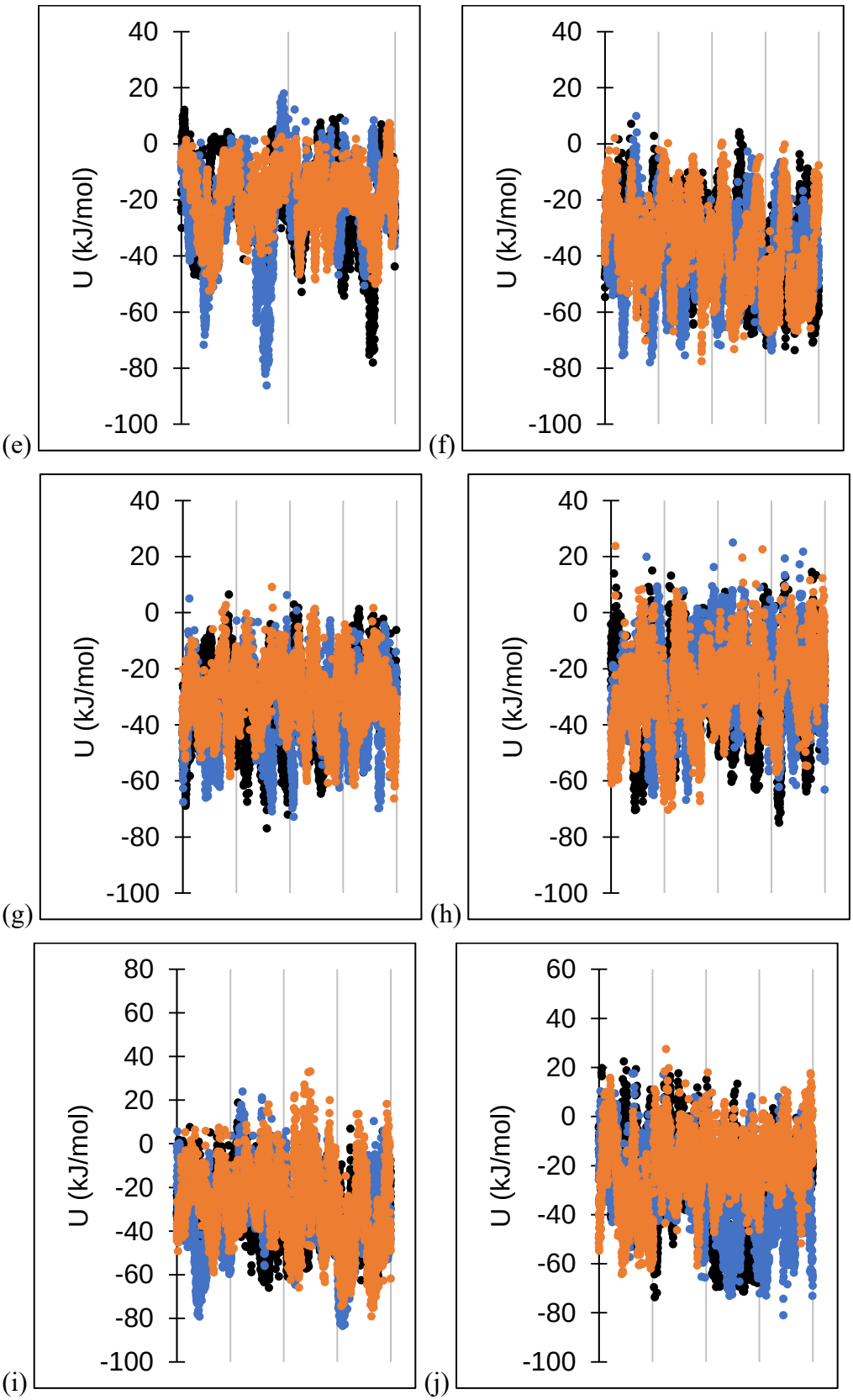
(e)
(f)
(g)
(h)
(i)
(j)
U (kJ/mol)
40
20
0
-20
-40
-60
-80
-100
80
60

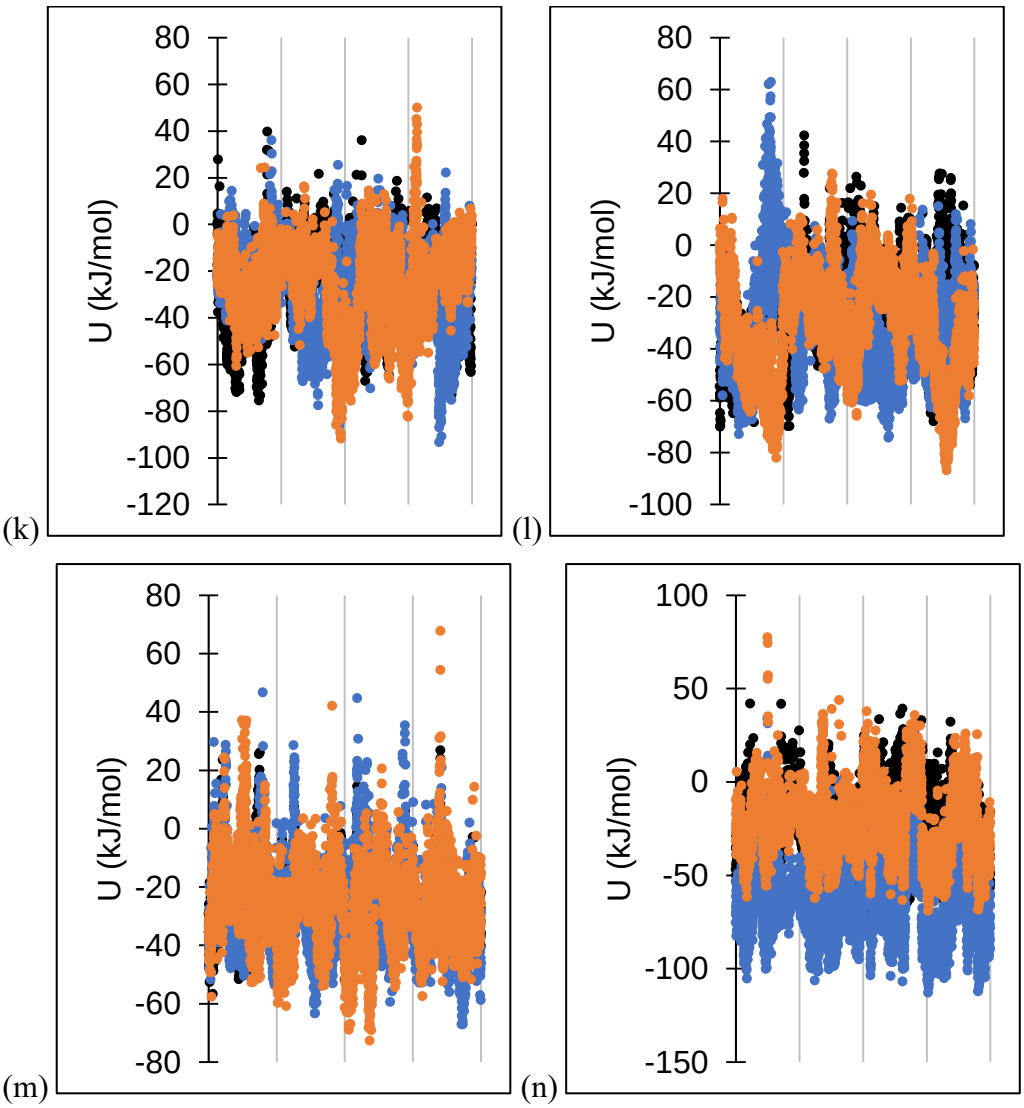

Figure S12. MOF - CPT potential energy barrier along the coordinate path of the pull simulations. Shown for (a) UiO-66, (b) UiO-67, (c) UiO-67(NH_2), (d) UiO-68, (e) UiO-68(NH_2), (f) 2MA, (g) 4MA, (h) 6MA, (i) 2EA, (j) 4EA, (k) 6EA, (l) 2TFA, (m) 4TFA, and (n) 6TFA. (k=5,000 kJ/mol.nm^2, v=0.0025 nm/ps). Different coloured series are independent SMD simulations.

Section S8. Closing of the MA structures upon optimisation

Figure S13 shows the structures of 4MA and 6MA before and after geometry and cell optimisation in CP2K.

(a)

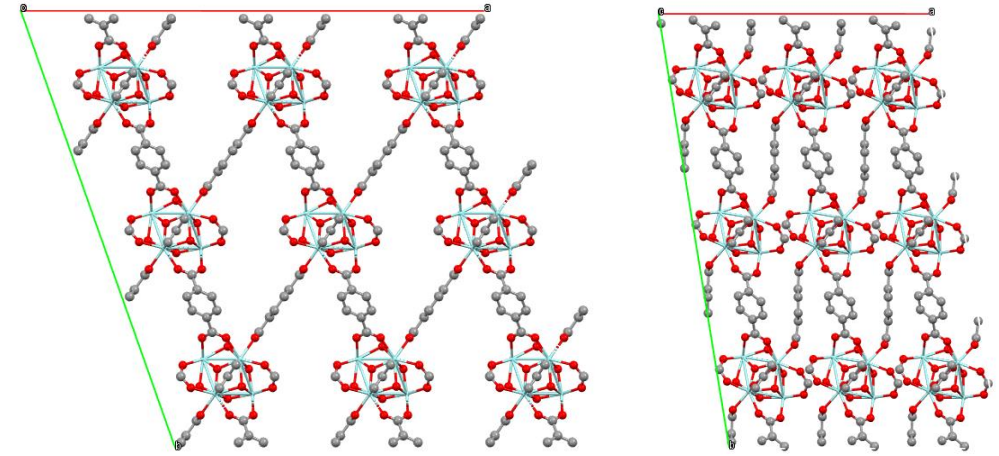

(b)

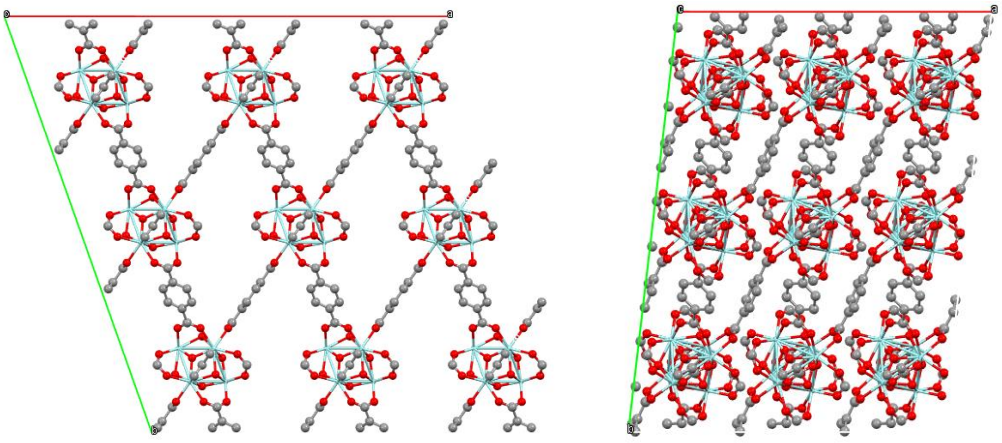

Figure S13. Structure of (a) 4MA and (b) 6MA, before and after (left to right) optimisation. View down c axis.

CHAPTER 6. CISPLATIN UPTAKE AND RELEASE IN PH SENSITIVE ZEOLITIC IMIDAZOLE FRAMEWORKS

6.1. Motivation: screen pH sensitive zeolitic-imidazole frameworks for targeted chemotherapy

Tumours exhibit lower pH compared to the rest of the body [1, 2], and this is something that can be targeted using pH sensitive ZIFs. The ZIFs selected for screening in this work (ZIFs – 8/11/68/70/78/79/82) are stable at pH 7, and will break down in more acidic environments [3]. This chapter uses the conclusions previously derived in this thesis to screen these ZIFs and make recommendations for future experimental studies.

6.2. Summary: Maximum uptake and interaction energies from GCMC simulations and pore-hop energy barriers from SMD and umbrella sampling

Each ZIF was screened based on the properties of the pristine bulk crystal (since Chapter 3 shows that the effects of the external surface on uptake and adsorption energies are negligible). GCMC simulations were used to get a (relatively) quick screening of the maximum uptake and interaction energies, though as shown in Chapter 4 and as discussed in Section 6.6 experimentally these values will be significantly lower depending on the uptake method used.

Release rates were quantified based on the energy barriers calculated using SMD + GASP and umbrella sampling simulations carried out on single cisplatin molecules in otherwise empty frameworks (as shown in Chapter 5, the diffusivities and energy barriers directly correlate in systems with and without water).

Based on the results, a MOF was selected based on how well it uptakes cisplatin during encapsulation and how well it will retain cisplatin in healthy parts of the patient.

6.3. Results: polar MOFs with large window diameters are ideal for enhanced encapsulation and retention

As before, the maximum uptake is governed by the pore volume. There are two ways of increasing the pore-hop energy barrier, either by decreasing the pore window size (thus

inducing energy penalties associated with displacing framework atoms), or by enhancing MOF – CPT interaction energies. However, based on the conclusions drawn from previous chapters, the interaction energy should be enhanced using polar groups as it will enhance uptake from solution (as opposed to hydrophilic groups) and it will slow down the diffusivity of water (hence cisplatin). The benefit of manipulating interaction energies as opposed to the pore window size is that the latter will hinder both release and encapsulation.

6.4. Errata

Not applicable as paper not yet submitted

6.5. Chapter 6 Preamble References

1. Kato, Y., et al., *Acidic extracellular microenvironment and cancer.* Cancer cell international, 2013. **13**(1): p. 89-89.
2. Chen, M., et al., *Extracellular pH is a biomarker enabling detection of breast cancer and liver cancer using CEST MRI.* Oncotarget, 2017. **8**(28): p. 45759-45767.
3. Howarth, A.J., et al., *Chemical, thermal and mechanical stabilities of metal–organic frameworks.* Nature Reviews Materials, 2016. **1**(3): p. 15018.

This declaration concerns the article entitled:			
Cisplatin uptake and release in pH sensitive zeolitic imidazole frameworks			
Publication status (tick one) **Draft manuscript** / **Submitted** ☐ **In review** ☐ **Accepted** ☐ **Published** ☐			
Publication details (reference)	Thompson, M. Wells, S. Düren, T. 2020. Cisplatin uptake and release in pH sensitive zeolitic imidazole frameworks.		
Copyright status (tick the appropriate statement) I hold the copyright for this material ☐ Copyright is retained by the publisher, but I have been given permission to replicate the material here ☐			
Candidate's contribution to the paper (provide details, and also indicate as a percentage)	The candidate contributed to / considerably contributed to / predominantly executed the… Formulation of ideas: The candidate predominantly formulated the detailed ideas (90 %). The idea to use GASP was formulated by S. A. Wells (10 %). Design of methodology: The candidate predominantly designed the method for the simulations (90 %). The idea to use GASP was formulated by S. A. Wells (10 %). Experimental work: The candidate predominantly conducted the simulations (90 %). GASP simulations were performed by S. A. Wells (10 %). Presentation of data in journal format: The candidate predominantly presented the work in a journal format (100 %)		
Statement from Candidate	This paper reports on original research I conducted during the period of my Higher Degree by Research candidature.		
Signed		**Date**	01/09/2020

Cisplatin uptake and release in pH sensitive zeolitic imidazole frameworks

Megan J. Thompson, Stephen A. Wells, Tina Düren[*]

AUTHOR ADDRESS Prof. T. Düren, Centre for Advanced Separations Engineering, Department of Chemical Engineering, University of Bath, BA2 7AY, UK
E-mail: t.duren@bath.ac.uk

ABSTRACT

Cancer remains one of the hardest diseases to treat, partially due to the non-specificity of chemotherapeutics. Metal-organic frameworks as drug delivery carriers are a promising method for achieving targeted chemotherapy, however to date there have been very few detailed studies to systematically enhance the uptake while maintaining controlled release rates. In this work a series of biocompatible, pH sensitive ZIFs have been computationally screened for their ability to retain cisplatin in healthy parts of the patient and release it in the vicinity of a tumour. Molecular simulations highlight that the uptake depends on the pore volume, and retention can be controlled either using the pore window diameters or by manipulating framework – cisplatin interaction energies. The ZIFs best suited for cisplatin drug delivery are ZIFs 8, 70, and 82. Of these ZIF-82 is the most promising because it shows large cisplatin uptake and large energy barriers associated with cisplatin interpore movement. While ZIF-70 also exhibits good drug delivery properties, its lack of polar groups means that hydrophilic cisplatin will preferentially move into solution as oppose to the framework. ZIF-8 exhibits large uptakes and energy barriers, yet the latter is caused by a small pore window diameter which will also slow down the rate of encapsulation, particularly given the hydrophilic nature of ZIF-8.

INTRODUCTION

In 2018, the World Health Organisation (WHO) reported that cancer is responsible for 17 % deaths globally [1], and the number of cases are expected to rise by 2030 [2]. Chemotherapy is one of the primary cancer treatment methods, during which cytotoxic drugs such as cisplatin (*cis*-diaminedichloroplatinum (II), CPT) are usually administered intravenously.

Once incorporated into a cell, cisplatin activates and is able to form covalent bonds with nucleotides [3]. This damages DNA, preventing cell mitosis and activating apoptosis (i.e. the controlled self-destruction of cells).

Unfortunately, intravenous administration is non-specific and therefore cisplatin (amongst other cytotoxic drugs) can have adverse impacts on normal healthy cells. This causes the harmful side effects of chemotherapy such as haemorrhages, fatigue, damage to the nervous system, kidneys, bladder and so on. Furthermore, indirect administration reduces the dose reaching cancerous cells, increasing the chance of the tumour developing CPT resistance. To combat these issues, a non-toxic carrier can be used to deliver cisplatin directly to the tumour.

Existing drug delivery carriers can be subcategorised as organic and inorganic. Organic carriers are typically biocompatible, and they include materials such as polymeric structures [4], liposomes [5], and nanocapsules [6]. However, they usually have low loading efficiency and slow drug release. Inorganic carriers include materials such as ferromagnetic [7], gold [8] and mesoporous silica nanoparticles [9], the properties of which can be easily tailored for targeted drug delivery and high loadings. However, they tend to be inert and non-biocompatible [10]. Metal-organic frameworks can offer the best of both worlds. MOFs consist of metal nodes coordinated by organic ligands forming highly porous materials with large specific internal surface areas, and easily tuneable compositions and functionalities. Weak coordination bonds between the primary building units allow some MOFs to deconstruct inside the body, and their large pore volumes and internal surface areas enable high drug loading capacities [11].

Various experimental groups have successfully loaded cisplatin into metal-organic frameworks, which enabled them to achieve controlled release rates. For example, Lin et al successfully loaded CPT into MIL-101(Fe), and to reduce the release rate they coated the MOF nanoparticles with sodium metasilicate which slowed down the deconstruction of the framework [12]. Several groups have focussed on using members of the UiO series of MOFs ($Zr_6O_4(OH)_4$ nodes) because the strong Zr – O bonds and high connectivity of the nodes increases their stability in aqueous environments. For example, He et al incorporated cisplatin into UiO nanoparticles via conjugation (i.e. the covalent binding of a cisplatin prodrug to functional groups in the framework), and functionalised the surface for the attachment of small interfering RNAs to achieve CPT/siRNA co-delivery [13]. Lin et al

incorporated missing ligand defects in UiO-66 to increase the specific cisplatin uptake compared to the defect free structure [14]. Mocniak et al compared encapsulation and conjugation as methods to uptake a cisplatin pro-drug into UiO-66 and the amine functionalised variant UiO-66(NH_2). They achieved a higher uptake and a slower release rate using conjugation as opposed to encapsulation, since the conjugation method involves the formation of pro-drug framework covalent bonds. Compared to encapsulated cisplatin which can passively diffuse through the framework, conjugated cisplatin can only move through the framework provided the peptide bonds are broken via hydrolysis [15].

Whilst a slow release rate is beneficial in healthy parts of the body, when in the vicinity of the tumour it could be problematic, particularly if the carrier is not anchored in its vicinity. One way to speed up delivery is to induce framework degradation. Some MOFs undergo structural changes in response to variations in external stimuli, for example changes in pH can hydrolyse metal – ligand bonds [16]. For the application of chemotherapy, this is advantageous as the extracellular pH (pH_e) of tumour tissues are often acidic (pH_e = 6.5 – 6.9) due to their enhanced lactate secretion from anaerobic glycolysis [17]. On the other hand, the pH_e surrounding normal healthy cells is heavily regulated at pH_e = 7.2 – 7.5 [18]. If the carrier MOF can retain cisplatin whilst intact in normal areas of the body, and rapidly release it in the vicinity of a tumour as the framework degrades, this could result in effective targeted drug delivery.

In this work we computationally screen a series of biocompatible, pH sensitive zeolitic imidazole frameworks (ZIFs – 8/11/68/70/78/79/82) that are stable at pH > 7 and that will deconstruct in more acidic environments [16] and highlight property – performance relationships with respect to the ability of each ZIF to uptake and retain cisplatin.. Out of the ZIFs screened, ZIF-8 ($Zn_2(mIm)_{12}$) has been the most widely investigated material for multiple applications. It has a sodalite (SOD) topology that consists of uniform 11.6 Å pores constructed of 24 vertices (Zn nodes) each coordinated by four methyl imidazole ligands (*mIm*) forming eight 8 MR and six 4MR per cavity. ZIF-11 consists of 14.6 Å cavities constructed of benzene imidazole ligands (*bIm*) that coordinate 48 Zn nodes into a RHO topology. This forms pores that consist of six octahedral, eight hexagonal, and 12 square windows, and octagonal channels that connect the main cavities [19] The structures are shown in Figure 1.

(a) 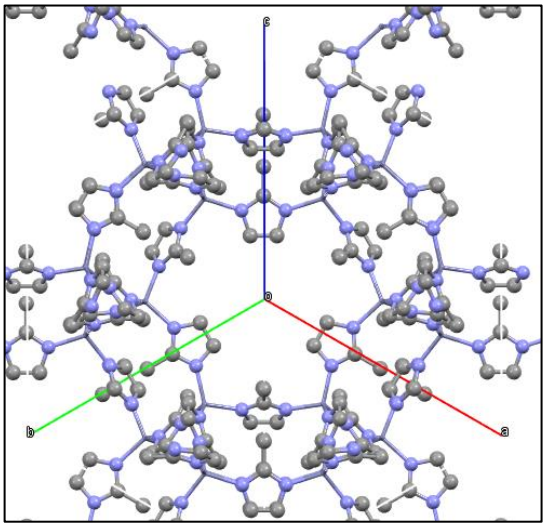 (b) 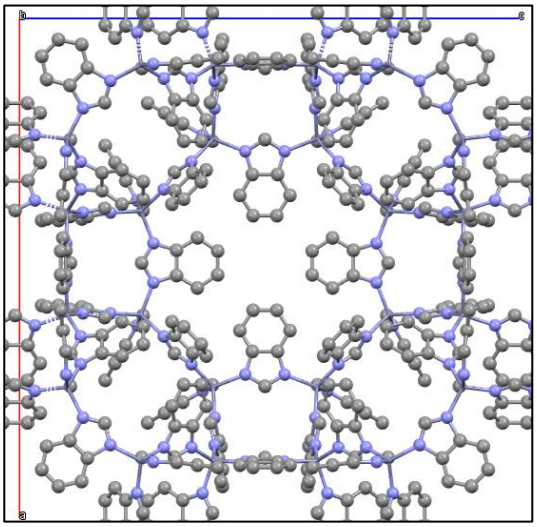

Figure 1. Structure of (a) ZIF-8, and (b) ZIF-11. Hydrogens are omitted for clarity. (Grey = carbon, blue = nitrogen, purple = zinc)

ZIFs-68/70/78/79/82 consist of three cage types: (i) *hpr*, (ii) *gme*, and (iii) *kno*. The cages consist of Zn nodes, each coordinated to four imidazole ligands (two *nIm* and two *substitute-Im*, as shown in Figure 2). Each structure consists of channels formed by the larger *kno* cages (24 Zn connecting of three 4MR, three 8MR, two 12MR) down the c-axis. These channels are surrounded by four parallel rows of *gme* cavities (18 Zn connecting nine 4MR, two 6MR, and three 8MR) which are connected by *hpr* cages (12 Zn connecting six 4MR, and two 6MR) [20].

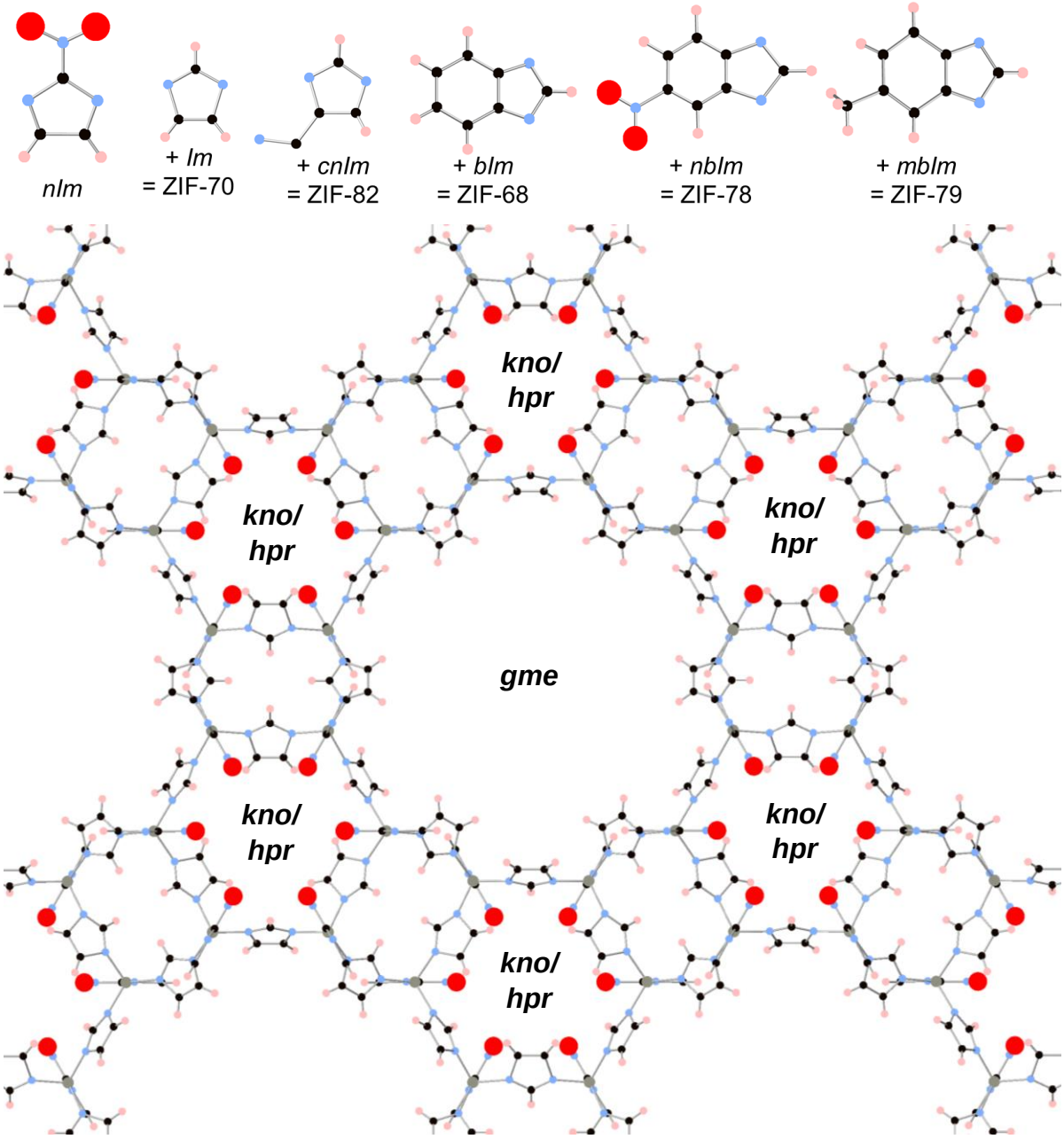

Figure 2. Top: Ligands used in ZIFs-68/70/78/79/82 [20]. (Pink = hydrogen, black = carbon, blue = nitrogen, red = oxygen). Bottom: The structure of ZIF-70 as a representative example of the topologies for the isostructural ZIFs-68/70/78/79/82.

METHOD

We use the methodologies validated in our previous work where we compared simulation results to available experimental data for cisplatin uptake and release rates in UiO-66 and UiO-66(NH_2) [21].

For cisplatin, the model developed by Yesylevskyy et al was used [22]. For the frameworks, the structures were taken from the Cambridge Structural Database and periodic boundary

conditions were used in all directions to model infinite crystals. Non-bonded Lennard Jones and bonded parameters for the frameworks were obtained from the Universal forcefield [23]. Electrostatic interactions were calculated using Mulliken charges, determined using *ab-initio* static energy calculations on fragments of the bulk (as described in the SI, Section 1).

Grand-canonical Monte Carlo (GCMC) simulations were used to characterise cisplatin adsorption at 310 K (representing body temperature) inside the static frameworks using the multipurpose simulation code (MuSiC) [24]. ZIF – CPT and CPT – CPT Coulombic interactions were calculated using Ewald summation [25] and the Wolf summation method respectively [25]. All non-Coulombic interactions were calculated using the Lennard-Jones 12-6 potential. 10 million iterations of insertion, deletion, translation and rotation moves were used for each pressure point, and the first 40 % of microstates were ignored to ensure that the microstates sampled are at equilibrium.

Molecular dynamics (MD) simulations were used to pre-equilibrate the structures, and characterise the movement and associated energy barrier of intracell and intercell cisplatin movement. For this purpose, the Groningen Machine for Chemical Simulations (GROMACS) [26-31] was used, and the framework topologies were generated using OBGMX [32] which implements the Universal Forcefield [23]. The framework was fully flexible during the simulations. The particle mesh Ewald algorithm [33, 34] was used to model long ranged electrostatic interactions. Separate temperature coupling baths set to 310 K were used for cisplatin and the framework.

Free energy landscapes (used to calculate the energy barriers for cisplatin moving between cavities though the frameworks), were calculated using umbrella sampling. Since the bulk crystal would confine the volume of a unit cell, these simulations were conducted using the NVT ensemble. A single cisplatin molecule was placed in the centre of the largest pore and the structure was relaxed using a steepest descents energy minimization and pre-equilibration for 100 ps in the NVT ensemble. The temperature was regulated using a modified Berendsen coupling method [35].

Cisplatin was then dragged through the most accessible channels using the GROMACs pull code. The simulation time was adjusted to ensure cisplatin moves from one pore to the same position in a neighbouring pore. For all simulations, a pull rate of 0.01 nm/ps was used with a time step of 0.001 ps. A spring constant of 1000 kJ/mol.nm^2 was used for all ZIFs with the

exception of ZIF-11 for which a tighter constraint potential was needed to adequately sample cisplatin movement at the window. Sampling windows for the umbrella simulations were collected at least every 0.1 nm along the simulation path, though more sampling windows were taken as necessary in the high energy regions of the pore windows. As in our previous work [21], the sampling configurations were not pre-equilibrated, but each were subjected to 10 ns of MD simulations in which cisplatin is constrained by the harmonic potential [36]. The weighted histogram method was used to obtain the free energy profiles along the pull direction [37]. At least six pull and umbrella sampling repeats were carried out for each MOF (more repeats were used in systems where the PMFs were less consistent). During both the pull and umbrella simulations, separate temperature coupling of CPT and the framework was achieved using a Nosé-Hoover thermostat [38, 39].

The intrinsic flexibility of the ZIF frameworks were determined using the GASP (geometric analysis and simulation of polyhedra) software [40].GASP was used in combination with the SMD simulations to determine the potential energy barrier associated with cisplatin moving through the frameworks, identify the bonded and non-bonded contributions to this energy barrier, and to determine whether cisplatin can pass through the pore windows without breaking the localised bonding. In this approach, the local atomic geometry of the input structure is constrained by a series of superimposed templates, while the simulation cell parameters are varied. This identifies a range of cell parameters, termed a "flexibility window", within which the global geometry can vary without alterations to the local geometry. (Detailed information on the GASP simulations can be found in the SI, Section 2). The variants produced using GASP were then analysed using PoreBlazer [41] and *ab-initio* static energy calculations.

RESULTS AND DISCUSSION

Both the maximum loading and the strength of the interaction of cisplatin with the MOF carrier are important properties for drug delivery. The adsorption energy will act as a driving force for cisplatin to move out of solution and into the framework during encapsulation, and a high interaction energy will improve retention during drug release (preventing the premature release of cytotoxic drugs in healthy areas of the patient). The specific maximum cisplatin loading (n_{MAX}) should be as high as possible to increase the dosage to the tumour for a given amount of MOF which will later need to decompose inside the patient. The maximum loading is governed by accessible pore volume since more cisplatin molecules

can pack into larger void spaces, as shown in Figure 3a. (For calculated and experimental structural properties, see the SI, Section 3). ZIF-70 displays the highest uptake due to its relatively small *nIm* + *Im* ligands resulting in larger pore volume. This in turn leads to relatively weak interactions. In contrast, ZIF-78 has the strongest average adsorption energy at the maximum loading (U_{AVE}) attributed to its polar ligands in combination with small pore sizes (Figure 3b). However, since U_{AVE} decreases with a higher cisplatin loading and a lower density of framework atoms, there is a clear trade-off between n_{MAX} and U_{AVE}.

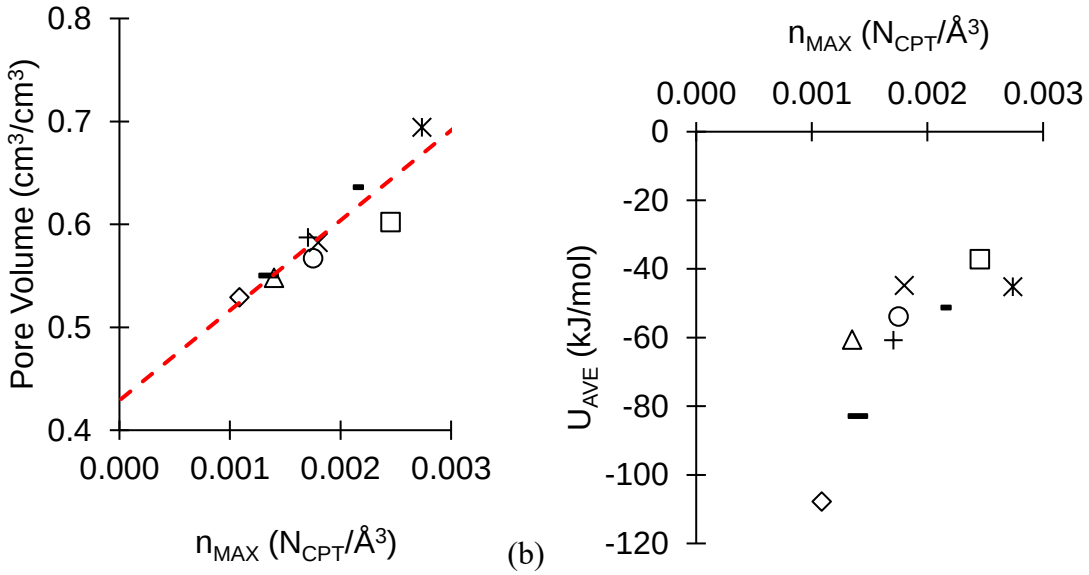

Figure 3. Maximum loading of cisplatin, n_{MAX}, as a function of (a) accessible pore volume, and (b) average adsorption energy at maximum loading, U_{AVE}. Symbols: UiO-66 (X), UiO-66(NH_2) (△) [21], ZIF-8 (□), ZIF-11 (○), ZIF-68 (+), ZIF-70 (✳), ZIF-78 (◇) ZIF-79 (▬), ZIF-82 (-)

Before recommending a MOF as a drug delivery carrier, we need to consider that n_{MAX} will not necessarily be the loading achieved experimentally due to the issue of accessibility. For example, in UiO-66 and UiO-66(NH_2) the maximum loading of cisplatin calculated using GCMC simulations is 1:1.5 Pt:Zr and 1:2.0 Pt:Zr respectively. Cisplatin ($d \approx 5$ Å) takes over 48 hours to encapsulate in UiO-66 (pore limiting diameter, PLD = 3.6 Å) and UiO-66(NH_2) (PLD = 3 Å) due to diffusion hinderance through narrow windows and/or unfavourable energies in the MOF as opposed to solution [21]. Eventually a small loading of 1:15.9 Pt:Zr (UiO-66) and 1:17.4 Pt:Zr (UiO-66(NH_2)) is achieved via encapsulation [15]. If on the other hand, there are strong bonds between the MOF and cisplatin (for example using the conjugation method where cisplatin covalently binds to functional groups on the framework) the loading can be enhanced. For example, in UiO-66(NH_2) the conjugation method can

yield a loading of 1:1.8 Pt:Zr (≈ n_{MAX} = 1:2.0 Pt:Zr) [15]. Therefore, to enhance encapsulation our next criteria is for the MOFs to have strong adsorption energy sites (e.g. hydrophilic channels that cisplatin will favourably move into from solution) as well as large pore window sizes. It should be emphasised at this point that screening based solely on pore window sizes is not enough as most frameworks show at least some degree of flexibility (i.e. the local geometry can move whilst retaining bonds) which can change the window diameter.

Looking closer at ZIF-8, the Type 1 adsorption isotherm (Figure 4a) shows a pore filling mechanism with weak MOF-CPT interaction energies ($U_{MOF-CPT}$) of -36 kJ/mol due to the hydrophobic nature of the 11 Å pore cavities (Figure 4b-d). In ZIF-11, $U_{MOF-CPT}$ is strongest at the cavity edges where larger *bIm* ligands form rings (< -90 kJ/mol Figure 4d). These sites are the first to become occupied at low pressures and then there is pore filling (leading to the steps in Figure 4a-b and dual peaks in Figure 4c). Windows connecting the cavities in ZIF-8 (PLD = 2.9 Å) and ZIF-11 (PLD = 2 Å) are narrower than those in the UiO-66 structures. Combined with weak $U_{MOF-CPT}$, there is little driving force and a large energy barrier for cisplatin to enter the cavities of these MOFs. We therefore conclude that these structures will not exhibit good cisplatin loading by encapsulation.

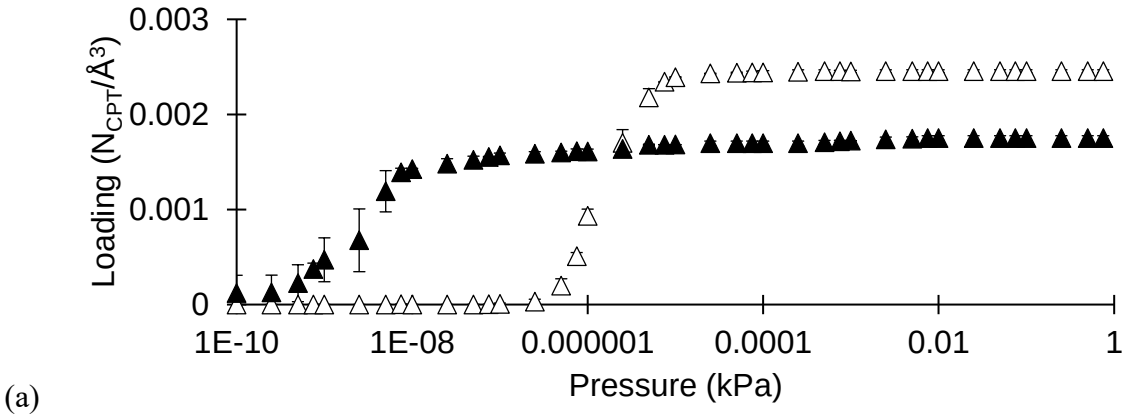

(a)

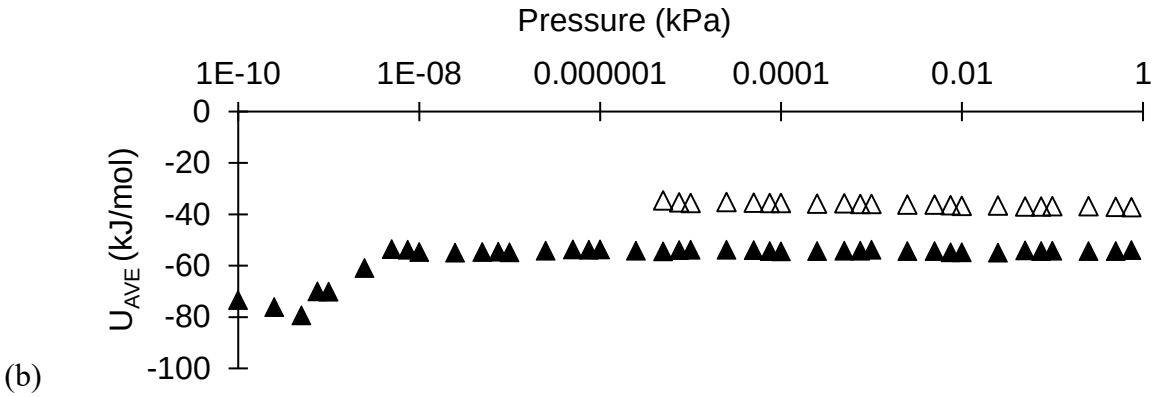

(b)

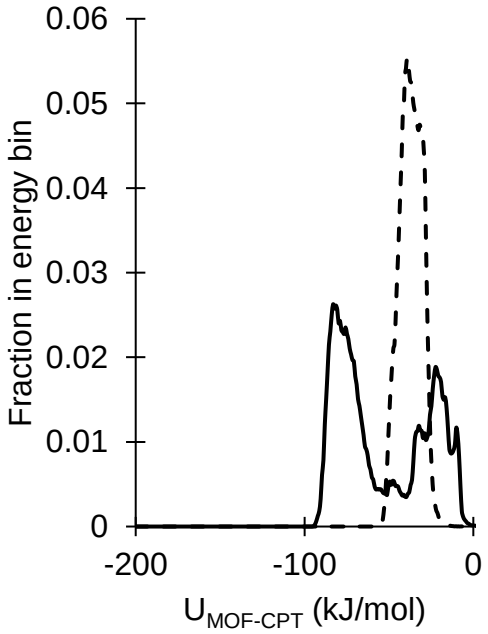

(c)

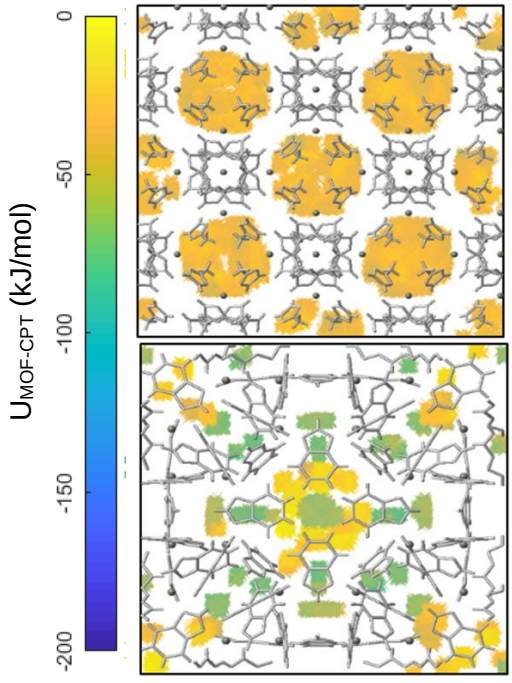

(d)

Figure 4. (a) Adsorption isotherms (error bars show the standard deviation from three repeat simulations), (b) U_{AVE} as a function of pressure, (c) $U_{MOF-CPT}$ histograms, and (d) $U_{MOF-CPT}$ maps in ZIF-8 and ZIF-11 (top and bottom) at 310 K. Open triangles/dashed line = ZIF-8. Filled triangles/solid line = ZIF-11.

ZIFs-68/70/78/79/82 consist of large *kno* channels (diameter ≈ 3.7 – 12.9 Å [20]) surrounded by channels of smaller *gme-hpr* cages that are parallel to the c-axis. Hydrophilicity of the

gme-hpr channels (diameter ≈ 3.6 Å [42]) is attributed to the *nIm* ligands, whereas *kno* pores in ZIFs 68, 70, and 79 are hydrophobic because they consist of non-polar ligands and the *nbIm* and *cnIm* ligands in ZIFs 78 and 82 improve the hydrophilicity in their *kno* pores [20]. Adsorption isotherms and interaction energies (Figure 5a-b) show a small step in the uptake at low pressures as cisplatin occupies the high energy adsorption sites (typically $U_{MOF\text{-}CPT}$ = -150 kJ/mol in the smaller hydrophilic *gme* pores – except in ZIF-78 where it initially fills the high energy sites next to *nbIm* ligands in its hydrophilic *kno* pores). At higher pressures, there is a larger step in the isotherms due to adsorption in the low energy sites ($U_{MOF\text{-}CPT}$ < -100 kJ/mol typically in the larger hydrophobic *kno* cages). This "two step" behaviour is similar to that seen by Van der Perre who performed adsorption experiments of polar guest molecules in ZIF-68 [42]. Compared to ZIF-8 and ZIF-11, the window diameters of the *kno* channels are larger and so there would be less diffusion limitation during encapsulation. There is however no interconnectivity between the larger *kno* and smaller *gme* channels, and hence uptake into the *gme* pores will face hinderance. Strong MOF-CPT interactions in these polar cavities however will act as a driving force to encapsulate polar guest molecules such as cisplatin, and furthermore Van der Pierre witnessed the filling of the *gme* pores of ZIF-68 using for example TMB molecules which are larger than cisplatin and contain similar functional groups [42]. Out of the ZIFs screened in this work, ZIF-70 and 82 show the highest uptake due to the smaller ligand size. ZIF-82 also has polar groups in the *kno* channel, so at this stage it would appear to be the most promising framework for enhanced cisplatin encapsulation.

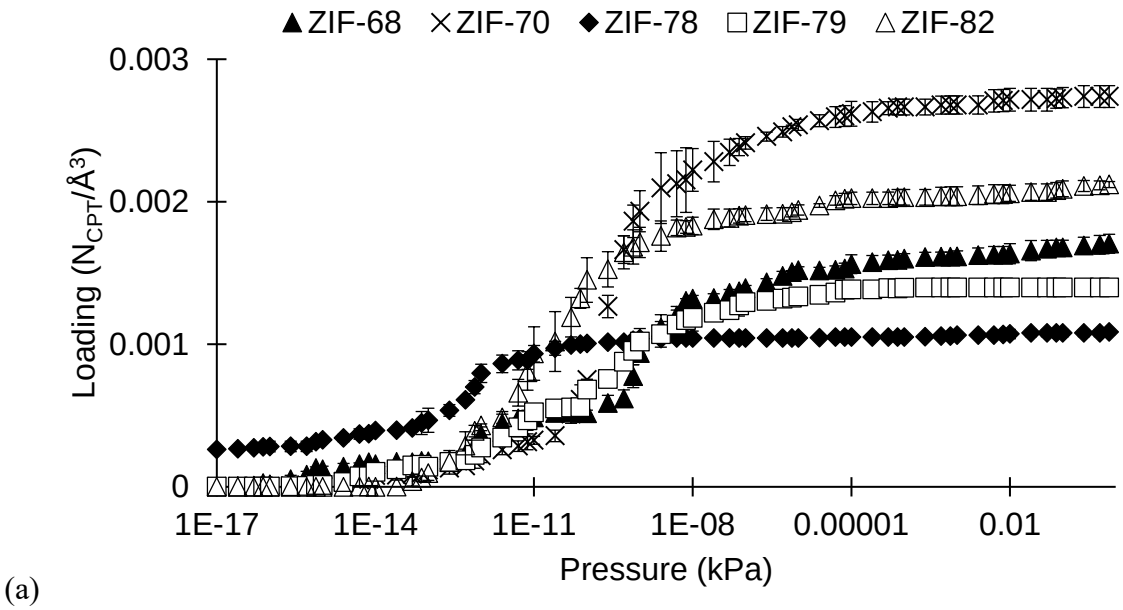

(a)

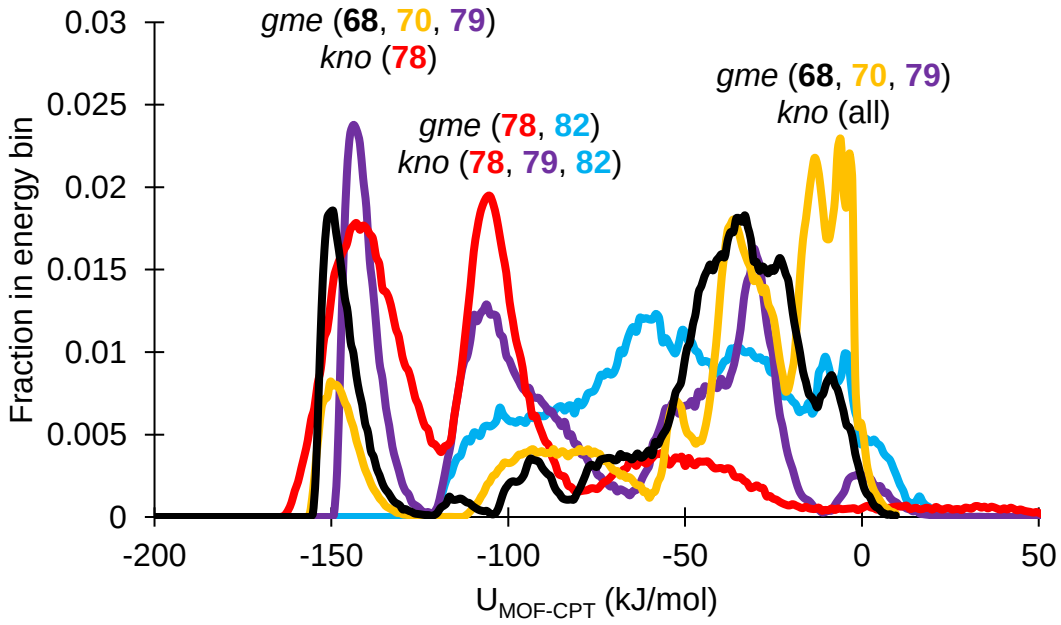

(b)

Figure 5. (a) Adsorption isotherms (error bars show the standard deviation from three repeat simulations), and (b) $U_{MOF-CPT}$ histograms in **ZIF-68**, **ZIF-70**, **ZIF-78**, **ZIF-79**, and **ZIF-82** at 310 K. (Corresponding energy maps and energies as a function of pressure are shown in the SI, Section 4).

The benefits of large cisplatin uptakes are forfeit if the payload is released prematurely in the healthy parts of chemotherapy patients. To maintain good retention (in healthy parts of the patient where the framework stays intact) it is important to decrease cisplatin diffusivity in the MOFs, hence for our next selection criteria we considered the energy barrier associated with pore-hopping.

Diffusivity will be lower (hence retention will be higher) in ZIFs with large pore-hopping energy barriers. Figure 6 shows that the total (bonded + non-bonded) Helmholtz free energy barrier (ΔA_{PH}) is relatively constant in MOFs with PLD ≥ PLD_{UiO-66} (≈ 4 Å). As the PLD decreases below 4 Å, ΔA_{PH} increases rapidly due to the energy associated with displacing framework atoms during pore-hopping. ZIF-11 has the smallest PLD out of the frameworks screened (2 Å), and hence the highest energy barrier – therefore the best retention properties. The issue is that (as shown in the SI, Section 5) pore-hopping requires the pore windows in ZIF-11 to open beyond the extent of its flexibility window (i.e. pore-hopping is likely to break the localised bonding). Therefore, we remove this framework from our list of potential drug delivery carriers as encapsulation would be limited. On the other hand, cisplatin can pass through the pore windows of ZIF-8 causing structural changes that are within its flexibility window (i.e. pore-hopping is feasible without breaking the localised bonding). Furthermore, as seen in Figure 6b ZIF-8 exhibits a good combination of a large ΔA_{PH} and n_{MAX}, therefore it would appear to be a promising candidate for cisplatin drug delivery. However, (as mentioned) cisplatin encapsulation will be hindered in ZIF-8 due to a combination of weak $U_{MOF-CPT}$ and high ΔA_{PH}.

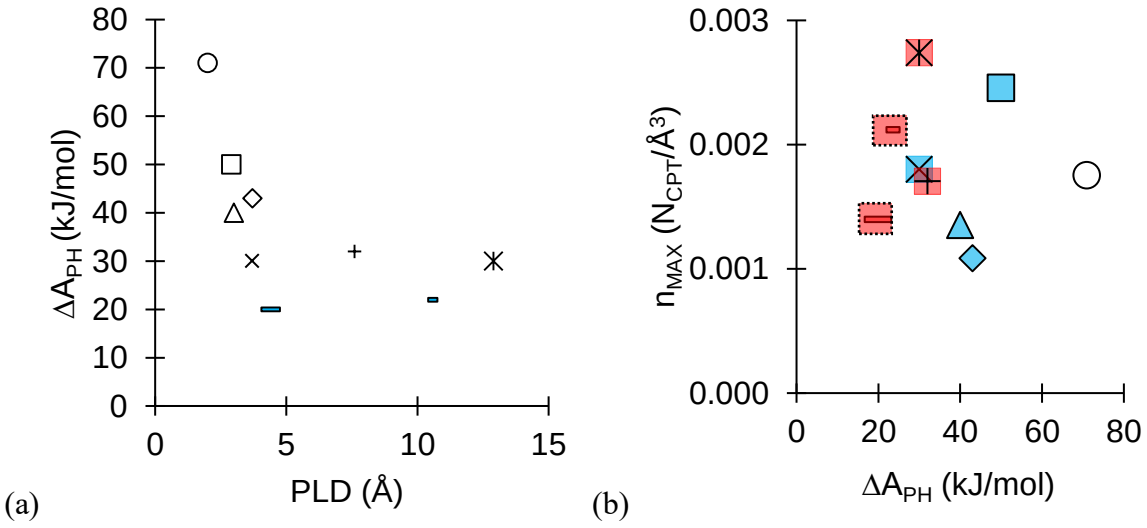

Figure 6. (a) Difference in the Helmholtz free energy, ΔA_{PH}, associated with cisplatin movement through the largest channel in the framework at 310 K. (b) Maximum uptake, n_{MAX}, as function of ΔA_{PH} (red: PLD > 4 Å | blue: PLD < 4 Å | white = rejected from screening process). Symbols: UiO-66 (x), UiO-66(NH_2) (△), ZIF-8 (□), ZIF-11 (○), ZIF-68 (+), ZIF-70 (✳), ZIF-78 (◇) ZIF-79 (▬), ZIF-82 (-)

The pore-hopping energy barrier in Figure 6a becomes constant (≈ 30 kJ/mol) for PLD > 4 Å. This is on-par with UiO-66, which has been shown in experimental papers to be a

promising drug delivery carrier since its rate of release is ideal for reducing tumour cell viability [15]. UiO-66 has pore windows which are slightly smaller than the collision diameter of cisplatin, therefore the pore-hop energy barrier in UiO-66 is governed by its PLD and the energy penalty associated with framework flexibility induced as cisplatin moves through the windows [21]. Since the *gme* channels are generally larger than the pore windows in UiO-66, it would be expected that they pose an even lower pore-hop energy barrier, however this is not the case as the MOF-CPT interaction energies ($U_{MOF\text{-}CPT}$) dominate the pore-hop energy barrier as opposed to framework flexibility. (This is also evident from the higher MOF – CPT interaction energy barriers for MOFs with PLD > 4 Å, as shown in Figure 7 and discussed next). In other words, stronger $U_{MOF\text{-}CPT}$ result in similar ΔA_{PH} in frameworks that have large open *kno* cages as in UiO-66 (in which the energy barrier is governed by the PLD). This is important as it would enhance encapsulation whilst maintaining similar levels of cisplatin retention as UiO-66.

However, the issue is that when water is present, strong hydrogen bonds between water and the polar arms of cisplatin result in the formation of a solvation shell. Unless there are equally strong MOF – cisplatin interaction energies, the solvation shell has the potential to displace cisplatin from the favourable adsorption sites and carry it through the large open *kno* pores [21]. In this work, water was not included in the simulations, since the scope is to screen a variety of MOFs to identify promising candidates for further investigation. As shown in our previous work [43], the diffusivity in water is substantially reduced, even if small polar groups are present (e.g. NH_2 functionalised UiO-68). Therefore, our final screening criteria is to prevent cisplatin displacement by water by enhancing $U_{MOF\text{-}CPT}$ using polar functional groups.

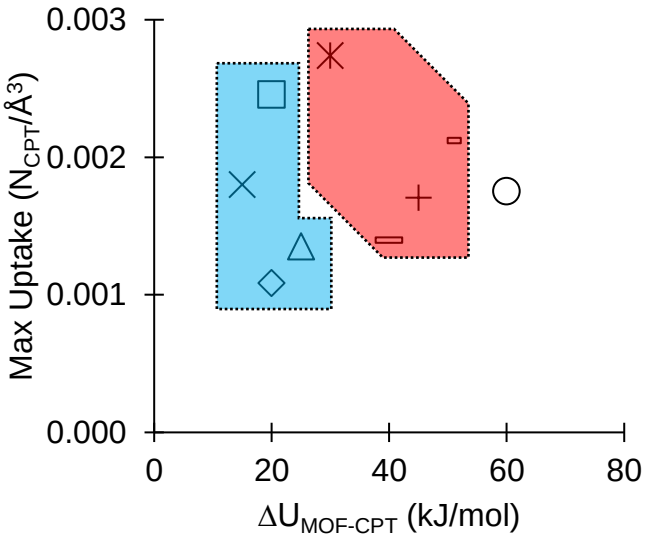

Figure 7. MOF-CPT potential energy barrier and the maximum cisplatin uptake in UiO-66 (X), UiO-66(NH_2) (△), ZIF-8 (□), ZIF-11 (○), ZIF-68 (+), ZIF-70 (✳), ZIF-78 (◇) ZIF-79 (▬), ZIF-82 (-). (Red: PLD > 4 Å | blue: PLD < 4 Å | white = rejected from screening process).

The interaction between cisplatin and the MOF framework, $U_{MOF-CPT}$ is enhanced in the *kno* pores with larger ligands (ZIF-79) or polar functional groups (ZIF-78 and ZIF-82) (Figure 5). However, there needs to be a large *variation* in $U_{MOF-CPT}$ (i.e. strong adsorption sites spread out between weak adsorption sites) to increase the potential energy barrier. As seen in Figure 7, the potential energy is uniformly distributed in ZIF-78 and ZIF-79, and so despite favourable interaction energies the potential energy barriers ($\Delta U_{MOF-CPT}$) are low, meaning cisplatin can move relatively freely in these frameworks. In ZIF-82 however, there are strong interaction energies in the vicinity of the C≡N groups and weak interaction energies elsewhere which enhances $\Delta U_{MOF-CPT}$. The phenomena of large steps between favourable adsorption sites (i.e. large variations in energy) increasing the energy barrier was also seen by Amirjalayer et al who simulated benzene diffusion through variants of IRMOF-1 [44].

We therefore draw the following recommendation: In situations where cisplatin uptake is hindered by encapsulation, encapsulation in the larger *kno* pores can be enhanced whilst retaining a similar rate of retention (ΔA_{PH}) as in UiO-66 which has been shown to have ideal release rates for killing cancer cells [15]. To further enhance encapsulation and to prevent premature release rates caused by water displacement, $\Delta U_{MOF-CPT}$ can be enhanced by the addition of polar groups – as in the case of ZIF-82. As a next step, the intrapore and interpore

diffusivities would need to be calculated in the presence of water to fully determine the influence of the solvation shell prior to experimental screening. However, such calculations are computationally expensive and beyond the scope of this paper (which is to screen ZIFs and identify promising materials that can be further investigated in more detail).

Table 1. Summary of cisplatin uptake and release properties in the screened MOFs. Colour scheme: green = more promising values, white = less promising values. Colour scale is based on columns (not rows).

System	Polar groups in travel path?	PLD (Å)	$\Delta U_{PH,max}$ (kJ/mol)	$\Delta G_{PH,max}$ (kJ/mol)	V (cm^3/cm^3)	η_{MAX} ($N_{CPT}/Å^3$)
UiO-66	No	3.7	15	30	0.582	0.0018
UiO-66(NH_2)	Yes	3	25	40	0.55	0.0014
ZIF-8	No	2.9	20	50	0.602	0.0025
ZIF-11	No	2	60	71	0.567	0.0018
ZIF-68	No	7.6	45	32	0.587	0.0017
ZIF-70	No	12.9	30	30	0.694	0.0027
ZIF-78	Yes	3.7	20	43	0.529	0.0011
ZIF-79	No	4.4	40	20	0.548	0.0014
ZIF-82	Yes	10.4	50	22	0.636	0.0021

Table 1 summarises the findings for each framework screened and emphasises the importance to include a variety of properties even in an initial screening process to identify promising materials. Overall, cisplatin uptake depends on the available pore volume, and small pore window diameters can be used to improve retention. Based on this, ZIF-8 appeared to be a promising drug delivery carrier, however in hindsight the small pore window diameters will also hinder the rate of encapsulation. Instead, as in the case of ZIF-70 and ZIF-82 (which also show good uptake due to their large pore volumes) the rate of retention can be enhanced (without substantially compromising uptake) by adding functional groups to MOFs with large open cavities. As a next step, the strength of the functional group – cisplatin interaction energy will need to be tested in the presence of water to ensure the solvation shell does not simply displace it. The spacing in between strong adsorption sites is also very important with respect to the energy barrier associated with interpore movement. Overall, the properties in Table 1 are important for uptake and release, and by combining them in different ways it is to make a promising material for cisplatin drug delivery.

CONCLUSION

In this work we have screened a selection of biocompatible pH sensitive MOFs for their ability to achieve a high maximum loading of cisplatin as well as a high energy barrier to increase the payload reaching the tumour in chemotherapy patients and decrease release rates in healthy parts of the body. The maximum uptake is predominately governed by the accessible pore volume. The pore-hop energy barrier (i.e. the energy barrier associated with cisplatin movement between pores, which is inversely proportional to the drug molecule release rates from the framework) can be enhanced by decreasing the pore window diameter at a compromise that this will reduce accessibility of cisplatin entering the framework during encapsulation. Instead, similar energy barriers can be achieved without compromising encapsulation rates in frameworks with large open pores but with enhanced MOF-cisplatin interaction energies.

Ultimately this work has highlighted the structural properties to aim for when designing an ideal cisplatin drug delivery carrier. From the MOFs screened in this work, ZIF-8, ZIF-70, and ZIF-82 all exhibit good maximum uptakes. Out of these, the pore window diameter in ZIF-8 is the bottleneck for diffusion thus reducing release rates, yet this will also hinder encapsulation i.e. the uptake cisplatin into the drug carrier. In ZIF-70, there are fewer polar groups and therefore weaker interaction energies will hinder encapsulation whilst enabling premature release rates. ZIF-82 is the most promising material due to its large uptake, variation in interaction energies and the addition of polar groups to anchor cisplatin and prevent premature drug release.

ASSOCIATED CONTENT

Details of the static energy calculations, GASP simulations, MOF structural characteristics and potential energy maps can be found in the Supporting Information.

ACKNOWLEDGEMENTS

This work was supported by funding from the European Research Council (ERC) under the European Union's Horizon 2020 research and innovation programme (grant agreement No 648283 "GROWMOF"). It made use of the Balena High Performance Computing (HPC) Service at the University of Bath.

ABBREVIATIONS

MOF, metal-organic framework; CPT, cisplatin; UiO, Universitetet i Oslo; ZIF, zeolitic-imidazole framework

REFERENCES

1. WHO. *Cancer*. 2020 [cited 2020 07/02/2020]; Available from: http://tiny.cc/rzwpjz.
2. P Boyle, L.B., *World Cancer Report 2008*. 2008, Lyon: IARC Press.
3. Lind, M.J., *Principles of cytotoxic chemotherapy.* Medicine, 2008. **36**(1): p. 19-23.
4. Moreno, D., et al., *Pharmacodynamics of cisplatin-loaded PLGA nanoparticles administered to tumor-bearing mice.* European Journal of Pharmaceutics and Biopharmaceutics : official journal of Arbeitsgemeinschaft für Pharmazeutische Verfahrenstechnik e.V, 2009. **74**: p. 265-74.
5. Meerum Terwogt, J.M., et al., *Phase I and pharmacokinetic study of SPI-77, a liposomal encapsulated dosage form of cisplatin.* Cancer Chemotherapy and Pharmacology, 2002. **49**(3): p. 201-10.
6. Burger, K.N., et al., *Nanocapsules: lipid-coated aggregates of cisplatin with high cytotoxicity.* Nature Medicine, 2002. **8**(1): p. 81-4.
7. Kettering, M., et al., *Characterization of iron oxide nanoparticles adsorbed with cisplatin for biomedical applications.* Physics in Medicine & Biology, 2009. **54**(17): p. 5109-21.
8. Ren, L., et al., *Cisplatin-loaded Au-Au2S nanoparticles for potential cancer therapy: cytotoxicity, in vitro carcinogenicity, and cellular uptake.* Journal of Biomedical Materials Research Part A, 2008. **85**(3): p. 787-96.
9. Yang, P., S. Gai, and J. Lin, *Functionalized mesoporous silica materials for controlled drug delivery.* Chemical Society Reviews, 2012. **41**(9): p. 3679-98.
10. Duan, X., et al., *Nanoparticle formulations of cisplatin for cancer therapy.* Wiley interdisciplinary reviews. Nanomedicine and nanobiotechnology, 2016. **8**(5): p. 776-791.
11. Yaghi, O., et al., *Reticular Synthesis and the Design of New Materials.* Nature, 2003. **423**: p. 705-714.

12. Taylor-Pashow, K.M.L., et al., *Postsynthetic Modifications of Iron-Carboxylate Nanoscale Metal−Organic Frameworks for Imaging and Drug Delivery.* Journal of the American Chemical Society, 2009. **131**(40): p. 14261-14263.
13. He, C., et al., *Nanoscale Metal–Organic Frameworks for the Co-Delivery of Cisplatin and Pooled siRNAs to Enhance Therapeutic Efficacy in Drug-Resistant Ovarian Cancer Cells.* Journal of the American Chemical Society, 2014. **136**(14): p. 5181-5184.
14. Lin, S.-X., et al., *Effective loading of cisplatin into a nanoscale UiO-66 metal–organic framework with preformed defects.* Dalton Transactions, 2019. **48**(16): p. 5308-5314.
15. Mocniak, K.A., et al., *Incorporation of cisplatin into the metal–organic frameworks UiO66-NH2 and UiO66 – encapsulation vs. conjugation.* Royal Society Chemistry Advances, 2015. **5**(102): p. 83648-83656.
16. Howarth, A.J., et al., *Chemical, thermal and mechanical stabilities of metal–organic frameworks.* Nature Reviews Materials, 2016. **1**(3): p. 15018.
17. Kato, Y., et al., *Acidic extracellular microenvironment and cancer.* Cancer cell international, 2013. **13**(1): p. 89-89.
18. Chen, M., et al., *Extracellular pH is a biomarker enabling detection of breast cancer and liver cancer using CEST MRI.* Oncotarget, 2017. **8**(28): p. 45759-45767.
19. Park, K.S., et al., *Exceptional chemical and thermal stability of zeolitic imidazolate frameworks.* Proceedings of the National Academy of Sciences, 2006. **103**(27): p. 10186-10191.
20. Banerjee, R., et al., *Control of Pore Size and Functionality in Isoreticular Zeolitic Imidazolate Frameworks and their Carbon Dioxide Selective Capture Properties.* Journal of the American Chemical Society, 2009. **131**(11): p. 3875-3877.
21. Thompson, M., S. Wells, and T. Düren, *Molecular simulations of cisplatin uptake and release in UiO-66 and UiO-66(NH2)*. 2020, University of Bath.
22. Yesylevskyy, S., et al., *Empirical force field for cisplatin based on quantumdynamics data: case study of new parameterization scheme for coordinationcompounds.* Journal of Molecular Modeling, 2015. **21**(10): p. 268.
23. Rappe, A.K., et al., *UFF, a full periodic table force field for molecular mechanics and molecular dynamics simulations.* Journal of the American Chemical Society, 1992. **114**(25): p. 10024-10035.
24. Gupta, A., et al., *Object-oriented Programming Paradigms for Molecular Modeling.* Molecular Simulation, 2003. **29**(1): p. 29-46.

25. Wolf, D., et al., *Exact method for the simulation of Coulombic systems by spherically truncated, pairwise r−1 summation.* The Journal of Chemical Physics, 1999. **110**(17): p. 8254-8282.
26. Berendsen, H.J.C., D. van der Spoel, and R. van Drunen, *GROMACS: A message-passing parallel molecular dynamics implementation.* Computer Physics Communications, 1995. **91**(1): p. 43-56.
27. Bekker, H., et al., *Gromacs - a Parallel Computer for Molecular-Dynamics Simulations.* Physics Computing '92, 1993: p. 252-256.
28. Lindahl, E., B. Hess, and D. van der Spoel, *GROMACS 3.0: a package for molecular simulation and trajectory analysis.* Molecular modeling annual, 2001. **7**(8): p. 306-317.
29. Van Der Spoel, D., et al., *GROMACS: Fast, flexible, and free.* Journal of Computational Chemistry, 2005. **26**(16): p. 1701-1718.
30. Hess, B., et al., *GROMACS 4: Algorithms for Highly Efficient, Load-Balanced, and Scalable Molecular Simulation.* Journal of Chemical Theory and Computation, 2008. **4**(3): p. 435-447.
31. Pronk, S., et al., *GROMACS 4.5: a high-throughput and highly parallel open source molecular simulation toolkit.* Bioinformatics, 2013. **29**(7): p. 845-54.
32. Garberoglio, G., *OBGMX: A web-based generator of GROMACS topologies for molecular and periodic systems using the universal force field.* Journal of Computational Chemistry, 2012. **33**(27): p. 2204-2208.
33. Darden, T., D. York, and L. Pedersen, *Particle mesh Ewald: An N·log(N) method for Ewald sums in large systems.* The Journal of Chemical Physics, 1993. **98**(12): p. 10089-10092.
34. Essmann, U., et al., *A smooth particle mesh Ewald method.* The Journal of Chemical Physics, 1995. **103**(19): p. 8577-8593.
35. Bussi, G., D. Donadio, and M. Parrinello, *Canonical sampling through velocity rescaling.* The Journal of Chemical Physics, 2007. **126**(1): p. 014101.
36. Torrie, G.M. and J.P. Valleau, *Nonphysical sampling distributions in Monte Carlo free-energy estimation: Umbrella sampling.* Journal of Computational Physics, 1977. **23**(2): p. 187-199.
37. Kumar, S., et al., *THE weighted histogram analysis method for free-energy calculations on biomolecules. I. The method.* Journal of Computational Chemistry, 1992. **13**(8): p. 1011-1021.

38. Nosé, S., *A unified formulation of the constant temperature molecular dynamics methods.* The Journal of Chemical Physics, 1984. **81**(1): p. 511-519.
39. Hoover, W.G., *Canonical dynamics: Equilibrium phase-space distributions.* Physical Review A, 1985. **31**(3): p. 1695-1697.
40. Wells, S.A. and A. Sartbaeva, *GASP: software for geometric simulations of flexibility in polyhedral and molecular framework structures.* Molecular Simulation, 2015. **41**(16-17): p. 1409-1421.
41. Sarkisov, L. and A. Harrison, *Computational structure characterisation tools in application to ordered and disordered porous materials.* Molecular Simulation, 2011. **37**(15): p. 1248-1257.
42. Van der Perre, S., et al., *Adsorptive Characterization of the ZIF-68 Metal-Organic Framework: A Complex Structure with Amphiphilic Properties.* Langmuir, 2014. **30**(28): p. 8416-8424.
43. Thompson, M. and T. Düren, *Tailoring defects or building units for controlled cisplatin drug delivery*. 2020, University of Bath.
44. Amirjalayer, S. and R. Schmid, *Influence of Pore Dimension on the Host–Guest Interaction in Metal–Organic Frameworks.* The Journal of Physical Chemistry C, 2016. **120**(48): p. 27319-27327.

Cisplatin uptake and release in pH sensitive zeolitic imidazole frameworks

Supporting Information

Megan J. Thompson, Stephen A. Wells, Tina Düren[*]

AUTHOR ADDRESS Prof. T. Düren, Centre for Advanced Separations Engineering, Department of Chemical Engineering, University of Bath, BA2 7AY, UK
E-mail: t.duren@bath.ac.uk

Table of Contents

Section S1. Static energy calculations

Static energy calculations were used to determine the partial atomic charges of each framework. They were also used to determine the internal energy of each GASP variant. The Quickstep module in CP2K [1-6] was used to carry out the static energy calculations. Quickstep uses Gaussians to model the core electron density and planewaves to model the valence electron density. All atoms were modelled using triple-zeta Gaussian basis sets with the exception of zinc and platinum which were modelled using double-zeta basis sets [7]. The planewave cutoff and relative cutoff were set to 500 Ry and 50 Ry, and exchange correlation energies were determined using the Perdew-Burke-Ernzerhof functional [8] with DFT-D3 dispersion corrections [9, 10]. For both the Gaussians and the planewaves, core electrons were described using pseudopotentials derived by Goedecker, Teter and Hutter [2, 11, 12]. The wavefunction was considered to be converged at a tolerance of 10^{-6}.

Partial atomic charges were calculated using static energy simulations on fragments of each MOF. The fragments consisted of the ligand for which the charges were being calculated, bonded to two Zn nodes, which were coordinated to three hydrogen capped "dummy" monodentate ligands (the charges for which were not used).

Table S1. Partial atomic charges for each atom type used in this work.

ZIF	**8**	**11**	**68**	**70**	**78**	**79**	**82**
C1	0.138	0.108	0.134	0.140	0.029	0.218	-0.046
C2	-0.122	0.015	0.052	-0.081	-0.096	-0.069	0.205
C3	-0.403	-0.146	-0.126	0.216	-0.116	0.117	0.001
C4		-0.153	-0.136	-0.103	0.050	0.024	-0.001
C5			0.196		0.041	-0.109	-0.102
C6			-0.021		-0.076	-0.137	0.120
C7					0.125	-0.021	
C8					0.192	-0.360	
C9					-0.040	-0.087	
C10						0.029	
H1	0.143	0.092	0.134	0.171	0.166	0.127	0.155
H2	0.120	0.133	0.128	0.133	0.123	0.115	0.149
H3		0.142	0.146	0.122	0.121	0.109	0.134
H4			0.122		0.118	0.149	
H5					0.134	0.140	
H6						0.090	
N1	-0.175	-0.186	-0.141	-0.231	0.149	0.071	-0.125
N2			-0.104	-0.259	-0.179	-0.198	0.058
N3			-0.290	-0.009	-0.186	-0.159	-0.302
N4					0.058	-0.157	-0.145
N5					-0.145		-0.214
O1			-0.135	-0.227	-0.240	-0.226	-0.169
O2					-0.171		
Zn1	0.377	0.383	0.440	0.433	0.405	0.422	0.466

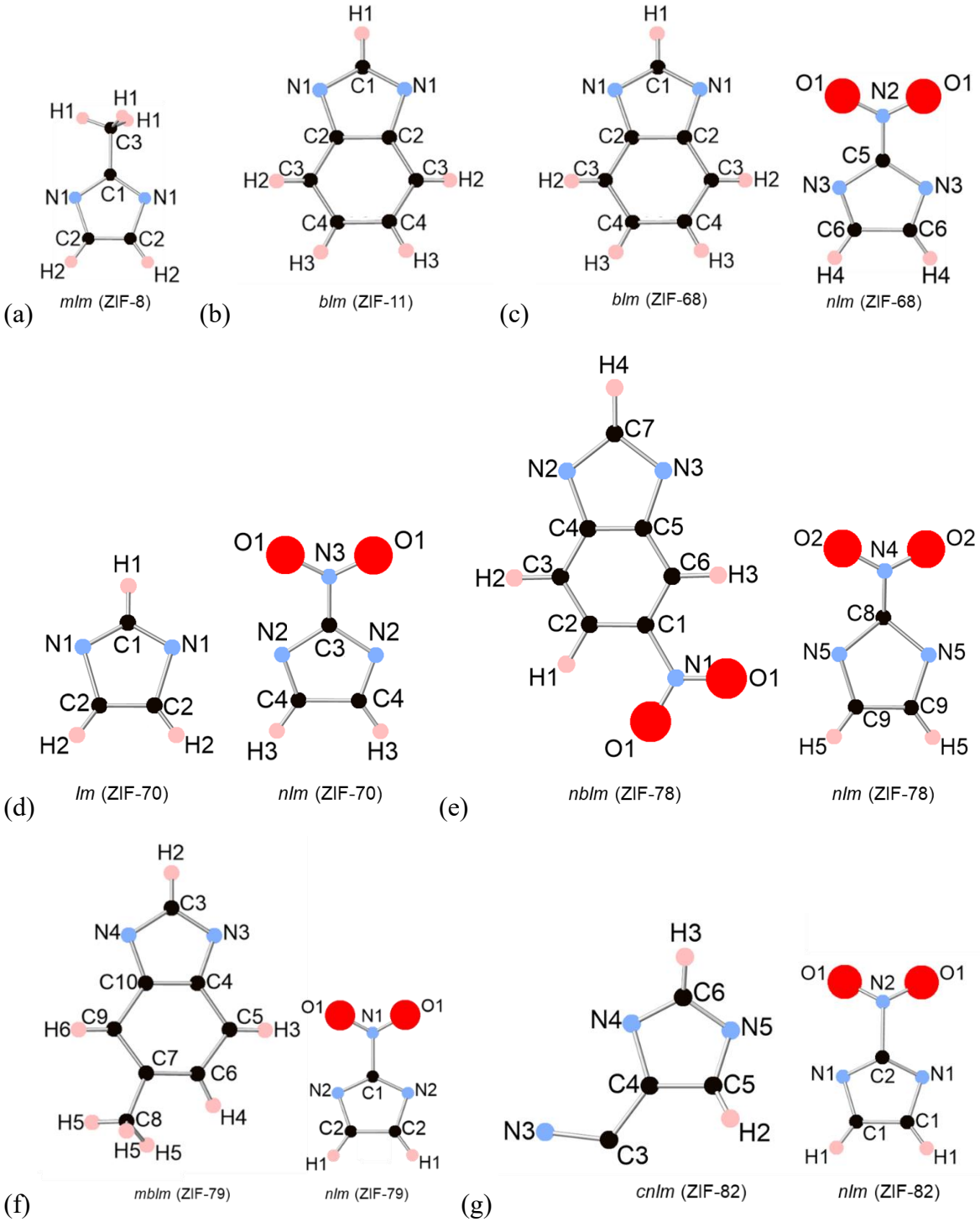

Figure S1. Atom label references in (a) – (g) ZIF 8 – 82. Colour scheme: black = carbon, red = oxygen, pink = hydrogen, grey = zinc, blue = nitrogen.

Section S2. GASP simulation details

We have investigated the intrinsic flexibility of ZIF frameworks using the GASP (geometric analysis and simulation of polyhedra) software [13]. In this approach, the local atomic geometry (e.g. bond lengths and angles) of the input structure is constrained by a series of superimposed templates, while the simulation cell parameters are varied. This identifies a

range of cell parameters, termed a "flexibility window", within which the global geometry can vary without alterations to the local geometry.

ZIF frameworks consist of zinc nodes tetrahedrally coordinated by the nitrogen atoms of imidazolate rings in the ligands. In geometric simulations, we treat the ligand as an essentially rigid unit (constraining all the bond lengths and angles in the ligand to have the same values as in the input structure), and the coordination around each zinc centre as a rigid, approximately tetrahedral, cluster (constraining the bond lengths and angles around the zinc atom). The Zn-N-C angles and associated dihedral angles, however, are not explicitly constrained. As a result, ZIF frameworks display substantial internal flexibility enabled by cooperative rotations and displacements of the ligands and nodes.

GASP includes a "search" functionality which systematically varies the cell parameters of the simulation cell while geometrically relaxing the cell contents to maintain bonding geometry and steric exclusion. This identifies a range of cell parameters, termed a "flexibility window", within which the cell contents can display global flexibility while retaining local rigidity. Outside this "window", distortions of the geometry are inevitable. Various search schemes are available, from the very simple "cubic" search which increases or decreases all the cell edge lengths together, and the "six fold" scheme in which each cell parameter is varied individually, to the lengthy and deprecated "triclinic" scheme which attempts every possible combination of variations of the six cell parameters. In this case, we have found it convenient to represent each framework in an orthorhombic form and to explore an orthorhombic search strategy, where the cell angles are all held constant at 90 degrees while the three cell edge lengths are permitted to vary independently.

Bonds are assigned around bonding centres as follows. From a zinc atom to any nitrogen atom within 2.0 Å; from a carbon atom to any carbon, nitrogen or oxygen atom within 1.8 Å, and to any hydrogen atom within 1.3 Å; from a nitrogen atom to any carbon atom (and, if the structure contains $-NO_2$ groups, to any oxygen atom) within 1.8 Å. Our set of frameworks did not include any with hydroxyl groups in the ligands; were such a group present, bonds should likewise be assigned from oxygen to carbon and to hydrogen. The default behaviour of GASP is to identify any carbon or nitrogen atom with three or fewer bonded neighbours as an sp^2 hybridised centre, and unite sp^2 bonded atoms into a single rigid cluster. This behaviour correctly rigidifies each imidazolate ligand into a rigid unit whose bonding geometry is defined by a single template. During geometric simulations, the

following steric radii are assigned to atoms by species: carbon and nitrogen, 1.4 Å; oxygen, 1.35 Å; hydrogen, 1.0 Å; zinc, 1.5 Å. A geometric relaxation of as ZIF structure is terminated if the largest "mismatch" in the structure - the deviation of atomic positions from the template bonding geometry of the input structure - is less than 0.01 Å; or, alternatively, if the largest "move" of an atomic position being proposed is less than 10^{-6} Å. If the relaxation is terminated by the mismatch criterion, then the structure is considered to be within the flexibility window, while if it is terminated by the move criterion, the relaxation has jammed without being able to satisfy the bonding geometry, and thus lies outside the flexibility window.

A GASP search generates as output a series of (serially numbered) CIF files representing the "edges" of the flexibility window, that is, the greatest variations of the structure before distortions become inevitable.

The ZIFs display substantial cooperative rotations of the ligands and nodes as the cell parameters are varied in the GASP search. The question of interest is now: to what extent can this internal flexibility be displayed without cell parameter variation? That is, can the internal flexibility enable local variations of the pore and void geometry without macroscopic alterations of the structure?

We investigate this question using a combination of GASP features. In particular, GASP can take a "structure" input (a CIF file, defining the starting atomic geometry), a "new structure" input (another CIF file, defining cell parameters and fractional coordinates to which the atoms are moved before the simulation starts), and also a "new cell" input (a set of cell parameters which are imposed on the simulation cell before the simulation starts).

It is therefore possible to provide GASP with the crystal structure of a ZIF, thus defining the bonding geometry to be maintained; then to provide, as a "new structure", one of the "edge" structures generated during the flexibility window search; and also to provide, as a "new cell" the cell parameters of the original crystal. A geometric simulation then begins with the cell parameters and template bonding geometry of the crystal structure, but with fractional coordinates representing rotations of the nodes and ligands. Geometric relaxation then re-fits the atoms and their templates together until bonding geometry is restored.

This strategy lends itself to automation in a two-stage process. In the first stage, GASP runs a window search on a ZIF to generate a suite of variant structures with different cell parameters. In the second stage, using shell scripting, we loop over the variant structures, carrying out GASP relaxations using the "structure/new structure/new cell" approach described above.

When applied to our ZIFs, this strategy is successful in producing variant structures which have the cell parameters and bonding geometry of the crystal structure while displaying different pore profiles and void geometry through collective, cooperative rigid-body motion of the ligands and nodes. This immediately suggests that guest molecules entering and passing through a ZIF structure may encounter a range of pore profiles and void geometries, and thus a range of diffusion energy barriers and binding-site energies, differing from those seen in the static crystal structure.

Section S3. MOF properties

Table S2. Structural properties of the MOFs calculated using PoreBlazer [14] used in this work. Where available, values from literature are provided for comparison.

System	**CSD Entry**	**Pore Volume (cm^3/cm^3)**	**Window Diameter (Å)**	**Max Cavity Size (Å)**
UiO-66	1405739 [15]	0.58	3.7	8.3 (11.0 [16])
UiO-66(NH_2)	1405739 [15]	0.55	3.0	7.3
ZIF-8	602542 [17]	0.60 (0.66 [17])	2.9 * (2.9 [18])	11.3 (11.6 [17])
ZIF-11	602545 [17]	0.57 (0.58 [17])	2.0 ** (3.0 [19])	14.4 (14.6 [17])
ZIF-68	671075 [20]	0.59	7.6 (7.5 [20])	10.4 (10.3 [20])
ZIF-70	671078 [20]	0.69	12.9 (13.1 [20])	14.8 (15.9 [20])
ZIF-78	704995 [20]	0.53	3.7 (3.8 [20])	8.2 (7.1 [20])
ZIF-79	704997 [20]	0.55	4.4 (4.0 [20])	7.9 (7.5 [20])
ZIF-82	705002 [20]	0.64	10.4 (8.1 [20])	12.9 (12.3 [20])

* value for the “closed pore” structure. ** discrepancy due to crystal disorder in the published structure

Section S4. Potential energy maps and energy as a function of pressure in ZIFs 68-82

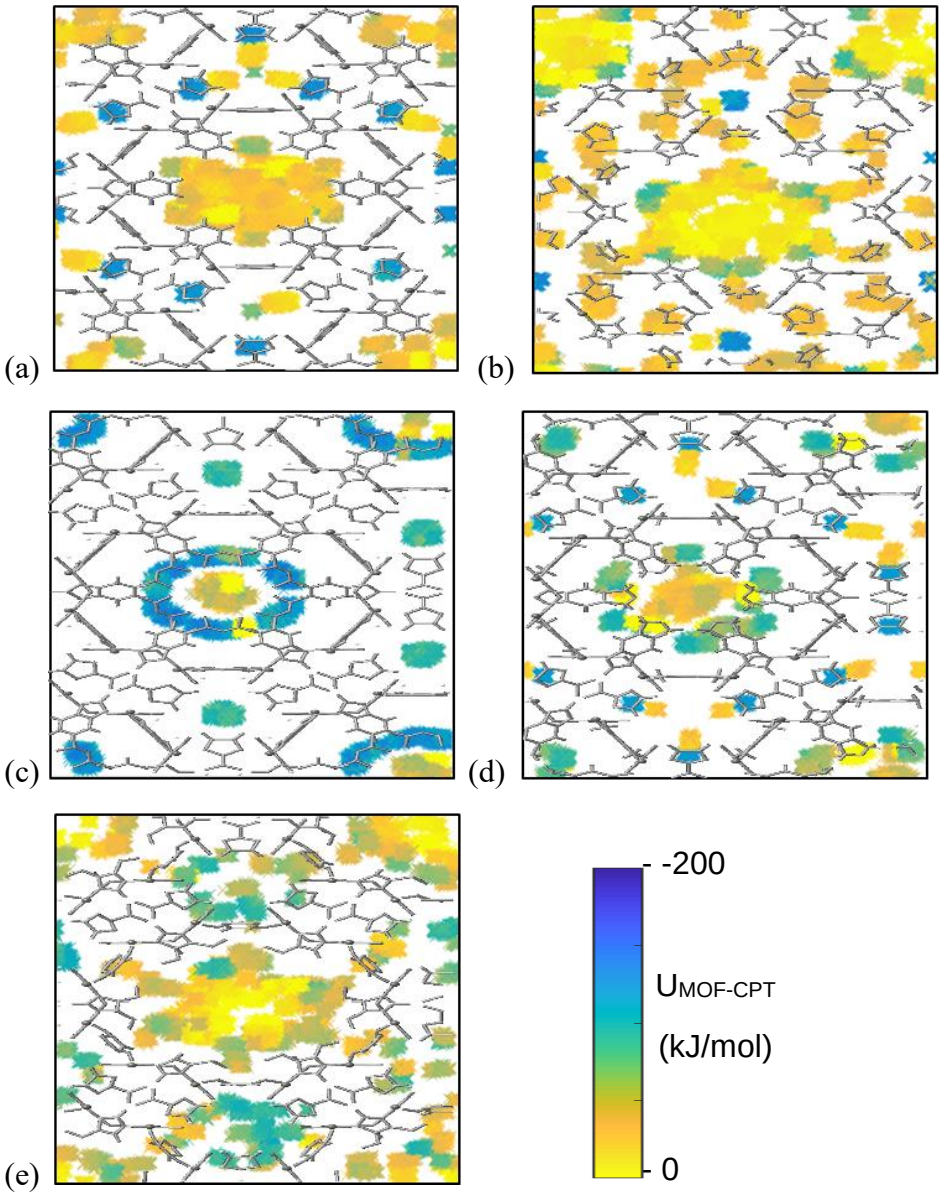

Figure S2. $U_{MOF-CPT}$ energy maps in (a) ZIF-68, (b) ZIF-70, (c) ZIF-78, (d) ZIF-79, and (e) ZIF-82.

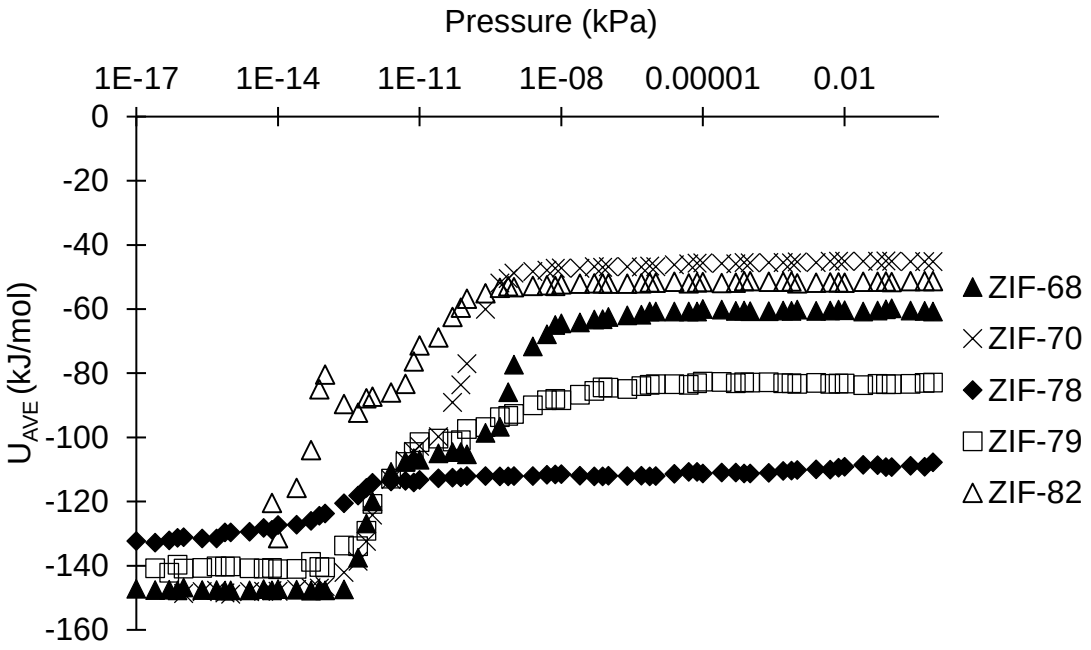

Figure S3. U_{AVE} as a function of pressure in ZIF-68, ZIF-70, ZIF-78, ZIF-79, and ZIF-82

Section S5. Testing the flexibility window of ZIFs 8, 11, and 78

We used GASP [13] to generate a series of structures within the flexibility windows of ZIF-8, ZIF-11, and ZIF-78, and performed *ab-initio* static energy calculations on the output to determine the relative potential energies of each structure compared to their lowest energy variant (i.e. the bonded contribution to the total energy barrier). We then compared the results to the PLD obtained during SMD simulations to determine whether or not the forcefield used (UFF [21]) allows for too much flexibility of the pore window, therefore allowing us to determine whether or not cisplatin really can move through the pore windows. Figure S4 shows the bonded energy barriers and PLD for each GASP variant and the SMD configurations during pore-hopping. For ZIFs-8/78, the PLD at the time of pore-hopping is within the flexibility window. For ZIF-11, the pore-hop PLD is slightly larger than those achieved using GASP. By uniformly expanding the unit cell, it is therefore not possible to move cisplatin through ZIF-11 without breaking the local geometry.

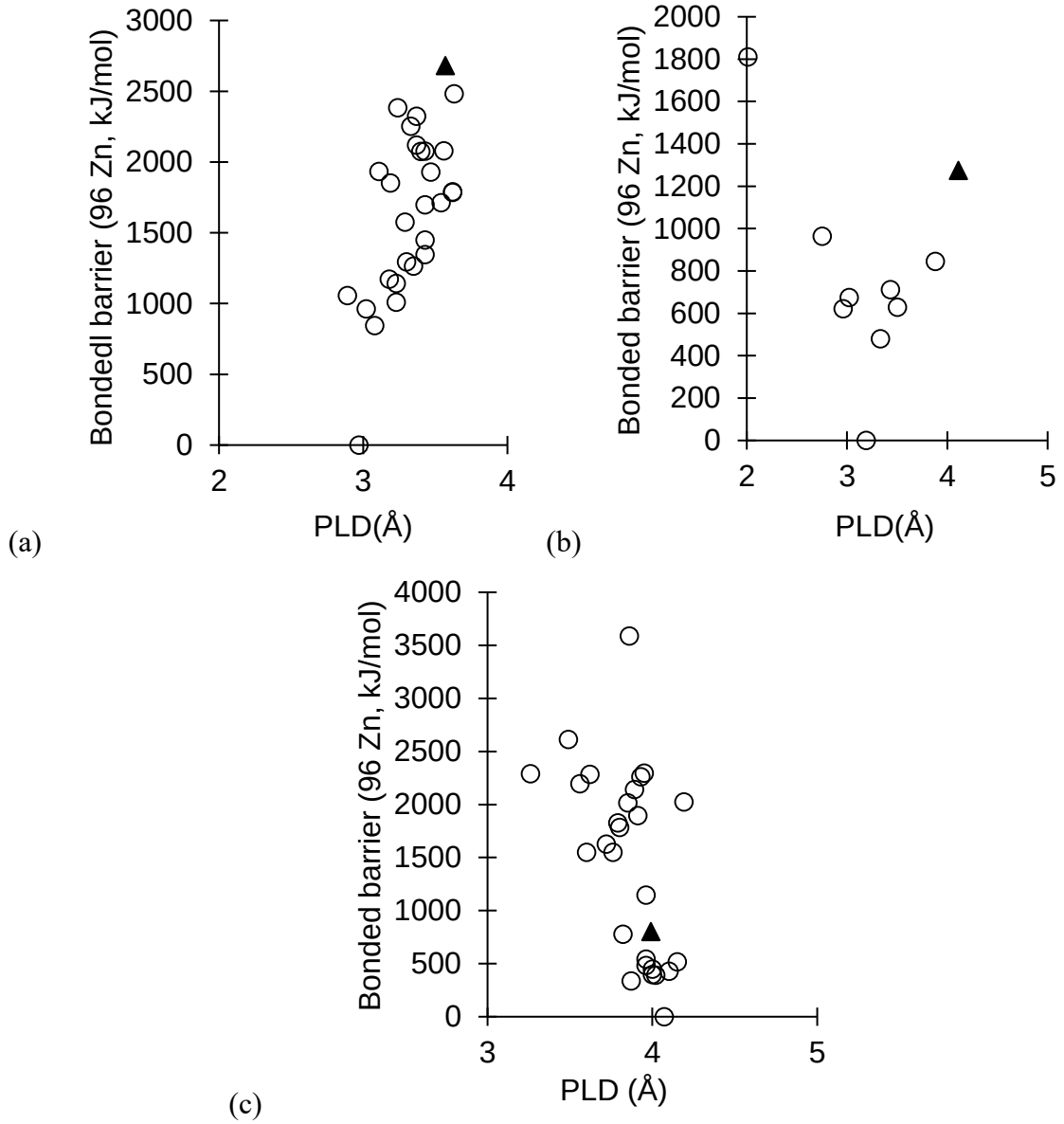

Figure S4. Potential energy barrier as a function of PLD in the GASP variants and the SMD configuration during pore-hopping. Points with zero energy barrier are the PLD of the lowest energy variant. Shown for ZIFs (a) 8, (b) 11, and (c) 78.

References

1. Hutter, J., et al., *cp2k: atomistic simulations of condensed matter systems.* Wiley interdisciplinary reviews. Computational molecular science, 2014. **4**: p. 25.
2. VandeVondele, J., et al., *Quickstep: Fast and accurate density functional calculations using a mixed Gaussian and plane waves approach.* Computer Physics Communications, 2005. **167**(2): p. 103-128.
3. Borštnik, U., et al., *Sparse matrix multiplication: The distributed block-compressed sparse row library.* Parallel Computing, 2014. **40**(5): p. 47-58.

4. Frigo, M. and S.G. Johnson, *The Design and Implementation of FFTW3.* Proceedings of the IEEE, 2005. **93**(2): p. 216-231.
5. VandeVondele, J. and J. Hutter, *An efficient orbital transformation method for electronic structure calculations.* The Journal of Chemical Physics, 2003. **118**(10): p. 4365-4369.
6. Lippert, B.G., J.H. Parrinello, and Michele, *A hybrid Gaussian and plane wave density functional scheme.* Molecular Physics, 1997. **92**(3): p. 477-488.
7. VandeVondele, J. and J. Hutter, *Gaussian basis sets for accurate calculations on molecular systems in gas and condensed phases.* The Journal of Chemical Physics, 2007. **127**(11): p. 114105.
8. Perdew, J.P., K. Burke, and M. Ernzerhof, *Generalized Gradient Approximation Made Simple.* Physical Review Letters, 1996. **77**(18): p. 3865-3868.
9. Grimme, S., S. Ehrlich, and L. Goerigk, *Effect of the damping function in dispersion corrected density functional theory.* J Comput Chem, 2011. **32**(7): p. 1456-65.
10. Grimme, S., et al., *A consistent and accurate ab initio parametrization of density functional dispersion correction (DFT-D) for the 94 elements H-Pu.* The Journal of Chemical Physics, 2010. **132**(15): p. 154104.
11. Hartwigsen, C., S. Goedecker, and J. Hutter, *Relativistic separable dual-space Gaussian pseudopotentials from H to Rn.* Physical Review B, 1998. **58**(7): p. 3641-3662.
12. Goedecker, S., M. Teter, and J. Hutter, *Separable dual-space Gaussian pseudopotentials.* Physical Review B, 1996. **54**(3): p. 1703-1710.
13. Wells, S.A. and A. Sartbaeva, *GASP: software for geometric simulations of flexibility in polyhedral and molecular framework structures.* Molecular Simulation, 2015. **41**(16-17): p. 1409-1421.
14. Sarkisov, L. and A. Harrison, *Computational structure characterisation tools in application to ordered and disordered porous materials.* Molecular Simulation, 2011. **37**(15): p. 1248-1257.
15. Trickett, C.A., et al., *Definitive Molecular Level Characterization of Defects in UiO-66 Crystals.* Angewandte Chemie International Edition, 2015. **54**(38): p. 11162-11167.
16. Zhu, X., et al., *Inherent anchorages in UiO-66 nanoparticles for efficient capture of alendronate and its mediated release.* Chemical Communications, 2014. **50**(63): p. 8779-8782.

17. Park, K.S., et al., *Exceptional chemical and thermal stability of zeolitic imidazolate frameworks.* Proceedings of the National Academy of Sciences, 2006. **103**(27): p. 10186-10191.
18. Hobday, C.L., et al., *Understanding the adsorption process in ZIF-8 using high pressure crystallography and computational modelling.* Nature Communications, 2018. **9**(1): p. 1429.
19. He, M., et al., *Toluene-assisted synthesis of RHO-type zeolitic imidazolate frameworks: synthesis and formation mechanism of ZIF-11 and ZIF-12.* Dalton Transactions, 2013. **42**(47): p. 16608-16613.
20. Banerjee, R., et al., *Control of Pore Size and Functionality in Isoreticular Zeolitic Imidazolate Frameworks and their Carbon Dioxide Selective Capture Properties.* Journal of the American Chemical Society, 2009. **131**(11): p. 3875-3877.
21. Rappe, A.K., et al., *UFF, a full periodic table force field for molecular mechanics and molecular dynamics simulations.* Journal of the American Chemical Society, 1992. **114**(25): p. 10024-10035.

CHAPTER 7. CONCLUSIONS

MOF nanoparticles are promising drug delivery carriers and molecular simulations provide a useful tool for screening frameworks for this application. Typically, MOFs are modelled as infinite periodic crystals, yet surprisingly few studies have addressed the influence of particle size on the crystal's performance. Size-dependent N_2 adsorption and induced flexibility in DUT-8(Ni) was modelled in Chapter 3, which focussed on the influence of the external surface. Adsorption energies on the external surface are significantly reduced where the typical ligands are replaced by smaller modulators. This effect is short-ranged however, and all pores in the crystal (regardless of their distance from the external surface) will exhibit the same adsorption sites so long as the pores remain intact. For Chapters 4-6, it was therefore concluded that the bulk crystal was sufficient for modelling drug uptake and release rates in MOF nanoparticles. Modulators on the external surface influence dispersion interactions within the framework, allowing us to manipulate the internal energy and hence the gate-opening/closing behaviour. Larger modulators enhance dispersion interactions which favour the closed pore structure, and this principle is generally applicable. This demonstrates for the first time that modulators can be systematically used to control the gate opening / closing pressure.

In Chapter 4, a variety of simulation methods were assessed against experimental results for their ability to model cisplatin uptake and release in biocompatible MOFs, UiO-66 and UiO-66(NH_2). Pure-component GCMC simulations are usually used to model drug molecule uptake, and when applied they accurately capture the maximum cisplatin loading achieved using conjugation. However, this loading substantially exceeds that achieved using encapsulation due to favourable energies associated with cisplatin's solvation shell which drives the polar guest molecules out of the pores too small to accommodate the shell (as shown by BAR simulations with water). Interaction energies (from pure-component GCMC or *ab-initio* simulations) or energy landscapes (from biased MD simulations) can be used as a semi-quantitative way of comparing release rates in different MOFs, however solvated MD simulations show that such models are slightly naive due to the formation of the solvation shell which displaces cisplatin from the favourable adsorption sites. In the case of polar cisplatin molecules, polar functional groups in UiO-66(NH_2) form hydrogen bonds with water which in turn anchors cisplatin. This shows the crucial role of water in the uptake and release of polar guest molecules from solution, and though we can infer a system's behaviour

using pure-component simulations, it is essential to understand the limitations associated with doing so.

A MOF's drug loading capacity is predominantly governed by its accessible pore volume, which can be systematically increased by adding defects or using different building units. In Chapter 5, UiO-66 (which is prone to missing ligand defects) was compared against its isoreticular variants UiO-67 and UiO-68 (which are comparatively defect-free) for their ability to retain cisplatin. Non-solvated MD simulations in defective UiO-66 predictably showed that cisplatin diffusivity decreases with the pore-window size and polarity of modulators. Unexpectedly, the exact positions of defects significantly influenced cisplatin diffusivity, indicating the lack of control defects impose. MOF – cisplatin interaction energies in UiO-67 and UiO-68 resulted in similar diffusivities compared to defective UiO-66. When water was added, the same comparison could be made for UiO-67(NH_2) and UiO-68(NH_2), showing that the larger pores of functionalised frameworks can offer the same level of cisplatin retention as defective UiO-66. It was hence recommended that manipulating MOF – drug interaction energies in wider pore frameworks using functional groups is a superior means of retaining drug cargo compared to using the narrow pore-window diameters as the diffusion bottleneck. This conclusion is important due to the additional benefit that more accessible pores with stronger MOF – drug interaction energies will also enhance the rate of uptake from solution.

In Chapter 6, a variety of pH sensitive ZIFs were screened for their ability to uptake and retain cisplatin. Pure-component GCMC simulations show that the maximum loading is proportional to the accessible pore volume, and biased MD simulations show that the energy barriers associated with interpore movement can be enhanced with smaller pore-window diameters or by incorporating strong, discretised adsorption sites. Out of the ZIFs screened, non-polar ZIFs 8 and 11 were excluded because of their small pore window diameter which hinder encapsulation. Polar groups on the other hand enhance encapsulation and anchor polar cisplatin molecules, yet this effect is forfeit if the polar sites are in close proximity as they can form channels with low energy barriers for cisplatin to freely move along as is the case e.g. in ZIF-78. The most promising frameworks have a large variation in interaction energies as for example in ZIF-82 where the alternation of polar/non-polar regions which creates large energy barriers. Ultimately, an ideal drug delivery carrier will have dispersed polar and non-polar functional groups in large channels with interconnecting windows that are wider than the drug molecule of interest.

Overall, the future selection of drug delivery carriers needs to be carried out with consideration of all stages of the process, from uptake into the framework (which relies on accessibility, thermodynamic equilibrium, and kinetic factors), to release in the vicinity of the tumour (which further relies on the stability of the MOF). This work has shown that although a framework might appear promising for one of these stages, it could be ineffective as a drug delivery carrier because of shortcomings in another stage (e.g. UiO-66 shows good retention properties, however as this is due to kinetic hinderance the initial uptake is also hindered). It has also shown that due to the sensitivity of drug molecule movement and adsorption with respect to precise details of the framework (such as the precise positions of functional groups and defects), we should focus on promising materials with which we have good control of the structure experimentally. In the case of cisplatin, it is recommended to focus on using structures in which the bulk material is defect-free, with inherent, dispersed functionality controlling the adsorption and release rates as-opposed to kinetic hinderance controlled by pore window size.

When screening MOFs for the general delivery of chemotherapeutics, it is proposed that pH sensitive frameworks (in which either only the MOF-drug bonds hydrolyse, or the framework fully degrades when exposed to acidic environments) are considered at the first stage of screening. This work emphasises that molecular simulations are a useful tool in secondary screening stages, as they provide vast amounts of thermodynamic insight into drug uptake and delivery. It also shows that we cannot rely on conclusions drawn from molecular simulations alone unless we are fully aware and forthcoming on the entirety of the limitations. As an example, it would be easy to claim that cisplatin is retained in amine functionalised variants of MOFs because of enhanced MOF-cisplatin interaction energies yet adapting the model to include water invalidates this conclusion due to the solvation shell. It is crucial to understand the pros and cons of different simulation techniques, and the artefacts that can arise from over-simplistic methods and models. For example, assuming specific defect configurations or neglecting water can have substantial impacts on the calculated cisplatin diffusion rates. Finally, this work accentuates the future need for combined simulation – experimental collaboration, to determine what happens in real-life MOF-drug delivery systems, and to gain thermodynamic insights into why this happens, so that future carriers can be systematically improved. Suggestions for future work specific to cisplatin delivery are highlighted in Chapter 8.

CHAPTER 8. FUTURE WORK

8.1. Shortcomings of the presented work and proposed solutions

One of the main shortcomings of the presented work is that the forcefields are not specifically derived for cisplatin in solvated MOFs. Therefore, the results could loosely represent the real-life system (highlighting the need for experimental contributions). Though the results obtained in this work were qualitatively validated against *ab-initio* simulations, to obtain meaningful quantitative results the forcefield should ideally be derived for cisplatin/water adsorption. For example, MOF-cisplatin forcefields can be developed using DFT simulations: First, initial forcefield parameters can be used to generate random configurations of cisplatin in the MOF. Single-point static energy calculations can then be used to calculate the system energy. By comparing the DFT energy to the potential energy function, the forcefield parameters can be updated and used to regenerate configurations in an iterative loop until the parameters no longer need updating [1]. Alternatively, forcefields can be derived experimentally, however this top-down approach is mainly used for fluids (for example based on vapour-liquid equilibria [2]) and it is a challenging to produce an accurate forcefield for chemically diverse solids like MOFs [3]. Instead, to avoid the need for forcefield development, systems can be modelled using *ab-initio* methods. However, this is computationally demanding. For screening purposes, it may be futile to create system-specific forcefields, because the main reason they would be used is to reduce computational cost, however individual forcefields would need to be derived for each framework, which (in itself) would be computationally demanding. It is therefore proposed that *ab-initio* methods should be used as a next screening step, focussing on the MOFs already screened from a wider range using universal classical forcefields (e.g. ZIF-82, ZIF-8 or UiO-68(NH_2), as recommended in Chapters 5/6).

Simulations in Chapters 5 and 6 show that slight variations in the framework (e.g. the exact position of functional groups, defects, or slight motion of the framework atoms) can significantly impact cisplatin diffusivity and uptake. Therefore, results that rely on marginal differences in the MOF structure are at best predictions. The motion of atoms in the framework have been captured to an extent in this thesis using simulation techniques such as GASP [4] and keeping the framework unrestrained during MD simulations (however atomic displacements in this work are determined using the Universal Forcefield which is parameterised for alike chemical environments [5], not for specific MOFs). Alternatively,

extreme case scenarios based on the root-mean-square displacement of atoms often reported with structures derived from X-Ray diffraction could be used to obtain a prediction for the accuracy of results. The precise position of functional groups and defects in the structure cannot be easily confirmed, yet experimental techniques are being developed to improve controllability of such uncertainties. For instance, techniques such as sequential linker installation (a multi-stage synthesis method where ligands are sequentially added to a pre-made MOF, and the positions are controlled based on the ligand/pre-made MOF connectivity and compatibility [6]) are progressing, giving researchers better control over precise functionalisation. Defects are also becoming better understood and easier to controlled, for instance they can be reduced in UiO-66 using enhanced synthesis temperatures or more acidic modulators which increase correction rates (of defects) during crystallisation [7, 8]. These synthesis techniques could be used to create promising drug-delivery carriers with more control, which could then be compared to theoretical models that better represent the real system.

Finally, this work has highlighted how changing the model to account for water influences diffusivity and adsorption. In reality, plasma contains ~90 % water, and the remaining 10 % consists of coagulants, proteins, electrolytes, and immunoglobulins [9]. Most of the components (besides water and electrolytes) cannot enter the pores of microporous MOFs, therefore including the additional components in simulations is unlikely to change the results. However, the initial selection of pH sensitive MOFs (that are stable in water) in Chapter 6 needs to be further tested to check their stability in plasma. For example, it is known from PXRD experiments that UiO-66 shows no degradation when immersed in water for over 24 hours [10], but in phosphate buffer saline (a solution containing salts that is isotonic like blood) uncoated UiO-66 nanoparticles degrade by 85 % after six hours [11].

8.2. Simulation perspectives on future work

From a computational perspective, it is now known what bulk properties of a MOF to aim for to achieve an ideal cisplatin drug delivery carrier. Simulations are useful for understanding fundamental property – performance relationships, screening drug delivery carriers and running what-if scenarios (e.g. what-if certain functional groups are present in the framework, how will this influence the drug delivery efficiency). Future computational contributions should revolve around functionalising the external surface to prevent premature release (e.g. conjugating polymers onto the surface to block pores and/or prevent

hydrolysis of metal – ligand bonds by repelling water [12]), prevent nanoparticle agglomeration (e.g. via the impregnation of polymers into the framework to create steric hinderance against agglomeration [13]), or to target the tumour (e.g. conjugating targeting molecules onto the external surface such as folic acid [14]).

For example, Chapter 3 revealed that dispersion interactions between modulators on the external surface of DUT-8 can be used as a tool to manipulate gate-opening and gate-closing [15]. Using biocompatible breathing MOFs (e.g. iron (III) carboxylate MOFs such as MIL-53(Fe) [16]), it is worth applying OFAST [17] to determine the most energetically favourable structure of the framework upon the adsorption of drug + water molecules (based on experimental characterisation of MIL-53(Fe)@[water + lutidine] and MIL-53(Fe)@[water + pyridine], the favourable pore size will depend on guest – host interaction energies [18]). The most energetically favourable structure will further depend upon what biomolecules are used to cap the external surface (as shown in Chapter 3, this will depend on how they influence the internal energy of the structure [15]). For instance, folate or hyaluronic acid could be used to prevent premature release and target tumours [14], and these groups are substantially larger than those used in this thesis, hence should enhance dispersion interactions potentially favouring a closed pore structure. Normal and biased classical MD simulations could then be used to quantify release rates in the presence of water for each of the optimised structures. Alternatively (depending on the availability of computational resources), *ab-initio* simulations could be carried out to accurately model diffusion in completely flexible structures which are not imposed with the typical constraints used in classical simulations (the simulations would not depend on the starting structures used to build the MD topology). A hypothetical smart delivery device could consist of pH sensitive conjugation bonds between targeting biomolecules such as folate and the external surface of the framework. As mentioned, large biomolecules will (likely) favour a closed pore structure, yet if hydrolysed an open pore variant may be more optimal (to accommodate more water molecules and enhance the host-guest interaction energies). Therefore, it could be possible to get enhanced release only upon a change in pH in the microenvironment of the tumour, since (as shown by simulations in Chapters 5 and 6) drug molecule diffusion is easier in larger open pore structures.

Other useful research directions would be to engineer the nanoparticle's shell (external surface) to: (i) enable tumour recognition, (ii) enable pH sensitive drug release, (iii) block pores at the external surface, (iv) not interfere with pores in the bulk crystal, and (v) avoid

nanoparticle agglomeration [19]. While (i) and (ii) can be achieved by careful selection of the MOF – capping biomolecule combination, (iii) and (iv) can be tested using DFT and MD simulations to investigate the binding energy associated with incorporating (via impregnation or conjugation) different capping biomolecules onto the external surface to study the most likely interfacial properties (e.g. similar to the work of Semino et al [20]). Nanoparticle agglomeration (v) can potentially be quantified using bias MD simulations such as umbrella sampling.

8.3. Experimental perspectives on future work

One of the main conclusions drawn from this thesis is that large interconnecting windows between functionalised pores are a better means of controlling drug molecule diffusion compared to using the pore-window diameter as a bottleneck (because the former will likely enhance encapsulation). It would be beneficial to test the MOFs recommended from this conclusion, by determination of cisplatin loading by encapsulation, in vitro release rates (initially), and cell viability studies [21]. In particular, the high diffusion energy barriers associated with channels interconnected by large pore windows rely on segregated adsorption sites. It is worth clarifying whether (or not) this conclusion is valid at higher loadings of cisplatin (since some of the molecules could feasibly bypass the discretised favourable sites).

Other information that would be useful from a screening perspective is ideal release rates for a specific cancer type. For instance, if experiments show that release rates are too fast to retain cisplatin in the large, interconnected pores of recommended MOFs ZIF-82 or UiO-68(NH_2), then they could be reduced further by enhancing the MOF – cisplatin interaction energies (e.g. via conjugation). Alternatively, (as mentioned) target specific biomolecules (e.g. pH sensitive conjugated biomolecules) could be used on the surface to block pores and prevent premature release. However, at what point should the release rate be declared too fast or too slow? Potentially this could preliminary be answered by comparing release rates and testing the cell viability in vitro using samples of cancer cells and normal cells. However in vitro samples will not correctly represent the variation in pH usually targeted during chemotherapy due to the buffers used to maintain a cell culture and the lack of physiological structure of the tumour's microenvironment. For this reason, in vivo studies would be more representative to trial potential frameworks and it could provide useful targets to aim for in future computational screening studies of MOF – drug systems.

One of the key issues in chemotherapy is that tumours can develop drug resistance. As well as increasing the initial dose using drug delivery carriers, an alternate drug with different attack mechanism could be used. Cisplatin mainly forms intrastrand crosslinks with DNA [22], however an isomer of cisplatin, transplatin, forms interstrand crosslinks [23] which are more effective at disrupting critical cell processes [24]. To date, transplatin is ineffective as a chemotherapeutic because it is highly reactive and deactivates in the circulatory system [25]. If transplatin is protected from degradation however, for instance using a pH activated prodrug or nanocarrier, it could be a highly effective anti-cancer drug [26]. Should an ideal MOF for targeted drug delivery be discovered and thoroughly tested in future, it may be beneficial to use a more potent chemotherapeutic such as transplatin.

8.4. Chapter 8 References

1. Demir, H., et al., *DFT-based force field development for noble gas adsorption in metal organic frameworks.* Journal of Materials Chemistry A, 2015. **3**(46): p. 23539-23548.
2. Eggimann, B.L., et al., *An online parameter and property database for the TraPPE force field.* Molecular Simulation, 2014. **40**(1-3): p. 101-105.
3. Heinen, J. and D. Dubbeldam, *On flexible force fields for metal–organic frameworks: Recent developments and future prospects.* WIREs Computational Molecular Science, 2018. **8**(4): p. e1363.
4. Wells, S.A. and A. Sartbaeva, *GASP: software for geometric simulations of flexibility in polyhedral and molecular framework structures.* Molecular Simulation, 2015. **41**(16-17): p. 1409-1421.
5. Rappe, A.K., et al., *UFF, a full periodic table force field for molecular mechanics and molecular dynamics simulations.* Journal of the American Chemical Society, 1992. **114**(25): p. 10024-10035.
6. Yuan, S., et al., *Sequential Linker Installation: Precise Placement of Functional Groups in Multivariate Metal–Organic Frameworks.* Journal of the American Chemical Society, 2015. **137**(9): p. 3177-3180.
7. Morris, W., et al., *Role of Modulators in Controlling the Colloidal Stability and Polydispersity of the UiO-66 Metal–Organic Framework.* ACS Applied Materials & Interfaces, 2017. **9**(39): p. 33413-33418.

8. DeStefano, M.R., et al., *Room-Temperature Synthesis of UiO-66 and Thermal Modulation of Densities of Defect Sites.* Chemistry of Materials, 2017. **29**(3): p. 1357-1361.
9. Mathew, J., P. Sankar, and M. Varacallo, *Physiology, Blood Plasma*. 2020: StatPearls.
10. Cavka, J.H., et al., *A New Zirconium Inorganic Building Brick Forming Metal Organic Frameworks with Exceptional Stability.* Journal of the American Chemical Society, 2008. **130**(42): p. 13850-13851.
11. Abánades Lázaro, I., et al., *Selective Surface PEGylation of UiO-66 Nanoparticles for Enhanced Stability, Cell Uptake, and pH-Responsive Drug Delivery.* Chem, 2017. **2**(4): p. 561-578.
12. Zhong, J., et al., *Recent Advances in Polymeric Nanocomposites of Metal-Organic Frameworks (MOFs).* Polymers, 2019. **11**(10): p. 1627.
13. Horcajada, P., et al., *Porous metal–organic-framework nanoscale carriers as a potential platform for drug delivery and imaging.* Nature Materials, 2010. **9**(2): p. 172-178.
14. Gao, X., et al., *Controllable synthesis of smart multifunctional nanoscal metal-organic framework for magnetic resonance/optical imaging and targeted drug delivery.* ACS applied materials & interfaces, 2017. **9**.
15. Thompson, M., et al., *Size-dependent adsorption and framework flexibility in DUT-8(Ni)*. 2020, University of Bath.
16. Baati, T., et al., *In depth analysis of the in vivo toxicity of nanoparticles of porous iron(iii) metal–organic frameworks.* Chemical Science, 2013. **4**(4): p. 1597-1607.
17. Coudert, F.-X., *The osmotic framework adsorbed solution theory: predicting mixture coadsorption in flexible nanoporous materials.* Physical Chemistry Chemical Physics, 2010. **12**(36): p. 10904-10913.
18. Millange, F., et al., *Selective Sorption of Organic Molecules by the Flexible Porous Hybrid Metal−Organic Framework MIL-53(Fe) Controlled by Various Host−Guest Interactions.* Chemistry of Materials, 2010. **22**(14): p. 4237-4245.
19. Ploetz, E., et al., *The Chemistry of Reticular Framework Nanoparticles: MOF, ZIF, and COF Materials.* Advanced Functional Materials. **n/a**(n/a): p. 1909062.
20. Semino, R., et al., *Microscopic Model of the Metal–Organic Framework/Polymer Interface: A First Step toward Understanding the Compatibility in Mixed Matrix Membranes.* ACS Applied Materials & Interfaces, 2016. **8**(1): p. 809-819.

21. Mocniak, K.A., et al., *Incorporation of cisplatin into the metal–organic frameworks UiO66-NH2 and UiO66 – encapsulation vs. conjugation.* Royal Society Chemistry Advances, 2015. **5**(102): p. 83648-83656.
22. Eastman, A., *The formation, isolation and characterization of DNA adducts produced by anticancer platinum complexes.* Pharmacology & Therapeutics, 1987. **34**(2): p. 155-166.
23. Brabec, V. and M. Leng, *DNA interstrand cross-links of trans-diamminedichloroplatinum(II) are preferentially formed between guanine and complementary cytosine residues.* Proceedings of the National Academy of Sciences, 1993. **90**(11): p. 5345-5349.
24. Enoiu, M., J. Jiricny, and O.D. Schärer, *Repair of cisplatin-induced DNA interstrand crosslinks by a replication-independent pathway involving transcription-coupled repair and translesion synthesis.* Nucleic Acids Research, 2012. **40**(18): p. 8953-8964.
25. Jung, Y. and S.J. Lippard, *Direct Cellular Responses to Platinum-Induced DNA Damage.* Chemical Reviews, 2007. **107**(5): p. 1387-1407.
26. Li, W., et al., *Turning Ineffective Transplatin into a Highly Potent Anticancer Drug via a Prodrug Strategy for Drug Delivery and Inhibiting Cisplatin Drug Resistance.* Bioconjugate Chemistry, 2016. **27**(8): p. 1802-1806.